System-Level Performance of Interference-Aware Spatial Frequency Reuse

Ratheesh Kumar Mungara

TESI DOCTORAL UPF / 2016

Director de la tesi

Dr. Angel Lozano Solsona
Wireless Communications Research Group
Dept. of Information and Communication Technologies

Wireless Communications Research Group (`http://wicom.upf.edu/`), Department of Information and Communication Technologies (`http://www.upf.edu/etic`), Universitat Pompeu Fabra (`http://www.upf.edu`), Barcelona, Spain

The doctoral defense was held on ..... at the Universitat Pompeu Fabra and scored as .....

Dr. Angel Lozano Solsona
(Thesis Supervisor)
Universitat Pompeu Fabra (UPF), Barcelona

Dr. Matilde Sánchez Fernández
(Thesis Committee Member)
Universidad Carlos III de Madrid (UC3M), Spain

Dr. Alfonso Martinez
(Thesis Committee Member)
Universitat Pompeu Fabra (UPF), Barcelona

Dr. Radha Krishna Ganti
(Thesis Committee Member)
Indian Institute of Technology Madras (IITM), Chennai

Dedicated to my parents

Ramachandraiah and Prameela Mungara.

Acknowledgements

The last five years have been an incredible learning experience, while simultaneously nurturing my research career along the way. It is my great pleasure to acknowledge several individuals who have contributed to make this journey memorable.

I would first like to express my deepest gratitude to my dissertation advisor, Prof. Angel Lozano, for his valuable guidance and support throughout my stay at UPF, Barcelona. I am constantly being inspired by his outstanding style of research with its distinctive trait of challenging conventional wisdom through first principles, and his great sense of aesthetics. I shall be highly indebted to him for his encouraging words, providing the flexibility and freedom to pursue my academic interests. Most of the improvement in my academic writing and presentation skills is attributed to his critical comments and feedback. The formulation of meaningful research problems and high moral and ethical standards are the two important qualities that I wish to retain from him for my future research career.

I would also like to thank my committee members Prof. Matilde Sánchez Fernández, Prof. Alfonso Martinez, Prof. Radha Krishna Ganti, Prof. Olga Muñoz Medina and Prof. Vanesa Daza Fernandez for their insightful comments and feedback. During these years, I am fortunate to have collaborations and stimulating discussions with some exceptional researchers. I'm extremely grateful to Prof. Markku Juntti for giving me an opportunity to work—before moving to Barcelona—at the Centre for Wireless Communications (CWC), Oulu, and to Dr. Antti Tölli, who had introduced and encouraged me to pursue Interference Alignment, which later became one of the topics of my dissertation. I owe a debt of gratitude to Prof. Robert

Heath Jr., for hosting me in Austin during the Spring of 2014, which gave me an opportunity to had interactions with several researchers at Wireless and Networking Communications Group (WNCG). Part of my dissertation work was inspired from the discussions that I had with Dr. Xinchen Zhang and Prof. Heath at WNCG. Thanks also to Dr. David Morales-Jiménez for his collaboration and to Dr. Ilaria Thibault for sharing the Vodafone field test data as well as for her collaboration. My special thanks are due to Geordie George for being a joyful and inspiring office mate for all these years. The cooperation and joint work with him proved to be very fruitful and I hope it will continue in the future.

The work presented in the dissertation has been funded through the doctoral fellowship, in part, with teaching assistantship from the Department of Information and Communication Technologies (DTIC) at UPF; and they are gratefully acknowledged. Additionally, the work in parts was conducted in the European Union's project HIATUS, the Spanish government's MINECO projects, and Intel's University 5G Research Program. This financial support stimulated me to engage even more in my research work. I take this opportunity to thank the DTIC Secretariat as well as the research staff service unit of the Human Resources Department, for their advice in many practical matters and for taking care of my paper work.

I have also had the pleasure to be surrounded by cheerful colleagues and friends inside and outside of UPF. I wholeheartedly thank them, for all the great moments during these years.

Words fail me in expressing my gratitude towards my family. Dear Mom and Dad, without the inspiration, drive and support you gave me, I can't imagine coming so far and fulfilling my career aspirations. The sacrifices you have made during my life are priceless. I can only express my love to you. I thank my brother Manoj for all his company and care when he was in Barcelona, during the second and third years of my research, and my sister Sireesha and my brother-in-law Raghu for their encouragement. I express my sincere gratitude to my uncle Ramesh, for imparting the value of education from my childhood. I also thank my parents-in-law for instilling a positive spirit in me. Finally, love to my wife Ashlesha. Though we met only a year before I completed my dissertation, she brought so much love to my life and has been there by my side during all these moments.

Ratheesh Kumar Mungara

Barcelona, 20th September 2016

Abstract

Spatial frequency reuse is a long-established approach for enhancing the capacity of wireless systems through increased spectral efficiency (bits per second per unit bandwidth). The future 5th generation of wireless systems is expected to incorporate various forms of frequency reuse. This includes multiple-input multiple-output (MIMO) communication enabling frequency reuse across antennas, device-to-device (D2D)-based densification allowing spectrum reuse across direct communication links, and full duplexing utilizing the same spectrum for communication in the transmit and receive directions.

This dissertation aims at determining the performance limits of emerging wireless systems underpinned by dense spatial frequency reuse and interference suppression, and to glean key system design insights. Stochastic geometry is the toolbox invoked to conduct the analysis, with network locations modeled as points of a Poisson process. A new framework is developed by introducing a Gaussian fit to the interference and variable degrees of spatial averaging, which enable more meaningful results and compact expressions compared to those of existing analyses.

Within this framework, we first consider MIMO spatial multiplexing and interference alignment (IA). The former scheme utilizes all available spatial dimensions for signaling and the latter minimizes interference at the expense of knowing the instantaneous fading states at both transmitters and receivers and of a reduction in spatial signaling dimensions. Despite the intense work on IA and spatial multiplexing, there is limited work aimed at understanding their engineering tradeoff in the context of practically relevant cellular settings such as propagation losses, fading dynamics due to user mobility and imperfect knowledge of the fading states. We have

studied this problem in depth through both system- and link-level analyses. Even under perfect knowledge of the fading, IA is seen to be beneficial over spatial multiplexing only in very specific and relatively infrequent network situations, and IA loses all its advantages at vehicular speeds when the fading knowledge is imperfect.

Second, we focus on ITLinQ and FlashLinQ, the two principal channelization schemes proposed to date for controlling the interference in D2D networks. An analytical characterization of ITLinQ scheme is provided, opening the door to optimizing its controllable parameters. It is shown that both channelization schemes outperform the unchannelized baseline, with a slight edge for ITLinQ. On the most unfavorable network geometries, ITLinQ yields multiple-fold improvements in spectral efficiency with respect to an unchannelized network.

Finally, we introduce full-duplex transceivers in cellular networks and characterize the impact of increased interference on their performance. It is established through analysis and complemented by simulations on a Vodafone LTE field test network that additional user-to-user interference only has a minor impact while base-to-base interference would render full-duplex operation unfeasible in dense microcellular networks without any interference management.

In summary, MIMO spatial multiplexing and D2D-based densification are seen to play a vital role in improving wireless system capacity while IA and full duplexing are found to be ineffective.

Resum

La reutilització de la freqüència espacial és l'aproximació més acceptada per tal de millorar la capacitat dels sistemes wireless mitjançant l'increment de l'eficiència espectral (bits per segon per unitat d'ample de banda). S'espera que la futura cinquena generació de sistemes wireless incorpori diverses formes de reutilització de freqüència. Això inclou la comunicació multi-input multi-output (MIMO) que permet la reutilització a través d'antenes, densificació dispositiu-a-dispositiu (D2D) que permet reutilitzar l'espectre a través denllaços de comunicació directa, així com un full-dúplex emprant el mateix espectre per a la comunicació en la transmissió i recepció de direccions.

Aquest treball pretén determinar els límits de rendiment dels sistemes wireless emergents, basats en una densa reutilització de la freqüència espacial i en la supressió d'interferències, així com espigolar coneixement clau per al disseny de sistemes d'aquest tipus. La geometria estocàstica és l'eina que s'aplicarà a l'anàlisi que es durà a terme, modelitzant les localitzacions dins la xarxa com a punts d'un procés de Poisson. La introducció d'un ajust Gaussià a la interferència, conjuntament amb la consideració de nivells variables d'expectació espacial, han permès definir un nou marc matemàtic que fa possible unes expressions més compactes i uns resultats més significatius en comparació amb els anàlisis existents.

Dins d'aquest marc, en primer lloc es prenen en consideració la multiplexació MIMO i l'aliniament d'interferència (IA, en les seves sigles en anglès). El primer esquema empra totes les dimensions espacials disponibles per a la senyalització i el segon minimitza la interferència a costa de conèixer els estats de esvaïment instantani dels transmissors i receptors, i d'una reducció en les dimensions de senyalització espacial. Malgrat l'intens treball en l'IA i la multiplexació espacial,

s'ha prestat escassa atenció a tractar de comprendre el seu balanç denginyeria en el context d'xarxes cel·lulars de rellevància pràctica, com els de propagació de pèrdues, o les dinàmiques de esvaïment degudes a la mobilitat de l'usuari i al coneixement imperfecte dels estats de esvaïment. En aquest treball s'ha estudiat en profunditat aquest problema a través d'anàlisis tant a nivell dels enllaços com del sistema. Fins i tot en condicions de coneixement perfecte del esvaïment, l'IA resulta beneficiós sobre la multiplexació només en situacions de xarxa molt específiques i relativament infreqüents, mentre que perd tots els seus avantatges a velocitats vehiculars quan el coneixement del esvaïment és imperfecte.

En segon lloc, el treball es centra en el ITLinQ i el FlashLinQ, els dos principals esquemes de canalització proposats fins al moment per controlar la interferència en xarxes D2D. S'ofereix una caracterització analítica de l'esquema ITLinQ, obrint així la porta a l'optimització dels seus paràmetres controlables. Es mostra que tots dos esquemes de canalització aconsegueixen millors resultats que l'esquema no canalitzat, amb un lleuger avantatge per al ITLinQ. Considerant la geometria de xarxa més desfavorable, el ITLinQ produeix millores múltiples en l'eficiència espectral en comparació amb la xarxa no canalitzada.

Finalment, el treball introdueix els transreceptors full-dúplex en xarxes cel·lulars i caracteritza l'impacte de la interferència incrementada en el seu funcionament. A través d'anàlisis i de simulacions complementàries en una xarxa de test de Vodafone LTE, s'estableix que la interferència d'usuari a usuari té un impacte poc significatiu mentre que la interferència de base a base faria inviable l'operació full-dúplex en xarxes microcel·lulars sense gestió de les interferències.

En resum, aquest tesis doctoral aporta evidència de que el multiplexat MIMO i la densificació basada en D2D juguen un paper vital en la millora de la capacitat dels sistemes wireless mentre que el IA i el full-dúplex resulten inefectius.

Contents

List of Figures

List of Tables

Acronyms, Notation, and Symbols

Acronyms

3GPP	3rd Generation Partnership Project
5G	5th Generation
ARQ	Automatic Repeat reQuest
AWGN	Additive White Gaussian Noise
CA	Collision Avoidance
CDF	Cumulative Distribution Function
CoMP	Coordinated MultiPoint
CSI	Channel State Information
CSMA	Carrier Sense Multiple Access
CTS	Clear To Send
DoF	Degrees of Freedom
D2D	Device-to-Device
FDD	Frequency-Division Duplexing
IA	Interference Alignment
IID	Independent Identically Distributed
ISI	InterSymbol Interference
LTE	Long-Term Evolution
MIMO	Multiple-Input Multiple-Output
MMSE	Minimum Mean-Square Error
MU-MIMO	Multiuser MIMO
PDF	Probability Density Function
PPP	Poisson Point Process
RTS	Request To Send

SIR	Signal-to-Interference Ratio
SINR	Signal-to-Interference-plus-Noise Ratio
SNR	Signal-to-Noise Ratio
SU-MIMO	Single-User MIMO
TDD	Time-Division Duplexing
TDMA	Time-Division Multiple Access
TIN	Treat Interference as Noise

Notation

$\mathbb{1}(\cdot)$	Indicator function
${}_2F_1(\cdot,\cdot\,;\cdot\,;\cdot)$	Gaussian hypergeometric function
a, A	Scalars
$\boldsymbol{a}$	Column vector
$\boldsymbol{A}$	Matrix variable
$\lvert a\rvert$	Magnitude of a
$\Re(a)$	Real part of a
$\binom{A}{a}$	Binomial coefficient
$\lvert\lvert\boldsymbol{a}\rvert\rvert_2$	Vector 2-norm of $\boldsymbol{a}$
$\lvert\lvert\boldsymbol{A}\rvert\rvert_{\mathrm{F}}$	Frobenius norm of $\boldsymbol{A}$
$\det(\boldsymbol{A})$	Determinant of $\boldsymbol{A}$
$\mathrm{tr}(\boldsymbol{A})$	Trace of $\boldsymbol{A}$
$\boldsymbol{A}^{\mathrm{T}}$	Matrix transpose
$\boldsymbol{A}^*$	Matrix conjugate transpose
$\boldsymbol{A}^{-1}$	Matrix inverse
$A^\star$	Value of A that solves an optimization problem
$[\boldsymbol{A}]_{i,j}$	Entry of $\boldsymbol{A}$ in the ith row and jth column
$a\rvert_{\mathrm{dB}}$	$10\log_{10} a$
$\boldsymbol{I}_N$	$N \times N$ identity matrix
$\boldsymbol{0}_N$	$N \times N$ all-zero matrix
$\mathcal{B}_b(R)$	Circle centered at b with radius R
$\mathbb{C}^{N\times M}$	$N \times M$ complex space
$\mathcal{E}_n(\cdot)$	Exponential integral
$\mathbb{E}[\cdot]$	Expectation operator
$F_A(\cdot)$	Cumulative distribution function of A
$f_A(\cdot)$	Probability density function of A
$\Gamma(\cdot)$	Gamma function
$\bar{\Gamma}(\cdot,\cdot)$	Lower incomplete Gamma function
$G_{p,q}^{k,\ell}\left(\cdot \mid \begin{smallmatrix}\cdot,\ldots,\cdot\\ \cdot,\ldots,\cdot\end{smallmatrix}\right)$	Meijer-G function
i	Imaginary unit $\mathrm{i} = \sqrt{-1}$
$J_n(\cdot)$	Bessel function of the first kind
$\mathcal{L}_A(\cdot)$	Laplace transform of A
$\mathbb{M}$	Mark space
$\mathcal{N}_{\mathbb{C}}(\boldsymbol{a},\boldsymbol{A})$	Complex Gaussian distribution with mean $\boldsymbol{a}$ and covariance matrix $\boldsymbol{A}$
$\mathbb{P}[\cdot]$	Probability of an event
$\mathbb{R}^N$	N-dimensional real space
$\sim$	Distributed as

Common Symbols

α	Pilot symbol overhead
$\mathfrak{B}$	Bounded closed set
b	Transmitter location
B	Signal bandwidth (in Hz)
B_{c}	Channel coherence bandwidth (in Hz)
β	Pathloss intercept of base-to-user link
β_{u}	Pathloss intercept of user-to-user link
β_{b}	Pathloss intercept of base-to-base link with distance $\leq R_{\mathrm{c}}$
β_{B}	Pathloss intercept of base-to-base link with distance $> R_{\mathrm{c}}$
C	Ergodic link spectral efficiency (in b/s/Hz)
$\vec{C}$	Forward link ergodic spectral efficiency
$\overleftarrow{C}$	Reverse link ergodic spectral efficiency
$\bar{C}$	Average link spectral efficiency
$\bar{\vec{C}}$	Forward link average spectral efficiency
$\bar{\overleftarrow{C}}$	Reverse link average spectral efficiency
$\bar{C}^{\mathrm{sum}}$	Average sum spectral efficiency
$\bar{\mathcal{C}}$	Average area spectral efficiency (in b/s/Hz/km^2)
χ	Shadow fading
d	Spatial degrees of freedom
d	D2D intended link distance (in meters)
e	Retaining indicator of D2D link
η	Pathloss exponent of base-to-user link
η_{u}	Pathloss exponent of user-to-user link
η_{b}	Pathloss exponent of base-to-base link with distance $\leq R_{\mathrm{c}}$
η_{B}	Pathloss exponent of base-to-base link with distance $> R_{\mathrm{c}}$
F_{N}	Noise figure
$\gamma_{\mathrm{TX}}, \gamma_{\mathrm{RX}}$	FlashLinQ parameters
G_{b}	Base station antenna gain (in dBi)
γ_{EM}	Euler-Mascheroni constant
h_{b}	Base station antenna height (in meters)
h	Scalar channel
$\boldsymbol{h}$	Vector channel
$\boldsymbol{H}$	$N_{\mathrm{r}} \times N_{\mathrm{t}}$ channel matrix
$\hat{\boldsymbol{H}}$	Estimate of $\boldsymbol{H}$
$\tilde{\boldsymbol{H}}$	$\boldsymbol{H} - \hat{\boldsymbol{H}}$

$\bar{I}^{\text{sum}}$	Average sum mutual information (in b/s/Hz)
INR^{in}	Incoming interference-to-noise ratio
$\mathsf{INR}^{\text{out}}$	Outgoing interference-to-noise ratio
K	IA cluster size
$\mathcal{L}_\infty$	High-SNR power offset
λ	Wavelength (in meters)
λ	Density (intensity) of PPP Φ
λ_{b}	Base station density (in base stations/km^2)
λ_{u}	User device density (in users/km^2)
$\lambda_{\Psi_{\text{I}}}$	Density of Ψ_{I} (in links/km^2)
$\lambda_{\Psi_{\text{II}}}$	Density of Ψ_{II} (in links/km^2)
M, μ	ITLinQ parameters
m	Priority (time stamp) mark of D2D link
N_{d}	IA solution update interval (in symbols)
N_{fb}	CSI feedback sequence length (in symbols)
$N_{\max}$	$\max(N_{\text{r}}, N_{\text{t}})$
$N_{\min}$	$\min(N_{\text{r}}, N_{\text{t}})$
N_{p}	$N_{\text{pf}} + N_{\text{pr}} + N_{\text{fb}} + N_{\text{pd}}$ (in symbols)
N_{pf}	Forward common pilot sequence length (in symbols)
N_{pd}	Forward dedicated pilot sequence length (in symbols)
N_{pr}	Reverse common pilot sequence length (in symbols)
N_{r}	Number of receive antennas
N_{t}	Number of transmit antennas
ν_{M}	Maximum Doppler frequency (in Hz)
ρ^{eff}	Effective average SI(N)R
ρ_0	Local-average SI(N)R at the typical receiver
$\vec{\rho}_0$	Forward link local-average SIR at the typical receiver
$\overleftarrow{\rho}_0$	Reverse link local-average SIR at the typical receiver
φ	Realization of Φ
$\hat{\varphi}$	Realization of $\hat{\Phi}$
Φ	PPP on $\mathbb{R}^2$
$\hat{\Phi}$	Marked PPP on $\mathbb{R}^2 \times \mathbb{M}$
Φ_{b}	Base station point process
Φ_{u}	User point process
Ψ_{I}	ITLinQ type I transmitter point process
Ψ_{II}	ITLinQ type II transmitter point process
P	Transmit power (in Watts)
$\overleftarrow{P}$	Reverse link pilot power (in Watts)
P_{b}	Base station power (in Watts)
P_{u}	User device power (in Watts)

P	Palm distribution of point process
$\hat{\mathsf{P}}$	Palm distribution of marked point process
$r_{u,b}$	Distance from b to u
R	Exclusion region radius (in meters)
R	Averaging circle radius (in meters)
R_{c}	Critical distance (in meters)
σ_{dB}	Standard deviation of the shadow fading in dB
$\sigma^2_{\tilde{\boldsymbol{H}}}$	Variance of the entries of $\tilde{\boldsymbol{H}}$
σ^2_{N}	Variance of noise
$\boldsymbol{s}$	$\mathsf{d} \times 1$ data symbol vector
SIR	Instantaneous signal-to-interference ratio
SINR	Instantaneous signal-to-interference-plus-noise ratio
SNR	Instantaneous signal-to-noise ratio
T_{s}	Symbol period (in seconds)
θ	Orientation angle between transmitter and receiver (in radians)
u	Receiver location
$\boldsymbol{V}$	$N_{\mathrm{t}} \times \mathsf{d}$ transmit precoder
$\boldsymbol{W}$	$N_{\mathrm{r}} \times \mathsf{d}$ receive filter
$\boldsymbol{x}$	$N_{\mathrm{t}} \times 1$ transmitted signal (after precoding)
$\boldsymbol{y}$	$N_{\mathrm{r}} \times 1$ received signal
$\boldsymbol{z}$	$N_{\mathrm{r}} \times 1$ noise vector
$\boldsymbol{z}'$	$N_{\mathrm{r}} \times 1$ interference vector

Chapter 1

Introduction

> If you want to shine like a sun, first burn like a sun.
>
> A. P. J. Abdul Kalam

Wireless communication has advanced swiftly over the last three decades. During this epoch, wireless connectivity has transformed from an expensive novelty to an indispensable commodity, just like electricity. This transformation along with the widespread penetration of advanced devices such as smartphones and tablets, in turn, is resulting in a faster growth of mobile data traffic. For instance, the global mobile data traffic has increased by 74% in 2015 [1]. It has been forecasted that the number of interconnected devices will increase to 50 billion while the volume of mobile data traffic will grow 1000-fold in the near future [2]. This 1000× capacity goal exerts immense pressure on the wireless network operators to improve the capacity (bits per second, b/s, of bandwidth) of the network. Besides this, the success of social networking applications (e.g., Facebook and Instagram) and an emerging trend of using wearables (e.g., eye glasses and watches) are giving rise to an increasingly diverse set of requirements, ranging from low power wide area Internet-of-Things to extremely low latency and high reliability services [2].

Therefore, the future 5th generation (5G) wireless technology needs to improve upon the current mobile broadband user experience by offering extremely large bandwidth services, while simultaneously expanding the network functionality to support considerably more connected devices and new use case requirements [2–4]. The current approach of cellular network design and deployment will not

Table 1.1: Requirements of key performance metrics for 5G wireless systems [2, 4]

Dimension	Improvement [value, if available]
System capacity	$1000\times$ [$10\,\mathrm{Tb/s/km^2}$]
Cell-edge capacity	$100\times$ [$100\,\mathrm{Mb/s}$]
Roundtrip latency	$1/30\times$ [$1\,\mathrm{ms}$]
Energy consumption	$1/10\times$
Network management cost	$1/5\times$
Number of connected devices	$100\times$ [$2\times10^5\,/\mathrm{km^2}$]

be able to meet the demands faced by 5G networks, because it requires orders of magnitude improvement (cf. Table 1.1) over the current technology. It should be emphasized that the requirements in Table 1.1 need not be satisfied simultaneously and can be relaxed in certain dimensions based on the type of application. For instance, autonomous vehicles or industrial automation applications may require ultra-low latency and ultra-high reliability with relatively lower data rates compared to virtual reality applications, where the primary requirement is on data rates.

1.1 $1000\times$ Capacity Goal: An Information-Theoretic Vantage

The daunting requirement of 5G is to meet the ever-increasing demand for wireless capacity with limited radio resources. In order to attain some potential solutions to this physical layer problem, we pursue information theory that establishes fundamental limits of communication systems. The capacity (b/s) of a point-to-point additive white Gaussian noise (AWGN) channel with signal power P, noise variance σ_{N}^2 and bandwidth B equals [5]

$$B\log_2\left(1+\frac{P}{\sigma_{\mathrm{N}}^2}\right). \tag{1.1}$$

This formula can be extended to the cellular case to determine the system capacity under standard fading conditions, in terms of the number of base stations per unit area λ_{b} and the number of spatial signaling dimensions between the base station and user N, as

$$\lambda_{\mathrm{b}}NB\log_2\left(1+\rho\right) \tag{1.2}$$

where ρ is the expected signal-to-interference-plus-noise ratio (SINR) at the receiving user, defined as the ratio of the intended signal power to the unintended interference-plus-noise power. The validity of (1.2) is subject to a number of assumptions: the received interference plus noise follows a Gaussian distribution, sophisticated channel coding and decoding techniques at the transmitters and receivers, and no fading.

We can glean the following insights from (1.2).

(a) Allocating more frequency spectrum (Hz) increases the signal bandwidth B that in turn leads to an increase in the system capacity.

(b) Adding more spatial dimensions to each end of the link (antennas) increases the number of signal streams per user N that allows the user capacity to be improved (consequently, the system capacity) without additional frequency spectrum.

(c) Deploying more base stations per unit area (base stations/km^2) allows the traffic to be evenly distributed as well as to support more active users per unit area and Hz.

In reference to (a), a large swath of spectrum can be allocated to each user either by aggregating several chunks of underutilized lower frequency bands[1] or by unleashing the higher frequency bands ranging from 10 GHz to 300 GHz. For instance, 28, 38, 71-76, 81-86 GHz frequencies are under investigation—due to their lower atmospheric absorption and scattering loss—with typical propagation ranges of 30 to 100 meters [7–9]. The design of cellular systems based on these millimeter wave frequencies is more than adequately treated elsewhere and we particularly focus on (b) and (c) in this dissertation.

In reference to (b) and (c), the common underlying principle is *spatial frequency reuse*, where the spectrum is shared among multiple antennas or base stations, i.e., several links that may or may not be in spatial proximity operate on the same channel (meaning time-frequency signaling resource). However, due to the broadcast nature

[1]This approach has already been featured as carrier aggregation in the long-term evolution (LTE)-advanced standard. Under typical network loading conditions, it promises to provide either 2.5× user experience gain or 2× user load gain [6].

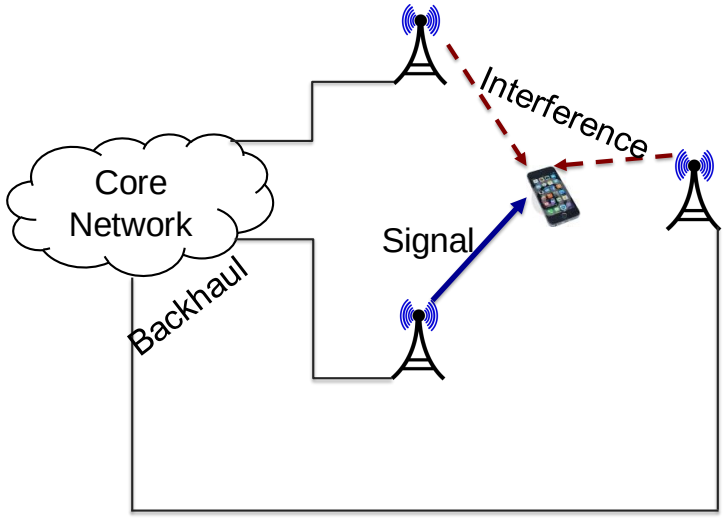

Figure 1.1: Interference-limited scenario in cellular systems. For the user at the cell edge, both signal and interference powers are comparable and results in low spectral efficiency.

of the wireless medium, spatial frequency reuse causes interference at each receiver and creates an interference-limited scenario in cellular systems (cf. Fig. 1.1). The following approaches are widely considered to suppress interference and improve the system capacity:

- Orthogonalize the transmission across resources (time or frequency) so that they do not interfere with each other, or in other words, time or frequency division multiple access. This is not a resource-effective solution, especially, for emerging dense wireless systems.

- Treat interference as noise (TIN), i.e., ignore interference, when it is weak to moderate. Due to its low complexity and robustness, this approach is more appealing from both theoretical and practical perspectives. Recently, through an information-theoretic analysis, it has been established that in some interference channel settings the TIN-based schemes are optimal or near-optimal with respect to capacity in the context of infrastructureless wireless networks [10]. Paraphrasing [10], for each transmitter-receiver pair in an interference channel, if

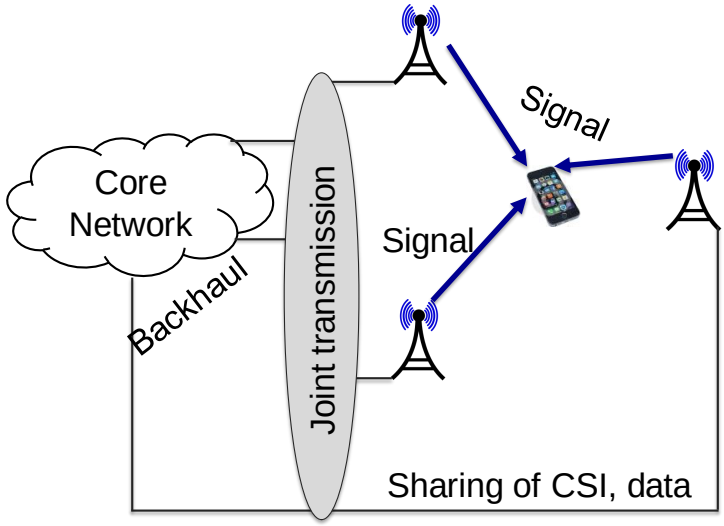

Figure 1.2: Illustration of joint transmission.

the intended signal level is at least the product of maximum outgoing interference level from the transmitter to the unintended receivers and maximum incoming interference level to the receiver from the unintended transmitters, then the TIN approach is optimum. For example, information-theoretic link scheduling or, in short, ITLinQ [11] is inspired by this approach.

- A recent concept that has gained much attention is base station cooperation, where the transmission or reception among multiple cells is coordinated in order to minimize interference, creating a noise-limited scenario within the cooperating region. Various forms of cooperation have been considered under the name of coordinated multipoint (CoMP) transmission or reception [12], ranging from fully-cooperated *joint transmission* [13] to loosely-cooperated *interference alignment* (IA) [14, 15].

  - In joint transmission (Fig. 1.2), multiple base stations behave as a single super base station and simultaneously serve the same user. In addition to tight synchronization, joint transmission involves the exchange of channel-state information (CSI) and user data across cooperating base

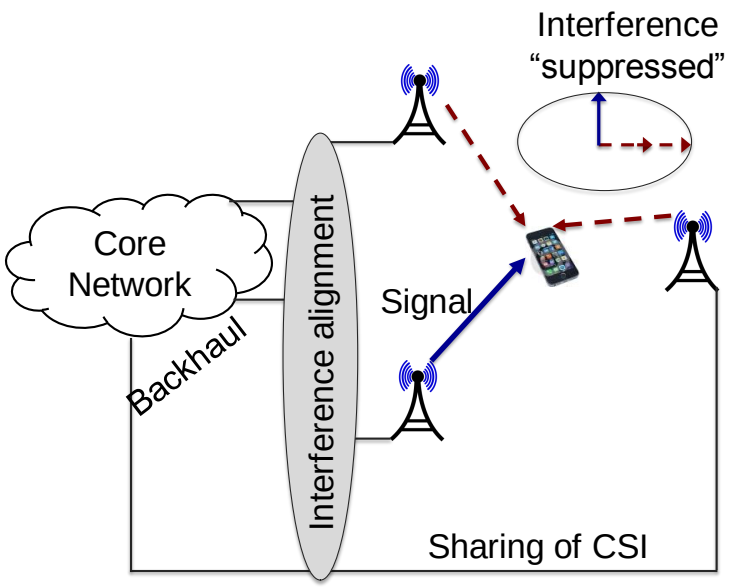

Figure 1.3: Illustration of IA.

stations. CSI represents the changes in amplitude and phase of the channels between each pair of transmit and receive antennas due to channel fading.

– The idea of IA (Fig. 1.3) is to align multiple interfering signals in a signal subspace with dimensions smaller than the number of interferers and suppress the interference at each user by means of spatial signal processing performed locally at each base station. IA can be performed along the time, frequency, or space dimensions. However, it involves significant latency in processing in the time dimension or massive bandwidth expansion in the frequency dimension [16]. IA in the spatial or antenna domain is more practical that can be achieved by spatial precoding or filtering.

1.2 Key Basis of the Dissertation

This section elaborates on spatial frequency reuse and stochastic geometry that form the basis upon which the thesis is built. Various forms of frequency reuse for enhancing area spectral efficiency and

the increasing role of stochastic geometry in the analysis of wireless networks are discussed. Also, some open questions in the realm of wireless systems engineering are highlighted.

1.2.1 Spatial Frequency Reuse for Enhanced Area Spectral Efficiency

MIMO Transmission

A first technique is called multiple-input multiple-output (MIMO), where multiple antennas are used at the transmitters and receivers of wireless communication system. Various MIMO signaling schemes have been adopted in wireless standards:

- Spatial diversity improves the link reliability, by transmitting the same signal over independent fading links.
- Spatial multiplexing improves the link spectral efficiency (b/s per Hz of bandwidth), by transmitting multiple independent signal streams over independent fading links to a single user, i.e., single-user MIMO (SU-MIMO) or to different users, i.e., multiuser MIMO (MU-MIMO).

However, interference from neighboring cells weakens the effectiveness of spatial frequency reuse. Such intercell interference mainly degrades the performance of cell-edge users (cf. Fig. 1.1) and consequently the area spectral efficiency [17]. For instance, the reported cell-edge spectral efficiencies in LTE are about 0.05 b/s/Hz. Recently, base station cooperation has gained the perception of being the best way to counter intercell interference. Among the various cooperation schemes being considered is IA (in antenna-domain), which has the advantage of admitting distributed implementations [18]. This is the first topic of the dissertation with the goal of understanding the tradeoff between spatial multiplexing and IA in cellular networks.

In toy settings where all the users can participate in the alignment and the fading states of all the links are instantaneously and perfectly known by every base station and every user, IA is shown to yield major increase in spectral efficiency. In practical cellular systems, however, there is cooperation among a limited number of users that are inevitably exposed to interference from all the other users in the system. A few system-level simulations reported in [19–21],

including our previous work [22], had already indicated that the spectral efficiency gains due to IA are marginal. To acquire better insights and broader generality in conclusions, and in contrast with simulations, this dissertation studies the performance of IA through analysis and precisely characterizes how frequently IA is beneficial in cellular networks.

In practice, through known pilot symbols, the fading states are obtained at the users and conveyed to the base stations, and these fading states are subject to estimation errors. In addition, user mobility induces dynamics (roughly independent realizations across symbol blocks) in the fading. As time evolves, the known fading states become outdated, the IA solution suffers growing misalignment and interference leaks through. The question then arises as to how robust IA's performance is under inherent physical layer issues such as fading dynamics and imperfect knowledge of the fading states. In [23], the performance of IA is gauged by accounting channel estimation errors and overhead signaling for pilots. This work assumes that the channel remains constant over a block consisting of multiple symbols while changing across blocks. However, this block-fading model is not accurate when conducting the complete link-level analysis of pilot-assisted IA and it becomes important to resort to continuous (symbol-by-symbol) fading, which is precisely what is invoked in our work.

Network Densification

Another big challenge faced by the wireless operators is handling the extreme non-uniformity of cellular networks. For instance, a recent study revealed that 90% of the data is consumed by 10% of the users within 5% of the area [24]. Such a spatial non-uniformity of data traffic is addressed by overlaying multiple low-cost base stations onto macrocell networks in the areas of high user density, which results in a heterogeneous network (or HetNet), e.g., femtocells (consumer-deployed with a range of 100 m) and picocells (operator-deployed with a range of 10 m). While HetNet enhances the system spectral efficiency by multiple-fold factors in certain scenarios [6], it may not be a scalable approach in practice due to the following constraints:

- Backhaul: Fast dedicated connections are needed to backhaul the traffic to the core network, which increases the network management cost [4].

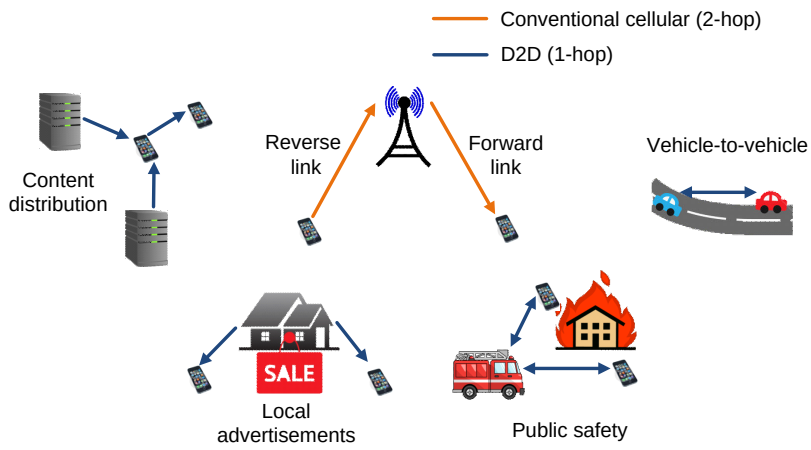

Figure 1.4: Applications of D2D communication [25].

- Excessive handoffs: A user moving through a HetNet with vehicular velocity may experience frequent handoffs among the various types of cells.

- Asymmetric forward and reverse links: In the forward link (or downlink), the base stations transmit at different power levels with a large disparity while, in the reverse link (or uplink), the user transmission power levels are uniform. As a result, the optimal cell association in the forward link may not be necessarily optimal for the reverse link transmission.

- Dynamic interference: Unplanned deployment of many base stations and large disparities in their transmit powers result in diverse interference scenarios, which are difficult to handle.

A rising alternative technique for enhancing system capacity without the need for additional infrastructure is direct communication between users in close proximity, termed *device-to-device (D2D) communication*. Provided there is sufficient spatial locality in the wireless traffic, several application scenarios (cf. Fig. 1.4) are envisioned by the D2D connectivity including direct communication in emergency situations, broadcasting of location-specific advertisements, vehicle-to-vehicle communication in the Internet of vehicles, and media content dissemination. Consequently, D2D-based densification is increasingly being viewed as a potential complement to

HetNets (which densify the network by means of additional infrastructure) with the ensuing merits:

- Hop savings by replacing two long hops via the infrastructure with a single hop.
- Edgeless connectivity by integrating the users into the network with new technologies such as multihop communication.
- Reduced network load by means of offloading the traffic, whenever possible.

There are overlay or underlay options, where respectively the D2D links use separate licensed spectrum or reuse the cellular uplink. In the dissertation we concentrate on the former, which has the advantage of admitting implementations with fewer changes in the standards [26–28].

Despite the remarkable system spectral efficiency exhibited by D2D without a careful allocation of users to orthogonal resources [29], a certain share of the users do experience strong interference and thus see low individual spectral efficiencies. One way to address this problem is to parse D2D transmissions into noninterfering sets to be allocated to separate channels, a process classically termed *dynamic channel allocation* [30] and that in the D2D context herein we shorten as *channelization*. This is the second topic of the dissertation with the goal of quantifying the spectral efficiency advantages of channel allocation schemes in D2D communication networks. Specifically, we consider FlashLinQ [31] and ITLinQ [11], which are the two most popular schemes proposed to date in the D2D context. The former was formulated on a heuristic basis and the latter had been proposed based on information-theoretic optimality principles. In contrast with the original work [11] that relied on simulations to establish ITLinQ's performance, the dissertation aims at quicker parameter optimization and broader generality via analysis.

Simultaneous Transmission and Reception

Existing cellular systems–and the aforementioned new techniques–are presumed to operate in half-duplex by utilizing separate signaling resources for transmission and reception, because of self-interference from its own transmit chain to receive chain. With

staggering progress in analog and digital cancellation architectures [32–35], self-interference cancellation is now becoming possible. Although this technology is still in its infancy and challenges need to be addressed in relation to its form factors, it has the potential to enable many new applications in the wireless landscape, e.g., flexible radio frequency filtering for easier and more agile spectrum management, wireless backhauling, adjacent channel interference suppression for better coexistence, and simultaneous transmission and reception in the same channel [36–38]. The latter refers to *full-duplex wireless communication*, which is the third and final topic of the dissertation. In addition to doubling of the spectral efficiency and reducing the end-to-end latency, full-duplex communication can offer solutions to problems such as decoupling of forward and reverse links, and spectrum sharing [39].

By pushing self-interference below the noise level, a near-doubling of the spectral efficiency is theoretically possible for an isolated link. However, this may not extrapolate to links embedded in a network because of the additional interference. For instance, in the half-duplex reverse link, each base station receives interference from the co-channel users whereas, in the full-duplex reverse link, each base station receives interference from the co-channel users as well as from the co-channel base stations. The question then arises as to whether and when full-duplex is beneficial over half-duplex. Several preliminary studies [40–44] have already explored the potential of full-duplex in wireless networks, by modeling the pathloss at a distance r as $\beta r^{-\eta}$ where η is the exponent while β is the intercept, defined as the pathloss at a unit distance. This single-slope model is inadequate to represent the pathloss among base stations, which as we shall see is critical in full-duplex networks, and a multi-slope model is much more adequate. Moreover, these studies have only focused on the networks with single antenna at each transmitter and receiver. These limitations in the existing work are treated in the dissertation with the goal of studying the viability of full-duplex communication in multi-antenna cellular networks.

1.2.2 Stochastic Geometry for Wireless Network Analysis

Traditionally, wireless network design and characterization relied on the Monte-Carlo simulations over grid networks, where the base stations are placed in deterministic locations with hexagonal coverage regions. However, the incorporation of advanced concepts (cf.

Section 1.2.1) and irregularly deployed infrastructure into wireless network leads to a complex network with a wide range of simulation scenarios. Investigating such a complex network through simulations is a time-consuming and tedious task. Therefore, it is desirable to have a stochastic model for the network locations that is able to capture the key aspects of wireless network. This naturally raises the question of which stochastic process should be chosen to model the network locations. Fortunately, in order to address this question, there is the powerful discipline of stochastic geometry, which allows for models that (*i*) are amenable to analytical treatment, and (*ii*) are arguably more representative of the spatial behavior of emerging wireless systems. Although its initial application was limited to ad-hoc network analysis [45–47], a seminal paper by Andrews et al. [48] demonstrated the remarkable effectiveness of stochastic modelling in the context of cellular networks as well and expanded its horizon.

Despite the considerable effort that has been devoted to advance stochastic geometry [49–59], some important issues have been neglected with respect to the performance metrics:

- Much of the existing work postulated a block-fading model for small-scale variations of the channel (i.e., non-ergodic setting) and characterized the outage probability (i.e., the probability of the event that desirable communication rate is not possible reliably on a link). However, this metric is mainly applicable to previous generation wireless systems that are fixed-rate and narrowband. In fact, by means of variable modulation and coding with rate matched to the average channel conditions, outages due to small-scale fading are eliminated in modern wireless systems that are adaptive and wideband. Then, the right setting is an ergodic channel, where the fading states also vary over a codeword but with the same moments across the codewords. In addition, the *ergodic spectral efficiency*, defined as the spectral efficiency expected over the distribution of small-scale fading, is the most operationally relevant metric in contemporary systems where codewords span many fading realizations in frequency (because of the wide bandwidths), in space (because of the multiplicity of antennas) and in time (because of hybrid-automatic repeat request (ARQ)) [60].

- Furthermore, existing analyses mostly characterized the average network performance. This quantity can only gauge

system-level benefits, but not the performance of users in specific situations, e.g., users on the edge of a cell.

In light of these limitations, we focus on the ergodic spectral efficiency for both averaged and specific network geometries throughout our analysis.

1.3 Contributions

We characterize the performance of wireless systems underpinned by dense spatial frequency reuse and interference suppression. In order to obtain more meaningful results and tractable expressions than previous approaches in the literature, a novel interference modeling framework has been developed with the following features:

- A Gaussian approximation for the interference distribution, which has sound operational justifications for existing encoders and decoders designed to combat AWGN.
- Classification of the interference terms in two sets, respectively corresponding to nearby and faraway transmissions. The terms in the first set are modelled explicitly while the rest are replaced by their spatial average. If the classification is done prudently, this step simplifies the analysis drastically with hardly any loss in accuracy.
- Variable degree of spatial averaging, which allows for an evaluation of the performance for specific locations in addition to the average network-wide performance.

Within this modeling framework, the contributions of the dissertation are listed below.

- Derivation of compact expressions to quantify the spectral efficiency of IA in cellular networks without the need for simulation.
- Characterization of the benefits of IA with respect to the SU-MIMO baseline for both averaged and specific network geometries.

- Optimization of the pilot overhead and the IA update intervals for maximum sum spectral efficiency in a K-user MIMO interference channel as a function of the fading selectivity, signal-to-noise ratio (SNR) and number of users. This optimization problem at high SNR adopts a particularly tractable form.

- Assessment of the robustness of pilot-assisted IA in operationally relevant time-selective continuous fading under both frequency-division duplexing (FDD) and time-division duplexing (TDD).

- Derivation of the exact D2D link density under different implementations of ITLinQ and the (approximated) spectral efficiency expressions in integral forms. These expressions facilitate quicker optimization of ITLinQ's parameters so as to maximize the system spectral efficiency for given user density and distance distribution.

- Evaluation of the ultimate performance of ITLinQ with respect to other D2D channel allocation schemes such as FlashLinQ and quantification of their gains with respect to an unchannelized network.

- Developement of a unified stochastic geometry framework that encompasses both the forward link and the reverse link in a full-duplex MIMO cellular network.

- Quantification of the increase in spectral efficiency due to full-duplex communication, and identification of new needs in interference management. As a complement to the analysis, Monte-Carlo simulations on a Vodafone LTE field test network are also presented.

1.4 Organization

The dissertation is organized as follows: In Chapter 2, important mathematical results of stochastic geometry are couched in our notation and tailored to our models. A novel approach to model interference in large wireless networks is developed and compact expressions for the ergodic performance metrics are derived based on this approach. Chapter 3, the results of which have been presented in [61, 62], is devoted to studying IA in large cellular networks. Analytical expressions for the spectral efficiency of IA are derived in

compact forms and the system-level benefits of IA are characterized. Chapter 4, the results of which have been documented in [63, 64], provides a joint analysis of pilot overhead and spectral efficiency for pilot-assisted IA in time-selective fading channels. The link-level performance of pilot-assisted IA is assessed as function of the fading selectivity, SNR and number of users under both TDD and FDD. Chapter 5, the results of which have been presented in [65–67], focuses on channel allocation schemes for D2D-based densification. The exact permissible D2D link density and the achievable spectral efficiency under different ITLinQ implementations are derived. In particular, performance evaluation comparisons with the FlashLinQ scheme are provided, and the gains with respect to an unchannelized network are quantified. Chapter 6, the results of which are documented in [68, 69], presents a unified stochastic geometry framework that encompasses both forward and reverse links in full-duplex cellular networks. The actual increase in system spectral efficiency due to full-duplex over the standard half-duplex is characterized, and new needs in interference management are also identified. Then, the key outcomes of the dissertation and an outline of future research directions are summarized in Chapter 7. The proofs of the Lemmas and Propositions corresponding to Chapters 2–6 are relegated to Appendices A–E, respectively.

List of Publications

Journal Articles

- G. George, R. K. Mungara, A. Lozano and M. Haenggi, "Ergodic Spectral Efficiency in MIMO Cellular Networks", Submitted to the IEEE Transaction on Wireless Communications, Jul. 2016.
- R. K. Mungara, I. Thibault and A. Lozano, "Full-Duplex MIMO in Cellular Networks: System-level Performance", Submitted to the IEEE Transaction on Wireless Communications, Feb. 2016.
- R. K. Mungara, X. Zhang, A. Lozano and R. W. Heath Jr., "Analytical Characterization of ITLinQ: Channel Allocation for Device-to-Device Communication Networks", *IEEE Trans. Wireless Commun.*, vol. 15, no. 5, pp. 3603–3615, May 2016.
- G. George, R. K. Mungara and A. Lozano, "An Analytical Framework for Device-to-Device Communication in Cellular Networks", *IEEE Trans. Wireless Commun.*, vol. 14, no. 11, pp. 6297–6310, Nov. 2015.
- R. K. Mungara, D. Morales-Jiménez, and A. Lozano, "System-level Performance of Interference Alignment", *IEEE Trans. Wireless Commun.*, vol. 14, no. 2, pp. 1060–1070, Feb. 2015.
- R. K. Mungara, G. George and A. Lozano, "Overhead and Spectral Efficiency of Pilot-Assisted Interference Alignment in Time-Selective Fading Channels", *IEEE Trans. Wireless Commun.*, vol. 13, no. 9, pp. 4884–4895, Sep. 2014.

Refereed Conference Papers

- R. K. Mungara and A. Lozano, "Interference Surge in Full-Duplex Wireless Systems", *IEEE Asilomar Conference on Signals, Systems and Computers*, Pacific Grove, CA, USA, Nov. 2015, pp. 21–25.
- R. K. Mungara, X. Zhang, A. Lozano and R. W. Heath Jr., "Performance Evaluation of ITLinQ and FlashLinQ for Overlaid Device-to-Device Communication", *IEEE ICC Workshop on Device-to-Device Communication for Cellular and Wireless Networks* (ICC'15), London, UK, Jun. 2015, pp. 596–601.

- G. George, R. K. Mungara and A. Lozano, "Optimum Exclusion Regions for Interference Protection in Device-to-Device Wireless Networks", *International Symposium on Modeling and Optimization in Mobile, Ad Hoc, and Wireless Networks* (WiOpt'15), Bombay, India, May 2015, pp. 102–109.

- R. K. Mungara, D. Morales-Jiménez, A. Lozano, "System-level Performance of Interference Alignment", *IEEE Global Communications Conference* (GLOBECOM'14), Austin, TX, USA, Dec. 2014, pp. 1673–1678.

- G. George, R. K. Mungara and A. Lozano, "Overlaid Device-to-Device Communication in Cellular Networks", *IEEE Global Communications Conference* (GLOBECOM'14), Austin, TX, USA, Dec. 2014, pp. 3659–3664.

- R. K. Mungara, X. Zhang, A. Lozano and R. W. Heath Jr., "On the Spatial Spectral Efficiency of ITLinQ", *IEEE Asilomar Conference on Signals, Systems and Computers*, Pacific Grove, CA, USA, Nov. 2014, pp. 1806–1810.

- R. K. Mungara, G. George and A. Lozano, "Pilot-Assisted Interference Alignment in Time-Selective Fading Channels", *IEEE Global Communications Conference* (GLOBECOM'13), Atlanta, GA, USA, Dec. 2013, pp. 3977–3982.

- R. K. Mungara, G. George and A. Lozano, "System-level Performance of Distributed Cooperation", *IEEE Asilomar Conference on Signals, Systems and Computers*, Pacific Grove, CA, USA, Nov. 2012, pp. 1561–1565.

Chapter 2

Mathematical Preliminaries

> Information is the resolution of uncertainty.
>
> Claude Shannon

This chapter provides a mathematical interlude before analyzing the real systems of interest and borrows some essential principles and results from stochastic geometry [51, 70] in the context of wireless networks. Firstly, we describe the standard wireless network including signal and propagation models. Next, to ensure that the dissertation is as self-contained as possible, the notion of Poisson point process (PPP) to model network locations and the central facts associated with PPP are summarized. Then, we present a new interference modeling framework, which can serve as a stepping stone towards the analysis presented in the dissertation. Finally, within this framework, we characterize the two important performance metrics in contemporary wireless systems: the local-average SIR and the ergodic spectral efficiency.

2.1 System Model

Any wireless communication link can be modeled as three building blocks, namely transmitter, channel, and receiver. The transmitter processes information (such as text, voice or video) and sends encoded data symbols to its intended receiver. Denoting by s the data symbol at the transmitter and by y the observation at the receiver, s may be chosen from a complex-valued finite constellation such as quadrature amplitude modulation or from a Gaussian

codebook. Throughout the dissertation, we choose complex Gaussian data symbols with zero mean and unit variance entries, i.e., $s \sim \mathcal{N}_{\mathbb{C}}(0,1)$, which maximize the mutual information between the observation y and data symbol s in the absence of interference at the receiver.

The observed signal at the receiver is subject to various large-scale and small-scale effects over wireless channel. The large-scale fading represents signal variations that occur on a scale spanning many wavelengths, e.g., distance-dependent pathloss and blockage-induced shadow fading. On the other hand, the small-scale fading represents signal variations that occur on a scale comparable to the wavelength, e.g., scattering-induced signal variations. These effects can be modeled as follows:

- The pathloss at a distance r is modeled as $\beta r^{-\eta}$ with η the exponent and β the intercept.
- Given the prevalence of log-normal shadow fading in terrestrial wireless systems, the shadow fading between any transmitter and its receiver is represented by $\chi \sim 10^{\mathcal{N}_{\mathbb{C}}(0,\sigma^2_{\mathrm{dB}})/10}$ with σ_{dB} the standard deviation.
- Depending on the local scattering at the transmitter and the receiver, the amplitude of small-scale fading can be modeled as Rayleigh, Rician or can be disregarded [71]. As the transmitter and receiver are in non-line-of-sight path in a majority of cases, the fading amplitude is modeled as Rayleigh distribution

$$f_{|h|}(h) = he^{-\frac{h^2}{2}} \tag{2.1}$$

meaning that the fading coefficients are complex Gaussian with zero mean and unit variance, i.e., $h \sim \mathcal{N}_{\mathbb{C}}(0,1)$, and the fading power is exponentially distributed with unit mean

$$f_{|h|^2}(h) = e^{-h}. \tag{2.2}$$

Additionally, we assume that the fading is frequency-flat, i.e., the signal bandwidth is well below the frequency range over which the channel remains almost constant (called the coherence bandwidth of the channel). Alternatively, if the signal bandwidth is large compared to the channel coherence bandwidth, then different frequency components of the signal fade

differently. Such frequency-selective fading leads to intersymbol interference (ISI), i.e., successively transmitted symbols interfere at the receiver, or in other words, a transmitted symbol arrives at the receiver during the next symbol periods. In single-carrier systems, ISI is countered by equalizers derived either from channel estimates or directly from the training data, e.g., linear equalizers such as minimum mean-square error (MMSE) and zero-forcing equalizers, non-linear equalizers such as decision-feedback equalizer and maximum-likelihood sequence detector. In multi-carrier systems, ISI is suppressed by modulating data onto orthogonal subcarriers in the frequency domain so that each subcarrier experiences flat fading, e.g., orthogonal frequency division multiplexing.

With spatial reuse of spectrum in a wireless network, each receiver also gets interference from all co-channel transmitters in addition to its intended signal. Then, under the foregoing transmit signal and propagation models, the observation y_0 at the receiver of the link indexed by 0 can be expressed as

$$y_0 = \sqrt{P\chi_0\,\beta\,r_0^{-\eta}}h_0 s_0 + \sum_{k=1}^{\infty}\sqrt{P\chi_k\,\beta\,r_k^{-\eta}}h_k s_k + z_0 \tag{2.3}$$

whose first term is the intended signal component while the second and third terms are the aggregate interference and thermal noise, respectively. In turn, P is the (fixed) transmit power, r_k is the distance between the receiver and the kth transmitter, h_k is the corresponding small-scale fading, χ_k accounts for shadow fading, s_k is the data symbol communicated over the kth link, and $z_0 \sim \mathcal{N}_{\mathbb{C}}(0, \sigma_{\mathrm{N}}^2)$. Denoting by $z_0'' = z_0' + z_0$ the aggregate interference plus noise with

$$z_0' = \sum_{k=1}^{\infty}\sqrt{P\chi_k\,\beta\,r_k^{-\eta}}h_k s_k, \tag{2.4}$$

we can rewrite (2.3) as

$$y_0 = \sqrt{P\chi_0\,\beta\,r_0^{-\eta}}h_0 s_0 + z_0''. \tag{2.5}$$

2.2 Poisson Point Process

By abstracting the spatial distribution of transmitters and receivers into appropriate point processes, stochastic geometry was initially

applied to characterize interference in wireless ad-hoc networks [45–47] and then, over the last two decades, it has extensively been adopted to analyze cellular systems [48, 56, 72], ultrawideband [73], cognitive networks [57, 74], femto cells [75], and heterogeneous networks [52, 53]. While most previous stochastic geometry analyses utilized PPPs to model the locations, the methodology could be equally applied with more sophisticated spatial distributions [76–79] that could accurately capture the tendency of users to cluster and dependences between the spatial distributions of users and base stations. Since the actual behaviors under strong shadow fading converge to a PPP behavior and PPP-based characterizations represent the impact of network geometry on performance metrics remarkably well [80–82], we model the locations of base stations and users via PPPs in the dissertation.

2.2.1 Mathematical Description

A point process can be described in terms of either random sets or random counting measures [51].

- A point process can be viewed as a countable random set of points in a measurable space, say the Euclidean space $\mathbb{R}^2$. For instance, if we consider the point process $\Phi = \{b_0, b_1, \ldots\} \subset \mathbb{R}^2$ as a set that represents the base station locations in a cellular network, then the set $\{b_0, b_1, \ldots\}$ constitutes a random pattern of points in $\mathbb{R}^2$ with each location b_k being a random variable.

- In lieu of a random set, a random counting measure can be used to define the point process as a collection of random counting measures $N(\mathfrak{B})$ indexed by $\mathfrak{B} \subset \mathbb{R}^2$, where $\mathfrak{B}$ is a bounded closed set and $N(\mathfrak{B})$ equals the number of points falling in $\mathfrak{B}$.

These two representations admit a duality. If Φ is given, then $N(\mathfrak{B})$ is computed simply by counting the number of points in $\Phi \cap \mathfrak{B}$. Conversely, if $N(\mathfrak{B})$ for all subsets $\mathfrak{B}$ are given, then one can reconstruct all the points of Φ.

The point process Φ with some intensity measure $\upsilon(\mathfrak{B})$ is called Poisson if it possesses the following properties:

- The counting measure $N(\mathfrak{B})$ is Poisson distributed with mean $\upsilon(\mathfrak{B})$.
- For any disjoint bounded sets $\mathfrak{B}_1, \mathfrak{B}_2, \ldots, \mathfrak{B}_n$, the corresponding measures $N(\mathfrak{B}_1), N(\mathfrak{B}_2), \ldots, N(\mathfrak{B}_n)$ are independent.

It is common to assume that the point process is locally finite for all bounded closed sets $\mathfrak{B} \subset \mathbb{R}^2$, i.e., $N(\mathfrak{B}) < \infty$ with probability 1, or in other words, the number of points in any bounded region is finite. From the aforementioned random set representation, it is also implicit to assume that the point process is simple, i.e., $N(\{b\}) \in \{0, 1\}$ $\forall b \subset \mathbb{R}^2$ with probability 1, or in other words, no two points of the point process are coincident.

2.2.2 Homogeneity

Homogeneous process implies both *(i)* stationarity, i.e., the process $\Phi = \{b_k\} \subset \mathbb{R}^2$ and its translated process $\Phi + b = \{b_k + b\}$ are identically distributed $\forall b \in \mathbb{R}^2$, and *(ii)* isotropy, i.e., Φ and $\theta\Phi$ have the same distribution for every rotation θ around the origin. The transmitter or receiver locations in a wireless network are often modeled as a homogeneous PPP Φ with density λ, meaning that the number of transmitters in a unit area is Poisson distributed with mean λ, or the probability that the number of transmitters in a given area A equals n is

$$\mathbb{P}\left(N(A) = n\right) = e^{-\lambda A} \frac{(\lambda A)^n}{n!}. \tag{2.6}$$

If the density λ is not constant, then the process is said to be inhomogeneous.

2.2.3 Notion of Palm Distribution

It is useful to study the properties (or events) of a point process at a specific location such as the average number of points in a circle centered at $b_0 \in \Phi$ with radius R, or the conditional probability of the distance from a specific location $b_0 \in \Phi$ to its nearest neighbor of the point process (in short, the nearest-neighbor distance) being higher than r. While such conditional probabilities can be computed by applying the basic probability principles in certain scenarios (cf. [83, Example 3.2]), yet there exists a problem in general due to $\mathbb{P}(b_0 \in \Phi) = 0$. The concept of Palm distribution resolves this issue

by mathematically formalizing the conditioning events. Short of a detailed mathematical formalization (that is available in [51]), we provide the intuitive interpretation of the Palm distribution.

Let us consider that Φ has a property V (such as having no point in $\mathcal{B}_{b_0}(r)$ representing the circle centered at b_0 with radius r), which we represent as $\Phi \in \mathsf{V}$. The Palm distribution of Φ at b_0 is the probability of an event V given $b_0 \in \Phi$, i.e.,

$$\mathsf{P}_{b_0}(\mathsf{V}) = \mathbb{P}(\Phi \in \mathsf{V} | b_0 \in \Phi) \tag{2.7}$$

which can be interpreted as the limiting value of the probability $\mathbb{P}(\Phi \in \mathsf{V} | N(\mathcal{B}_{b_0}(\epsilon)) > 0)$ as $\epsilon \to 0$, if the limit exists. Then, we have

$$\mathbb{P}(\Phi \in \mathsf{V} | N(\mathcal{B}_{b_0}(\epsilon)) > 0) = \frac{\mathbb{P}(\Phi \in \mathsf{V}, N(\mathcal{B}_{b_0}(\epsilon)) > 0)}{\mathbb{P}(N(\mathcal{B}_{b_0}(\epsilon)) > 0)}. \tag{2.8}$$

Invoking the stationarity property, we can write

$$\mathsf{P}_{b_0}(\mathsf{V}) = \mathsf{P}_{b_k}(\mathsf{V}). \tag{2.9}$$

2.2.4 Slivnyak's Theorem

Since the distributions of points in disjoint sets are independent for a PPP, conditioning on the PPP having a point at b_0 does not change the distribution of the other points of the process. This property is particularly useful in characterizing the co-channel interference in cellular networks with PPP distributed base station locations, i.e., even if the serving base station is excluded from the PPP, the distribution of the interfering base station locations remains the same as PPP. Mathematically, if Φ is a PPP with density λ, then the Palm distribution is [51, 70]

$$\mathsf{P}_{b_0}(\mathsf{V}) = \mathbb{P}(\Phi \in \mathsf{V} | b_0 \in \Phi) \tag{2.10}$$

$$= \mathbb{P}(\Phi \cup \{b_0\} \in \mathsf{V}) \tag{2.11}$$

which means that conditioning on $b_0 \in \Phi$ in a PPP is the same as adding a point at b_0. This can be extended to multiple points. Specifically, this theorem allows the receiver to be conditioned at a fixed location and the analysis conducted on its link, which can serve as the typical link in the network.

2.2.5 Marked PPP

A marked PPP is a Poisson process, where "marked" means that each point is labeled with a mark whose distribution features additional information such as transmit power, fading or link priority [51]. The marks can be either continuous variables or indicators.

2.2.6 Distance Distributions

As the performance of the typical receiver is essentially a function of its position relative to the transmitters, it is convenient for the analysis that we import some distance distributions related to Poisson distributed network.

Lemma 2.1. Given a homogeneous PPP Φ of intensity λ with r_n representing the distance from a point to its $(n+1)$th neighbor, the probability density function (PDF) of r_n is [84]

$$f_{r_n}(r_n) = \frac{2(\pi\lambda)^{n+1}}{n!} r_n^{2n+1}\, e^{-\pi\lambda r_n^2} \tag{2.12}$$

and the joint PDF of r_n and r_k with $0 \le n < k$ is [85]

$$f_{r_n,r_k}(r_n, r_k) = \frac{4(\pi\lambda)^{k+1}}{(k-n-1)!\, n!} (r_k^2 - r_n^2)^{k-n-1} r_n^{2n+1} r_k\, e^{-\pi\lambda r_k^2}. \tag{2.13}$$

From (2.12), the density function of the distance between a point to its first neighbor is seen to be

$$f_{r_0}(r_0) = 2\pi\lambda r_0 e^{-\pi\lambda r_0^2}. \tag{2.14}$$

Lemma 2.2. If a_n denotes the ratio of the distances from a point to its $(n+1)$th and Nth neighbors, i.e., $a_n = r_n/r_{N-1}$, then the joint PDF of r_n and a_n with $0 \le n < N-1$ is

$$f_{r_n,a_n}(r_n, a_n) = \frac{4(\pi\lambda)^N}{(N-n-2)!\, n!} \frac{(1-a_n^2)^{N-n-2}}{a_n^{2N-2n-1}} r_n^{2N-1}\, e^{-\frac{\pi\lambda r_n^2}{a_n^2}}. \tag{2.15}$$

Marginalizing this PDF over r_n yields the PDF of a_n as

$$f_{a_n}(a_n) = \frac{2\,\Gamma(N)}{(N-n-2)!\, n!} a_n^{2n+1} (1-a_n^2)^{N-n-2} \tag{2.16}$$

from which the PDF of r_n conditioned on a_n can be written as

$$f_{r_n|a_n}(r_n|a_n) = \frac{f_{r_n,a_n}(\cdot,\cdot)}{f_{a_n}(\cdot)} \tag{2.17}$$

$$= \frac{2(\pi\lambda)^N r_n^{2N-1}}{\Gamma(N)\, a_n^{2N}} e^{-\pi\lambda(r_n/a_n)^2} \tag{2.18}$$

where $\Gamma(N) = \int_0^\infty e^{-t} t^{N-1}\, \mathrm{d}t$ is the Gamma function.

Proof: See Appendix A.1.

2.2.7 Interference Functionals

Two of the most fundamental results of stochastic geometry are Campbell's theorem and probability generating functional [51, 70]. The former is useful in computing the aggregate interference expected over all possible locations and the latter is useful in computing the Laplace functional of the aggregate interference. Based on these theorems, we obtain the following interference functionals in compact forms, which shall be useful throughout the dissertation.

Lemma 2.3. If $\mathcal{I} = \sum_{k:R_1<r_k<R_2} \beta\, r_k^{-\eta}$ and $\eta > 2$, then the expected interference power $\mathbb{E}[\mathcal{I}]$ equals

$$\mathbb{E}[\mathcal{I}] = \frac{2\pi\lambda\beta}{\eta-2}(R_1^{2-\eta} - R_2^{2-\eta}) \tag{2.19}$$

For the limiting case, $R_2 \to \infty$, we get

$$\lim_{R_2\to\infty} \mathbb{E}[\mathcal{I}] = \frac{2\pi\lambda\beta}{\eta-2} R_1^{2-\eta}. \tag{2.20}$$

Proof: See Appendix A.2.

It is worth mentioning that the mean interference $\mathbb{E}[\mathcal{I}] \to \infty$ (cf. (2.20)) when $R_1 \to 0$. While this divergence can be avoided by modeling the pathloss at a distance r as $\min(1, r^{-\eta})$, for our purposes $r^{-\eta}$ is sufficient.

Lemma 2.4. If $\mathcal{I} = \sum_{k:R_1<r_k<R_2} \beta\, r_k^{-\eta}$ and $\mathcal{L}_\mathcal{I}(t) = \mathbb{E}[e^{-t\mathcal{I}}]$ represents the Laplace transform of $\mathcal{I}$, then

$$\mathcal{L}_\mathcal{I}(t) = \pi\lambda(R_1^2 - R_2^2) + \frac{2\pi\lambda}{\eta}\left(R_2^2\, \mathcal{E}_{\frac{\eta+2}{\eta}}\left(\frac{t\beta}{R_2^\eta}\right) - R_1^2\, \mathcal{E}_{\frac{\eta+2}{\eta}}\left(\frac{t\beta}{R_1^\eta}\right)\right) \tag{2.21}$$

For the limiting cases, we get

$$\lim_{R_2\to\infty} \mathcal{L}_{\mathcal{I}}(t) = \exp\left(\pi\lambda R_1^2 + \frac{2\pi\lambda}{\eta}(\beta\, t)^{\frac{2}{\eta}}\, \bar{\Gamma}\left(\frac{-2}{\eta}, \frac{\beta}{R_1^{\eta}} t\right)\right) \tag{2.22}$$

$$\lim_{\substack{R_1\to 0\\ R_2\to\infty}} \mathcal{L}_{\mathcal{I}}(t) = \exp\left(-\pi\lambda\,(\beta\, t)^{\frac{2}{\eta}}\, \Gamma\left(1-\frac{2}{\eta}\right)\right) \tag{2.23}$$

where $\bar{\Gamma}(\cdot,\cdot)$ is the lower incomplete Gamma function.

Proof: See Appendix A.3.

2.3 Revised System Model with PPP Distributed Locations

For the analysis that follows in the remainder of this chapter, we consider the forward link of a cellular network where base stations are distributed according to a homogeneous PPP $\Phi_{\mathrm{b}} \subset \mathbb{R}^2$ with density λ_{b} and each user is served by a single base station. Recognizing the convergence of the actual behavior of network under strong shadow fading to a PPP-distributed network behavior [80–82], the subsequent analysis is conducted without an explicit modeling of the shadow fading. (The density λ_{b} depends on the type and strength of the shadow fading as well as the actual positions of the base stations.) The analysis will be generalized to networks featuring IA, D2D or full-duplex communication in subsequent chapters.

By Slivnyak's Theorem, we consider a receiving user at the origin (cf. Fig. 2.1) and focus the analysis on its link, indexed by 0. Denote by r_k the distance between the user at the origin and the kth base station. Without loss of generality, we index the base stations in increasing order of r_k, i.e., $r_k < r_{k+1}\ \forall k$ and the base station corresponding to r_0 is the serving base station of the typical user.

Throughout the dissertation, we largely focus on interference-limited networks with negligible thermal noise or, equivalently, $P/\sigma_{\mathrm{N}}^2 \to \infty$. In light of the foregoing considerations, the observation y_0 in (2.5) can be written as

$$y_0 = \sqrt{P\beta\, r_0^{-\eta}}\, h_0 s_0 + z_0' \tag{2.24}$$

with

$$z_0' = \sum_{k=1}^{\infty} \sqrt{P\beta\, r_k^{-\eta}}\, h_k s_k. \tag{2.25}$$

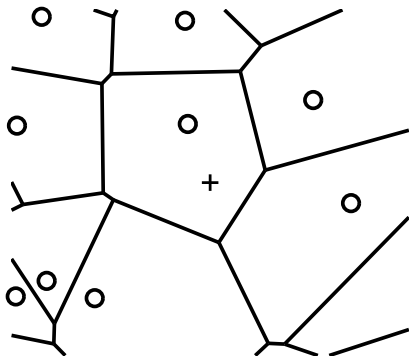

Figure 2.1: Tesselation of a cellular network with base station locations sampled from a PPP. Base stations are indicated by $\circ$ markers and the typical user is indicated by $+$ marker.

2.4 Local-average SIR Distribution

Recalling the intended signal term in (2.24) and the aggregate interference in (2.25), the local-average signal-to-interference ratio (SIR) at the typical user is

$$\rho_0 = \frac{r_0^{-\eta}}{\sum_{k=1}^{\infty} r_k^{-\eta}}. \tag{2.26}$$

The spatial distribution of the transmitter locations induces a distribution of its own for ρ_0, i.e., a long-term distribution for the local-average SIR, which is derived next. As the exact distribution of the local-average aggregate interference generally does not admit a closed-form, certain approximate characterizations are proposed [59, 72, 74, 86]. Here, we adapt the approach in [59]: obtain the distribution of $1/\rho_0$ exactly in the Laplace domain and then express the Laplace numerical inverse via Euler series expansion.

Lemma 2.5. For a given intended link distance r_0, the cumulative distribution function (CDF) of ρ_0 is

$$F_{\rho_0|r_0}(\gamma) \approx 1 - \gamma \, \frac{e^{\frac{\mathsf{A}}{2}}}{2^{\mathsf{L}}} \sum_{\ell=0}^{\mathsf{L}} \binom{\mathsf{L}}{\ell} \sum_{\mathsf{m}=0}^{\mathsf{M}+b} \frac{(-1)^{\mathsf{m}}}{D_{\mathsf{m}}} \Re\left\{ \frac{\mathcal{L}_{1/\rho_0|r_0}(\iota)}{\iota} \right\} \tag{2.27}$$

where

$$\iota = \frac{(\mathsf{A} + \mathrm{i}\, 2\pi \mathsf{m})\, \gamma}{2} \tag{2.28}$$

while $D_0 = 2$ and $D_{\mathsf{m}} = 1$ for $\mathsf{m} \geq 1$. The parameters A, L and M control the accuracy, with suggested values for multiple-digit precision being $\mathsf{A} = 18.4$, $\mathsf{L} = 11$ and $\mathsf{M} = 15$ [87]. For our purposes, $\mathsf{A} = 9.21$, $\mathsf{L} = 5$ and $\mathsf{M} = 8$ yield a more-than-sufficient accuracy [88].

Proof: See Appendix A.4.

To solve $\mathcal{L}_{1/\rho_0|r_0}(\cdot)$ in (2.27), we effect the change of variables $R_1 \to r_0$, $R_2 \to \infty$ and $\beta \to r_0^\eta$ in Lemma 2.4 (cf. (2.22)) to obtain

$$\mathcal{L}_{1/\rho_0|r_0}(t) = \exp\left(\pi\lambda_{\mathrm{b}} r_0^2 + \frac{2\pi\lambda_{\mathrm{b}}}{\eta}\,(r_0^\eta\, t)^{\frac{2}{\eta}}\,\bar{\Gamma}\left(\frac{-2}{\eta}, t\right)\right) \tag{2.29}$$

from which the CDF $F_{\rho_0|r_0}$ specializes to

$$F_{\rho_0|r_0}(\gamma) \approx 1 - \gamma\,\frac{e^{\frac{\mathsf{A}}{2}}}{2^{\mathsf{L}}}\sum_{\ell=0}^{\mathsf{L}}\binom{\mathsf{L}}{\ell}\sum_{\mathsf{m}=0}^{\mathsf{M}+b}\frac{(-1)^{\mathsf{m}}}{D_{\mathsf{m}}}\Re\left\{\frac{1}{\iota}e^{\pi\lambda_{\mathrm{b}} r_0^2 + \frac{2\pi\lambda_{\mathrm{b}}}{\eta}\left(r_0^\eta\, t\right)^{\frac{2}{\eta}}\bar{\Gamma}\left(\frac{-2}{\eta},\iota\right)}\right\}. \tag{2.30}$$

Eq. (2.29) can be unconditioned via the density function in (2.14) to obtain

$$\mathcal{L}_{1/\rho_0}(t) = \int_0^\infty \mathcal{L}_{1/\rho_0|r_0}(t) f_{r_0}(r_0)\,\mathrm{d}r_0 \tag{2.31}$$

$$= \frac{-\eta}{t^{1+\frac{2}{\eta}}\bar{\Gamma}\left(\frac{-2}{\eta}, t\right)} \tag{2.32}$$

where (2.32) follows from evaluating the integral by virtue of [89, Eq. 3.326.2]. Consequently, the unconditional CDF $F_{\rho_0}(\cdot)$ specializes to

$$F_{\rho_0}(\gamma) = 1 - \gamma\,\frac{e^{\frac{\mathsf{A}}{2}}}{2^{\mathsf{L}}}\sum_{\ell=0}^{\mathsf{L}}\binom{\mathsf{L}}{\ell}\sum_{\mathsf{m}=0}^{\mathsf{M}+b}\frac{(-1)^{\mathsf{m}}}{D_{\mathsf{m}}}\Re\left\{\frac{-\eta}{\iota^{1+\frac{2}{\eta}}\bar{\Gamma}\left(\frac{-2}{\eta}, \iota\right)}\right\}. \tag{2.33}$$

Example 2.6. Consider a network with single-antenna base stations of density $\lambda_{\mathrm{b}} = 7.95$ base stations/km^2 (which amounts to an average of one base station per circular cell of radius 200 m) and with the pathloss exponent $\eta = 3.75$. Shown in Fig. 2.2 is a comparison of the CDFs $F_{\rho_0|r_0=150}(\gamma)$ and $F_{\rho_0}(\gamma)$ in (2.30) and (2.33), with $\mathsf{A} = 9.21$, $\mathsf{L} = 5$ and $\mathsf{M} = 8$, against their Monte-Carlo counterparts. An excellent match is observed, supporting the validity of the Euler series expansion of the inverse Laplace transform.

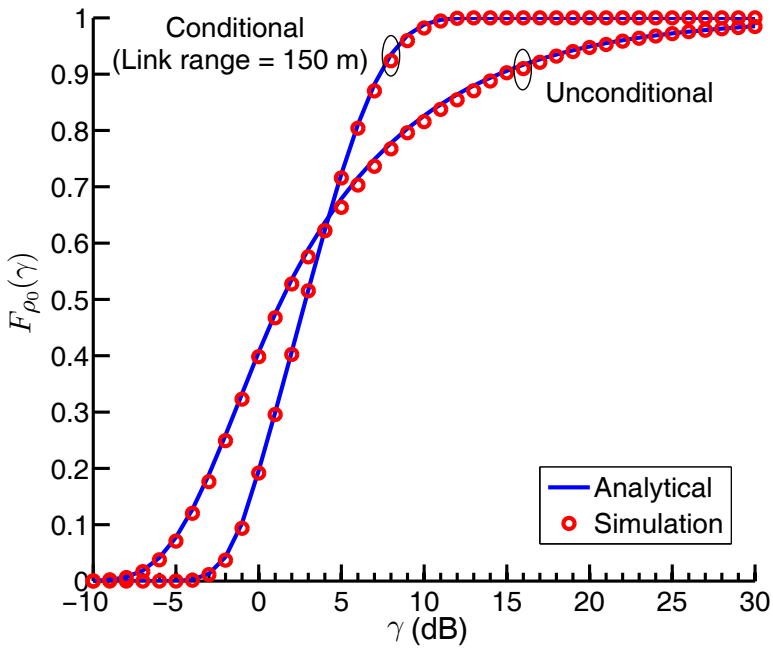

Figure 2.2: CDF of forward link local-average SIR in a cellular network with single-antenna base stations.

2.5 A Novel Interference Modeling Approach

As can be gauged from (2.25), conditioned on $\{r_k\}$, z_0' involves a linear combination of terms involving products of Gaussian variates, which are altogether difficult to manipulate and conduct analysis with. Albeit certain characterizations of its exact distribution are plausible [48, 90], in the dissertation we take an alternative path that promises a better payoff in terms of analytical insight. The most novel aspects of our modeling framework are summarized below with the validating examples.

A Gaussian Approximation for the Interference Distribution

The short-term distribution of z_0' is modeled as zero-mean complex Gaussian with matched conditional variance $\mathbb{E}[|z_0'|^2|\{r_k\}]$, where the expectation is over data and fading distributions. This step yields,

$$\mathbb{E}\left[|z_0'|^2|\{r_k\}\right] = \sum_{k=1}^{\infty} P\beta\, r_k^{-\eta}\mathbb{E}\left[h_k s_k s_k^* h_k^*\right] \tag{2.34}$$

$$= \sum_{k=1}^{\infty} P\beta\, r_k^{-\eta} \mathbb{E}\left[h_k h_k^*\right] \tag{2.35}$$

$$= \sum_{k=1}^{\infty} P\beta\, r_k^{-\eta} \tag{2.36}$$

where (2.34) follows from the mutual independence of $\{s_k\}$ while (2.36) follows from the fact that h_k is a zero-mean unit-variance random variable.

Besides the central limit theorem, there are information-theoretic arguments in favor of modeling the aggregate interference as complex Gaussian with a power dictated by the locations of the interferers:

- If the exact distribution of the interference is either unknown or ignored by the receiver, with a codebook and decoder designed to handle Gaussian noise, then the achievable spectral efficiency is precisely as if the interference were indeed Gaussian [91]. Thus, the spectral efficiencies obtained with this model can be interpreted as those achievable with standard Gaussian-noise signaling and decoding.
- Gaussian noise is the worst-case additive noise in wireless networks with Gaussian signaling [92]. Thus, the results obtained under our model are operationally more relevant than the quantities computed under the non-Gaussian interference in (2.4) and the former are always (tight) lower bounds to the latter.

Classification of the Interference Terms

Note that $\mathbb{E}[|z_0'|^2|\{r_k\}]$ in (2.36) consists of infinite terms, which is still unwieldy. Faced with this obstacle, we classify the interference terms into two sets depending on whether they correspond to nearby or faraway transmissions. Denoting by K' the number of interferers in the first set, the K' terms are modeled explicitly and the rest are replaced by their spatial average (cf. Fig. 2.3). The choice of K' should be chosen to balance simplicity and accuracy in capturing the performance for specific user locations. This step yields,

$$\mathbb{E}\left[|z_0'|^2|r_k\right] \approx P\beta \sum_{k=1}^{K'} r_k^{-\eta} + P\beta\, \mathbb{E}_{\Phi}\left[\sum_{k=K'+1}^{\infty} r_k^{-\eta}\right] \tag{2.37}$$

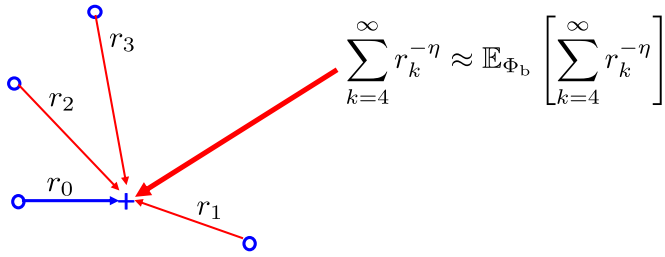

Figure 2.3: Interference modeling illustration where the intended link distance is r_0, and the closest $K' = 3$ interfering base stations are explicitly modeled. The aggregate interference emanating from the remaining base stations is replaced by its expectation over the corresponding interferer locations.

$$= P\beta \sum_{k=1}^{K'} r_k^{-\eta} + \frac{2\pi\lambda_b P\beta}{\eta - 2} r_{K'}^{2-\eta}. \tag{2.38}$$

where the expectation in (2.37) is evaluated by virtue of Lemma 2.3 with $R_1 \to r_{K'}$ and $R_2 \to \infty$.

With the interference thus modeled and recalling the intended signal term in (2.24), the instantaneous SIR experienced by the typical receiver is

$$\mathsf{SIR}_0 = \frac{P\beta\, r_0^{-\eta} \mathbb{E}\left[|h_0 s_0|^2 | h_0\right]}{P\beta \sum\limits_{k=1}^{K'} r_k^{-\eta} + \frac{2\pi\lambda_b P\beta}{\eta-2} r_{K'}^{2-\eta}} \tag{2.39}$$

$$= \rho_0 |h_0|^2 \tag{2.40}$$

where the expectation is over $s_0 \sim \mathcal{N}(0,1)$ and

$$\rho_0 = \frac{r_0^{-\eta}}{\sum\limits_{k=1}^{K'} r_k^{-\eta} + \frac{2\pi\lambda_b}{\eta-2} r_{K'}^{2-\eta}} \tag{2.41}$$

is the local-average SIR at the user. For a specific network realization, i.e., given $\{r_k\}_{k=0}^{K'}$, the value of ρ_0 becomes determined. Since $|h_0|^2$ is exponentially distributed with unit mean, it follows from (2.40) that the instantaneous SIR exhibits an exponential distribution with mean ρ_0 and thus its conditional CDF is

$$F_{\mathsf{SIR}_0|\rho_0}(\gamma) = 1 - e^{-\gamma/\rho_0}. \tag{2.42}$$

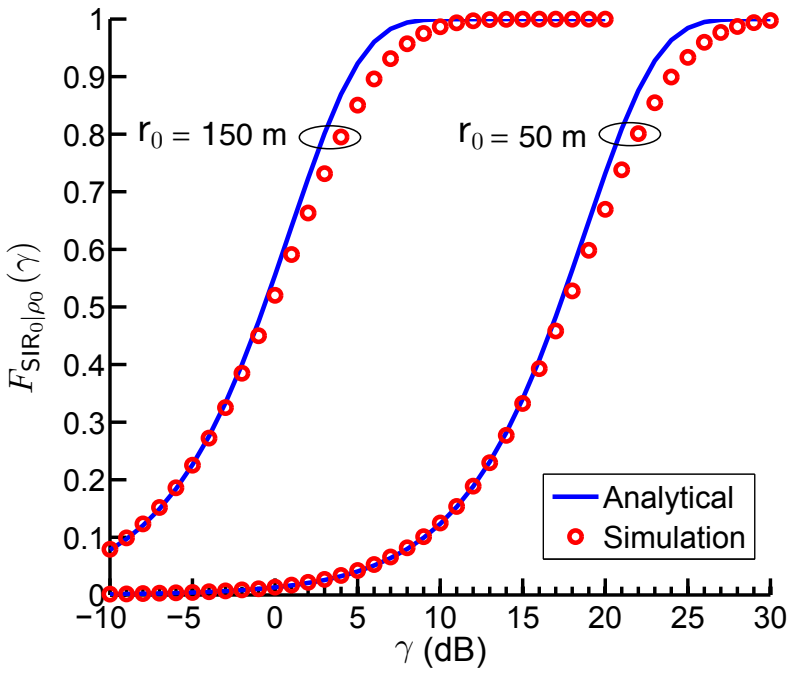

Figure 2.4: CDF of instantaneous SIR for $r_0 = 50$ m and $r_0 = 150$ m. In each case, $\lambda_\mathrm{b} = 7.95$ base stations/km^2, $\eta = 3.75$ and $K' = 3$ while r_1, r_2 and r_3 are set to their mean values.

Example 2.7. Consider $\lambda_\mathrm{b} = 7.95$ base stations/km^2 and $\eta = 3.75$ as in Example 2.6. The number of interference terms explicitly modeled equals $K' = 3$ and r_k for $k = 1, \ldots, K'$ is set to the expected distance to the kth nearest neighboring point in a PPP with density λ_b [93]. This gives $r_k = \Gamma(0.5 + k)/(\sqrt{\pi\lambda_\mathrm{b}}\Gamma(k))$. Shown in Fig. 2.4 is a comparison between $F_{\mathsf{SIR}_0|\rho_0}(\gamma)$ and the numerically computed CDF of the instantaneous SIR with z_0' as in (2.25).

A satisfactory agreement is observed in every case, supporting the validity of a complex Gaussian approximation for the interference even if the information-theoretic arguments in support of a complex Gaussian interference model were ignored. Similar agreement has been observed for other values of the parameters.

As we demonstrate in the following section, the main advantage of our modeling framework is a variable degree of spatial averaging, which allows computing the spectral efficiency for both averaged

and specific network geometries.

2.6 Spectral Efficiency

2.6.1 Specific Network Geometry

For a specific network geometry we recover well-known expressions for Rayleigh fading, only with the role of noise played by the interference [94, 95]. The ergodic spectral efficiency spawned by $F_{\mathsf{SIR}_0|\rho_0}(\cdot)$ in (2.42) is

$$C(\rho_0) = \int_0^\infty \log_2(1+\gamma)\,\mathrm{d}F_{\mathsf{SIR}_0|\rho_0}(\gamma) \tag{2.43}$$

$$= e^{1/\rho_0}\mathcal{E}_1\left(\frac{1}{\rho_0}\right)\log_2 e \tag{2.44}$$

where $\mathcal{E}_n(\zeta) = \int_1^\infty t^{-n}e^{-\zeta t}\,\mathrm{d}t$ is an exponential integral and ρ_0 was given in (2.41). Through ρ_0, the spectral efficiency depends on $r_0, r_1, \ldots, r_{K'}$, as well as on the pathloss exponent and the transmitter density. The expression in (2.44) has a reduced degree of spatial averaging that allows for a characterization of the performance of users in specific situations, as demonstrated in the following example.

Example 2.8. Reconsider Example 2.6 with $\lambda_\mathrm{b} = 7.95$ base stations per km^2, $\eta = 3.75$, $K' = 3$ and $r_k = \Gamma(0.5+k)/(\sqrt{\pi\lambda_\mathrm{b}}\Gamma(k))$ for $k = 1, \ldots, K'$. Shown in Fig. 2.5 is a comparison of $C(\rho_0)$ against its simulated counterpart with z_0' as in (2.25). As indicated in Fig. 2.5, the simulated result corresponds to the exact mutual information under the non-Gaussian interference in (2.25) for many snapshots of the interferer locations corresponding to $\{r_k\}_{k=4}^\infty$, computed through lengthy Monte-Carlo histograms and averaged over many fading realizations. The match is very satisfactory, supporting the validity of our interference modeling approach: a complex Gaussian approximation for the interference and averaging of weak interference terms. Similar agreement has been observed for other values of parameters.

2.6.2 Average Network Geometry

The link spectral efficiency $C(\rho_0)$ can be further expected over ρ_0 in order to characterize the average performance over all possible geometries, as in the conventional stochastic geometry analyses. The

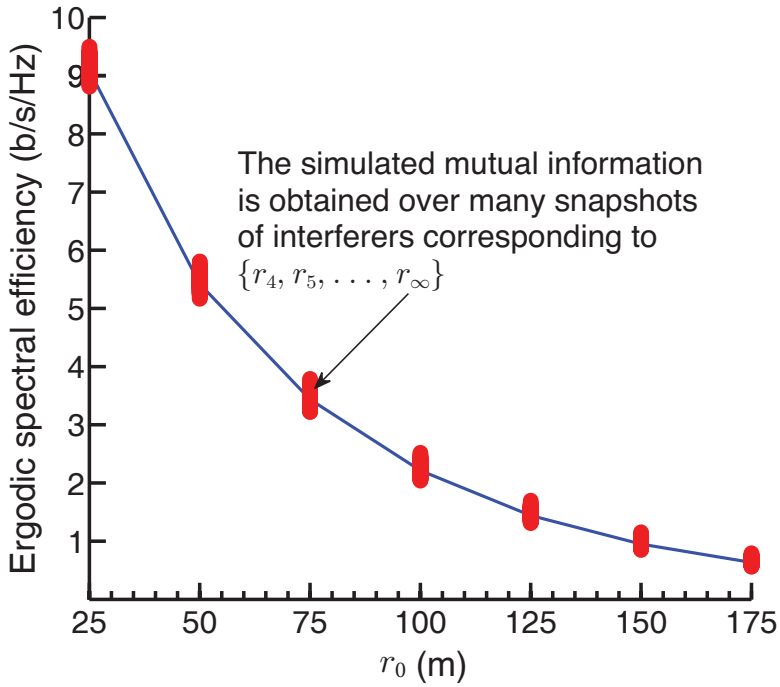

Figure 2.5: Ergodic spectral efficiency as function of r_0 for $\lambda_b = 7.95$ base stations/km^2, $\eta = 3.75$, $K' = 3$, and $\{r_k\}_{k=1}^{K'}$ set to their mean values.

Table 2.1: Average link spectral efficiency (b/s/Hz) as function of η

η	Analytical	Simulation (99% confidence interval)
3.5	1.61	1.63 ($\pm$0.008)
4.0	2.00	2.03 ($\pm$0.0109)
4.5	2.39	2.45 ($\pm$0.0117)

spatially averaged forward link spectral efficiency of a cellular network with Rayleigh fading is (cf. Appendix A.5)

$$\bar{C} = \int_0^\infty \frac{\log_2 e}{1+\gamma} \frac{-\eta/2}{\bar{\Gamma}(-2/\eta, \gamma)\gamma^{2/\eta}} \, \mathrm{d}\gamma. \tag{2.45}$$

Example 2.9. Shown in Table 2.1 is a comparison of $\bar{C}$ computed via (2.45) against its simulated counterpart for $\eta = 3.5$, $\eta = 4$ and

$\eta = 4.5$, which essentially delimit the range of pathloss exponents encountered in terrestrial systems. Again, the simulated result corresponds to the exact mutual information under the non-Gaussian interference in (2.25) averaged over many fading realizations, transmitter and interference locations. The match is excellent, again evincing the goodness of our interference modeling approach.

Altogether, our developed framework enables more meaningful results and compact expressions than those in previous works, while preserving the necessary precision.

2.7 Chapter Summary

The signal and propagation models that will be used throughout the dissertation have been described. Important results of stochastic geometry in the context of wireless network analysis have been presented. A new interference modeling framework has been introduced and the two principal metrics used to quantify the system-level performance of wireless networks, namely the local-average SIR and the ergodic spectral efficiency, have been defined. Finally, by leveraging the framework, the ergodic spectral efficiency is characterized for both averaged and specific geometries.

Chapter 3

Interference Alignment for Cellular Networks

> No model is ever a perfect fit to reality. Deductions based on the model must be regarded with appropriate suspicion.
>
> Solomon W. Golomb, "Mathematical Models: Uses and Limitations", *IEEE Trans. Reliab.*, 1968.

This chapter generalizes the framework in Chapter 2 to incorporate multiantenna transmission schemes such as IA, and characterizes the system-level benefits of IA over the standard SU-MIMO in cellular networks.

3.1 Related Work and Motivation

At the expense of instantaneous CSI at both transmitters and receivers, IA ensures that the interference from all participating users aligns at each receiver along a certain subspace leaving the remaining dimensions free of interference [14, 15]. In toy settings where all the users can participate in the alignment and the CSI is perfect, IA can deliver unbounded growth of the spectral efficiency with the SNR.

The favorable IA behavior encountered in small toy settings, however, does not extrapolate to larger wireless networks. Depending on the antenna counts, only a limited number of users can participate in the alignment; with two antennas, for instance, at most

three users can participate. This necessarily leads to the formation of relatively small IA clusters that are inevitably exposed to interference from all other users in the system. Thus, even the subspaces that IA protects from in-cluster interference are bound to experience out-of-cluster interference [96]. In addition, IA restricts the spatial dimensionality of the transmit signals; in the two-antenna three-user example, the spatial dimensionality of the signals cannot exceed one; without IA, in contrast, a two-dimensional signal could be transmitted applying standard SU-MIMO techniques. Altogether then, IA can create subspaces with reduced interference in exchange for a sacrifice in signal dimensions. Naturally, the question arises of whether and when this tradeoff is justified in the context of modern wireless networks. This question is precisely what motivates the work presented in this chapter.

In contrast with some prior works on the system-level performance of IA, which relied on simulations over grid networks [19–22], we set out to address the matter analytically in order to attain broader generality and more pronounced guidance in the conclusions.

In order to address the afore-posed question of whether and when the dimensionality sacrifice entailed by IA is advantageous, we posit SU-MIMO as a baseline for interference-oblivious techniques that utilize all available dimensions for signalling. SU-MIMO is a conservative baseline in the sense that it has less stringent requirements than IA in every respect, chiefly in terms of CSI. Then, for given antenna counts and relevant propagation conditions, we seek to compare the system-level spectral efficiencies achievable reliably with IA and with SU-MIMO. In order to keep the comparison indeed conservative, assumptions that are highly favorable to IA are made throughout. Specifically:

- Perfect transmit and receive CSI is assumed, with all the corresponding overheads neglected.
- Instantaneous availability of the optimum IA precoders is also assumed, neglecting the iterative processes that might be required to actually compute such precoders.
- The clusters of base stations effecting IA are determined dynamically, with (user) locations and propagation conditions taken into account. This improves the performance of IA relative to static clusters defined a-priori [22, 97, 98].

- Interference-limited conditions are considered, with thermal noise neglected. Everything else being the same, this maximizes the benefits of IA.

The analysis is conducted for the downlink, which is the link that seems more apt to accommodate IA.

3.2 System Model

Consider a cellular network with base stations located according to a homogeneous PPP $\Phi_{\mathrm{b}} \subset \mathbb{R}^2$ with density λ_{b}. The user locations are modeled by another independent PPP Φ_{u} with density λ_{u}. The base stations and users are respectively equipped with N_{t} transmit and N_{r} receive antennas, and each link carries $\mathsf{d} \leq N_{\min} = \min(N_{\mathrm{t}}, N_{\mathrm{r}})$ signal streams. We denote by P_{b} the fixed power transmitted by each base station. By Slivnyak's Theorem (cf. Section 2.2.4), we consider a receiving user at the origin and focus the analysis on its link, which can serve as the typical link in the network.

A set of base stations jointly performing IA are collectively referred to as a cluster. Denote by r_k the distance between the user at the origin and the kth base station. Without loss of generality, we index the base stations in increasing order of r_k, i.e., $r_k < r_{k+1}$ $\forall k$. We consider dynamic clustering, where the K base stations with the strongest links or, equivalently, the smallest distances, $\{r_0, \ldots, r_{K-1}\}$, compose the IA cluster. The first of them ($k = 0$) acts as the serving base station.

In light of the foregoing considerations, the observation $\boldsymbol{y}_0 \in \mathbb{C}^{N_{\mathrm{r}} \times 1}$ at the user of the typical link can be written as

$$\boldsymbol{y}_0 = \sum_{k=0}^{K-1} \sqrt{\frac{P_{\mathrm{b}}}{\mathsf{d}} \beta \, r_k^{-\eta}} \boldsymbol{H}_k \boldsymbol{x}_k + \boldsymbol{z}_0' \tag{3.1}$$

where the leading term contains the in-cluster signals while

$$\boldsymbol{z}_0' = \sum_{k=K}^{\infty} \sqrt{\frac{P_{\mathrm{b}}}{\mathsf{d}} \beta \, r_k^{-\eta}} \boldsymbol{H}_k \boldsymbol{x}_k \tag{3.2}$$

represents the out-of-cluster interference. In turn, β is the pathloss intercept, $\boldsymbol{x}_k \in \mathbb{C}^{N_{\mathrm{t}} \times 1}$ is the signal transmitted by the kth base station, and $\boldsymbol{H}_k \in \mathbb{C}^{N_{\mathrm{r}} \times N_{\mathrm{t}}}$ is the fading matrix between the kth base station and the user, perfectly known at both ends. The entries of

$\boldsymbol{H}_k$ are IID samples drawn from $\mathcal{N}_{\mathbb{C}}(0,1)$. The signal transmitted by the kth base station is $\boldsymbol{x}_k = \boldsymbol{V}_k \boldsymbol{s}_k$ where $\boldsymbol{V}_k = [\boldsymbol{v}_{k,1} \cdots \boldsymbol{v}_{k,\mathsf{d}}] \in \mathbb{C}^{N_\mathrm{t} \times \mathsf{d}}$ is a unitary precoder (meaning a matrix whose columns are orthonormal) and $\boldsymbol{s}_k \in \mathbb{C}^{\mathsf{d} \times 1}$ is a vector of IID complex Gaussian symbols satisfying $\mathbb{E}[\boldsymbol{s}_k \boldsymbol{s}_k^*] = \boldsymbol{I}_\mathsf{d}$. With that, the power is uniformly allocated across the d signal streams and $\mathbb{E}[\|\boldsymbol{x}_k\|^2] = \mathsf{d}$. At the receiver, the kth user applies a unitary filter $\boldsymbol{W}_k$.

3.3 Interference Alignment

With perfect CSI and $N_{\min} \geq 2\mathsf{d}$, IA yields a d-dimensional channel free of in-cluster interference for every link iff [99]

$$N_\mathrm{t} + N_\mathrm{r} \geq (K+1)\,\mathsf{d}. \tag{3.3}$$

The precoders $\boldsymbol{V}_0, \ldots, \boldsymbol{V}_{K-1}$ and the receive filter $\boldsymbol{W}_0$ that effect IA satisfy

$$\operatorname{rank}(\boldsymbol{W}_0^* \boldsymbol{H}_0 \boldsymbol{V}_0) = \mathsf{d} \tag{3.4}$$

$$\boldsymbol{W}_0^* \boldsymbol{H}_k \boldsymbol{V}_k = \boldsymbol{0} \qquad k \neq 0 \tag{3.5}$$

as well as similar conditions for the other $K-1$ users being served concurrently in the same cluster. After applying the filter $\boldsymbol{W}_0 = [\boldsymbol{w}_{0,1}, \ldots, \boldsymbol{w}_{0,\mathsf{d}}] \in \mathbb{C}^{N_\mathrm{r} \times \mathsf{d}}$, the receiver at the origin observes

$$\boldsymbol{W}_0^* \boldsymbol{y}_0 = \sqrt{\frac{P_\mathrm{b}}{\mathsf{d}} \beta\, r_0^{-\eta}}\, \boldsymbol{W}_0^* \boldsymbol{H}_0 \boldsymbol{V}_0 \boldsymbol{s}_0 + \boldsymbol{W}_0^* \boldsymbol{z}_0' \tag{3.6}$$

where, by virtue of (3.5), there is no interference contribution from the in-cluster base stations.

Throughout this chapter, the precoders and receive filters are obtained through the Min-Leakage algorithm [18] with the overheads associated with running this algorithm neglected.

3.4 Out-of-Cluster Interference Modeling

In contrast with previous works (cf. [98, 100–103]), the out-of-cluster interference $\boldsymbol{z}_0'$ is modeled as per the approach in Section 2.5 whose validity for IA purposes is examined later in the chapter.

As per the first step, $\boldsymbol{z}_0'$ is modeled as a zero-mean complex Gaussian random vector with matching covariance $\mathbb{E}\,[\boldsymbol{z}_0' \boldsymbol{z}_0'^*]$. From (3.2), the

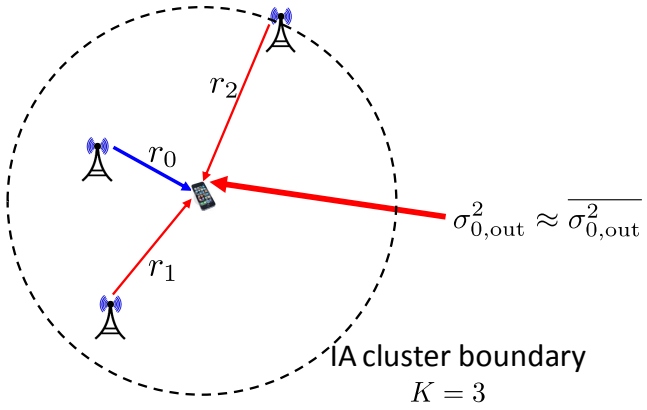

Figure 3.1: Out-of-cluster interference modeling illustration where the intended link distance is r_0, the IA cluster size $K = 3$, and the interfering base stations within the cluster are explicitly modeled. The aggregate interference $\sigma^2_{0,\text{out}}$ emanating from outside the IA cluster is replaced by its expectation (over the corresponding interferer locations).

conditional covariance of $\boldsymbol{z}'_0$ for given interferer locations is

$$\mathbb{E}\left[\boldsymbol{z}'_0\boldsymbol{z}'^{*}_0 \,|\, \{r_k\}\right] = \frac{P_{\text{b}}\beta}{\mathsf{d}} \sum_{k=K}^{\infty} r_k^{-\eta}\, \mathbb{E}\left[\boldsymbol{H}_k \boldsymbol{x}_k \boldsymbol{x}_k^* \boldsymbol{H}_k^*\right] \tag{3.7}$$

$$= \frac{P_{\text{b}}\beta}{\mathsf{d}} \sum_{k=K}^{\infty} r_k^{-\eta}\, \mathbb{E}\left[(\boldsymbol{H}_k \boldsymbol{V}_k)(\boldsymbol{H}_k \boldsymbol{V}_k)^*\right] \tag{3.8}$$

$$= P_{\text{b}}\beta \sum_{k=K}^{\infty} r_k^{-\eta} \boldsymbol{I}_{N_{\text{r}}} \tag{3.9}$$

where (3.7) follows from the mutual independence of $\{\boldsymbol{x}_k\}_{k=K}^{\infty}$ while (3.9) follows from the fact that $(\boldsymbol{H}_k\boldsymbol{V}_k)$ is an $N_{\text{r}} \times d$ matrix with IID zero-mean unit-variance entries such that $\mathbb{E}\left[(\boldsymbol{H}_k\boldsymbol{V}_k)(\boldsymbol{H}_k\boldsymbol{V}_k)^*\right] = \mathsf{d}\, \boldsymbol{I}_{N_{\text{r}}}$. Defining $\sigma^2_{0,\text{out}} = \sum_{k=K}^{\infty} r_k^{-\eta}$, we can write

$$\mathbb{E}\left[\boldsymbol{z}'_0\boldsymbol{z}'^{*}_0 \,|\, \{r_k\}\right] = P_{\text{b}}\sigma^2_{0,\text{out}} \boldsymbol{I}_{N_{\text{r}}}. \tag{3.10}$$

Next, as per the second step (cf. Fig. 3.1), the interfering base stations within the cluster surrounding the user of interest are explicitly modeled while the aggregate interference emanating from

outside the IA cluster is replaced by its expected (over the interferer locations) value. Then,

$$\overline{\sigma^2_{0,\text{out}}} = \mathbb{E}_{\Phi_\text{r}}\left[\sum_{k=K}^{\infty} \beta\, r_k^{-\eta}\right] \tag{3.11}$$

and the potency of the stochastic modelling approach is shown in full force by the fact that this expectation can be computed explicitly, yielding (cf. Lemma 2.3 with $R_1 \to r_{K-1}$, $R_2 \to \infty$ and $\lambda \to \lambda_\text{b}$)

$$\overline{\sigma^2_{0,\text{out}}} = \frac{2\pi\lambda_\text{b}\beta}{\eta-2} r_{K-1}^{2-\eta}. \tag{3.12}$$

With the out-of-cluster interference thus modeled, and recalling the intended signal term in (3.6), the instantaneous SIR experienced by the ℓth signal stream of the typical user is

$$\mathsf{SIR}_{0,\ell} = \frac{\frac{P_\text{b}\beta}{\mathsf{d}} r_0^{-\eta}\, \mathbb{E}\left[|[\boldsymbol{W}_0^* \boldsymbol{H}_0 \boldsymbol{V}_0 \boldsymbol{s}_0]_\ell|^2 \,|\, \{\boldsymbol{H}_k\}\right]}{P_\text{b}\overline{\sigma^2_{0,\text{out}}}} \tag{3.13}$$

where $[\cdot]_\ell$ indicates the ℓth entry of a vector and the expectation in the numerator is over $\boldsymbol{s}_0$, conditioned on the fading (and therefore on the precoders and receivers). Evaluating such expectation,

$$\mathsf{SIR}_{0,\ell} = \frac{\frac{P_\text{b}\beta}{\mathsf{d}} r_0^{-\eta} |\boldsymbol{w}_{0,\ell}^* \boldsymbol{H}_0 \boldsymbol{v}_{0,\ell}|^2}{P_\text{b}\overline{\sigma^2_{0,\text{out}}}} \tag{3.14}$$

$$= \frac{\rho_0^\text{IA} |\boldsymbol{w}_{0,\ell}^* \boldsymbol{H}_0 \boldsymbol{v}_{0,\ell}|^2}{\mathsf{d}} \tag{3.15}$$

where

$$\rho_0^\text{IA} = \frac{r_0^{-\eta}}{\overline{\sigma^2_{0,\text{out}}}} \tag{3.16}$$

$$= \frac{r_{K-1}^{\eta-2}}{r_0^\eta} \frac{\eta-2}{2\pi\lambda_\text{b}} \tag{3.17}$$

is the local-average SIR at the user of interest.

Note that $\{\mathsf{SIR}_{0,\ell}\}_{\ell=1}^{\mathsf{d}}$ are mutually dependent, through $\boldsymbol{H}_0$, but identically distributed and hence to characterize the marginal distribution of the per-stream SIR we can drop the stream index ℓ. Such characterization is the object of Section 3.5, as a stepping stone towards the evaluation of the spectral efficiency in Section 3.6. Receivers whose performance depends on the joint distribution of the SIRs of all d streams are tackled directly in Section 3.6.

3.5 SIR Distribution

In this section we provide three different characterizations of the marginal per-stream SIR distribution, each accompanied by a corresponding interpretation. We begin with the most informative one, and then proceed onto more marginalized forms thereof.

3.5.1 Specific Absolute Cluster Geometry

For given locations, i.e., for given $r_0, \ldots, r_{K-1}$, the value of ρ_0^{IA} becomes determined. Since $\boldsymbol{v}_{0,\ell}$ and $\boldsymbol{w}_{0,\ell}$ are columns of matrices that are unitary and independent of $\boldsymbol{H}_0$, the effective instantaneous gain $|\boldsymbol{w}_{0,\ell}^* \boldsymbol{H}_0 \boldsymbol{v}_{0,\ell}|^2$ for any stream ℓ is exponentially distributed with unit mean [18]. It follows from (3.17) that the instantaneous per-stream SIR exhibits Rayleigh fading with local-average $\rho_0^{\mathrm{IA}}/\mathsf{d}$ and hence its conditional CDF is

$$F_{\mathsf{SIR}_0|\rho_0^{\mathrm{IA}}}(\gamma) = 1 - e^{-\gamma \mathsf{d}/\rho_0^{\mathrm{IA}}}. \tag{3.18}$$

Through ρ_0^{IA}, the above distribution depends on the distance to the serving base station, r_0, and on the distance delimiting the IA cluster, r_{K-1}, and it can be utilized to establish the performance of IA as a function of these two key quantities. In contrast, the location of the other in-cluster base stations, $r_1, \ldots, r_{K-2}$, is immaterial because, by virtue of IA, they do not contribute any interference.

3.5.2 Specific Relative Cluster Geometry

Let us now marginalize the instantaneous SIR over r_0 and r_{K-1} while keeping their ratio $a_0 = r_0/r_{K-1}$ fixed. Note that $0 < a_0 < 1$ with probability 1.

Proposition 3.1. For a given $a_0 = r_0/r_{K-1}$,

$$F_{\mathsf{SIR}_0|a_0}(\gamma) = 1 - \left(1 + \frac{2\, a_0^{\eta}\, \mathsf{d}}{\eta - 2}\, \gamma\right)^{-K}. \tag{3.19}$$

Proof: See Appendix B.1.

In contrast with (3.18), which—through ρ_0^{IA}—depends on the base station density λ_{b}, the CDF in Proposition 3.1 no longer depends on λ_{b}. In this distribution, the geometry of the cluster is captured by a single parameter, a_0, which informs of the location of the serving base station relative to the edge of the IA cluster and thus relative

to the out-of-cluster interferers. Put differently, a_0 informs in a compact fashion of where the user of interest is within the cluster: values close to 0 map to situations where the user is in the inner part of the cluster while values close to 1 map to situations where the user is in the periphery thereof. As will be seen, this characterization, conveniently scale independent, is highly indicative of IA performance. Additionally, as one would anticipate, a_0 is also tightly related to the marginalized local-average per-stream SIR, something that can be verified by applying (3.19) to compute

$$\int_0^\infty \gamma \, \mathrm{d}F_{\mathsf{SIR}_0|a_0}(\gamma) = \frac{\eta - 2}{2a_0^\eta \, \mathsf{d} \, (K-1)} \tag{3.20}$$

which must be interpreted with care because a_0 and K are not independent: its presence in the denominator notwithstanding, a larger K increases (3.20) because, everything else being the same, it results in a smaller a_0 and such contraction is magnified by the pathloss exponent η ultimately shrinking the denominator.[1] A proper interpretation of the marginalized distribution in Proposition 3.1 is of the utmost importance. It does not correspond to the distribution of the SIR experience by any actual user in the system, but rather it is a stepping stone towards the computation of other quantities later in the chapter.

At this point, we validate $F_{\mathsf{SIR}_0|a_0}(\cdot)$ by contrasting it with its counterpart, obtained numerically, where $\boldsymbol{z}_0'$ is as in (3.2).

Example 3.2. Shown in Fig. 3.2 is a comparison of $F_{\mathsf{SIR}_0|a_0}(\cdot)$ with the simulated CDF of the corresponding SIR with $\boldsymbol{z}_0'$ as in (3.2). The comparison is conducted for $K = 3$ and $a_0 = 0.45$, for $K = 5$ and $a_0 = 0.32$, and for $K = 7$ and $a_0 = 0.25$, in all cases with $\eta = 4$.

A satisfactory agreement is observed in every case, supporting the validity of a complex Gaussian approximation for the out-of-cluster interference. Similar agreement has been observed for other values of the parameters.

3.5.3 Average Cluster Geometry

As the final step in the characterization of its distribution, we can average the instantaneous per-stream SIR over the ratio a_0.

[1] Our formulation in this section is tailored to IA and hence it is only valid for $K > 1$. A slightly different approach would be required for $K = 1$.

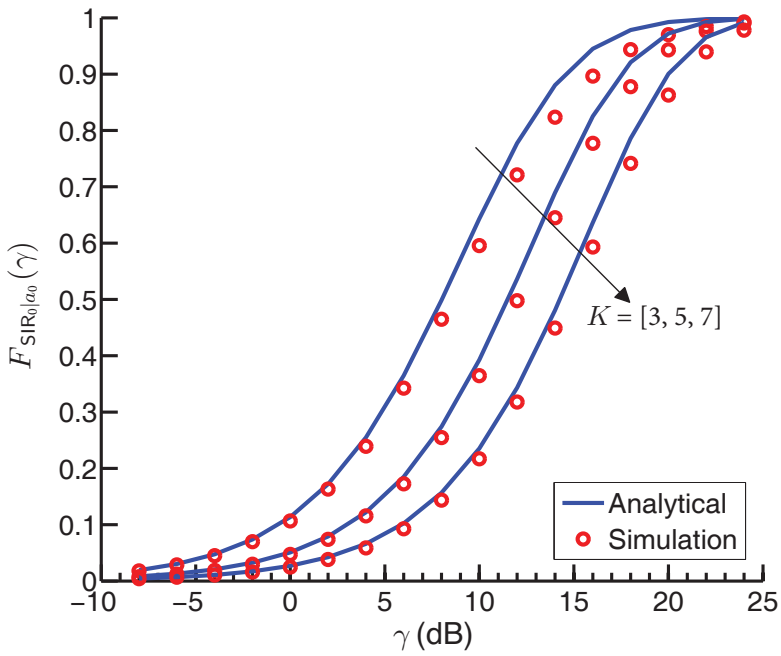

Figure 3.2: CDF of marginalized instantaneous per-stream SIR for IA with $\mathsf{d} = 1$ and $\eta = 4$. Analytical and simulation results for $K = 3$ and $a_0 = 0.45$, for $K = 5$ and $a_0 = 0.32$, and for $K = 7$ and $a_0 = 0.25$.

Proposition 3.3. Unconditioned on a_0,

$$F_{\mathsf{SIR}_0}(\gamma) = 1 - \sum_{n=0}^{K-2} \frac{(-1)^n \Gamma(K)}{n!\,(K-2-n)!\,(n+1)} \cdot {}_2F_1\left(K, \frac{2(n+1)}{\eta}; 1 + \frac{2(n+1)}{\eta}; \frac{-2\mathsf{d}\,\gamma}{\eta - 2}\right) \tag{3.21}$$

where ${}_2F_1(a, b\,; c\,; z)$ is the Gaussian hypergeometric function [104].

Proof: See Appendix B.2.

Marginalized to the point that it depends only on the cluster size K and the number of signal streams d, the expression in Proposition 3.3 is less informative than the ones earlier in this section. In particular, it does not allow discrimination between situations that are either favorable or adverse to IA. And, as was the case for Proposition 3.1, it does not correspond to the distribution of

the SIR experience by any actual user in the system, but rather it is a stepping stone towards the computation of average quantities. Moreover, its limited significance is buttressed by the fact that, barring an exclusion zone around the serving base station, the local-average SIR unconditioned on a_0 does not exist.

3.6 Spectral Efficiency

The SIR improvements brought about by IA come at the expense of a sacrifice in the dimensionality of the transmit signal. Despite having N_{t} transmit and N_{r} receive antennas, only $\mathsf{d} < N_{\min}$ parallel signals are conveyed and, therefore, to have a complete picture it is essential to look at the spectral efficiency, which is where the balance of signal dimensionality and SIR emerges. This section is devoted to characterizations of the spectral efficiency for each of the geometry marginalization scenarios put forth in Section 3.5. Precisely, we characterize the ergodic spectral efficiency, which is the most operationally relevant quantity in contemporary systems.

3.6.1 Specific Absolute Cluster Geometry

For a specific absolute cluster geometry we recover well-known expressions for Rayleigh fading [94, 95], only with the role of noise played by the out-of-cluster interference. For $\mathsf{d} = 1$, the ergodic spectral efficiency spawned by $F_{\mathsf{SIR}_0|\rho_0^{\mathrm{IA}}}(\cdot)$ in (3.18) is

$$C^{\mathrm{abs}}(\rho_0^{\mathrm{IA}}) = \int_0^\infty \log_2(1+\gamma)\, \mathrm{d}F_{\mathsf{SIR}_0|\rho_0^{\mathrm{IA}}}(\gamma) \tag{3.22}$$

$$= e^{1/\rho_0^{\mathrm{IA}}} \mathcal{E}_1\left(\frac{1}{\rho_0^{\mathrm{IA}}}\right) \log_2 e \tag{3.23}$$

where ρ_0^{IA} was given in (3.17). Through ρ_0^{IA}, the spectral efficiency depends on r_0 and r_{K-1}, as well as on the large-scale propagation parameters and the base station density.

For $d > 1$, (3.23) generalizes differently depending on whether the receiver applies separate per-stream decoding or joint decoding of the d streams. With separate per-stream decoding,

$$C^{\mathrm{abs}}(\rho_0^{\mathrm{IA}}) = \mathsf{d}\, e^{d/\rho_0^{\mathrm{IA}}} \mathcal{E}_1\left(\frac{\mathsf{d}}{\rho_0^{\mathrm{IA}}}\right) \log_2 e \tag{3.24}$$

while, recalling (3.6) and (3.16), under joint decoding

$$C^{\text{abs}}(\rho_0^{\text{IA}}) = \mathbb{E}\left[\log_2 \det\left(\boldsymbol{I} + \frac{\rho_0^{\text{IA}}}{\mathsf{d}} \boldsymbol{W}_0^* \boldsymbol{H}_0 \boldsymbol{V}_0 \boldsymbol{V}_0^* \boldsymbol{H}_0^* \boldsymbol{W}_0\right) | \rho_0^{\text{IA}}\right] \quad (3.25)$$

with expectation over the distribution of the effective fading component $\boldsymbol{W}_0^* \boldsymbol{H}_0 \boldsymbol{V}_0 \in \mathbb{C}^{\mathsf{d}\times\mathsf{d}}$. Given the unitary nature of $\boldsymbol{V}_0$ and $\boldsymbol{W}_0$ and their independence from $\boldsymbol{H}_0$, we have that $\boldsymbol{W}_0^* \boldsymbol{H}_0 \boldsymbol{V}_0$ has IID entries drawn from $\mathcal{N}_{\mathbb{C}}(0,1)$. It follows that the right-hand-side of (3.25) is nothing but the ergodic spectral efficiency of a $\mathsf{d} \times \mathsf{d}$ Rayleigh-faded MIMO channel with IID entries and average signal-to-noise ρ_0^{IA}, under uniform power allocation, and thus

$$C^{\text{abs}}(\rho_0^{\text{IA}}) = C^{\text{MIMO}}_{\mathsf{d},\mathsf{d}}(\rho_0^{\text{IA}}) \quad (3.26)$$

where the function [105]

$$\begin{aligned} C^{\text{MIMO}}_{N_{\text{r}},N_{\text{t}}}(\rho) = \log_2(e)\, e^{N_{\text{t}}/\rho} \sum_{i=0}^{m-1} \sum_{j=0}^{i} \sum_{\ell=0}^{2j} \Bigg[& \binom{2i-2j}{i-j} \\ & \cdot \binom{2j+2N_{\max}-2N_{\min}}{2j-\ell} \frac{(-1)^\ell\,(2j)!\,(N_{\max}-N_{\min}+\ell)!}{2^{2i-\ell}\,j!\,\ell!\,(N_{\max}-N_{\min}+j)!} \\ & \cdot \sum_{q=0}^{N_{\max}-N_{\min}+\ell} \mathcal{E}_{q+1}\left(\frac{N_{\text{t}}}{\rho}\right) \Bigg] \end{aligned} \quad (3.27)$$

with $N_{\max} = \max(N_{\text{t}}, N_{\text{r}})$ returns the ergodic capacity of a $N_{\text{r}} \times N_{\text{t}}$ Rayleigh-faded MIMO channel with IID entries and average signal-to-noise ρ.

3.6.2 Specific Relative Cluster Geometry

The spectral efficiency expressions in (3.24) and (3.26) depend, through ρ_0^{IA}, on both r_0 and r_{K-1} and they are thus fully general—in fact unnecessarily general for the purpose of assessing the benefits of IA. For that purpose, specifying the ratio a_0 is largely sufficient, as that allows marginalizing out the network dimensions while retaining the discrimination of relative in-cluster positions. Hence, we next seek a leaner characterization in the form of the average spectral efficiency over all possible cluster geometries that share a given a_0.

For arbitrary d under separate per-stream decoding, the marginalized ergodic spectral efficiency is

$$C^{\text{rel}}(a_0) = \mathsf{d}\,\mathbb{E}\left[\mathbb{E}\left[\log_2(1+\mathsf{SIR}_0)\,|\rho_0^{\text{IA}}\right] \,|\, \tfrac{r_0}{r_{K-1}} = a_0\right] \quad (3.28)$$

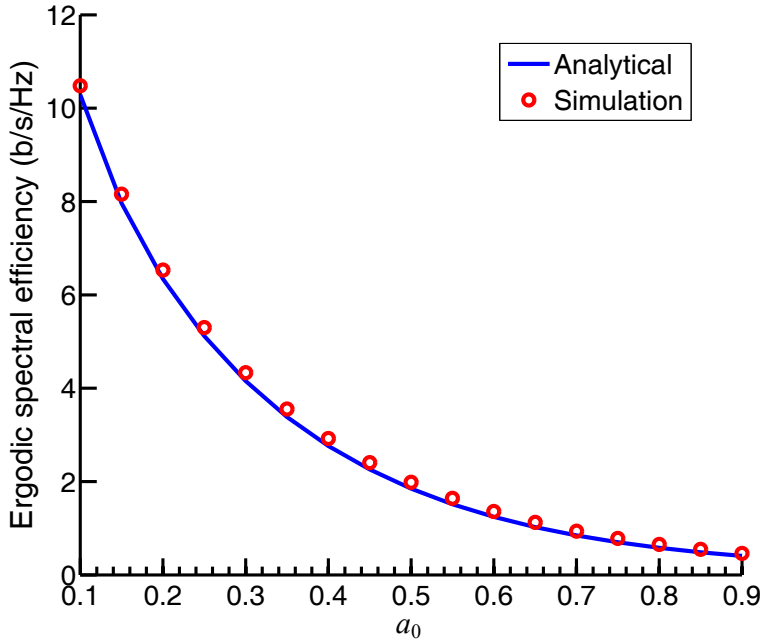

Figure 3.3: Marginalized ergodic spectral efficiency of IA as function of a_0 for $K = 5$, $\mathsf{d} = 1$ and $\eta = 4$.

$$= \mathsf{d}\,\mathbb{E}\left[\log_2(1+\mathsf{SIR}_0) \mid \tfrac{r_0}{r_{K-1}} = a_0\right] \tag{3.29}$$

$$= \mathsf{d}\int_0^\infty \log_2(1+\gamma)\,\mathrm{d}F_{\mathsf{SIR}_0|a_0}(\gamma) \tag{3.30}$$

and it is at this point that the conditional distribution $F_{\mathsf{SIR}_0|a_0}(\gamma)$ derived in Proposition 3.1 comes handy. Applying it to (3.30), the following result is obtained.

Proposition 3.4. For a given a_0 under separate per-stream decoding,

$$C^{\mathrm{rel}}(a_0) = \frac{\mathsf{d}\log_2 e}{K}\;{}_2F_1\left(1, K; K+1; 1 - \frac{2\mathsf{d}\,a_0^\eta}{\eta-2}\right). \tag{3.31}$$

Proof: See Appendix B.3.

Example 3.5. Shown in Fig. 3.3 is a comparison, for $K = 5$, $\mathsf{d} = 1$ and $\eta = 4$, of $C^{\mathrm{rel}}(a_0)$ against its simulated counterpart with $\boldsymbol{z}_0'$ as in (3.2). The simulated result corresponds to the exact mutual

information under the non-Gaussian interference in (3.2), computed through lengthy Monte-Carlo histograms and averaged over many fading realizations and out-of-cluster interference locations.

In turn, for $d > 1$ under joint decoding,

$$C^{\mathrm{rel}}(a_0) = \mathbb{E}\left[C^{\mathrm{MIMO}}_{\mathsf{d},\mathsf{d}}(\rho_0^{\mathrm{IA}}) \mid \tfrac{r_0}{r_{K-1}} = a_0\right] \tag{3.32}$$

where the expectation is over r_0 and r_{K-1}, conditioned on $r_0/r_{K-1} = a_0$. The right-hand side of (3.32) admits a closed form, given next.

Proposition 3.6. For $d > 1$ and a given a_0, under joint decoding,

$$C^{\mathrm{rel}}(a_0) = \log_2(e) \sum_{i=0}^{\mathsf{d}-1} \sum_{j=0}^{i} \sum_{\ell=0}^{2j} \frac{(-1)^\ell}{2^{2i-\ell}} \binom{2i-2j}{i-j} \binom{2j}{j} \binom{2j}{\ell} \cdot \sum_{m=0}^{\ell} \frac{1}{m+K} \, {}_2F_1\left(1, K; m+K+1; 1 - \frac{2\mathsf{d}\, a_0^\eta}{\eta - 2}\right). \tag{3.33}$$

Proof: See Appendix B.4.

3.6.3 Average Cluster Geometry

The spectral efficiencies in the previous section can be further expected over a_0 in order to characterize the average performance over all possible geometries. As was argued when the corresponding exercise was conducted for the SIR, this removes information on which the benefits of IA hinge, and hence what can be determined thereafter is only the average benefit of utilizing IA indiscriminately for all cluster geometries. At the same time, this computation evidences yet again the analytical muscle of stochastic geometry, yielding in compact form what in a deterministic model could only be attained through lengthy Monte-Carlo simulations.

For arbitrary d under separate per-stream decoding,

$$\bar{C} = \mathsf{d} \int_0^\infty \log_2(1+\gamma) \, \mathrm{d}F_{\mathsf{SIR}_0}(\gamma) \tag{3.34}$$

where the unconditional SIR distribution $F_{\mathsf{SIR}_0}(\cdot)$ is given in (3.21). Remarkably, in that case the above expectation can be expressed by means of the Meijer-G function [89]

$$G^{m,n}_{p,q}\left(z \;\middle|\; \begin{matrix} a_1, \ldots, a_n, a_{n+1}, \ldots, a_p \\ b_1, \ldots, b_m, b_{m+1}, \ldots, b_q \end{matrix}\right) \tag{3.35}$$

which is readily available in software packages such as Mathematica or MATLAB.

Proposition 3.7. Under separate per-stream decoding,

$$\bar{C} = \frac{4\mathsf{d}^2 \log_2 e}{\eta\,(\eta-2)} \sum_{n=0}^{K-2} \frac{(-1)^n}{n!\,(K-2-n)!} \cdot G_{3,3}^{2,3}\left(\frac{2\mathsf{d}}{\eta-2} \,\middle|\, \begin{matrix} -1, -K, -\frac{2(n+1)}{\eta} \\ -1, -1, -\frac{\eta+2(n+1)}{\eta} \end{matrix} \right) \tag{3.36}$$

which, for $\eta = 4$, simplifies to

$$\bar{C} = \frac{\mathsf{d}\log_2 e}{2^{K-1}} G_{4,4}^{2,4}\left(\mathsf{d} \,\middle|\, \begin{matrix} 0, \frac{1}{2}, 0, 1-K \\ 0, 0, \frac{1-K}{2}, \frac{2-K}{2} \end{matrix} \right). \tag{3.37}$$

Proof: See Appendix B.5.

For $d > 1$ under joint decoding, $\bar{C} = \mathbb{E}[C_{\mathsf{d},\mathsf{d}}^{\mathrm{MIMO}}(\rho_0^{\mathrm{IA}})]$ with expectation over r_0 and r_{K-1}, which ρ_0^{IA} is a function of.

Proposition 3.8. Under joint decoding,

$$\begin{aligned} \bar{C} = \frac{2\log_2 e}{\eta} \sum_{i=0}^{\mathsf{d}-1} \sum_{j=0}^{i} \sum_{\ell=0}^{2j} \frac{(-1)^\ell}{2^{2i-\ell}} \binom{2i-2j}{i-j} \binom{2j}{j} \binom{2j}{\ell} \\ \cdot \sum_{m=0}^{\ell} \frac{1}{m!} \left(\frac{2\mathsf{d}}{\eta-2} \right)^{m+1} \sum_{n=0}^{K-2} \frac{(-1)^n}{n!\,(K-2-n)!} \\ \cdot G_{3,3}^{2,3}\left(\frac{2\mathsf{d}}{\eta-2} \,\middle|\, \begin{matrix} -(m+1), -(m+K), -\frac{m\eta+2(n+1)}{\eta} \\ -(m+1), -1, -\frac{\eta(m+1)+2(n+1)}{\eta} \end{matrix} \right). \end{aligned} \tag{3.38}$$

Proof: See Appendix B.6.

3.7 System-level Benefits of IA

Having derived expressions for the ergodic spectral efficiency of IA, we can now put these expressions to work with the objective of ascertaining the system-level benefits of IA with respect to the SU-MIMO baseline.

3.7.1 SU-MIMO Baseline

As in IA, we consider a uniform power allocation for SU-MIMO, under which the ergodic spectral efficiency for a given absolute cluster geometry equals $C^{\mathrm{MIMO}}_{N_\mathrm{r},N_\mathrm{t}}(\rho_0^{\mathrm{MIMO}})$ where the local-average SIR accounting for in-cluster and out-of-cluster interference, both present in SU-MIMO, is

$$\rho_0^{\mathrm{MIMO}} = \frac{r_0^{-\eta}}{\sum_{k=1}^{K-1} r_k^{-\eta} + \sigma_0^2} \tag{3.39}$$

$$= \frac{1}{\sum_{k=1}^{K-1} \left(\frac{a_0}{a_k}\right)^{\eta} + \frac{1}{\rho_0^{\mathrm{IA}}}} \tag{3.40}$$

where $a_k = r_k / r_{K-1}$.

The average spectral efficiency over all geometries sharing some common $a_0, \ldots, a_{K-1}$ equals

$$\mathbb{E}\left[C^{\mathrm{MIMO}}_{N_\mathrm{r},N_\mathrm{t}}(\rho_0^{\mathrm{MIMO}}) \mid \tfrac{r_k}{r_{K-1}} = a_k\right] \tag{3.41}$$

with expectation over $r_0, \ldots, r_{K-1}$, which ρ_0^{MIMO} is function of, conditioned on $r_k/r_{K-1} = a_k$ for $k = 0, \ldots, K-1$.

Averaged over all cluster geometries, the SU-MIMO spectral efficiency is

$$\mathbb{E}\left[C^{\mathrm{MIMO}}_{N_\mathrm{r},N_\mathrm{t}}(\rho_0^{\mathrm{MIMO}})\right] \tag{3.42}$$

with unconditional expectation over $r_0, \ldots, r_{K-1}$.

3.7.2 Benefits for Specific Cluster Geometries

We begin by establishing the benefits of IA for specific geometries, in order to identify the range of situations in which IA outperforms the SU-MIMO baseline. For this purpose, and in order to make assessments that do not rest on the absolute scale of the network, we apply the expressions derived for relative cluster geometries. We begin by equating

$$C^{\mathrm{rel}}(\rho_0^{\mathrm{IA}}) = \mathbb{E}\left[C^{\mathrm{MIMO}}_{N_\mathrm{r},N_\mathrm{t}}(\rho_0^{\mathrm{MIMO}}) \mid \tfrac{r_k}{r_{K-1}} = a_k\right] \tag{3.43}$$

and, utilizing the expressions derived for $C^{\mathrm{rel}}(\cdot)$, ρ_0^{IA}, $C^{\mathrm{MIMO}}_{N_\mathrm{r},N_\mathrm{t}}(\cdot)$ and ρ_0^{MIMO}, numerically determine the values for $a_0, \ldots, a_{K-1}$ that define the boundary between the sets of geometries where IA and SU-MIMO are each superior.

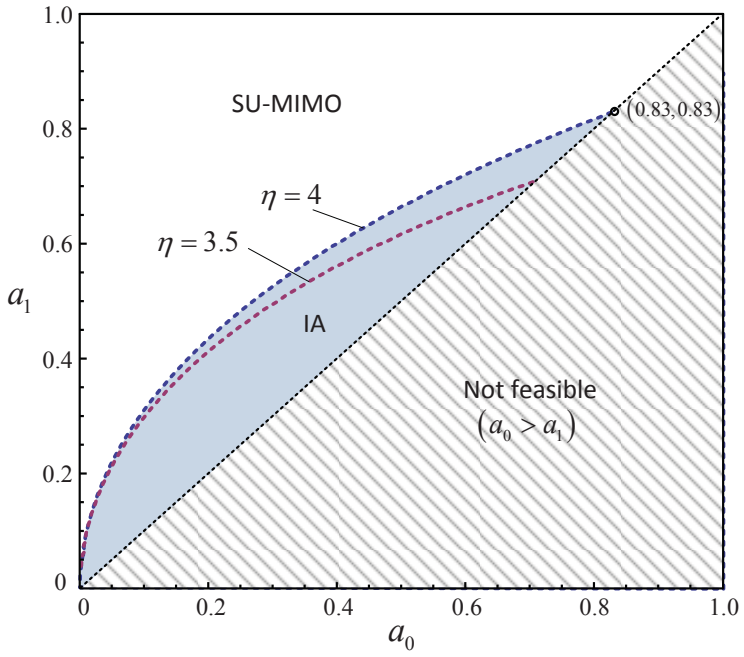

Figure 3.4: IA (with $K = 3$ and $\mathsf{d} = 1$) v. SU-MIMO (with $N_{\mathrm{t}} = N_{\mathrm{r}} = 2$) for $\eta = 3.5$ and $\eta = 4$.

Example 3.9. Let $K = 3$ and $\mathsf{d} = 1$, which can be supported with $N_{\mathrm{t}} = N_{\mathrm{r}} = 2$. Shown in Fig. 3.4 are the pairs (a_0, a_1) where IA and SU-MIMO are each superior for $\eta = 3.5$ and $\eta = 4$, which essentially delimit the range of pathloss exponents encountered in terrestrial systems. IA outperforms SU-MIMO in 20.5% and 26.7% of situations for $\eta = 3.5$ and $\eta = 4$, respectively.

Concentrating on $\eta = 4$, a more detailed snapshot of the comparison in Example 3.9 is offered in Fig. 3.5 where a contour plot of the relative improvement of IA over SU-MIMO is given. Notice that relatively important gains (say a doubling of the spectral efficiency) are attained in only a very small subset of geometries, specifically when a_0 is relatively small (weak out-of-cluster interference) and a_1 is similar to a_0 (strong in-cluster interference); only then does the removal of in-cluster interference compensate the sacrifice of signal dimensions.

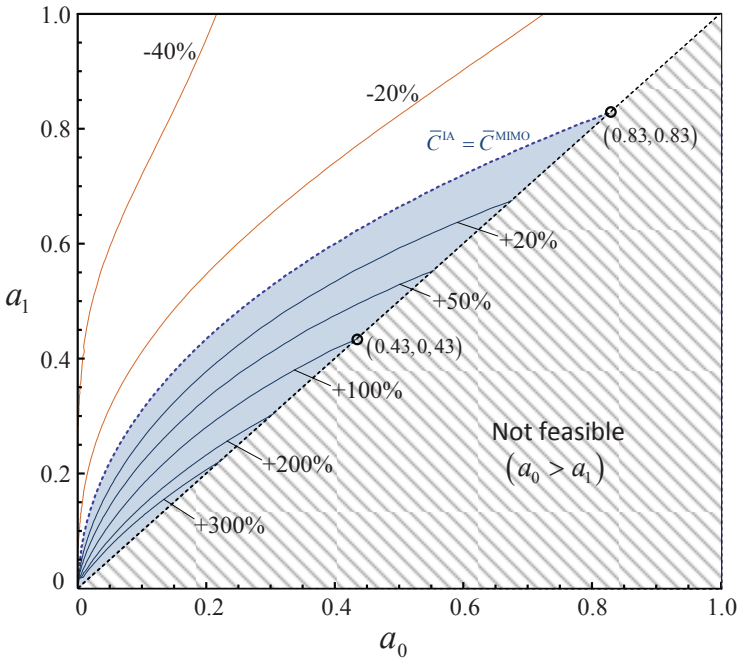

Figure 3.5: Spectral efficiency gain of IA (with $K = 3$ and $\mathsf{d} = 1$) over SU-MIMO (with $N_\mathrm{t} = N_\mathrm{r} = 2$), for $\eta = 4$.

To broaden the scope of the foregoing comparison, we next consider higher values of d and K along with the correspondingly higher values of N_t and N_r.

Example 3.10 (Maintain K, increase d)**.** Relative to Example 3.9 with $\eta = 4$, for $N_\mathrm{t} = N_\mathrm{r} = 4$ and $\mathsf{d} = 2$ (with $K = 3$) the subset of geometries where IA outperforms SU-MIMO shrinks to 24.6% with joint decoding and to 15.3% with separate decoding.

Example 3.11 (Maintain d, increase K)**.** Relative to Example 3.9 with $\eta = 4$, for $N_\mathrm{t} = 2$, $N_\mathrm{r} = 3$ and $K = 4$ (with $\mathsf{d} = 1$) the subset of geometries where IA outperforms SU-MIMO shrinks to 19.4%.

Short of an exhaustive comparison for all combinations of d and K (and the corresponding N_t and N_r), the above strongly suggest that IA can outperform the baseline in at most about a quarter of network geometries, often less.

Table 3.1: Spatially averaged spectral efficiencies of IA and SU-MIMO for various cluster configurations

IA		SU-MIMO	
Configuration	(b/s/Hz)	Configuration	(b/s/Hz)
$K = 3$, $\mathsf{d} = 1$	3.03	$N_\mathrm{t} = N_\mathrm{r} = 2$	3.89
$K = 3$, $\mathsf{d} = 2$	5.84	$N_\mathrm{t} = N_\mathrm{r} = 4$	7.70
$K = 5$, $\mathsf{d} = 1$	3.66	$N_\mathrm{t} = N_\mathrm{r} = 3$	5.76
$K = 5$, $\mathsf{d} = 2$	7.06	$N_\mathrm{t} = N_\mathrm{r} = 6$	11.39
$K = 7$, $\mathsf{d} = 1$	4.08	$N_\mathrm{t} = N_\mathrm{r} = 4$	7.70
$K = 7$, $\mathsf{d} = 2$	7.87	$N_\mathrm{t} = N_\mathrm{r} = 8$	15.08

Since the potential network geometries are not equally likely, a judgment based on average spectral efficiencies requires a further step.

3.7.3 Average Benefits

The small share of geometries in which IA outperforms the SU-MIMO baseline strongly suggests that, barring the possibility that those geometries occur very frequently, a blanket utilization of IA shall not improve the spatial averaged spectral efficiency over all geometries. To quantify this precisely, we can invoke the expressions derived for average cluster geometries. Shown in Table 3.1 we have a comparison of $\bar{C}^{\mathrm{IA}}$ and $\mathbb{E}\left[C^{\mathrm{MIMO}}_{N_\mathrm{r},N_\mathrm{t}}(\rho_0^{\mathrm{MIMO}})\right]$ for several values of K and d, and corresponding values of N_t and N_r, with $\eta = 4$. In every case, the average spectral efficiency of IA is inferior to that of SU-MIMO.

Although a blanket utilization of IA is not beneficial, there are situations (cf. Fig. 3.5) in which it is indeed advantageous. This points to a switched scheme that resorts to IA or SU-MIMO, whichever is best, depending on the geometry. From the joint distribution of $a_0, \ldots, a_{K-1}$, the average gain of such a switched scheme can be quantified.

Example 3.12. For $K = 3$, the average gain of a switched scheme relative to standalone SU-MIMO is 3.4% for $\mathsf{d} = 1$ and 2.9% for $\mathsf{d} = 2$.

3.8 Conclusions and Contributions

Leveraging the analytical potency of stochastic geometry and armed with a new modeling approach for out-of-cluster interference, we have derived analytical expressions for the ergodic spectral efficiency of IA. From these expressions, we observe that a universal utilization of IA in cellular networks would be ill-advised. IA can help in certain sets of base station and user locations—namely those resulting in strong in-cluster and weak out-of-cluster interference—and for users encountering such geometries the benefits can be substantial. However, these geometries are relatively infrequent and the ensuing improvements in terms of average spectral efficiency for the system are rather minute. The above observations have been made under assumptions highly favorable to IA and with a conservative baseline that does not even fully exploit the available CSI. With the degree of CSI required for IA, a superior MU-MIMO baseline could be implemented. Overheads associated with precoder computation [23] have also been disregarded, which is the focus of the next chapter.

Non-unitary precoders and MMSE receivers would improve upon pure IA, but mostly in geometries where baseline schemes are already preferable.

Chapter 4

Pilot-Assisted Interference Alignment

> The formulation of the problem is often more essential than its solution, which may be merely a matter of mathematical or experimental skill.
>
> Albert Einstein

The objective of this chapter is to assess the robustness of IA in operationally relevant continuous fading. To conduct the analysis, we consider an isolated K-user interference channel setting, which is a favorable model for IA operation. We note that this interference channel can be representative of realistic cellular networks only within a certain SNR range (cf. Chapter 3), for instance, network geometries corresponding to strong in-cluster and weak (or negligible) out-of-cluster interference.

4.1 Related Work and Motivation

With instantaneous and perfect CSI at transmitters and receivers, IA maximizes the number of interference-free signaling dimensions, i.e., the number of degrees of freedom (DoF) in a K-user interference channel [16]. Although recent results indicate that the instantaneous nature of the CSI may be dispensed with [106], the need for the CSI to be perfect seems unavoidable for the alignment to yield the corresponding number of DoF. This motivates the interest in assessing how IA might perform in the face of some inevitable CSI

imperfections. Broadly speaking, the issue of imperfect CSI involves three intertwined aspects:

(1) Fundamentally, it cannot be decoupled from the reality of fading selectivity. If the fading were not selective, the CSI could be arbitrarily precise; it is the selectivity that curbs the number of observations of each fading realization making it impossible to gather perfect CSI.

(2) An arguably less fundamental, but, in practice, equally relevant matter is the utilization of pilot symbols to obtain the CSI at the receivers. Pilots imply overhead.

(3) Finally, there is the issue of rendering the CSI gathered at the receivers available also to the transmitters; this is simpler with TDD or with full-duplex, because of fading reciprocity, and more challenging with FDD, where explicit feedback is unavoidable.

Some studies on the performance of IA with imperfect CSI have been put forth recently. In reference to (1) above, [107] bounded, by both above and below, the sum spectral efficiency achievable by IA in the face of noisy CSI. The impact of imperfect CSI and antenna correlation were jointly quantified in [108], where an approximate closed-form expression for the corresponding SINR was derived. Also, [109] presented simulation results suggesting that IA may be very fragile when (1) is accounted for; however, these results were for unoptimized IA and disregarded pilot overhead.

In reference to (2), parameters such as the number of pilot symbols and their power were optimized to maximize a mutual information lower bound in [110], for the case of single-user MIMO. Pilot-assisted transmission has subsequently been considered for IA, e.g., in [111], which studied the impact of pilot overhead in terms of DoF, and in [112], where it was argued that an unrestrained number of cooperating base stations can actually be detrimental because of excessive overhead.

Finally, in reference to (3), a variety of techniques have been proposed for CSI feedback in FDD systems [113–116]. The authors in [113] considered digital (quantized) feedback for single-antenna interference channels with Grassmannian codebooks utilized to quantize the channel coefficients. The results were subsequently extended

to MIMO interference channels in [114]. It was shown in [113, 114] that the number of DoF can be preserved in the face of quantized feedback as long as the number of feedback bits scales with the SNR, a result that directly extends to interference channels the original findings of [117]. In [115], a novel CSI feedback scheme was proposed by exploiting the structure of the IA equations and the Grassmannian representation of the CSI; the authors showed that this scheme can achieve better spectral efficiency compared to a naïve approach (which simply quantizes the channel matrices independently) for a given number of feedback bits, but still requires that such number scales with the SNR in order to preserve the DoF. As an attractive alternative to digital feedback, analog feedback[1] has been shown to sustain the number of DoF achieved by IA [116]. However, all the digital feedback analyses in [113–115] and the analog feedback analysis in [116] assumed perfect CSI at the receivers.

This chapter jointly tackles (1)–(3) with the goal of studying the robustness of IA with pilot and IA configurations optimized as a function of the fading selectivity, SNR, number of users, and other parameters of interest under both TDD and FDD. Additional related works include [118–120], which study (1)–(3) for the single-user and the broadcast channels. Particularly relevant is [23], which studies (1)–(3) for IA with block fading.

Like [23], most of the aforementioned references invoke block-fading structures, and once (1)–(3) are jointly considered and IA is to be optimized for minimum pilot and feedback overhead, it becomes important to resort to continuous fading [121–123]. With this finer model of the fading selectivity in place, the steps that must be considered for a complete analysis of the IA operation are:

- Periodic transmission of forward pilots to allow for CSI gathering at the receivers. The pilot symbols made available for this task are referred to as *common* pilots.
- Computation of the receive filters on the basis of the foregoing CSI.

[1] In analog feedback, the estimated CSI at the receiver is represented as continuous values and conveyed to the transmitter without modulation and coding. Then, the transmitter can recover the CSI from its observation (without demodulation and channel decoding), which may be different from the information at the receiver due to additive channel noise. However, in digital feedback, transmitter could recover the same information as receiver learned if it passes channel decoding.

- CSI feedback, in the case of FDD, or exploitation of fading reciprocity, in the case of TDD with carefully calibrated transceivers, to convey the CSI to the transmitters. In the FDD case, analog feedback is our choice and the coherent detection of the feedback entails a further process of reverse channel estimation [23].
- Computation of the transmit precoders on the basis of the CSI acquired by the transmitters.
- Transmission through the precoders of additional pilots, named *dedicated* pilots, in order to enable estimation of the precoded channel matrices at the receivers.[2] This, in turn, enables coherent detection of the subsequent payload data.
- Finally, transmission of such payload data.

All of the above steps, and the ensuing overheads, are considered here, under continuous fading. The utilization of a continuous fading model releases the choice of the interval between IA updates, which in block fading is implicitly given by the size of the fading blocks whereas in our work it becomes a free parameter as it is in an actual system. We formulate the optimization of pilot and feedback overheads, and of the IA update interval, to maximize the effective sum spectral efficiency for arbitrary SNRs. This general formulation is followed by a simplified version thereof that is tailored to the high-SNR regime, where IA is mostly of interest. The impact of asymmetric SNRs in the forward and reverse links is also explored and, to gauge the extent to which the IA performance degrades because of the various overheads, pilot-assisted time-division multiple access (TDMA) is invoked as a baseline throughout the chapter.

As mentioned in the previous chapter, IA precoders can be designed using the iterative algorithms that optimize the precoders and the receive filters to minimize the leakage interference by alternating between the forward and the reverse links. These algorithms can be either centralized or distributed.

- In centralized IA, all the base stations share their CSI. A central entity gathers the global CSI of all the forward and reverse

[2] Alternatively, the dedicated pilots could be suppressed in favor of coded messages directly conveying the precoders to the receivers, but this approach would be somewhat more susceptible to fading selectivity and might incur larger overheads.

links and computes the precoders. With global CSI available at that common point, iterations can be performed off-line at the central entity eliminating the need for over-the-air signaling.

- In distributed IA, there is no CSI sharing among the base stations and each transmitter locally computes its own precoder. The iterations must take place over the air, incurring further signaling overhead.

This work considers the centralized version, which is the most favorable one for IA.

4.2 System Model

We consider the standard interference channel setting with K transmitter and receiver pairs. Transmitters and receivers are equipped with N_{t} and N_{r} antennas, respectively, and each transmitter-receiver link conveys $\mathsf{d} \leq N_{\min}$ signal streams. The observed vector $\boldsymbol{y}_k \in \mathbb{C}^{N_{\mathrm{r}} \times 1}$ at receiver k is

$$\boldsymbol{y}_k = \sum_{j=1}^{K} \sqrt{\frac{P}{\mathsf{d}}} \boldsymbol{H}_{k,j} \boldsymbol{x}_j + \boldsymbol{z}_k \tag{4.1}$$

where $\boldsymbol{x}_j \in \mathbb{C}^{N_{\mathrm{t}} \times 1}$ is the signal from transmitter j while $\boldsymbol{H}_{k,j} \in \mathbb{C}^{N_{\mathrm{r}} \times N_{\mathrm{t}}}$ is the channel matrix from transmitter j to receiver k and P is the transmit power. The noise at receiver k is $\boldsymbol{z}_k \sim \mathcal{N}_{\mathbb{C}}(\boldsymbol{0}, \sigma_{\mathrm{N}}^2 \boldsymbol{I}_{N_{\mathrm{r}}})$ where σ_{N}^2 is the noise variance. The entries of $\boldsymbol{H}_{k,j}$ are IID, drawn from $\mathcal{N}_{\mathbb{C}}(0,1)$. The signal at transmitter k is $\boldsymbol{x}_k = \boldsymbol{V}_k \boldsymbol{s}_k$ where $\boldsymbol{V}_k = [\boldsymbol{v}_{k,1}, \ldots, \boldsymbol{v}_{k,\mathsf{d}}] \in \mathbb{C}^{N_{\mathrm{t}} \times \mathsf{d}}$ is the unitary precoding matrix at the kth transmitter and $\boldsymbol{s}_k = [s_{k,1}, s_{k,2}, \ldots, s_{k,\mathsf{d}}]^T \in \mathbb{C}^{\mathsf{d} \times 1}$ is the complex data symbol vector satisfying $\mathbb{E}[\boldsymbol{s}_k \boldsymbol{s}_k^*] = \boldsymbol{I}_{\mathsf{d}}$. While the data symbols could be chosen from any distribution, we focus on Gaussian codebooks, which maximize the mutual information between $\boldsymbol{x}_k$ and $\boldsymbol{y}_k$ with perfect IA. Power is uniformly allocated across streams, which is asymptotically optimal at high SNR. At receiver k, the vector $\boldsymbol{y}_k$ is filtered by a unitary matrix $\boldsymbol{W}_k = [\boldsymbol{w}_{k,1}, \boldsymbol{w}_{k,2}, \ldots, \boldsymbol{w}_{k,\mathsf{d}}] \in \mathbb{C}^{N_{\mathrm{r}} \times \mathsf{d}}$.

The SINR of the ℓth signal stream at receiver k is given by

$$\mathsf{SINR}_{k,\ell} = \frac{\frac{P}{\mathsf{d}} |\boldsymbol{w}_{k,\ell}^* \boldsymbol{H}_{k,k} \boldsymbol{v}_{k,\ell}|^2}{\mathcal{I}_{k,\ell} + \sigma_{\mathrm{N}}^2 \left\| \boldsymbol{w}_{k,\ell} \right\|_2^2} \tag{4.2}$$

where

$$\mathcal{I}_{k,\ell} = \sum_{\substack{m=1,\\ m\neq\ell}}^{\mathsf{d}} \frac{P}{\mathsf{d}} |\boldsymbol{w}_{k,\ell}^* \boldsymbol{H}_{k,k} \boldsymbol{v}_{k,m}|^2 + \sum_{\substack{j=1,\\ j\neq k}}^{K} \sum_{m=1}^{\mathsf{d}} \frac{P}{\mathsf{d}} |\boldsymbol{w}_{k,\ell}^* \boldsymbol{H}_{k,j} \boldsymbol{v}_{j,m}|^2. \quad (4.3)$$

4.3 Interference Alignment

Recall from Section 3.3 that, IA with d DoF per user is achieved if and only if the precoding and receiving filters of user k simultaneously satisfy

$$\boldsymbol{W}_k^* \boldsymbol{H}_{k,j} \boldsymbol{V}_j = \boldsymbol{0} \qquad \forall j \neq k \quad (4.4)$$

$$\operatorname{rank}(\boldsymbol{W}_k^* \boldsymbol{H}_{k,k} \boldsymbol{V}_k) = \mathsf{d} \qquad \forall k \quad (4.5)$$

where (4.4) are zero-forcing conditions on the interference while (4.5) guarantees the required dimensionality for the desired signal space. For a given d, a different number of antennas is required for IA to be feasible with each K (cf. (3.3)).

4.3.1 Perfect CSI

With perfect CSI provided as side information, IA results in a d-dimensional interference-free channel for every intended link. Then, the SINR of the ℓth stream at receiver k is

$$\mathsf{SINR}_{k,\ell} = \frac{P}{\mathsf{d}\sigma_{\mathrm{N}}^2} |\boldsymbol{w}_{k,\ell}^* \boldsymbol{H}_{k,k} \boldsymbol{v}_{k,\ell}|^2 \quad (4.6)$$

where $P/(\mathsf{d}\sigma_{\mathrm{N}}^2)$ represents the average per-stream SNR. Since $\boldsymbol{V}_k$ and $\boldsymbol{W}_k$ are unitary and independent of $\boldsymbol{H}_{k,k}$, the effective channels $\boldsymbol{w}_{k,\ell}^* \boldsymbol{H}_{k,k} \boldsymbol{v}_{k,\ell}$ are complex Gaussian with unit variance. The average sum spectral efficiency is then [94, 95]

$$\bar{C}^{\mathrm{sum}}\left(\frac{P}{\mathsf{d}\sigma_{\mathrm{N}}^2}\right) = \sum_{k=1}^{K} \sum_{\ell=1}^{\mathsf{d}} \mathbb{E}\left[\log_2\left(1 + \frac{P}{\mathsf{d}\sigma_{\mathrm{N}}^2} |\boldsymbol{w}_{k,\ell}^* \boldsymbol{H}_{k,k} \boldsymbol{v}_{k,\ell}|^2\right)\right] \quad (4.7)$$

$$= K\mathsf{d}\, e^{\mathsf{d}\sigma_{\mathrm{N}}^2/P} \mathcal{E}_1\left(\frac{\mathsf{d}\sigma_{\mathrm{N}}^2}{P}\right) \log_2 e. \quad (4.8)$$

4.3.2 Imperfect CSI

With precoders and receive filters computed on the basis of estimated rather than actual fading coefficients, the signals become

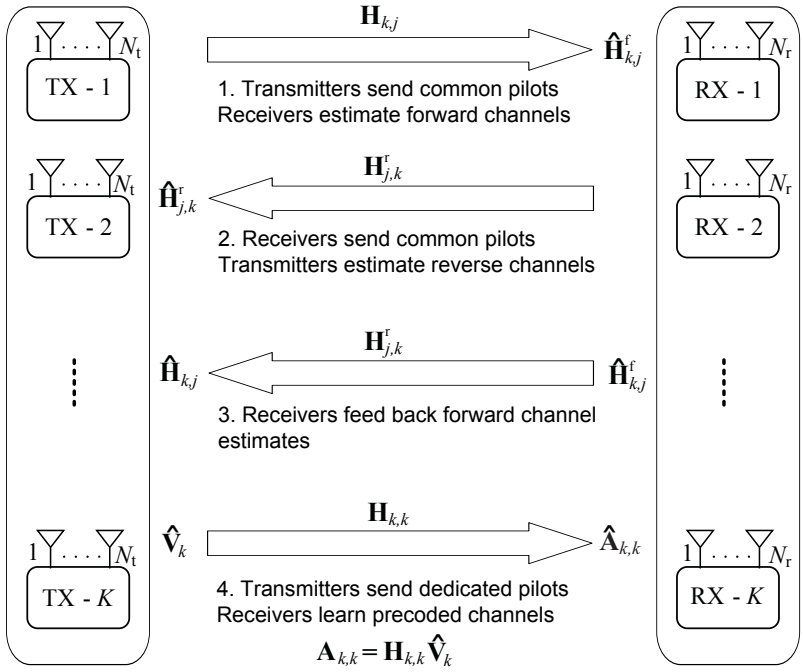

Figure 4.1: CSI transfer with FDD in a K-user MIMO interference channel. Notation: $\hat{\boldsymbol{H}}^{\mathrm{f}}_{k,j}$ represents the estimate of forward channel $\boldsymbol{H}_{k,j}$ at receiver k; $\boldsymbol{H}^{\mathrm{r}}_{j,k}$ represents the reverse channel from receiver k to transmitter j and $\hat{\boldsymbol{H}}^{\mathrm{r}}_{j,k}$ is its estimate at transmitter j; $\hat{\boldsymbol{H}}_{k,j}$ denotes the estimate of $\boldsymbol{H}_{k,j}$ available at transmitter k; $\hat{\boldsymbol{V}}_j$ is the IA precoder at transmitter j; $\boldsymbol{A}_{k,k}$ denotes the precoded channel matrix from transmitter k to receiver k and $\hat{\boldsymbol{A}}_{k,k}$ is its estimate at receiver k.

misaligned and interference leaks through. Figure 4.1 depicts the scheme considered in this chapter for CSI acquisition and transfer.

Let us denote by $\hat{\boldsymbol{H}}_{k,j}$ an imperfect estimate of $\boldsymbol{H}_{k,j}$ at transmitter k and by $\tilde{\boldsymbol{H}}_{k,j} = \boldsymbol{H}_{k,j} - \hat{\boldsymbol{H}}_{k,j}$ its estimation error. The IA precoders and receivers obtained on the basis of channel estimates are $\hat{\boldsymbol{V}}_k$ and $\hat{\boldsymbol{W}}_k$, for $k = 1, \ldots, K$. At receiver k, the ℓth signal stream is extracted by $\hat{\boldsymbol{w}}_{k,\ell}$ yielding

$$\hat{\boldsymbol{w}}^*_{k,\ell}\boldsymbol{y}_k = \sum_{j=1}^{K} \sqrt{\frac{P}{\mathsf{d}}}\hat{\boldsymbol{w}}^*_{k,\ell}\boldsymbol{H}_{k,j}\hat{\boldsymbol{V}}_j\boldsymbol{s}_j + \hat{\boldsymbol{w}}^*_{k,\ell}\boldsymbol{z}_k \tag{4.9}$$

$$
\begin{aligned}
&= \sum_{j=1}^{K} \sqrt{\frac{P}{\mathsf{d}}} \hat{\boldsymbol{w}}_{k,\ell}^{*} \left(\hat{\boldsymbol{H}}_{k,j} + \tilde{\boldsymbol{H}}_{k,j} \right) \hat{\boldsymbol{V}}_j \boldsymbol{s}_j + \hat{\boldsymbol{w}}_{k,\ell}^{*} \boldsymbol{z}_k \\
&= \sqrt{\frac{P}{\mathsf{d}}} \hat{\boldsymbol{w}}_{k,\ell}^{*} \hat{\boldsymbol{H}}_{k,k} \hat{\boldsymbol{v}}_{k,\ell} s_{k,\ell} \\
&\quad + \sum_{j=1}^{K} \sum_{m=1}^{\mathsf{d}} \sqrt{\frac{P}{\mathsf{d}}} \hat{\boldsymbol{w}}_{k,\ell}^{*} \tilde{\boldsymbol{H}}_{k,j} \hat{\boldsymbol{v}}_{j,m} s_{j,m} + \hat{\boldsymbol{w}}_{k,\ell}^{*} \boldsymbol{z}_k \qquad (4.10)
\end{aligned}
$$

where (4.10) follows from the fact that the IA solution computed on the basis of channel estimates satisfies $\hat{\boldsymbol{w}}_{k,\ell}^{*} \hat{\boldsymbol{H}}_{k,j} \hat{\boldsymbol{v}}_{j,m} = 0, \forall (k,\ell) \neq (j,m)$. If the decoders regard the channel estimates as the actual channel coefficients, as is customary, then the estimation error terms in (4.10) simply play the role of additional Gaussian noise [124]. In turn, $\hat{\boldsymbol{V}}_k$ and $\hat{\boldsymbol{W}}_k$ are unitary and independent of $\hat{\boldsymbol{H}}_{k,k}$ and $\tilde{\boldsymbol{H}}_{k,j}, \forall k,j$. However, the terms $\hat{\boldsymbol{w}}_{k,\ell}^{*} \hat{\boldsymbol{H}}_{k,k} \hat{\boldsymbol{v}}_{k,\ell} s_{k,\ell}$ and $\hat{\boldsymbol{w}}_{k,\ell}^{*} \tilde{\boldsymbol{H}}_{k,j} \hat{\boldsymbol{v}}_{j,m} s_{j,m}$ are in general dependent when $(k,\ell) = (j,m)$. By invoking MMSE estimation, $\hat{\boldsymbol{H}}_{k,j}$ and $\tilde{\boldsymbol{H}}_{k,j}$ become uncorrelated and, given their Gaussian nature, mutually independent; this renders the aforementioned terms also independent for $(k,\ell) = (j,m)$. The entries of $\tilde{\boldsymbol{H}}_{k,j}$ are IID $\mathcal{N}_{\mathbb{C}}(0, \sigma^2_{\tilde{\boldsymbol{H}}})$ whereas the entries of $\hat{\boldsymbol{H}}_{k,j}$ are $\mathcal{N}_{\mathbb{C}}(0, 1 - \sigma^2_{\tilde{\boldsymbol{H}}})$.

Then, the average sum spectral efficiency is[3]

$$
\bar{C}^{\text{sum}} = \sum_{k=1}^{K} \sum_{\ell=1}^{\mathsf{d}} \mathbb{E} \left[\log_2 \left(1 + \frac{\frac{P}{\mathsf{d}} |\hat{\boldsymbol{w}}_{k,\ell}^{*} \hat{\boldsymbol{H}}_{k,k} \hat{\boldsymbol{v}}_{k,\ell}|^2}{\sigma_{\text{N}}^2 + \sum_{j=1}^{K} \sum_{m=1}^{\mathsf{d}} \mathbb{E} \left[\frac{P}{\mathsf{d}} |\hat{\boldsymbol{w}}_{k,\ell}^{*} \tilde{\boldsymbol{H}}_{k,j} \hat{\boldsymbol{v}}_{j,m}|^2 \right]} \right) \right] \qquad (4.11)
$$

with the outer expectation taken over the direct fading channels, $\hat{\boldsymbol{H}}_{k,k}$. We note that this is the spectral efficiency achieved with separate decoding of each same-link stream; for $\mathsf{d} > 1$, joint decoding of all same-link streams would be required for optimality [107]. For $\mathsf{d} = 1$, as in all the examples in this chapter, this becomes immaterial.

[3]The spectral efficiency in (4.11) corresponds to decoders that, as mentioned earlier, regard the channel estimates as the actual channel coefficients, in which case the nearest-neighbor decoding rule applies. For decoders exploiting the joint distribution of the channel estimates and the corresponding estimation errors, (4.11) represents a lower bound to the achievable spectral efficiency [125]. The difference between these two quantities tends to be minute [126].

The precoder $\hat{\boldsymbol{V}}_k$ and the receive filter $\hat{\boldsymbol{W}}_k$ are designed such that $\hat{\boldsymbol{W}}_k^* \hat{\boldsymbol{H}}_{k,j} \hat{\boldsymbol{V}}_j = 0$ for $j \neq k$ based on the channel estimates $\hat{\boldsymbol{H}}_{k,j}$ available at transmitter k. The mismatch error variance

$$\mathbb{E}\left[|\hat{\boldsymbol{w}}_{k,\ell}^* \tilde{\boldsymbol{H}}_{k,j} \hat{\boldsymbol{v}}_{j,m}|^2\right]$$

for $j \neq k$ is proportional to the channel estimation error variance, $\sigma^2_{\tilde{\boldsymbol{H}}}$. For its part, the desired signal estimation error variance

$$\mathbb{E}\left[|\hat{\boldsymbol{w}}_{k,\ell}^* \tilde{\boldsymbol{H}}_{k,k} \hat{\boldsymbol{v}}_{k,\ell}|^2\right]$$

depends only on the dedicated pilots, i.e., it is proportional to the precoded channel estimation error variance denoted by $\sigma^2_{\tilde{\boldsymbol{A}}}$ (cf. Fig. 4.1). Defining the effective average SINR as

$$\rho^{\text{eff}} = \frac{P(1-\sigma^2_{\tilde{\boldsymbol{A}}})}{\sigma^2_{\text{N}} + P\left((K-1)\sigma^2_{\tilde{\boldsymbol{H}}} + \sigma^2_{\tilde{\boldsymbol{A}}}\right)} \tag{4.12}$$

the expression in (4.11) can be more compactly rewritten as

$$\bar{C}^{\text{sum}}\left(\frac{\rho^{\text{eff}}}{\mathsf{d}}\right) = \sum_{k=1}^{K}\sum_{\ell=1}^{\mathsf{d}} \mathbb{E}\left[\log_2\left(1 + \frac{\rho^{\text{eff}}}{\mathsf{d}}|\boldsymbol{h}_\ell^{\text{eff}}|^2\right)\right] \tag{4.13}$$

where $\boldsymbol{h}_\ell^{\text{eff}} = \hat{\boldsymbol{w}}_{k,\ell}^* \hat{\boldsymbol{H}}_{k,k} \hat{\boldsymbol{v}}_{k,\ell}$ is complex Gaussian and thus

$$\bar{C}^{\text{sum}}\left(\frac{\rho^{\text{eff}}}{\mathsf{d}}\right) = K\mathsf{d}\,\log_2(e) e^{\mathsf{d}/\rho^{\text{eff}}} \mathcal{E}_1\left(\frac{\mathsf{d}}{\rho^{\text{eff}}}\right). \tag{4.14}$$

4.3.3 Time Selectivity

Next, to tie the analysis in the previous section with the dynamics of the fading, consider a discrete-time stationary fading process $h[n]$ governed by a given Doppler spectrum or, equivalently, by the corresponding time-domain correlation function $\epsilon[m] = \mathbb{E}[h[n]h^*[n+m]]$. This model applies to every entry of each of the channel matrices.

Fading selectivity implies that the IA solution computed at a given instant suffers growing misalignment as time evolves. Precisely, if the IA solution is computed at time 0 on the basis of current channel estimates, at time n the signal extracted for stream ℓ at receiver k will be

$$\hat{\boldsymbol{w}}_{k,\ell}^* \boldsymbol{y}_k[n] = \sum_{j=1}^{K} \sqrt{\frac{P}{\mathsf{d}}} \hat{\boldsymbol{w}}_{k,\ell}^* \left(\epsilon[n]\boldsymbol{H}_{k,j}[0] + \sqrt{1-\epsilon[n]^2}\boldsymbol{\Psi}_{k,j}\right) \hat{\boldsymbol{V}}_j \boldsymbol{s}_j$$

$$+ \hat{\boldsymbol{w}}_{k,\ell}^{*} \boldsymbol{z}_k \tag{4.15}$$

where $\boldsymbol{H}_{k,j}[0]$ is the channel at time 0 and $\boldsymbol{\Psi}_{k,j}$, whose entries are $\mathcal{N}_{\mathbb{C}}(0,1)$ and independent of $\boldsymbol{H}_{k,j}[0]$, is the innovation between times 0 and n. Except where essential, time indices are dropped henceforth for the sake of notational compactness. Leveraging the derivations in Section 4.3.2, (4.15) can be rewritten as

$$\begin{aligned}\hat{\boldsymbol{w}}_{k,\ell}^{*} \boldsymbol{y}_k &= \sum_{j=1}^{K} \sqrt{\frac{P}{\mathsf{d}}} \hat{\boldsymbol{w}}_{k,\ell}^{*} \left(\epsilon[n] \left(\hat{\boldsymbol{H}}_{k,j} + \tilde{\boldsymbol{H}}_{k,j} \right) + \sqrt{1-\epsilon[n]^2} \boldsymbol{\Psi}_{k,j} \right) \hat{\boldsymbol{V}}_j \boldsymbol{s}_j \\ &\quad + \hat{\boldsymbol{w}}_{k,\ell}^{*} \boldsymbol{z}_k \qquad (4.16) \\ &= \epsilon[n] \sqrt{\frac{P}{\mathsf{d}}} \hat{\boldsymbol{w}}_{k,\ell}^{*} \hat{\boldsymbol{H}}_{k,k} \hat{\boldsymbol{v}}_{k,\ell} s_{k,\ell} + \hat{\boldsymbol{w}}_{k,\ell}^{*} \boldsymbol{z}_k \\ &\quad + \sum_{j=1}^{K} \sum_{m=1}^{\mathsf{d}} \sqrt{\frac{P}{\mathsf{d}}} \hat{\boldsymbol{w}}_{k,\ell}^{*} \left(\epsilon[n] \tilde{\boldsymbol{H}}_{k,j} + \sqrt{1-\epsilon[n]^2} \boldsymbol{\Psi}_{k,j} \right) \hat{\boldsymbol{v}}_{j,m} s_{k,m} \qquad (4.17)\end{aligned}$$

where (4.17) follows from the fact that $\hat{\boldsymbol{w}}_{k,\ell}^{*} \hat{\boldsymbol{H}}_{k,j} \hat{\boldsymbol{v}}_{j,m} = 0, \forall (k,\ell) \neq (j,m)$. In turn, the average sum mutual information at time n is

$$\bar{I}^{\text{sum}} = \sum_{k=1}^{K} \sum_{\ell=1}^{\mathsf{d}} \mathbb{E} \left[\log_2 \left(1 + \frac{\epsilon[n]^2 \frac{P}{\mathsf{d}} |\hat{\boldsymbol{w}}_{k,\ell}^{*} \hat{\boldsymbol{H}}_{k,k} \hat{\boldsymbol{v}}_{k,\ell}|^2}{\sigma_{\text{N}}^2 + \sum_{j=1}^{K} \sum_{m=1}^{\mathsf{d}} \mathbb{E} \left[\frac{P}{\mathsf{d}} |\hat{\boldsymbol{w}}_{k,\ell}^{*} (\epsilon[n] \tilde{\boldsymbol{H}}_{k,j} + \sqrt{1-\epsilon[n]^2} \boldsymbol{\Psi}_{k,j}) \hat{\boldsymbol{v}}_{j,m}|^2 \right]} \right) \right] \tag{4.18}$$

given by (4.18) in the next page with outer expectation over the direct fading channels.[4] The effective average SINR at time n is

$$\rho^{\text{eff}}[n] = \frac{P \, \epsilon[n]^2 (1 - \sigma_{\tilde{\boldsymbol{A}}}^2)}{\sigma_{\text{N}}^2 + P \left(K + \epsilon[n]^2 \left((K-1) \sigma_{\tilde{\boldsymbol{H}}}^2 - K + \sigma_{\tilde{\boldsymbol{A}}}^2 \right) \right)} \tag{4.19}$$

[4] We resist referring to (4.18) as a spectral efficiency because it is only the average sum mutual information at a given lag n relative to the time of computation of the IA solution. It is only once codewords are allowed to span many symbols at every lag that the operational significance of the average sum spectral efficiency is acquired, and this is deferred to later in the chapter.

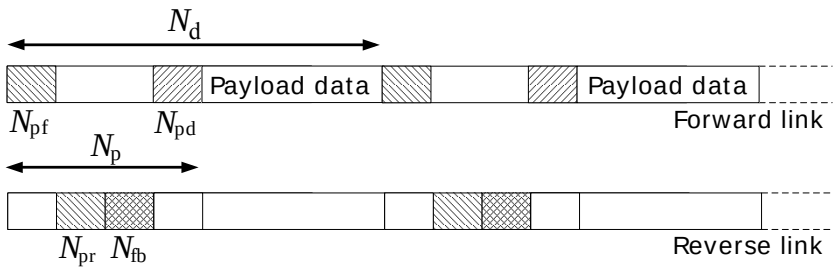

Figure 4.2: Pilot overhead model.

which follows from the uncorrelatedness of $\boldsymbol{\Psi}_{k,j}$ and $\tilde{\boldsymbol{H}}_{k,j}$. Thus, the average sum mutual information in (4.18) can be rewritten as

$$\bar{I}^{\mathrm{sum}}[n] = \sum_{k=1}^{K} \sum_{\ell=1}^{\mathsf{d}} \mathbb{E}\left[\log_2\left(1 + \frac{\rho^{\mathrm{eff}}[n]}{\mathsf{d}} |\boldsymbol{h}_{\ell}^{\mathrm{eff}}|^2\right)\right] \tag{4.20}$$

$$= K\mathsf{d}\log_2(e) e^{\mathsf{d}/\rho^{\mathrm{eff}}[n]} \mathcal{E}_1\left(\frac{\mathsf{d}}{\rho^{\mathrm{eff}}[n]}\right). \tag{4.21}$$

Note that $\rho^{\mathrm{eff}}[n]$ and $\bar{I}^{\mathrm{sum}}[n]$ are decreasing functions of n, as one would expect. Furthermore, by setting $\epsilon[n] = 1$ in (4.19) and (4.21), we recover (4.12) and (4.14) as derived for nonselective fading.

4.4 Pilot Overhead Model

4.4.1 FDD

With FDD, the forward and reverse links occupy distinct frequency bands separated by far more than the fading coherence bandwidth. Thus, the forward and reverse links are statistically independent and explicit CSI feedback is required.

Figure 4.2 shows the pilot overhead model adopted in this chapter. The IA solution is recomputed every N_{d} symbols, of which N_{pf}, N_{pr}, N_{fb} and N_{pd} are respectively reserved for forward common pilots, reverse common pilots, CSI feedback, and forward dedicated pilots; the rest of the symbols are available for payload data. The total overhead is hence $N_{\mathrm{p}} = N_{\mathrm{pf}} + N_{\mathrm{pr}} + N_{\mathrm{fb}} + N_{\mathrm{pd}}$. We make the very mild assumption that the fading remains constant over the pilot intervals[5] and consider equal power allocation for pilot and data symbols.

[5]The mildness of this assumption was validated by bounding the gap between the results with and without fading fluctuations within the pilot intervals; this

Forward Common Pilots

Each transmitter k broadcasts an orthogonal pilot sequence matrix $\boldsymbol{\Phi}_k$, such that $\boldsymbol{\Phi}_k \boldsymbol{\Phi}_j^H = \delta_{k,j} \boldsymbol{I}_{N_\mathrm{t}}$, spanning $N_\mathrm{pf} \geq K N_\mathrm{t}$ symbols [127]. Each receiver estimates the channel matrices corresponding to each of the K transmitters. The observation at receiver k is

$$\boldsymbol{Y}_k = \sqrt{\frac{N_\mathrm{pf} P}{N_\mathrm{t}}} \sum_{j=1}^{K} \boldsymbol{H}_{k,j} \boldsymbol{\Phi}_j + \boldsymbol{Z}_k \tag{4.22}$$

where $\boldsymbol{Z}_k \in \mathbb{C}^{N_\mathrm{r} \times N_\mathrm{pf}}$ is a matrix of noise terms. We indicate the MMSE estimate of the forward channel $\boldsymbol{H}_{k,j}$ by $\hat{\boldsymbol{H}}^\mathrm{f}_{k,j}$ while denoting the corresponding estimation error matrix by $\tilde{\boldsymbol{H}}^\mathrm{f}_{k,j}$. Given the observation $\boldsymbol{Y}_k$,

$$\hat{\boldsymbol{H}}^\mathrm{f}_{k,j} = \frac{\sqrt{\frac{N_\mathrm{pf} P}{N_\mathrm{t}}}}{\sigma_\mathrm{N}^2 + \frac{N_\mathrm{pf} P}{N_\mathrm{t}}} \boldsymbol{Y}_k \boldsymbol{\Phi}_j^* \qquad \forall j \tag{4.23}$$

where the entries of $\hat{\boldsymbol{H}}^\mathrm{f}_{k,j}$ are

$$\mathcal{N}_\mathbb{C}\left(0, \tfrac{N_\mathrm{pf} P / N_\mathrm{t}}{\sigma_\mathrm{N}^2 + N_\mathrm{pf} P / N_\mathrm{t}}\right) \tag{4.24}$$

while the entries of $\tilde{\boldsymbol{H}}^\mathrm{f}_{k,j}$ are IID and

$$\mathcal{N}_\mathbb{C}\left(0, \tfrac{\sigma_\mathrm{N}^2}{\sigma_\mathrm{N}^2 + N_\mathrm{pf} P / N_\mathrm{t}}\right).$$

Reverse Common Pilots

Here, the roles of transmitters and receivers are interchanged and the receivers transmit orthogonal pilot sequences over $N_\mathrm{pr} \geq K N_\mathrm{r}$ symbols. Denote the reverse channel matrix between transmitter k and receiver j as $\boldsymbol{H}^\mathrm{r}_{k,j}$. The corresponding channel estimate is $\hat{\boldsymbol{H}}^\mathrm{r}_{k,j}$ with entries that distributed according to

$$\mathcal{N}_\mathbb{C}\left(0, \tfrac{N_\mathrm{pr} \overleftarrow{P} / N_\mathrm{r}}{\sigma_\mathrm{N}^2 + N_\mathrm{pr} \overleftarrow{P} / N_\mathrm{r}}\right) \tag{4.25}$$

while the error matrix is $\tilde{\boldsymbol{H}}^\mathrm{r}_{k,j}$ with entries conforming to

$$\mathcal{N}_\mathbb{C}\left(0, \tfrac{\sigma_\mathrm{N}^2}{\sigma_\mathrm{N}^2 + N_\mathrm{pr} \overleftarrow{P} / N_\mathrm{r}}\right) \tag{4.26}$$

where $\overleftarrow{P}$ is the reverse link power.

gap was found to be very small, at most of a few percentage points (favoring IA) in terms of average spectral efficiency.

Analog CSI feedback

The forward channel estimates are transmitted via the reverse link by each receiver using unquantized quadrature-amplitude modulation over N_{fb} symbols. Each receiver k sends its $N_{\mathrm{r}} \times KN_{\mathrm{t}}$ concatenated channel feedback matrix $[\hat{\boldsymbol{H}}^{\mathrm{f}}_{k,1}, \ldots, \hat{\boldsymbol{H}}^{\mathrm{f}}_{k,K}]$ by post-multiplying it by a $KN_{\mathrm{t}} \times N_{\mathrm{fb}}$ unitary spreading matrix $\boldsymbol{\Theta}_k$ such that $\boldsymbol{\Theta}_k \boldsymbol{\Theta}_j^* = \delta_{k,j} \boldsymbol{I}_{KN_{\mathrm{t}}}$. The spreading matrices from different receivers must be orthogonal to enable interference-free estimation, which imposes the constraint $N_{\mathrm{fb}} \geq K^2 N_{\mathrm{t}}$. From receiver k, the transmitted channel feedback matrix can be written as [116, 128]

$$\boldsymbol{X}_k = \sqrt{\frac{N_{\mathrm{fb}} \overleftarrow{P}}{KN_{\mathrm{t}}N_{\mathrm{r}}} \left(\frac{N_{\mathrm{pf}} P / N_{\mathrm{t}}}{\sigma_{\mathrm{N}}^2 + N_{\mathrm{pf}} P / N_{\mathrm{t}}} \right)^{-1}} [\hat{\boldsymbol{H}}^{\mathrm{f}}_{k,1}, \ldots, \hat{\boldsymbol{H}}^{\mathrm{f}}_{k,K}] \boldsymbol{\Theta}_k \quad (4.27)$$

such that $\mathbb{E}[\mathrm{tr}(\boldsymbol{X}_k \boldsymbol{X}_k^*)] = N_{\mathrm{fb}} \overleftarrow{P}$. The approach in [23] can be followed to derive the error due to forward channel estimation, reverse channel estimation, and analog CSI feedback. The concatenated matrix of received feedback symbols by all the transmitters is

$$\begin{aligned} \boldsymbol{Y} = & \sqrt{\frac{N_{\mathrm{fb}} \overleftarrow{P}}{KN_{\mathrm{t}}N_{\mathrm{r}}} \left(\frac{N_{\mathrm{pf}} P / N_{\mathrm{t}}}{\sigma_{\mathrm{N}}^2 + N_{\mathrm{pf}} P / N_{\mathrm{t}}} \right)^{-1}} \\ & \times \sum_{k=1}^{K} \begin{bmatrix} \boldsymbol{H}^{\mathrm{r}}_{k,1} \\ \vdots \\ \boldsymbol{H}^{\mathrm{r}}_{k,K} \end{bmatrix} \begin{bmatrix} \hat{\boldsymbol{H}}^{\mathrm{f}}_{k,1} & \cdots & \hat{\boldsymbol{H}}^{\mathrm{f}}_{k,K} \end{bmatrix} \boldsymbol{\Theta}_k + \boldsymbol{Z} \end{aligned} \quad (4.28)$$

where $\boldsymbol{Z} \in \mathbb{C}^{KN_{\mathrm{t}} \times N_{\mathrm{fb}}}$ is the noise matrix. The channels $\boldsymbol{H}_{k,j}$, estimated and fed back by receiver k $\forall j$, are re-estimated at transmitter k by post-multiplying $\boldsymbol{Y}$ by $\boldsymbol{\Theta}_k^*$. Borrowing the derivations in [23, Section IV], which are summarized for the sake of completeness in Appendix C.1, the final expression for the variance of the channel estimation error is

$$\sigma^2_{\tilde{\boldsymbol{H}}} = \frac{N_{\mathrm{t}} \, \sigma_{\mathrm{N}}^2}{N_{\mathrm{pf}} \, P} + \frac{\tau_1 \, \sigma_{\mathrm{N}}^2}{(KN_{\mathrm{t}} - N_{\mathrm{r}}) P} \quad (4.29)$$

where

$$\tau_1 = \frac{N_{\mathrm{r}}^2 P}{N_{\mathrm{pr}} \overleftarrow{P}} + \frac{KN_{\mathrm{t}}N_{\mathrm{r}} P}{N_{\mathrm{fb}} \overleftarrow{P}}. \quad (4.30)$$

We note that the channel estimates $\hat{\boldsymbol{H}}_{k,j}$ available at the transmitters are no longer complex Gaussian due to the fading introduced

by the feedback channel. However, $\hat{\boldsymbol{H}}_{k,j}$ can be approximated as complex Gaussian with variance $1 - \sigma^2_{\tilde{\boldsymbol{H}}}$. This was verified in [23], where it was shown that the effect of this approximation is rather negligible.

It is important to realize that the concatenated $KN_{\mathrm{t}} \times N_{\mathrm{fb}}$ matrix $\boldsymbol{Y}$ in (4.28) can be constructed only if the transmitters share their locally observed rows; then, the computation of the IA precoders can be centralized as described in Section 4.1. This is in principle feasible in the downlink, where the transmitters are embodied by base stations connected through the backhaul, and such is the focus of our analysis. In the uplink, or in downlink settings where CSI sharing could not be implemented, one would have to resort to less desirable alternatives. The first such alternative would be distributed IA with over-the-air iterations, which would incur additional signaling overhead. The second alternative would be the closed-form computation of the precoders based on estimates of all the forward channels obtained from observing the $N_{\mathrm{t}} \times N_{\mathrm{fb}}$ feedback matrix locally. However, this second alternative would only be feasible for those configurations for which precoder closed forms are indeed available. Moreover, since in this approach every transmitter would observe the feedback matrix through a different reverse fading channel, each transmitter would have a differently perturbed estimate of the forward channels; this would cause an additional (small) performance loss [116].

Forward Dedicated Pilots

The precoder matrix $\hat{\boldsymbol{V}}_k$ at transmitter k, computed using the estimates $\hat{\boldsymbol{H}}_{k,j}\, \forall j \neq k$, is unknown at receiver k. An additional round of dedicated pilots is required once the transmitters have computed their precoders in order to enable each receiver k to learn the precoded channels. Precisely, each transmitter k transmits orthogonal pilots along its precoder $\hat{\boldsymbol{V}}_k \in \mathbb{C}^{N_{\mathrm{t}} \times \mathsf{d}}$ over $N_{\mathrm{pd}} \geq K\mathsf{d}$ symbols. The observed signal at receiver k is then

$$\boldsymbol{Y}_k = \sqrt{\frac{N_{\mathrm{pd}} P}{\mathsf{d}}} \sum_{j=1}^{K} \boldsymbol{H}_{k,j} \hat{\boldsymbol{V}}_j \boldsymbol{\Omega}_j + \boldsymbol{Z}_k \tag{4.31}$$

where $\boldsymbol{\Omega}_j$ is the dedicated pilot sequence matrix at transmitter j.

Each receiver k estimates its desired precoded channel $\boldsymbol{A}_{k,k} = \boldsymbol{H}_{k,k}$ $\hat{\boldsymbol{V}}_k$. Since $\hat{\boldsymbol{V}}_k$ is unitary and independent of $\boldsymbol{H}_{k,k}$, it follows that

$\boldsymbol{A}_{k,k}$ is complex Gaussian. The MMSE estimate of $\boldsymbol{A}_{k,k}$ is then

$$\hat{\boldsymbol{A}}_{k,k} = \frac{\sqrt{\frac{N_{\mathrm{pd}}P}{\mathsf{d}}}}{\sigma_{\mathrm{N}}^2 + \frac{N_{\mathrm{pd}}P}{\mathsf{d}}} \boldsymbol{Y}_k \boldsymbol{\Omega}_k^* \tag{4.32}$$

and the corresponding error $\tilde{\boldsymbol{A}}_{k,k} = \boldsymbol{A}_{k,k} - \hat{\boldsymbol{A}}_{k,k}$ is complex Gaussian with variance

$$\sigma_{\tilde{\boldsymbol{A}}}^2 = \frac{\sigma_{\mathrm{N}}^2}{\sigma_{\mathrm{N}}^2 + N_{\mathrm{pd}}P/\mathsf{d}} \tag{4.33}$$

$$= \frac{\mathsf{d}\,\sigma_{\mathrm{N}}^2}{\mathsf{d}\,\sigma_{\mathrm{N}}^2 + N_{\mathrm{pd}}P} \tag{4.34}$$

wheras $\hat{\boldsymbol{A}}_{k,k}$ is complex Gaussian with variance $1 - \sigma_{\tilde{\boldsymbol{A}}}^2$.

Plugging (4.29) and (4.34) into (4.19), the effective average SINR in (4.19) specializes into

$$\rho^{\mathrm{eff}}[n] = \frac{\frac{\epsilon[n]^2\,P}{\sigma_{\mathrm{N}}^2}\left(1 - \frac{\mathsf{d}\,\sigma_{\mathrm{N}}^2}{\mathsf{d}\,\sigma_{\mathrm{N}}^2 + N_{\mathrm{pd}}P}\right)}{1 + \frac{KP}{\sigma_{\mathrm{N}}^2} + \epsilon[n]^2\left(\frac{(K-1)N_{\mathrm{t}}}{N_{\mathrm{pf}}} + \frac{\left(\frac{N_{\mathrm{r}}^2 P}{N_{\mathrm{pr}}\overleftarrow{P}} + \frac{KN_{\mathrm{t}}N_{\mathrm{r}}P}{N_{\mathrm{fb}}\overleftarrow{P}}\right)}{(KN_{\mathrm{t}} - N_{\mathrm{r}})/(K-1)} - \frac{KP}{\sigma_{\mathrm{N}}^2} + \frac{\mathsf{d}P}{\mathsf{d}\sigma_{\mathrm{N}}^2 + N_{\mathrm{pd}}P}\right)} \tag{4.35}$$

which is a function of: the forward link common pilot overhead N_{pf}, the reverse link common pilot overhead N_{pr}, the feedback overhead N_{fb}, the dedicated pilot overhead N_{pd}, the average SNR per stream $P/(d\,\sigma_{\mathrm{N}}^2)$, the ratio of reverse and forward link powers $\overleftarrow{P}/P$, the DoF per user d, the time-domain fading correlation $\epsilon[\cdot]$, the number of users K, the number of transmit antennas N_{t}.

4.4.2 TDD

With TDD, the same frequency band is shared by the forward and reverse links and thus the corresponding over-the-air channels are transposed versions of each other. Then, with careful calibration, the analog CSI feedback phase is not required. Recall that the reverse channel from receiver k to transmitter j is $\boldsymbol{H}_{j,k}^{\mathrm{r}} = \boldsymbol{H}_{k,j}^*$ where $\boldsymbol{H}_{k,j}$ is the forward channel from transmitter j to receiver k. Further recalling the reverse channel estimate and the corresponding error matrix as $\hat{\boldsymbol{H}}_{k,j}^{\mathrm{r}}$ and $\tilde{\boldsymbol{H}}_{k,j}^{\mathrm{r}}$, with entries distributed according

to (4.25) and (4.26), respectively, transmitter k computes its forward channel estimate $\hat{\boldsymbol{H}}_{k,j}$ as simply the transpose of $\hat{\boldsymbol{H}}^{\mathrm{r}}_{j,k}$ and the variance of the channel estimation error is

$$\sigma^2_{\tilde{\boldsymbol{H}}} = \frac{\sigma^2_{\mathrm{N}}}{\sigma^2_{\mathrm{N}} + \frac{N_{\mathrm{pr}}\bar{P}}{N_{\mathrm{r}}}} \tag{4.36}$$

$$= \frac{1}{1 + \frac{N_{\mathrm{pr}}}{N_{\mathrm{r}}}\frac{\bar{P}}{\sigma^2_{\mathrm{N}}}}. \tag{4.37}$$

Utilizing (4.34) and (4.37) in (4.19), the effective average SINR can be derived for TDD as

$$\rho^{\mathrm{eff}}[n] = \frac{\frac{\epsilon[n]^2 P}{\sigma^2_{\mathrm{N}}}\left(1 - \frac{\mathsf{d}\,\sigma^2_{\mathrm{N}}}{\mathsf{d}\,\sigma^2_{\mathrm{N}} + N_{\mathrm{pd}}P}\right)}{1 + \frac{KP}{\sigma^2_{\mathrm{N}}} + \frac{\epsilon[n]^2 P}{\sigma^2_{\mathrm{N}}}\left(-K + \frac{\mathsf{d}\,\sigma^2_{\mathrm{N}}}{\mathsf{d}\,\sigma^2_{\mathrm{N}} + N_{\mathrm{pd}}P} + \frac{(K-1)N_{\mathrm{r}}\sigma^2_{\mathrm{N}}}{N_{\mathrm{r}}\sigma^2_{\mathrm{N}} + N_{\mathrm{pr}}\bar{P}}\right)}. \tag{4.38}$$

4.5 Optimum Pilot Overhead and IA Update Interval

4.5.1 FDD

The effective average sum mutual information is the solution to

$$\max_{N_{\mathrm{pf}},N_{\mathrm{pr}},N_{\mathrm{fb}},N_{\mathrm{pd}},N_{\mathrm{d}}} \frac{1}{N_{\mathrm{d}}} \sum_{n=1}^{N_{\mathrm{d}}-N_{\mathrm{p}}} \bar{I}^{\mathrm{sum}}[n] \tag{4.39}$$

subject to

$$N_{\mathrm{pf}} \geq KN_{\mathrm{t}} \tag{4.40}$$

$$N_{\mathrm{pr}} \geq KN_{\mathrm{r}} \tag{4.41}$$

$$N_{\mathrm{fb}} \geq K^2N_{\mathrm{t}} \tag{4.42}$$

$$N_{\mathrm{pd}} \geq K\mathsf{d} \tag{4.43}$$

with $\bar{I}^{\mathrm{sum}}[\cdot]$ given in (4.21) and $\rho^{\mathrm{eff}}[\cdot]$ given in (4.35). The optimum value of a given variable is henceforth indicated with a superscript $(\cdot)^\star$, e.g., $N^\star_{\mathrm{pf}}$. With coding spanning enough update intervals, (4.39) signifies the achievable average sum spectral efficiency.

Table 4.1: Minimum pilot overhead expressions for IA-FDD and IA-TDD

	IA-FDD	IA-TDD
N_{pf}	KN_{t}	KN_{t}
N_{pr}	KN_{r}	KN_{r}
N_{fb}	K^2N_{t}	—
N_{pd}	$K\mathsf{d}$	$K\mathsf{d}$
N_{p}	$K((K+1)N_{\mathrm{t}}+N_{\mathrm{r}}+d)$	$K(N_{\mathrm{t}}+N_{\mathrm{r}}+\mathsf{d})$

Optimization of N_{d} with Fixed Overhead

Increasing N_{pf}, N_{pr}, N_{fb} and N_{pd} improves the CSI accuracy yielding a higher effective SINR at the expense of a higher overhead. While the improvement in spectral efficiency associated with the SINR is ultimately logarithmic, the decrease associated with the overhead is always linear. Thus, at sufficiently high SNR the optimum overhead is bound to take the minimum value corresponding to $N_{\mathrm{pf}}^{\star}=KN_{\mathrm{t}}$, $N_{\mathrm{pr}}^{\star}=KN_{\mathrm{r}}$, $N_{\mathrm{fb}}^{\star}=K^2N_{\mathrm{t}}$, $N_{\mathrm{pd}}^{\star}=Kd$ and $N_{\mathrm{p}}^{\star}=K((K+1)N_{\mathrm{t}}+N_{\mathrm{r}}+\mathsf{d})$. Utilizing these values, which for the reader's convenience are summarized in Table 4.1, the corresponding effective average SINR becomes

$$\rho^{\mathrm{eff}}[n]=\frac{\frac{\epsilon[n]^2P^2K}{\sigma_{\mathrm{N}}^2(\sigma_{\mathrm{N}}^2+KP)}}{1+\frac{KP}{\sigma_{\mathrm{N}}^2}+\epsilon[n]^2\left(1+\frac{2(K-1)N_{\mathrm{r}}}{\beta K^2N_{\mathrm{t}}-\beta KN_{\mathrm{r}}}-\frac{KP}{\sigma_{\mathrm{N}}^2}-\frac{\sigma_{\mathrm{N}}^2}{K\sigma_{\mathrm{N}}^2+K^2P}\right)} \tag{4.44}$$

and the optimization in (4.39) simplifies to $\max_{N_{\mathrm{d}}} f(N_{\mathrm{d}})$ with

$$f(N_{\mathrm{d}})=\frac{1}{N_{\mathrm{d}}}\sum_{n=1}^{N_{\mathrm{d}}-N_{\mathrm{p}}^{\star}}\bar{I}^{\mathrm{sum}}[n]. \tag{4.45}$$

We are thus faced with an integer problem. With a continuous relaxation thereof, the argument of the optimization becomes

$$f(N_{\mathrm{d}})=\frac{1}{N_{\mathrm{d}}}\int_{1}^{N_{\mathrm{d}}-N_{\mathrm{p}}^{\star}}\bar{I}^{\mathrm{sum}}[n]\,\mathrm{d}n \tag{4.46}$$

with derivative

$$\dot{f}(N_{\mathrm{d}})=-\frac{1}{N_{\mathrm{d}}}f(N_{\mathrm{d}})+\frac{1}{N_{\mathrm{d}}}\bar{I}^{\mathrm{sum}}[N_{\mathrm{d}}-N_{\mathrm{p}}^{\star}]. \tag{4.47}$$

It can be easily verified that $f(.)$ has a unique stationary point and that, since $\bar{I}^{\text{sum}}[n]$ is a decreasing function of n, the second derivative at this point is negative [122, Appendix II]. Thus, its global maximum can be found by solving

$$-\frac{1}{N_{\text{d}}} f(N_{\text{d}}) + \frac{1}{N_{\text{d}}} \bar{I}^{\text{sum}}[N_{\text{d}} - N_{\text{p}}^{\star}] = 0. \tag{4.48}$$

This leads to the condition $f(N_{\text{d}}) = \bar{I}^{\text{sum}}[N_{\text{d}} - N_{\text{p}}^{\star}]$ or, more explicitly, to the fixed-point equation

$$\frac{1}{N_{\text{d}}} \sum_{n=1}^{N_{\text{d}}-N_{\text{p}}^{\star}} \bar{I}^{\text{sum}}[n] = \bar{I}^{\text{sum}}[N_{\text{d}} - N_{\text{p}}^{\star}]. \tag{4.49}$$

where, with all the overheads at their respective minima, $N_{\text{p}}^{\star} = K((K+1)N_{\text{t}} + N_{\text{r}} + d)$. Given the continuous relaxation used to reach (4.49), it is necessary to test the two nearest integer neighbors to its real-valued solution for N_{d} in order to identify $N_{\text{d}}^{\star}$.

High-SNR Optimization

For certain time-domain correlation functions, solving (4.49) is numerically challenging because $\bar{I}^{\text{sum}}[\cdot]$ in (4.21) contains an exponential integral. At high SNR, however, an alternative to (4.21) can be obtained by expanding (4.20) into [129]

$$\bar{I}^{\text{sum}}[n] = Kd \left(\log_2 \left(\frac{\rho^{\text{eff}}[n]}{\mathsf{d}} \right) - \mathcal{L}_{\infty}[n] \right) + o(1) \tag{4.50}$$

where $\mathcal{L}_{\infty} = \mathbb{E}\left[\log_2\left(|\boldsymbol{h}_{\ell}^{\text{eff}}|^2\right)\right]$. Since $\boldsymbol{h}_{\ell}^{\text{eff}}$ is complex Gaussian with unit variance, $|\boldsymbol{h}_{\ell}^{\text{eff}}|^2$ is exponentially distributed with mean one and with $\mathcal{L}_{\infty} = \gamma_{\text{EM}} \log_2 e$ where $\gamma_{\text{EM}} \approx 0.5772$ is the Euler-Mascheroni constant. Plugging the above expansion into (4.49), we obtain the far simpler fixed-point equation

$$N_{\text{d}}^{\star} \log_2 \left(\frac{\rho^{\text{eff}}[N_{\text{d}}^{\star} - N_{\text{p}}^{\star}]}{\mathsf{d}} \right) - \sum_{n=1}^{N_{\text{d}}^{\star}-N_{\text{p}}^{\star}} \log_2 \left(\frac{\rho^{\text{eff}}[n]}{\mathsf{d}} \right) = N_{\text{p}}^{\star} \mathcal{L}_{\infty} + o(1) \tag{4.51}$$

where, recall, $N_{\text{p}}^{\star} = K((K+1)N_{\text{t}} + N_{\text{r}} + \mathsf{d})$. From (4.51), $N_{\text{d}}^{\star}$ can be found conveniently down to the $o(1)$ term—which vanishes with growing SNR. Again, the two closest integer neighbors to the solution should be tested to overcome the effects of the continuous relaxation.

4.5.2 TDD

The problem formulation for TDD is similar to the one for FDD except for the absence of the analog CSI feedback stage. Then, the effective average sum spectral efficiency is optimized over N_{pf}, N_{pr}, N_{pd} and N_{d} with $N_{\mathrm{pf}} \geq KN_{\mathrm{t}}$, $N_{\mathrm{pr}} \geq KN_{\mathrm{r}}$ and $N_{\mathrm{pd}} \geq K\mathsf{d}$.

Optimization of N_{d} with Fixed Overheads

Leveraging the approach in Section 4.5.1, the minimum overhead in TDD is $N_{\mathrm{p}}^{\star} = K(N_{\mathrm{t}} + N_{\mathrm{r}} + \mathsf{d})$ while the corresponding effective average SINR in (4.38) reduces to

$$\rho^{\mathrm{eff}}[n] = \frac{\frac{\epsilon[n]^2 P^2 K}{\sigma_{\mathrm{N}}^2(\sigma_{\mathrm{N}}^2+KP)}}{1 + \frac{KP}{\sigma_{\mathrm{N}}^2} + \frac{\epsilon[n]^2\, P}{\sigma_{\mathrm{N}}^2}\left(-K + \frac{\sigma_{\mathrm{N}}^2}{\sigma_{\mathrm{N}}^2+KP} + \frac{(K-1)\sigma_{\mathrm{N}}^2}{\sigma_{\mathrm{N}}^2+K\tilde{P}}\right)}. \tag{4.52}$$

With the overhead at its minimum value, the optimum update interval $N_{\mathrm{d}}^{\star}$ at an arbitrary SNR can be computed as the solution of (4.49) while the corresponding high-SNR optimization solution can be found by solving (4.51). Once more, in both cases, the two closest integer neighbors to the real-valued solution should be tested.

4.6 Numerical Results

In order to generate some numerical results, we invoke the standard Clarke-Jakes correlation function $\epsilon[n] = J_0(2\pi\nu_{\mathrm{M}} n T_{\mathrm{s}})$ where T_{s} is the symbol period, ν_{M} is the maximum Doppler shift (in Hz) and $J_0(\cdot)$ is the zeroth-order Bessel function of the first kind. However, because of the oscillatory nature of $J_0(\cdot)$, such $\epsilon[n]$ is not a monotonically decreasing function of n and thus it does not strictly satisfy the conditions of our analysis. By replacing $J_0(\cdot)$ by its expansion

$$J_0(\mathsf{z}) = 1 - \frac{\mathsf{z}^2}{4} + \frac{\mathsf{z}^4}{64} + o(\mathsf{z}^4) \tag{4.53}$$

we obtain a monotonically decreasing correlation function that mimics very precisely the Clarke-Jakes behavior in the range of interest, for all reasonable values of the parameters' space.

The degradation associated with time selectivity is bound to subside as T_{s} shrinks, but, if B_{c} denotes the coherence bandwidth, T_{s} cannot fall below (roughly) $1/B_{\mathrm{c}}$ since otherwise the flat-fading condition in the formulation would be violated. For our results, we chose

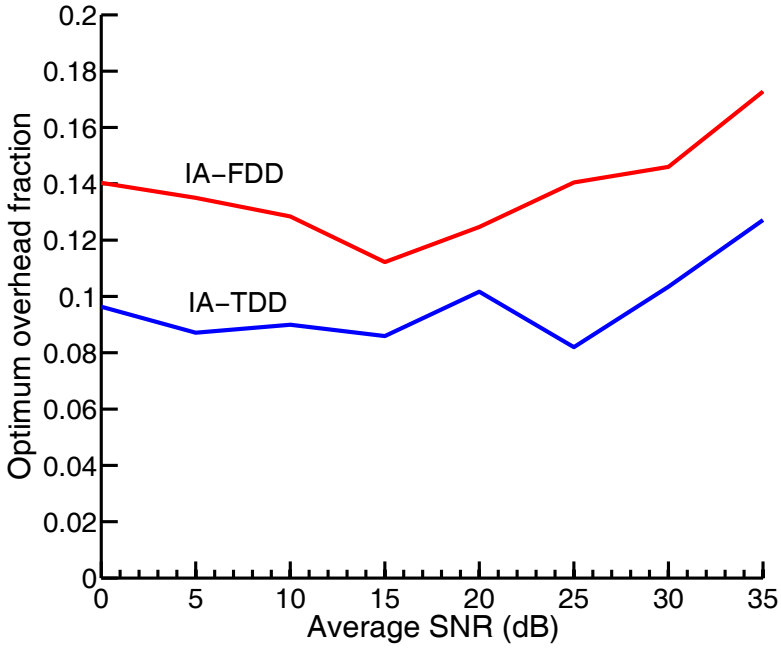

Figure 4.3: Optimum overhead fraction v. P/σ_{N}^2 for IA with $K = 3$, $\mathsf{d} = 1$, $N_{\mathrm{t}} = N_{\mathrm{r}} = 2$, $\nu_{\mathrm{M}} = 10$ Hz and $T_{\mathrm{s}} = 5.5\,\mu$s.

a very favorable value for IA and set $T_{\mathrm{s}} = 1/B_{\mathrm{c}}$ with $B_{\mathrm{c}} = 180$ kHz; this corresponds to one LTE signaling resource block [130]. Then, $T_{\mathrm{s}} = 5.5\,\mu$s. Furthermore, for the examples that follow, unless otherwise stated, $K = 3$, $N_{\mathrm{t}} = N_{\mathrm{r}} = 2$, $\mathsf{d} = 1$ and $\check{P} = P$.

Figure 4.3 shows, as function of the SNR, the optimal pilot overhead fraction, $N_{\mathrm{p}}^\star/N_{\mathrm{d}}^\star$, obtained by solving (4.39) numerically for both FDD and TDD. The maximum Doppler shift is $\nu_{\mathrm{M}} = 10$ Hz, which corresponds to a pedestrian velocity of 5 Km/h at a carrier frequency of 2 GHz. The lack of smoothness in the curves is a direct consequence of the integer nature of the problem. The optimum overhead is higher with FDD due to the need for explicit CSI feedback, as one would expect.

For a different perspective, Fig. 4.4 presents the optimal pilot overhead fraction, $N_{\mathrm{p}}^\star/N_{\mathrm{d}}^\star$, as function of ν_{M}. As one would again expect, $N_{\mathrm{d}}^\star$ declines as ν_{M} increases, and the overhead fraction worsens. Less foreseeable, and thus a much more interesting insight, is the dependence of the overhead fraction on the SNR: in contrast

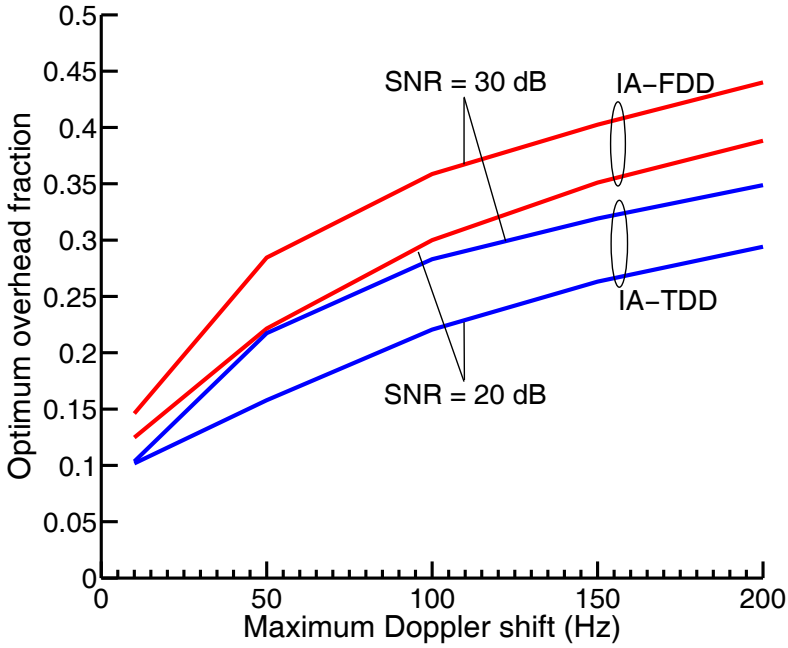

Figure 4.4: Optimum overhead fraction v. maximum Doppler shift at $P/\sigma_{\mathrm{N}}^2 = 20$ dB and $P/\sigma_{\mathrm{N}}^2 = 30$ dB with $K = 3$, $\mathsf{d} = 1$, $N_{\mathrm{t}} = N_{\mathrm{r}} = 2$ and $T_{\mathrm{s}} = 5.5\,\mu$s.

with single-user MIMO, where the overhead fraction shrinks with a growing SNR [123], in IA it increases, the reason being that with less noise the performance becomes more sensitive to Doppler-induced precoder deviations and this sensitivity triggers more frequent precoder updates, i.e., it also reduces $N_{\mathrm{d}}^{\star}$.

Figure 4.5 compares the optimal pilot overhead fraction obtained by solving (4.39) numerically against the solution $K((K+2)N_{\mathrm{t}}+\mathsf{d})/N_{\mathrm{d}}^{\star}$ where $N_{\mathrm{d}}^{\star}$ is derived from (4.49), and further against the solution provided by (4.51). The maximum Doppler shift is $f_{\mathrm{m}} = 10$ Hz. As anticipated, all the results agree at high SNR, once $N_{\mathrm{p}}^{\star}$ has reached its minimum value. The sustained increase of the overhead with the SNR is explained by the rising sensitivity to time selectivity: the channel estimation becomes more precise with the SNR, rendering the misalignment caused by selectivity proportionally more acute; this induces more frequent IA updates, i.e., a smaller $N_{\mathrm{d}}^{\star}$.

Turning our attention now to the effective sum spectral efficiency,

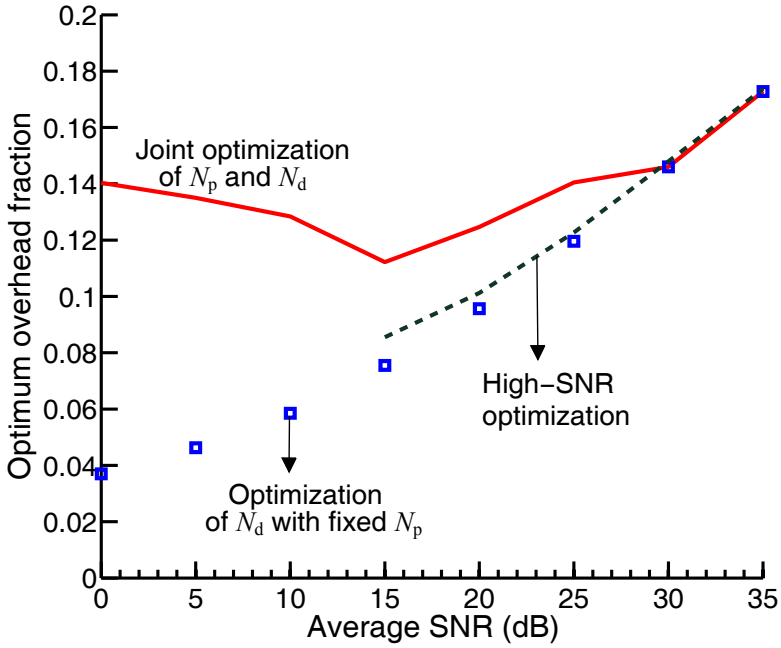

Figure 4.5: Optimum overhead fraction v. P/σ_N^2 for IA-FDD with $K = 3$, $\mathsf{d} = 1$, $N_t = N_r = 2$, $\nu_M = 10$ Hz and $T_s = 5.5\,\mu$s.

it is shown in Fig. 4.6 as function of the SNR for $\nu_M = 10$ Hz and $\nu_M = 200$ Hz, respectively corresponding to pedestrian and vehicular velocities at 2 GHz. Specifically, FDD is considered in these results.

Figure 4.7 compares the effective sum spectral efficiencies of IA-FDD, IA-TDD and TDMA as function of SNR in a pedestrian scenario. Here, settings with $K = 3$ and $K = 5$ users are contrasted. In both cases, IA-FDD and IA-TDD are seen to outperform TDMA, although with FDD the improvement is minor. In vehicular scenarios, the IA advantage vanishes entirely regardless of whether TDD or FDD is employed, confirming the widespread conjecture that IA is not applicable to these scenarios. For example, with $K = 3$ and $P/\sigma_N^2 = 20$ dB, we have observed that the IA-FDD advantage vanishes beyond $\nu_M = 100$ Hz while the IA-TDD advantage vanishes beyond $\nu_M = 200$ Hz. In the remainder we therefore focus exclusively on pedestrian settings.

After having exemplified the IA performance with typical cooperation sizes of $K = 3$ and $K = 5$, it is reasonable to wonder the

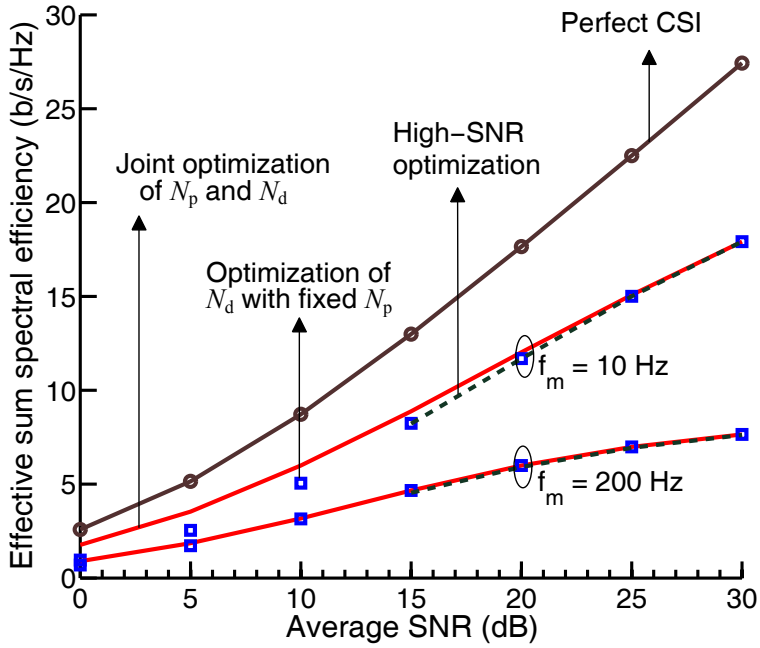

Figure 4.6: Effective sum spectral efficiency v. P/σ_{N}^2 for IA-FDD at $\nu_{\mathrm{M}} = 10$ Hz and $\nu_{\mathrm{M}} = 200$ Hz with $K = 3$, $\mathsf{d} = 1$, $N_{\mathrm{t}} = N_{\mathrm{r}} = 2$, and $T_{\mathrm{s}} = 5.5\,\mu$s.

extent to which the observations made for these values are general. Short of repeating the examples for all possible values of K, the best way to address this question is by assessing the optimum value of K as a function of the parameters of interest, chiefly the SNR. The result of this assessment is precisely what Fig. 4.8 presents: the best possible value of K as function of SNR in a pedestrian scenario ($f_{\mathrm{m}} = 10$ Hz). The numbers of antennas are chosen to satisfy the IA feasibility condition in (3.3) for $\mathsf{d} = 1$. As can be seen, K declines progressively and, at 30 dB, it equals the value of $K = 5$ utilized in some of the earlier examples.

Finally, we explore the impact of asymmetric forward and reverse channel strengths. Both IA-FDD and IA-TDD are considered, with a forward link average SNR of 30 dB. Figure 4.9 shows the variation of the optimum overhead fraction with respect to $P/\overleftarrow{P}$. Figure 4.10 quantifies the effective sum spectral efficiency as a function of $P/\overleftarrow{P}$ and compares it against the TDMA spectral efficiency at the same SNR. As the reverse link weakens with respect to the forward link,

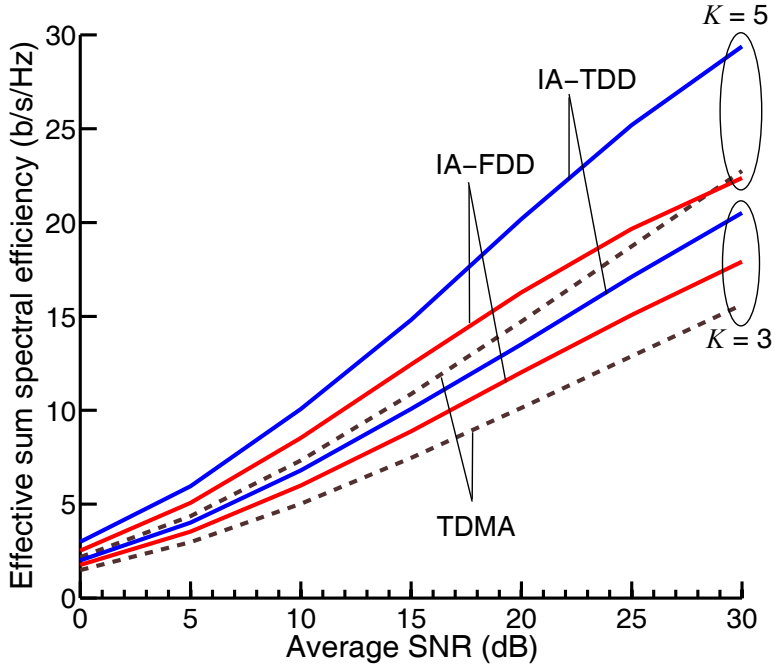

Figure 4.7: Effective sum spectral efficiency v. P/σ_{N}^2 for IA and TDMA with $K = 3$ and $K = 5$, $\nu_{\mathrm{M}} = 10$ Hz and $T_{\mathrm{s}} = 5.5\,\mu$s.

the performance of IA progressively degrades while that of TDMA remains unaffected. Hence, IA becomes unappealing in the presence of a sufficiently weak reverse link.

4.7 Conclusions and Contributions

The optimum pilot overhead and IA update interval in a K-user MIMO interference channel have been obtained as solutions to an optimization, which at high SNR adopts a particularly tractable form. This solution, in turn, allows for a straight computation of the spectral efficiency achievable by IA in time-selective fading channels. Variations of the formulation for both FDD and TDD have been provided.

A number of numerical examples have been presented, corresponding to typical operating conditions in terms of SNR, fading coherence, and numbers of antennas. Through these examples, it has been observed that, with fading selectivity and pilot-assisted chan-

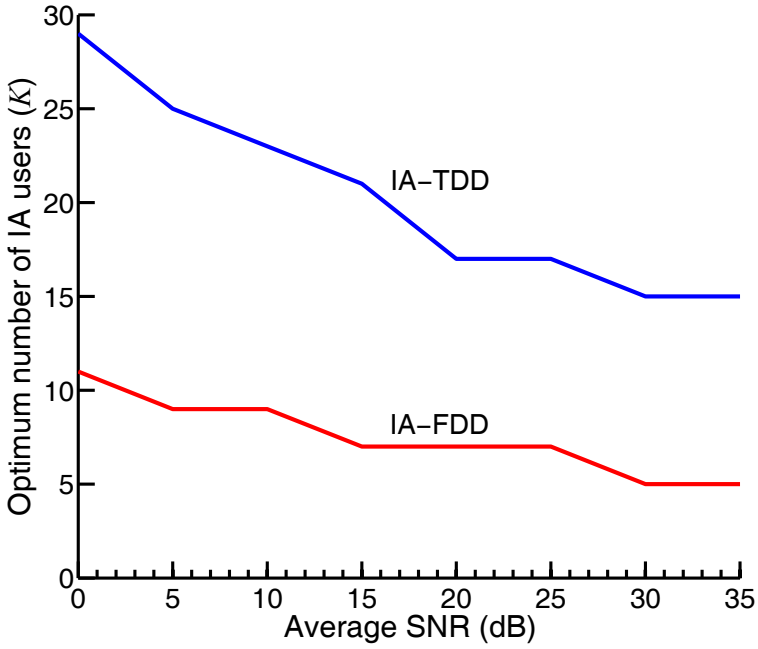

Figure 4.8: Optimal number of IA users (corresponding to maximum effective sum spectral efficiency) v. P/σ_{N}^2 for IA-FDD and IA-TDD with $\mathsf{d} = 1$, $\nu_{\mathrm{M}} = 10$ Hz and $T_{\mathrm{s}} = 5.5\,\mu$s.

nel estimation explicitly incorporated, IA loses all its advantage over TDMA at vehicular speeds, but remains somewhat superior at pedestrian speeds. The improvement is minor in the case of FDD, and more significant in the case of TDD.

Tempered by the observations made in Chapter 3, chiefly that the insights obtained from the K-user interference channel apply to large wireless networks only within a certain SNR range, IA is seen to retain the potential to play some role in the management of interference in pedestrian-oriented TDD wireless systems; that role, however, might be largely circumscribed to cell-edge users for which the interference channel is a reasonable model. In FDD and/or vehicular-oriented systems, conversely, the various overheads nullify the gains that IA would provide over TDMA if perfect CSI were available at no cost.

To be sure, maximum-SINR solutions would perform somewhat better than IA at intermediate SNR levels, but hardly in the high-SNR

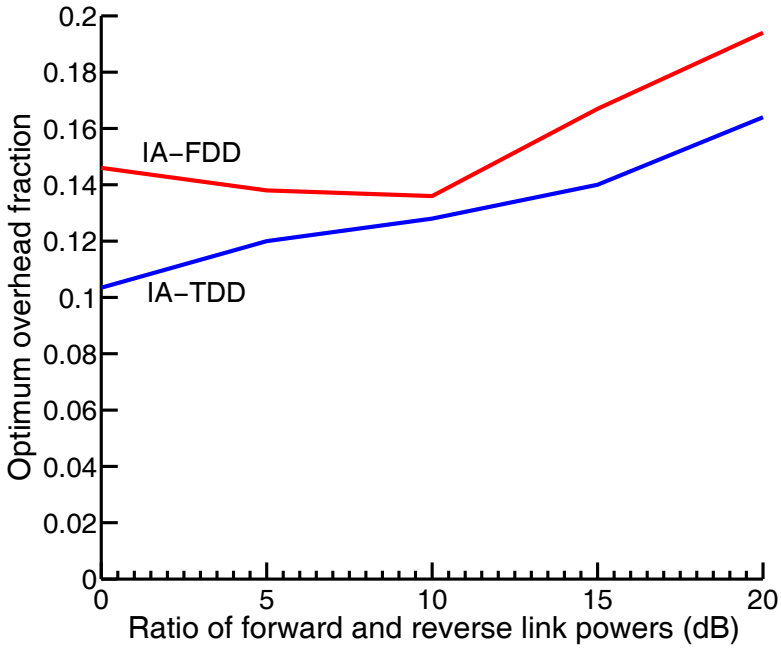

Figure 4.9: Optimum overhead fraction v. $P/\breve{P}$ for IA-FDD and IA-TDD with $K = 3$, $\mathsf{d} = 1$, $N_{\mathrm{t}} = N_{\mathrm{r}} = 2$, forward link average SNR = 30 dB, $\nu_{\mathrm{M}} = 10$ Hz and $T_{\mathrm{s}} = 5.5\,\mu$s.

regime where intercell interference becomes the dominating impairment.

We also note that techniques that can be leveraged to improve pilot-assisted communication in single-user communication, e.g., channel interpolation or data-aided channel tracking [126], cannot be directly applied in IA because the precoders and receive filters must be jointly computed. If, for instance, the precoders were to be modified at any intermediate point within the update intervals, new dedicated pilots would have to be transmitted to enable proper retuning of the receivers; this would increase the overheads even further. What could be done, respecting the regular IA update approach followed in this chapter and avoiding a further increase in the overheads, is to compute the precoders and receivers by considering not only the set of pilot observations preceding the current update interval, but also older ones. We have explored this possibility and observed that, because of the fading decorrelation across multiple update intervals, the corresponding improvements in spectral efficiency are minute.

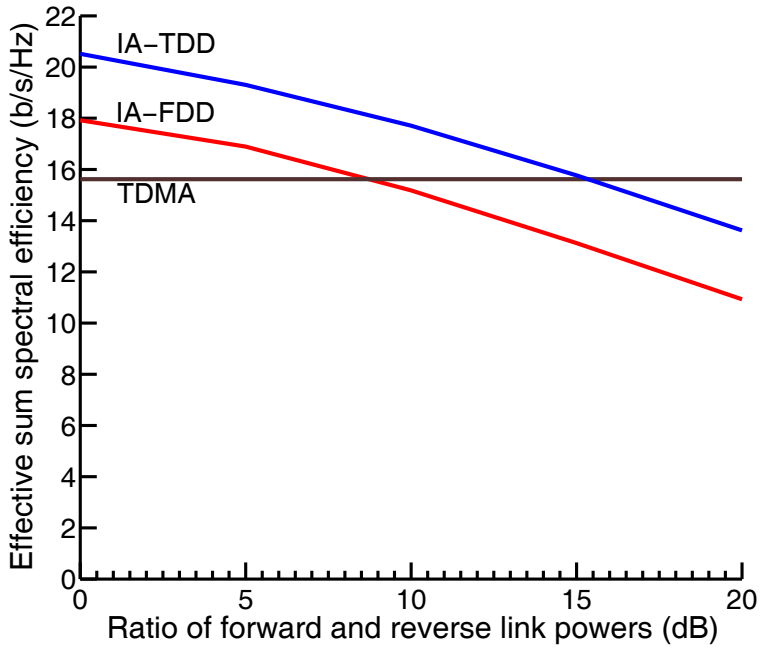

Figure 4.10: Effective sum spectral efficiency v. $P/\breve{P}$ for IA-FDD, IA-TDD and TDMA with $K = 3$, $\mathsf{d} = 1$, $N_{\mathrm{t}} = N_{\mathrm{r}} = 2$, forward link average SNR = 30 dB, $\nu_{\mathrm{M}} = 10$ Hz and $T_{\mathrm{s}} = 5.5\,\mu$s.

Finally, we hasten to emphasize that the performance of IA would further degrade should a distributed implementation be necessary, as this would entail a substantial number of over-the-air iterations (each involving forward and reverse pilot transmissions) within every update interval. The range of operational conditions where IA may be enticing would then be squeezed down very substantially and it might be the case that IA no longer retains any potential to play a role in wireless interference management.

Chapter 5

Channelization Schemes for Overlaid D2D Networks

> If you can imagine it, you can achieve it.
> If you can dream it, you can become it.
>
> William Arthur Ward

Device-to-device (D2D) communication is currently being touted as a potential ingredient of 5G wireless networks [3, 4] and allows for serving local wireless traffic bypassing the system's infrastructure. Having established in the previous two chapters that the role of IA is limited in improving the cellular system capacity, this chapter quantifies the gains in spectral efficiency due to channelization schemes in the context of D2D networks overlaid onto separate licensed spectrum.

5.1 Related Work and Motivation

The incorporation of D2D communication into infrastructure-based wireless networks promises major performance advantages provided there is sufficient locality in the traffic [3, 4, 27, 131–134]. Both academia and industry have conducted studies on D2D to support applications such as multicasting [135, 136], content distribution [137, 138], cellular offloading [139], machine-to-machine communication [140, 141] or proximity-aware internetworking [134, 142, 143]. Initially, most such works had relied on simulations. Recognizing the random network topology and behavior of D2D users, more

recent works [29, 144–146] have applied stochastic geometry tools in order to study D2D communication by modeling the user locations via PPP distributions. Much of this prior work has concentrated on underlay communication, where D2D transmissions reuse the existing uplink spectrum. Specifically, [144] and [145] proposed various resource allocation strategies to efficiently partition time and spectrum between cellular and D2D users, while [146] and [29] tackled the excessive interference from D2D users to cellular users by means of power control schemes and exclusion regions, respectively. However, substantial changes in the standards are required to accommodate underlay D2D and, as a result, there is growing interest in infrastructure-assisted overlay alternatives [26–28].

In overlay mode, a swath of the spectrum is reserved for D2D traffic, which is thereby segregated from both forward link and reverse link. On this dedicated spectrum, users in close proximity can establish direct communication, replacing two long hops via the infrastructure with a single (and typically shorter) hop. Such direct communication can improve the power efficiency [147], the end-to-end latency [139], and especially the spectral efficiency, all thanks to the reduced range and denser spectral reuse [29]. However, without a careful allocation of D2D link to orthogonal channels (i.e., channelization), a significant share of the links may experience strong interference from other unintended D2D transmissions that happen to originate nearby. Furthermore, as the density increases, this interference could progressively clog the network.

By leveraging stochastic geometry tools, channelization schemes have been studied in the context of wireless ad-hoc networks, where fixed infrastructure is absent [148–153], and cognitive networks [57, 154]. This prior work had focused either on improving transmission capacity [57, 148–151, 154], defined as the maximum permissible density of simultaneous transmissions that satisfies a target receiver SINR with a specified outage probability, or else on analyzing interference statistics [57, 152, 153]. With the growing interest in overlaid D2D, new channel allocation schemes are being discussed that can befit networks with an infrastructure-supported control plane and the ensuing ability to synchronize transmissions, discover neighbors, and disseminate side information.

A first such a scheme, termed FlashLinQ, was formulated in [31, 155] and experimentally demonstrated. A subsequent scheme, referred to as ITLinQ, was proposed in [11] and evaluated by means of

Monte-Carlo simulations. This latter scheme is enticing because it is underpinned by information-theoretic optimality notions, which potentially makes it (*i*) more suitable to analysis, with the ensuing broader generality and with the possibility of optimizing controllable parameters, and (*ii*) more apt to provide insight and understanding on the mechanisms exercised to manage interference.

5.2 Contributions and Outcomes

These arguments motivate the analysis of ITLinQ that we present here, with the following contributions:

- We derive the exact density of D2D links allowed under different ITLinQ implementations for both fixed and randomized intended link distances. In most previous analyses of channelization in ad hoc networks [57, 150, 153], every link had the same distance.
- By means of the link density expressions, the spatially averaged link spectral efficiency (i.e., b/s/Hz per link) and area spectral efficiency (i.e., b/s/Hz per unit area) are approximated in integral forms. Numerical results confirm the accuracy of these approximations.
- Based on the area spectral efficiency expressions, the ITLinQ parameters are tuned as function of the user density and link distance distribution.
- With the parameters optimized, the performance of ITLinQ is evaluated and compared with that of FlashLinQ, which we also optimize for this comparison. Both ITLinQ and FlashLinQ are shown to yield substantial improvements with respect to an unchannelized baseline, with a slight edge for ITLinQ over FlasLinQ.

Above all, the analysis in this work sheds light on the mechanisms that ITLinQ utilizes to shield users from excessive interference while attempting to pack as many concurrent D2D transmissions per unit area as possible. Synchronized through the infrastructure, ITLinQ can have dedicated periods for control signaling and data transfer and can offer a more efficient channel allocation than their asynchronous ad hoc counterparts [31]. Specifically, CSMA/CA (carrier

sense multiple access/collision avoidance) with RTS/CTS (request to send/clear to send) schemes sacrifice spatial reuse and excessively protect each transmission from interference in order to prevent hidden terminal problems.

5.3 System Model

5.3.1 User Spatial Distribution

We consider the Poisson bipolar model [156] where D2D transmitters are spatially distributed according to a marked homogeneous PPP

$$\hat{\Phi} = \{(b_k, \theta_k, m_k, e_k)\} \subset \mathbb{R}^2 \times [0, 2\pi) \times [0, 1] \times \{0, 1\}$$

where:

- $\Phi = \{b_k\} \subset \mathbb{R}^2$ is the uniform PPP with intensity λ_{u} representing the locations of all existing transmitters with b_k the location of the kth-link transmitter.
- θ_k denotes the IID orientation angle, uniformly distributed in $[0, 2\pi)$, between the transmitter at b_k and its intended receiver.
- m_k is an IID random mark associated with the kth link, uniformly distributed in $[0, 1]$, which may represent the time stamp or the priority of the kth link.
- $e_k \in \{0, 1\}$ is a retaining indicator that indicates whether the kth link is allowed on a given channel.

Denoting by r_{u_k,b_k} the distance between the kth-link transmitter and its intended receiver, the location of such receiver is

$$u_k = b_k + [r_{u_k,b_k} \cos\theta_k, r_{u_k,b_k} \sin\theta_k]^T. \tag{5.1}$$

In the absence of empirical data on how r_{u_k,b_k} is distributed, various canonical distributions have been entertained in the literature: Rayleigh distributions [144, 157, 158], inverse functions of the link density [11, 29], or uniform distributions within a circle centered on the transmitter [159]. In this work, we consider the flexible discrete marginal distribution (IID across links)

$$r_{u_k,b_k} = d_n \quad \text{with probability} \quad p_n \tag{5.2}$$

and with $\sum_{n=1}^{N} p_n = 1$. By choosing N and the appropriate values for $d_1, \ldots, d_N$ and $p_1, \ldots, p_N$, we can reproduce as approximately as desired the behavior of any of the aforementioned continuous distributions. We hasten to emphasize that each link's distance is independent of the rest, with their distributions IID.

5.3.2 Signal Model

Denoting by P_{u} the (fixed) signal powers of user devices, the receiver at the origin observes

$$y_0 = \sqrt{P_{\mathrm{u}} \beta_{\mathrm{u}} \, r_{u_0,b_0}^{-\eta_{\mathrm{u}}}} \, h_{u_0,b_0} s_0 + \sum_{k=1}^{\infty} \sqrt{P_{\mathrm{u}} \beta_{\mathrm{u}} \, r_{u_0,b_k}^{-\eta_{\mathrm{u}}}} \, e_k \, h_{u_0,b_k} s_k + z_0. \tag{5.3}$$

We can further rewrite (5.3) as

$$y_0 = \sqrt{P_{\mathrm{u}} \beta_{\mathrm{u}} \, r_{u_0,b_0}^{-\eta_{\mathrm{u}}}} \, h_{u_0,b_0} s_0 + z_0'' \tag{5.4}$$

whose first term is the intended signal while the second term is the aggregate interference plus noise

$$z_0'' = \sum_{k=1}^{\infty} \sqrt{P_{\mathrm{u}} \beta_{\mathrm{u}} \, r_{u_0,b_k}^{-\eta_{\mathrm{u}}}} \, e_k \, h_{u_0,b_k} s_k + z_0 \tag{5.5}$$

where the summation spans the co-channel transmitters in $\Phi \setminus \{b_0\}$ while z_0 denotes the AWGN. In turn, $\eta_{\mathrm{u}} > 2$ is the pathloss exponent of D2D link, β_{u} is the pathloss intercept of D2D link, r_{u_0,b_k} is the distance between u_0 and b_k (i.e., from the transmitter at b_k to the receiver at u_0), h_{u_0,b_k} denotes the corresponding fading, and s_k is the data symbol communicated over the kth link. The fading coefficients are IID complex Gaussian with zero mean and unit variance, i.e., $h_{u_0,b_k} \sim \mathcal{N}_{\mathbb{C}}(0,1)$. Likewise, $s_k \sim \mathcal{N}_{\mathbb{C}}(0,1)$ and $z_0 \sim \mathcal{N}_{\mathbb{C}}(0, \sigma_{\mathrm{N}}^2)$ where $\sigma_{\mathrm{N}}^2 = F_{\mathrm{N}} N_0 B$ is the noise variance with F_{N} the noise figure, N_0 the noise power spectral density and B the bandwidth.

The local-average SNR at the 0th-link receiver is

$$\mathsf{SNR} = \frac{P_{\mathrm{u}} \beta_{\mathrm{u}}}{\sigma_{\mathrm{N}}^2} \, r_{u_0,b_0}^{-\eta_{\mathrm{u}}}. \tag{5.6}$$

Shadow fading, not considered here, could possibly be incorporated by adopting the approach in [160]. Since it can be seen as a distortion of the spatial geometry, shadow fading would render any

circular region amorphous and modify the quantitative results, yet we would expect it not to alter the intuition and the qualitative assessments. This is indeed what has been observed in other stochastic geometry analyses, e.g., in [80–82].

5.4 ITLinQ Analysis

5.4.1 Description

ITLinQ is grounded on a certain information-theoretic optimality notion: it selects, for allocation to each channel, a subset of links whose mutual interference can be treated as noise while still achieving the capacity region of that subset to within a constant gap [11]. That amounts to assigning the 0th link to a channel if and only if its transmitter and receiver satisfy the necessary and sufficient condition[1]

$$\mathsf{SNR} \geq \max_{k\neq 0} \mathsf{INR}^{\mathrm{in}}_{0,k} \max_{i\neq 0} \mathsf{INR}^{\mathrm{out}}_{i,0} \tag{5.7}$$

where $\mathsf{INR}^{\mathrm{in}}_{0,k}$ is the incoming local-average INR (interference-to-noise ratio) from link k to link 0, i.e., the INR from the kth-link transmitter to the 0th-link receiver, given by

$$\mathsf{INR}^{\mathrm{in}}_{0,k} = \frac{P_{\mathrm{u}}\beta_{\mathrm{u}}}{\sigma^2_{\mathrm{N}}}\, r^{-\eta_{\mathrm{u}}}_{u_0,b_k} \tag{5.8}$$

while $\mathsf{INR}^{\mathrm{out}}_{i,0}$ is the outgoing local-average INR to link i from link 0, i.e., the INR from the 0th-link transmitter to the ith-link receiver

$$\mathsf{INR}^{\mathrm{out}}_{i,0} = \frac{P_{\mathrm{u}}\beta_{\mathrm{u}}}{\sigma^2_{\mathrm{N}}}\, r^{-\eta_{\mathrm{u}}}_{u_i,b_0}. \tag{5.9}$$

To implement (5.7), a centralized controller having local-average channel knowledge of all the links would be required. To relax this requirement, a distributed version of ITLinQ was proposed in [11, Section III] where each transceiver can check its own condition locally with respect to already retained links, in a sequential fashion. This distributed version of ITLinQ relies only on two sufficient conditions, derived from (5.7), which expressed for the 0th link amount

[1]The condition (5.7) is called as TIN-optimality condition and the set of transmitters satisfying (5.7) is called as an information-theoretic independent set.

to

$$\mathsf{SNR}^{1/2} \geq \max_{k \neq 0} \mathsf{INR}_{0,k}^{\text{in}} \tag{5.10}$$

$$\mathsf{SNR}^{1/2} \geq \max_{i \neq 0} \mathsf{INR}_{i,0}^{\text{out}} \tag{5.11}$$

where (5.10) must be satisfied at the receiver of link 0 while (5.11) must be satisfied at the corresponding transmitter. Because distributed ITLinQ is based on sufficient but not necessary conditions, it is overly conservative and hence it experiences a certain loss relative to centralized ITLinQ. This loss can be eliminated almost completely by heuristically modifying the sufficient conditions in (5.10) and (5.11) into [11]

$$M\mathsf{SNR}^{\mu} \geq \mathsf{INR}_{0,k}^{\text{in}} \qquad \forall k \neq 0 \tag{5.12}$$

$$M\mathsf{SNR}^{\mu} \geq \mathsf{INR}_{i,0}^{\text{out}} \qquad \forall i \neq 0 \tag{5.13}$$

where M and μ are positive parameters.

Two slightly different distributed forms of ITLinQ are considered here, inspired by the Matérn hard-core processes of type I and type II that are widely utilized to analyze CSMA [152, 153].

- ITLinQ type I, whereby the conditions are applied to all existing links simultaneously rather than in a sequential fashion. The 0th link is allowed in a channel if and only if conditions (5.12) and (5.13) are satisfied with respect to all existing transmitters or receivers. If not allowed in a given channel, then the 0th link is served on another channel and thus we can regard the analysis herein as corresponding to the channel where this link is served. On such channel, the network that results with type I channelization is indicated by $\hat{\Psi}_{\text{I}} = \{(b_k, \theta_k) : (b_k, \theta_k, e_k) \in \hat{\Phi} \text{ and } e_k = 1\}$ while the process of co-channel transmitter locations is represented by $\Psi_{\text{I}} = \{b_k : (b_k, \theta_k) \in \hat{\Psi}_{\text{I}}\}$.
- ITLinQ type II, whereby the sequentiality in the application of the conditions is replaced by a prioritization embodied by the marks m_k. Rather than against all links, the conditions are verified against lower-priority links, i.e., the links are prioritized by the network and the 0th link is allowed in a channel if and only if conditions (5.12) and (5.13) are satisfied with respect to the subset of transmitters or receivers with lower

mark, $i, k \in \{n : m_n < m_0\}$. On the channel serving the 0th link, the network that results with type II channelization is indicated by $\hat{\Psi}_{\mathrm{II}} = \{(b_k, \theta_k) : (b_k, \theta_k, m_k, e_k) \in \hat{\Phi} \text{ and } e_k = 1\}$ while the process of co-channel transmitter locations is represented by $\Psi_{\mathrm{II}} = \{b_k : (b_k, \theta_k) \in \hat{\Psi}_{\mathrm{II}}\}$.

5.4.2 Geometric Interpretation

Plugging into the condition in (5.12) the definitions of SNR and $\mathsf{INR}_{0,k}^{\mathrm{in}}$ given in (5.6) and (5.8), respectively, we obtain

$$r_{u_0,b_k} \geq \frac{r_{u_0,b_0}^{\mu}}{M^{1/\eta_{\mathrm{u}}}} \left(\frac{P_{\mathrm{u}} \beta_{\mathrm{u}}}{\sigma_{\mathrm{N}}^2} \right)^{\frac{1-\mu}{\eta_{\mathrm{u}}}} \tag{5.14}$$

leading to the equivalent condition

$$r_{u_0,b_k} \geq \mathsf{R} \tag{5.15}$$

with

$$\mathsf{R} = \frac{r_{u_0,b_0}^{\mu}}{M^{1/\eta_{\mathrm{u}}}} \left(\frac{P_{\mathrm{u}} \beta_{\mathrm{u}}}{\sigma_{\mathrm{N}}^2} \right)^{\frac{1-\mu}{\eta_{\mathrm{u}}}}. \tag{5.16}$$

Thus, ITLinQ surrounds the receivers with exclusion regions of radius R where either no transmitter whatsoever is present (type I) or no lower-priority transmitters are present (type II). Likewise, by plugging (5.6) and (5.9) into (5.13), it can be verified that ITLinQ surrounds the transmitters with exclusion regions of radius R where either no receiver is present (type I) or no lower-priority receivers are present (type II). From (5.16), it can be seen that ITLinQ's exclusion radius needs to be optimized according to the transmit SNR, $P_{\mathrm{u}}/\sigma_{\mathrm{N}}^2$.

These exclusion regions, illustrated in Fig. 5.1, curb interference from all other links (type I) or from lower-priority links (type II) and ensure that conditions (5.12) and (5.13) are satisfied as far as those links are concerned. As seen in Fig. 5.2, type II is less conservative than type I and allows for a tighter packing of co-channel links by means of link prioritization.

Note how letting $M \to \infty$ in (5.16) immediately yields $\mathsf{R} = 0$, which corresponds to an unchannelized network where all links are active.

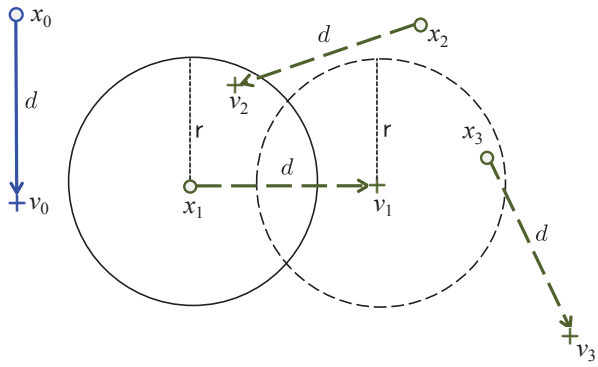

(a) Type I

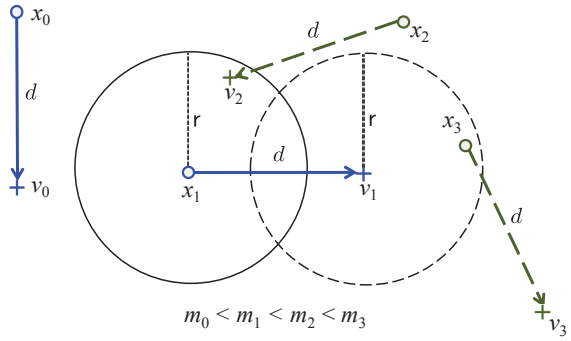

(b) Type II

Figure 5.1: Geometric interpretation of ITLinQ. A network with the same d for all links and with the link priority order $m_0 < m_1 < m_2 < m_3$ is considered. The interfering link distances satisfy $r_{u_0,b_k} > \mathsf{R}$ and $r_{b_0,u_j} > \mathsf{R}$ for $k, j \in \{1, 2, 3\}$, as well as $r_{b_1,u_2} < \mathsf{R}$ and $r_{b_3,u_1} < \mathsf{R}$. Type I: link 0 satisfies the ITLinQ conditions while links 1, 2 and 3 violate them; thus, only link 0 is allowed. Type II: link 0 is the lowest priority link and it is allowed independently of the ITLinQ conditions; link 1 is allowed to coexist as it satisfies the ITLinQ conditions against link 0; links 2 and 3 are not allowed to coexist as they both violate the ITLinQ conditions against link 1.

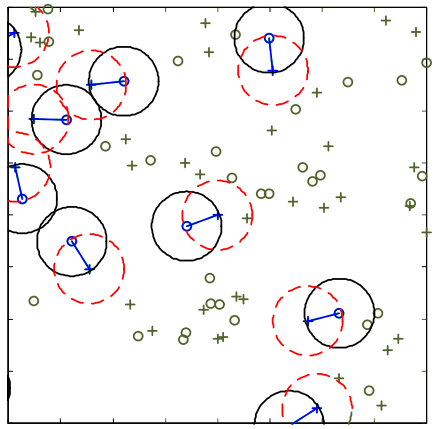

(a) Type I

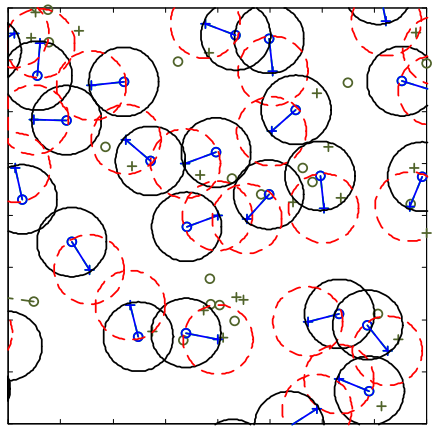

(b) Type II

Figure 5.2: Channelized network realization under ITLinQ. Transmitters and receivers are indicated by ∘ and +, respectively. Links allowed to coexist on the channel of interest are connected by solid lines while other links are not connected. Solid and dashed circles represent the exclusion regions around transmitters and receivers, respectively. In this example, and only for illustrative purposes, every link has the same distance and hence all exclusion regions are equally sized.

5.4.3 Co-Channel Link Density

The first and pivotal result we present characterizes the density of links that end up coexisting on a given channel when ITLinQ is applied.

Lemma 5.1. If the link distance is distributed according to (5.2), then the co-channel link densities of ITLinQ types I and II equal

$$\lambda_{\Psi_{\mathrm{I}}} = \sum_{n=1}^{N} p_n \, \lambda_{\mathrm{u}} \, e^{-\lambda_{\mathrm{u}} A(\mathsf{R}_n, d_\ell)} \tag{5.17}$$

$$\lambda_{\Psi_{\mathrm{II}}} = \sum_{n=1}^{N} \frac{p_n}{A(\mathsf{R}_n, d_\ell)} \left(1 - e^{-\lambda_{\mathrm{u}} A(\mathsf{R}_n, d_\ell)}\right) \tag{5.18}$$

where R_n is the exclusion region radius corresponding to $r_{u_0,b_0} = d_n$ in (5.16) while

$$A(\mathsf{R}_n, d_\ell) = \pi \mathsf{R}_n^2 + \sum_{\ell=1}^{N} p_\ell \int \left(1 - \mathbb{P}\left(u_i \notin \mathcal{B}_{b_0}(\mathsf{R}_n) | b_i, r_{u_i,b_i} = d_\ell\right)\right) \mathrm{d}b_i \tag{5.19}$$

with integration over $\mathcal{B}_{b_0}(\mathsf{R}_n + d_\ell) \setminus \mathcal{B}_{u_0}(\mathsf{R}_n)$ and with $\mathbb{P}\left(u_i \notin \mathcal{B}_{b_0}(\mathsf{R}_n) | b_i, r_{u_i,b_i} = d_\ell\right) =$

$$\begin{cases} \mathbb{1}(\mathsf{R}_n < d_\ell) & 0 \le r_{b_i,b_0} \le |\mathsf{R}_n - d_\ell| \\ 1 - \dfrac{\arccos\left(\frac{r_{b_i,b_0}^2 + d_\ell^2 - \mathsf{R}_n^2}{2\, r_{b_i,b_0} d_\ell}\right)}{\pi} & |\mathsf{R}_n - d_\ell| < r_{b_i,b_0} \le \mathsf{R}_n + d_\ell \\ 1 & r_{b_i,b_0} > \mathsf{R}_n + d_\ell \end{cases} \tag{5.20}$$

the probability that the receiver of the ith link is not in $\mathcal{B}_{b_0}(\mathsf{R}_n)$, conditioned on the location of the ith-link transmitter b_i.

Proof: See Appendix D.1.

Example 5.2. Let $\lambda_{\mathrm{u}} = 11.54$ links/km^2, which amounts to an average of 10 D2D users per circular cell of radius 525 m, with a pathloss exponent $\eta_{\mathrm{u}} = 4.5$. Further let $P_{\mathrm{u}}\beta_{\mathrm{u}}/\sigma_{\mathrm{N}}^2 = 117$ dB, corresponding for instance to $P_{\mathrm{u}}\beta_{\mathrm{u}} = 15$ dBm and $\sigma_{\mathrm{N}}^2 = -102$ dBm (i.e., $F_{\mathrm{N}} = 5$ dB, $N_0 = -174$ dBm/Hz and $B = 5$ MHz). In one case, every link has a distance of $d = 40$ m whereas, in another case, the link distances equiprobably take the values $d_1 = 20$ m, $d_2 = 40$ m and $d_3 = 60$ m. Shown in Table 5.1 are the co-channel link densities

Table 5.1: Co-channel link density (links/km^2)

	Fixed link distance		Random link distance	
(M, μ)	$\lambda_{\Psi_{\mathrm{I}}}$	$\lambda_{\Psi_{\mathrm{II}}}$	$\lambda_{\Psi_{\mathrm{I}}}$	$\lambda_{\Psi_{\mathrm{II}}}$
$(10, 0.5)$	8.61	10.00	8.69	10.04
$(10, 0.7)$	10.09	10.80	10.13	10.82
$(10, 0.9)$	10.88	11.21	10.86	11.20

of ITLinQ type I and type II computed via (5.17) and (5.18) for $M = 10$ with $\mu = 0.5, 0.7, 0.9$. As μ increases, R shrinks and hence the link density increases.

5.4.4 Interference Modeling

Invoking the interference modelling approach in Section 2.5, we have:

1. The short-term (local) distribution of z_0'' is modeled as zero-mean complex Gaussian with matched conditional variance $\mathbb{E}\left[|z_0''|^2 | \{r_{u_0,b_k}, e_k\}\right]$, where the expectation is over the data and fading distributions.

2. The interfering transmitters within an averaging circle surrounding the receiver of interest are explicitly modeled while the aggregate interference emanating from outside this circle is replaced by its expected (over the interferer locations) value. With an averaging circle radius $R = \sqrt{K/(\pi\lambda_{\mathrm{u}})}$, the average number of interferer transmitters explicitly modeled is K (cf. Fig. 5.3). As described in [29], the choice of K should be chosen to balance simplicity and accuracy in capturing the performance for specific user locations.

Recalling the definition in (5.5), the conditional variance σ_0^2 (i.e., the power of z_0'' for given interference locations $\{r_{u_0,b_k}\}$ and retaining indicators $\{e_k\}$) is

$$\sigma_0^2 = \underbrace{\sum_{k=1}^{K} P_{\mathrm{u}} \beta_{\mathrm{u}}\, e_k\, r_{u_0,b_k}^{-\eta_{\mathrm{u}}}}_{\sigma_{0,\mathrm{in}}^2} + \underbrace{\sum_{k=K+1}^{\infty} P_{\mathrm{u}} \beta_{\mathrm{u}}\, e_k\, r_{u_0,b_k}^{-\eta_{\mathrm{u}}} + \sigma_{\mathrm{N}}^2}_{\sigma_{0,\mathrm{out}}^2} \tag{5.21}$$

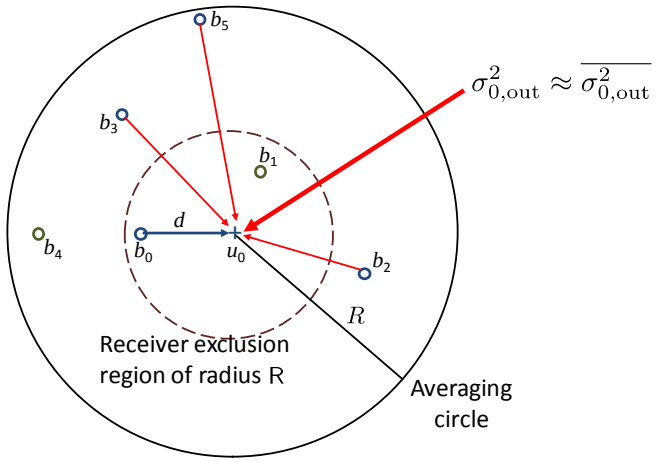

Figure 5.3: Interference modeling illustration where the intended link distance is d, the receiver exclusion region radius is R, and $K = 5$ interferer transmitters with retaining indicators $\{e_k\}_{k=1}^5 = \{0, 1, 1, 0, 1\}$ are explicitly modeled. The aggregate interference $\sigma^2_{0,\text{out}}$ emanating from outside the averaging circle of radius R is replaced by its expectation (over the corresponding interferer locations).

where, applying the second point in our interference modelling approach, $\sigma^2_{0,\text{in}}$ corresponds to the K transmitters in $\Phi \cap \mathcal{B}_{u_0}(R)$ while $\sigma^2_{0,\text{out}}$ corresponds to the transmitters in $\Phi \setminus \mathcal{B}_{u_0}(R)$ plus noise.

Computing the expectation of $\sigma^2_{0,\text{out}}$ over the locations of the interfering transmitters in that term is not straightforward because ITLinQ introduces dependencies (specifically, repulsions) across the locations of co-channel transmitters. These dependencies are quantified by the pair correlation function, defined as follows: denoting by $\lambda_{\text{u}}(\cdot)$ the intensity function and by $\varrho^{(2)}(b_i, b_k)$ the second moment density of point process Ψ, i.e., the joint probability that there will be points of Ψ at two specified locations b_i and b_k, then the pair correlation function is $\varrho^{(2)}(b_i, b_k)/\lambda_{\text{u}}(b_i)\lambda_{\text{u}}(b_k)$. If Ψ is uniform (e.g., PPP) then the pair correlation equals 1; if Ψ is repulsive (resp. clustered) then the pair correlation function is below 1 (resp. above 1). From the typical-link viewpoint, the locations of co-channel transmitters can be distinguished based on their pair correlations with the typical transmitter. The statistical properties of the Matérn process class, which is similar to ours, have been investigated in [152, 161]

and it has been shown that, when the separation between any two transmitters is at least R, the locations of co-channel transmitters within $2\,\mathsf{R}$ are correlated while those of co-channel transmitters beyond $2\,\mathsf{R}$ behave like a PPP. Applying this insight, we can borrow a modeling assumption introduced in [149] and whose validity for our purposes is examined later in the chapter.

Assumption 1: The locations of co-channel transmitters outside the receiver's exclusion region $\mathcal{B}_{v_0}(\mathsf{R})$ belong to a homogeneous PPP with scaled-down densities $\lambda_{\Psi_{\mathrm{I}}}$ and $\lambda_{\Psi_{\mathrm{II}}}$ for type I and type II, respectively.

Under Assumption 1, the locations of all interferers are modeled as PPP. Recalling that K dominant interferer locations are explicitly modeled, the expectation of $\sigma^2_{0,\mathrm{out}}$ over this PPP gives

$$\overline{\sigma^2_{0,\mathrm{out}}} = \mathbb{E}\left[\sum_{k=K+1}^{\infty} P_{\mathrm{u}}\beta_{\mathrm{u}}\, e_k\, r_{v_0,x_k}^{-\eta_{\mathrm{u}}}\right] + \sigma^2_{\mathrm{N}} \tag{5.22}$$

$$\approx \frac{2\pi\lambda_{\Psi} P_{\mathrm{u}}\beta_{\mathrm{u}}}{(\eta_{\mathrm{u}}-2)R^{\eta_{\mathrm{u}}-2}} + \sigma^2_{\mathrm{N}} \tag{5.23}$$

where (5.23) follows from Assumption 1 and Lemma 2.3 (cf. (2.20) with $R_1 \to R$, $\eta \to \eta_{\mathrm{u}}$ and $\lambda \to \lambda_{\Psi}$).

With the interference thus approximated, and recalling the intended signal term in (5.4), the instantaneous SINR is itself approximated by

$$\mathsf{SINR}_0 \approx \frac{P_{\mathrm{u}}\beta_{\mathrm{u}}\, r_{u_0,b_0}^{-\eta_{\mathrm{u}}}\, \mathbb{E}\big[|h_{u_0,b_0}s_0|^2 \mid h_{u_0,b_0}\big]}{\sigma^2_{0,\mathrm{in}} + \overline{\sigma^2_{0,\mathrm{out}}}} \tag{5.24}$$

$$= \rho_0\, |h_{u_0,b_0}|^2 \tag{5.25}$$

where

$$\rho_0 = \frac{P_{\mathrm{u}}\beta_{\mathrm{u}}\, r_{u_0,b_0}^{-\eta_{\mathrm{u}}}}{\sum_{k=1}^{K} P_{\mathrm{u}}\beta_{\mathrm{u}}\, e_k\, r_{u_0,b_k}^{-\eta_{\mathrm{u}}} + \frac{2\pi\lambda_{\Psi}P_{\mathrm{u}}\beta_{\mathrm{u}}}{(\eta_{\mathrm{u}}-2)R^{\eta_{\mathrm{u}}-2}} + \sigma^2_{\mathrm{N}}} \tag{5.26}$$

is the (approximate) local-average SINR at the receiver.

5.4.5 SINR Distribution

For a specific channelized network realization, i.e., given $\{r_{v_0,x_k}, e_k\}$, $k = 1,\ldots,K$, the value of ρ_0 becomes determined. Since $|h_{u_0,b_0}|^2$

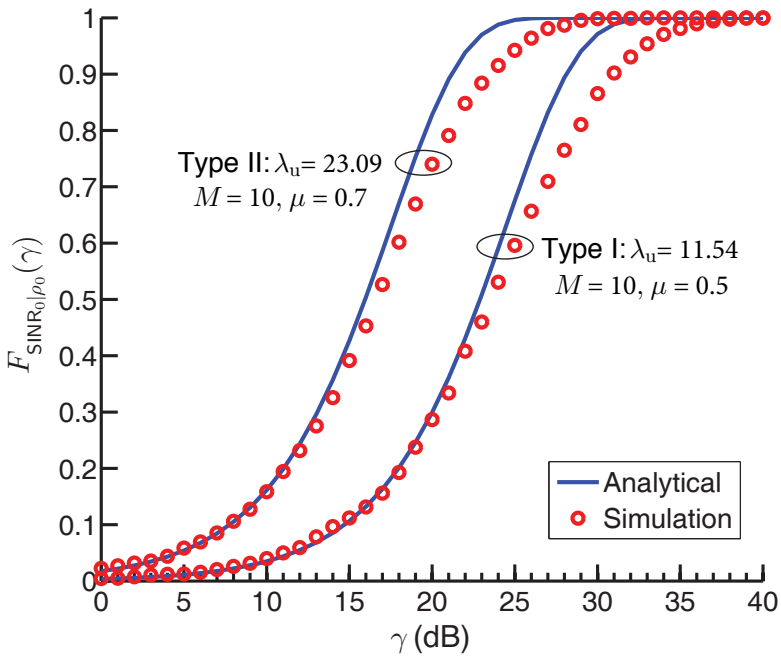

Figure 5.4: CDF of instantaneous SINR with fixed link distance $d = 40$ m.

is exponentially distributed with unit mean, it follows from (5.25) that the SINR exhibits an exponential distribution with mean ρ_0 and thus its conditional CDF is

$$F_{\mathsf{SINR}_0|\rho_0}(\gamma) = 1 - e^{-\gamma/\rho_0}. \tag{5.27}$$

Example 5.3. Reconsider Example 5.2 with the same distance $d = 40$ m for each link. The number of explicitly modelled interferers is set to $K = 5$ and, to render the system as typical as possible, r_{u_0,b_k} for $k = 1, \ldots, K$ is set to the expected distance to the kth nearest neighboring point in a PPP with density λ [93]. This gives $r_{u_0,b_k} = \Gamma(0.5 + k)/(\sqrt{\pi\lambda_u}\Gamma(k))$. Shown in Fig. 5.4 are the SINR distributions for ITLinQ types I and II obtained analytically under Assumption 1 (Eqs. (5.26) and (5.27)) alongside the simulated distributions with z_0'' as per (5.5), i.e., without any approximations. In the simulations, the locations of interferers outside the averaging circle no longer conform to a PPP, as the interferers within the exclusion regions are deactivated.

A satisfactory agreement is observed for both ITLinQ types, supporting the validity of our interference modeling approach. Similar agreement is observed for other values of the parameters.

5.4.6 Spectral Efficiency

Having validated our interference modeling approach in the previous subsection, we now turn our attention to the ergodic spectral efficiency.

Specific Network Geometry

For a specific network realization, i.e., for a given ρ_0, the ergodic spectral efficiency of the 0th link is

$$C(\rho_0) = \int_0^\infty \log_2(1+\gamma)\,\mathrm{d}F_{\mathsf{SINR}_0|\rho_0}(\gamma) \tag{5.28}$$

$$= e^{1/\rho_0}\mathcal{E}_1\left(\frac{1}{\rho_0}\right)\log_2 e. \tag{5.29}$$

Average Network Geometry

Next, we average the link spectral efficiency $C(\cdot)$ over all possible network realizations, obtaining the central result in the chapter.

Proposition 5.4. For transmitter density λ_{u}, the link distance distribution in (5.2) and parameters M and μ, the spatially averaged link spectral efficiency (b/s/Hz per link) of ITLinQ equals

$$\bar{C}(\lambda_{\mathrm{u}}, M, \mu) = \sum_{n=1}^{N} q_n \int_0^\infty \frac{\log_2 e}{\gamma+1}\exp\Bigg\{-\frac{\gamma}{d_n^{-\eta_{\mathrm{u}}}}\frac{\sigma_{\mathrm{N}}^2}{P_{\mathrm{u}}\beta_{\mathrm{u}}} + \pi\lambda_\Psi \mathsf{R}_n^2 + \frac{2\pi\lambda_\Psi}{\eta_{\mathrm{u}}}\gamma^{\frac{2}{\eta_{\mathrm{u}}}} d_n^2\,\bar{\Gamma}\left(-\frac{2}{\eta_{\mathrm{u}}}, \gamma\left(\frac{d_n}{\mathsf{R}_n}\right)^{\eta_{\mathrm{u}}}\right)\Bigg\}\mathrm{d}\gamma \tag{5.30}$$

where q_n is the fraction of co-channel links with distance d_n and λ_Ψ depends on λ_{u}, M and μ as per (5.17) for type I and (5.18) for type II.

Proof: See Appendix D.2.

Example 5.5. Shown in Fig. 5.5 is a comparison of $\bar{C}(\lambda_{\mathrm{u}}, M, \mu)$ as given in Proposition 5.4 against its simulated counterpart for $\lambda_{\mathrm{u}} = 11.54$ links/km^2, $\eta_{\mathrm{u}} = 4.5$ and $P_{\mathrm{u}}\beta_{\mathrm{u}}/\sigma_{\mathrm{N}}^2 = 117$ dB. Every link has

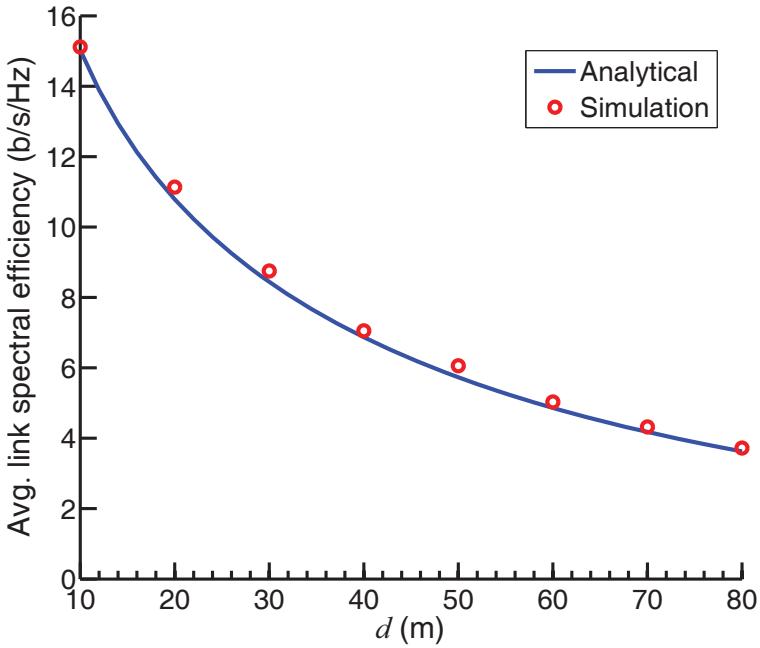

Figure 5.5: Average link spectral efficiency of ITLinQ type II as function of d for $\lambda_{\mathrm{u}} = 11.54$ links/km^2, $\mu = 0.7$ and $M = 10$.

the same intended distance d. The channelization is ITLinQ type II with $M = 10$ and $\mu = 0.7$. The simulated result corresponds to the exact mutual information under the non-Gaussian interference in (5.5), computed through Monte-Carlo histograms and averaged over many fading realizations and interference locations. The match is excellent, again evincing the goodness of our interference modeling approach. Additionally, as anticipated earlier, the results of our analysis are slightly below the mutual information computed under the non-Gaussian interference in (5.5).

From Proposition 5.4, we can obtain the spatially averaged area spectral efficiency (b/s/Hz per unit area) by scaling the spatially averaged link spectral efficiency $\bar{C}(\lambda_{\mathrm{u}}, M, \mu)$ by the co-channel link density λ_{Ψ}. This gives

$$\bar{\mathcal{C}}(\lambda_{\mathrm{u}}, M, \mu) = \lambda_{\Psi}\, \bar{C}(\lambda_{\mathrm{u}}, M, \mu) \tag{5.31}$$

from which the average benefits of channelization over all possible network geometries can be gauged. Moreover, the parameters M

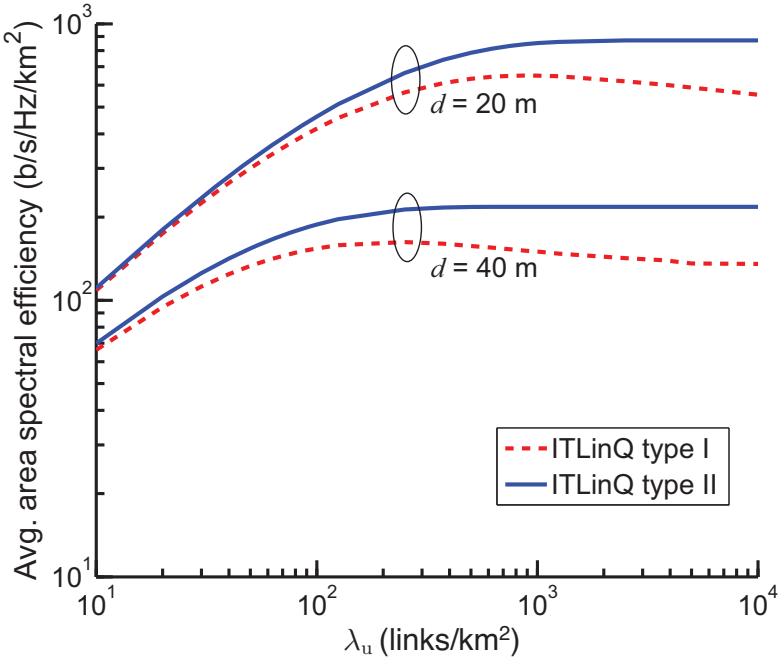

Figure 5.6: Average area spectral efficiency v. λ_u for optimized ITLinQ with $d = 20$ m and $d = 40$ m, and with $\eta_u = 4.5$ and $P_u\beta_u/\sigma_N^2 = 117$ dB.

and μ can be tuned as function of the user density and link distance distribution in order to maximize the average area spectral efficiency, i.e., to obtain

$$\bar{\mathcal{C}}^\star(\lambda_u) = \max_{M>0,\mu>0} \bar{\mathcal{C}}(\lambda_u, M, \mu). \tag{5.32}$$

Example 5.6. Shown in Fig. 5.6 is the average area spectral efficiencies of ITLinQ type I and type II obtained by numerically solving (5.32) with link distances fixed at either $d = 20$ m or $d = 40$ m. Type II is seen to be uniformly superior, with a performance advantage that increases with the user density, and hence we concentrate on this type henceforth. The limiting ($\lambda_u \to \infty$) area spectral efficiency of ITLinQ type II is presented in Fig. 5.7 as function of the link distance d, fixed for all users.

We observe that, for any fixed intended link distance, the co-channel link density $\lambda_{\Psi_{II}}$ increases with growing λ_u and eventually saturates.

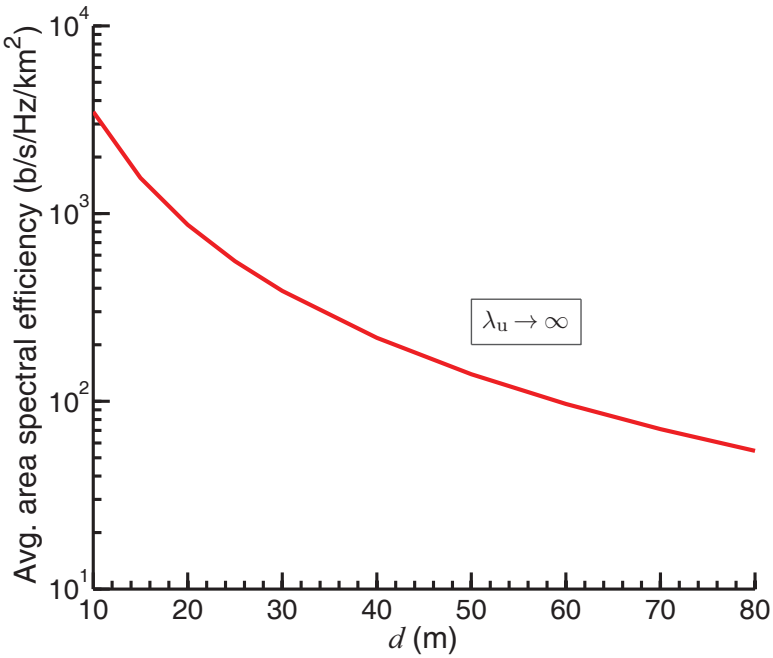

Figure 5.7: Average area spectral efficiency v. d for optimized ITLinQ type II with $\lambda_u \to \infty$, $\eta_u = 4.5$ and $P_u\beta_u/\sigma_N^2 = 117$ dB.

This, in turn, leads to saturation in the average area spectral efficiency.

5.5 Baseline Schemes

5.5.1 Baseline 1: Unchannelization

From Proposition 5.4, by taking $\lim_{M\to\infty} \bar{C}(\lambda_u, M, \mu)$ (equivalently, $\mathsf{R}_n = 0$), we can recover the spatially averaged link spectral efficiency for an unchannelized network (i.e., a network where all links are co-channel). This baseline,

$$\bar{C}(\lambda_u, \infty, \mu) = \sum_{n=1}^{N} p_n \int_0^\infty \frac{\log_2 e}{\gamma + 1} \cdot \exp\left(-\frac{\sigma_N^2 \, d_n^{\eta_u}}{P_u \beta_u} \gamma + \pi \lambda \gamma^{\frac{2}{\eta_u}} d_n^2 \, \Gamma\left(1 - \frac{2}{\eta_u}\right) \right) \mathrm{d}\gamma \quad (5.33)$$

shall be useful to establish the gains of ITLinQ.

5.5.2 Baseline 2: FlashLinQ

In addition to the baseline of a network with no channelization, a second interesting baseline for ITLinQ is FlashLinQ. In this section we briefly review how FlashLinQ operates, couching it in our notation and molding it to our models.

Description

In contrast with ITLinQ, whose channel allocation conditions are grounded in an information-theoretic optimality notion and then heuristically refined, FlashLinQ's channelization policy was formulated on a heuristic basis from the onset.

For the sake of consistency, and to ensure a fair comparison later, we consider a type II embodiment of FlashLinQ for which the 0th link is allowed in a channel if and only if two distinct conditions are satisfied with respect to links with a lower mark. The first condition is

$$\frac{\mathsf{SNR}}{\mathsf{INR}_{i,0}^{\text{out}}} \geq \gamma_{\text{TX}} \quad i \in \{n : m_n < m_0\} \tag{5.34}$$

which ensures that the outgoing interference caused by the 0th-link transmitter to any lower-mark receiver is within a specified limit determined by the threshold γ_{TX}; if (5.34) is not satisfied, then the 0th-link transmitter must *yield*, meaning that it must refrain from transmitting and thus the link must be allocated to another channel. In turn, the second condition is

$$\frac{\mathsf{SNR}}{\sum\limits_{k} \mathsf{INR}_{0,k}^{\text{in}}} \geq \gamma_{\text{RX}} \quad k \in \{n : m_n < m_0\} \tag{5.35}$$

where γ_{RX} is an additional threshold; if (5.35) is not satisfied, then the 0th-link receiver must yield, meaning again that the link must be allocated to another channel. It is worth to emphasize that the second condition is slightly restricted, expressed in terms of sum interference rather than individual interference, yielding a slight disadvantage to FlashLinQ in terms of performance.

An step-by-step description of FlashLinQ type II is given in *Algorithm 1*, under the hypothesis that the priority of the 0th link is the lowest.

Algorithm 1 FlashLinQ Type II Algorithm Summary

1. Set $e_0 = 1$, $e_n = 0$, $\epsilon_n^{\text{tx}} = 0$ and $\epsilon_n^{\text{rx}} = 0$ $\forall n \neq 0$, where ϵ_n^{tx} and ϵ_n^{rx} are temporary variables that indicate whether the FlashLinQ conditions are satisfied at the nth-link transmitter and receiver, respectively.
2. For every $i \in \{n : m_n < m_0\}$, set $\epsilon_i^{\text{rx}} = 1$ if the condition in (5.34) is satisfied.
3. For every $k \in \{n : m_n < m_0\}$, set $\epsilon_k^{\text{tx}} = 1$ if the condition in (5.35) is satisfied.
4. For every $n \neq 0$, compute $e_n = \epsilon_n^{\text{tx}} \epsilon_n^{\text{rx}}$.

Geometric Interpretation

Paraphrasing [31], the condition in (5.34) intends for the 0th link not to cause *too much interference* to other lower-mark links assigned to the channel under consideration. However, no specific SIR can be guaranteed for those other links as the condition limits the interference contribution of the 0th link without regard to how much other interference is present. Plugging into (5.34) the definitions of SNR and $\mathsf{INR}_{i,0}^{\text{out}}$ given in (5.6) and (5.9), respectively, we obtain for the ith lower-mark interfered link the equivalent condition

$$r_{u_i,b_0} \geq r_{u_0,b_0}\, \gamma_{\text{TX}}^{1/\eta_{\text{u}}} \tag{5.36}$$

whose enforcement amounts to forming around the transmitter a circular exclusion region that is free of any lower-mark receiver and whose radius is

$$r_{u_0,b_0}\, \gamma_{\text{TX}}^{1/\eta_{\text{u}}}. \tag{5.37}$$

Contrasting this definition with ITLinQ's exclusion radius R (cf. Eq. 5.16), we observe that the two coincide if $\mu = 1$ and $M = 1/\gamma_{\text{TX}}$. Furthermore, FlashLinQ's exclusion radius is—in contrast to ITLinQ's—insensitive to the transmit SNR, $P_{\text{u}}/\sigma_{\text{N}}^2$, and hence FlashLinQ yields robust performance with given thresholds irrespective of the transmit SNRs.

Given that the first FlashLinQ condition by itself cannot prevent possible situations of excessive interference, it is reinforced by the second condition meant to help achieve, again paraphrasing [31], a *reasonable SIR* for the 0th link. Once more though, no specific value can be guaranteed for the SIR because the second condition too

involves only links with lower marks; the interference from higher-mark links may push the SIR below γ_{RX} and, with some small probability, below even lower values. Furthermore, because the second condition involves not the interference from a specific link but a sum thereof, geometrically it amounts to forming an exclusion region that—even in the absence of shadow fading—is not circular; this renders FlashLinQ's analysis rather unwieldy.

Average Area Efficiency

In the original formulation of FlashLinQ, fixed values were employed for γ_{TX} and γ_{RX} with the further restriction that $\gamma_{\mathrm{TX}} = \gamma_{\mathrm{RX}}$. Then, in [162], this restriction was lifted and the performance of FlashLinQ was numerically computed for varying threshold values to find that:

- The average area spectral efficiency decreases with growing γ_{TX}.
- The average area spectral efficiency increases with growing γ_{RX} for lower values of γ_{RX} and then gradually decreases with growing γ_{RX} for higher values of γ_{RX}.

5.6 Performance Evaluation of ITLinQ

With the theoretical framework established in Section 5.4, we now proceed to evaluate the performance of optimized ITLinQ type II, and contrast it with the unchannelized baseline and with FlashLinQ.

Example 5.7. Fig. 5.8 shows, as function of λ_{u}, the average area spectral efficiency of optimized ITLinQ when every link has an intended distance $d = 40$ m. Both analytical and simulation results are provided. As baselines, analytical and simulation results for an unchannelized network, as well as simulation results for FlashLinQ.

Example 5.8. Fig. 5.9 shows, as function of λ_{u}, the average area spectral efficiency of optimized ITLinQ when the link distances equiprobably take the values $d_1 = 20$ m, $d_2 = 40$ m and $d_2 = 60$ m. Again, as baselines we include analytical and simulation results for an unchannelized network as well as simulation results for FlashLinQ.

From the foregoing examples, we can draw the following observations:

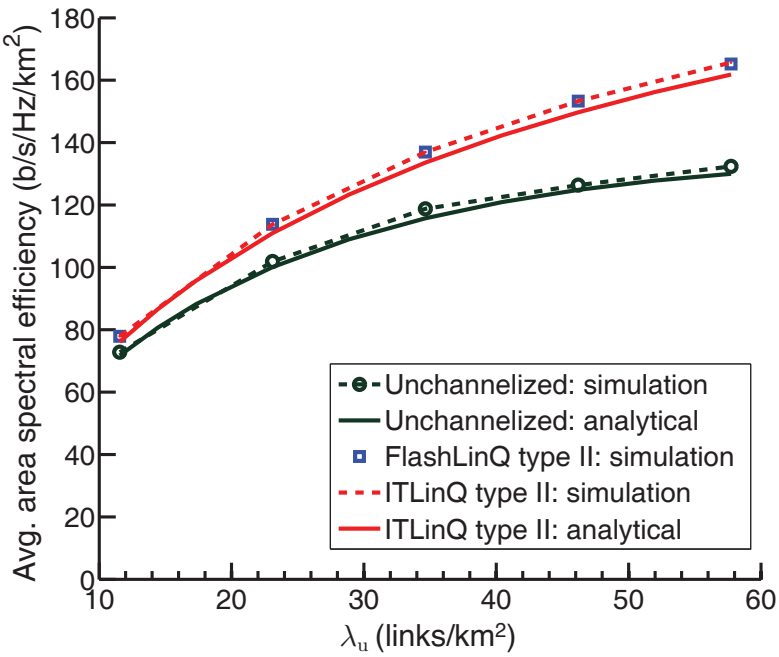

Figure 5.8: Average area spectral efficiency v. λ_u for optimized ITLinQ with $d = 40$, $\eta_u = 4.5$ and $P_u\beta_u/\sigma_N^2 = 117$ dB. Also shown are the corresponding spectral efficiencies for FlashLinQ and for an unchannelized network.

- Despite the PPP approximation in Assumption 1, the analytical expressions derived for ITLinQ are very accurate—slightly conservative for the reasons exposed in Section 5.4.4—and offer an efficient alternative to simulations. Indeed, the generation of each optimized simulation point in Examples 5.7 and 5.8 is an extremely time-consuming process.

- Both ITLinQ and FlashLinQ yield a significant improvement (on the order of 20–30% according to the foregoing examples) in average area spectral efficiency relative to the unchannelized baseline.

- ITLinQ has a slight edge over FlashLinQ, which despite its fully heuristic nature performs remarkably well if its thresholds are properly optimized.

Our observations have been verified to hold qualitatively for other

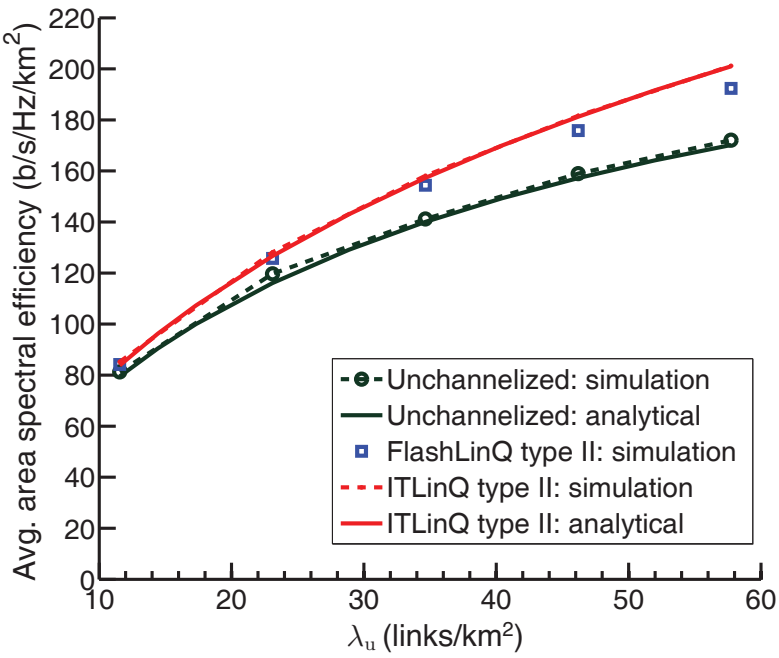

Figure 5.9: Average area spectral efficiency v. λ_u for optimized ITLinQ with randomized link distances (equiprobably: $d_1 = 20$ m, $d_2 = 40$ m and $d_2 = 60$ m) and with $\eta_u = 4.5$ and $P_u\beta_u/\sigma_N^2 = 117$ dB. Also shown are the corresponding spectral efficiencies for FlashLinQ and for an unchannelized network.

link distance distributions, for pathloss exponents ranging between $\eta_u = 3$ and $\eta_u = 4.5$, for dual-slope pathloss functions [163], and even with shadow fading incorporated.

While ITLinQ's improvement in average area spectral efficiency with respect to an unchannelized network is on the range of 20–30%, much more sizable gains are observed by users suffering from above-average interference. We next illustrate this potential in a typical situation where strong interference arises.

Example 5.9. Consider $\lambda_u = 23.09$ links/km^2, which amounts to an average of 20 D2D users per cell of radius 525 m, with the same distance $d = 40$ m for each link. As in earlier examples, $\eta_u = 4.5$ and $\frac{P_u\beta_u}{\sigma_N^2} = 117$ dB. The parameters of ITLinQ are set to maximize the average area spectral efficiency, i.e., $M = 10$ and $\mu = 0.5$, corresponding to an exclusion radius of $\mathsf{R} = 75.6$ m. Shown in

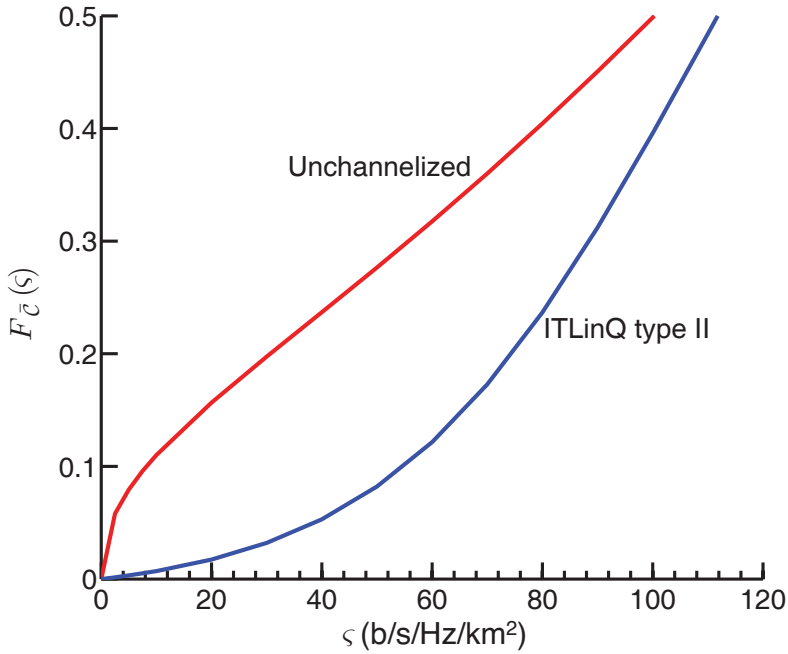

Figure 5.10: CDF of area spectral efficiency with intended link distances $d = 40$ m.

Fig. 5.10 are the distributions of area spectral efficiency for ITLinQ and for unchannelized network. ITLinQ exhibits a hefty advantage in the lower tail of the distribution, specifically a seven-fold gain in terms of the area spectral efficiency achieved by the worst 10% of network geometries. (The gain shrinks progressively as higher portions of the CDF are considered and, for the most favorable network geometries, ITLinQ is altogether unnecessary.)

5.7 Chapter Summary

The availability of multiple channels in D2D networks offers the possibility of parsing the available links onto various sets in such a way that excessive interference is avoided. ITLinQ and FlashLinQ operate by enforcing—through various parameters and thresholds—exclusion regions around transmitters and receivers. Both are effective, with a slight edge for ITLinQ. With respect to an unchannelized network, the gains in area spectral efficiency range between

20–30% on average and multiple-fold improvement factors on the most unfavorable network geometries.

Chapter 6

Full-duplex MIMO in Cellular Networks

Vision is the art of seeing what is invisible to others.

Jonathan Swift

The goal of this chapter is to examine full-duplex wireless communication, which allows simultaneous transmission and reception on each time-frequency channel. In addition to potentially doubling the spectral efficiency and reducing the end-to-end latency, such bidirectional communication can offer solutions to problems such as hidden terminals, decoupling of forward and reverse links, and spectrum sharing [39]. Besides cellular access, the potential applications of full duplexing include wireless backhauling for microcells and relaying in cooperative networks [36–38].

6.1 Related Work and Motivation

Previously unfeasible because of self-interference, full duplexing is now becoming possible thanks to advanced combinations of analog and digital techniques [32–35]. Among the various self-interference cancellation architectures being proposed stands the one in [35], which has the advantage of providing the highest isolation (up to 110 dB) between the transmit and receive chains for a single antenna. Given the prevalence of multiantenna transmitters and receivers in contemporary wireless systems, it is desirable to further have full-duplex architectures featuring MIMO, and indeed a MIMO full-

duplex platform has already been prototyped [164]. By pushing the self-interference below the noise level, it is possible to achieve a near-doubling of spectral efficiency for an isolated link. However, this may not extrapolate to wireless networks where every transmitter in the system interferes with every receiver. The question then arises as to whether, and by how much, full-duplex is beneficial over the standard half-duplex, and this question is precisely what motivates the chapter.

Initial studies of this issue are presented in [40–44], where the average performance of full-duplex schemes has been characterized in wireless ad-hoc networks [40, 41], cellular networks [42, 43], and heterogeneous networks [44]. Stochastic geometry is the toolbox invoked in all these studies, which allows for models that are both amenable to analysis and highly representative of the heterogeneous structure of emerging wireless networks.

6.2 Contributions and Outcomes

In our work, we seek to further advance the understanding of the matter by incorporating aspects that were missing in those pioneering studies and that turn out to have a major impact on the conclusions. A first such aspect relates to the pathloss exponent. Prior works [43] model the pathloss at a distance r as $\beta r^{-\eta}$; this single-slope model is inadequate to represent the pathloss among base stations, which as we shall see is critical in full-duplex networks, and a multi-slope model is much more adequate. A second aspect that is ignored in prior works, because of the complexity that it brings into the analysis, is MIMO. In addition, most previous stochastic geometry analyses characterize network coverage or outage on the basis of the instantaneous SIR. Nowadays, however, ergodic performance metrics obtained by expecting over the small-scale fading are operationally much more relevant (cf. Section 1.2.2). It is therefore more meaningful to focus on the local-average SIR and the ergodic spectral efficiency. This altogether motivates the analysis of full-duplex wireless networks that we present here, with the following contributions:

- We provide a unified stochastic geometry framework that encompasses both forward link and reverse link in full-duplex cellular networks, with each base station serving multiple users on each time-frequency channel.

- By leveraging the analytical potency of stochastic geometry, we derive expressions for the system-wide distributions of local-average SIR and for the ergodic spectral efficiencies. We also obtain the spatially averaged spectral efficiencies in integral forms, which serve to gauge the system-level benefits. And, to complement the analysis, we conduct Monte-Carlo simulations on a Vodafone LTE field test network.

- We establish that, without serious additional interference management, full-duplex macrocells are not viable because of the strong interference among macro base stations.

- We show that, in microcells, full-duplex can yield close to the expected doubling in spectral efficiency in the forward link. In the reverse link, and in absence of additional interference management, the base stations must be deployed with a certain minimum spacing in order to reap the benefits of full-duplex. This minimum spacing is considerable, and thus full-duplex is regretfully seen to be rather incompatible with densification.

The above observations have been made under the premise of balanced traffic demands in both forward link and reverse link, which is a reasonable assumption because of the increasing popularity of video uploading to social networking sites and recent growth in online storage services.

6.3 Network Model

We consider an interference-limited cellular network with both base stations and users supporting bidirectional communication, and conduct the analysis separately for forward link and reverse link. Each base station has N antennas and communicates independent signal streams to N single-antenna users. Each receiver has an estimate of the fading of its intended link(s), both in the forward link and in the reverse link. Advantageously in full-duplex, because of channel reciprocity each base station can further utilize its reverse link fading estimates to serve its user(s) in the reverse link. Since the penalty caused by the application of pilot-assisted fading estimates in lieu of perfect estimates has been shown to be marginal [165], we assume the fading estimates to be perfect. An explicit account of the pilot overhead incurred to gather these estimates would equally

affect half- and full-duplex systems, not having any bearing on the benefits of the latter over the former.

6.3.1 Forward Link

In the forward link, the receiver under consideration is a user and the transmitter is the closest base station. The base station locations $\{b_k\}$ are modeled by a homogeneous PPP, $\Phi_\mathrm{b} \subset \mathbb{R}^2$, with density λ_b. If the users are associated with their closest base stations, then the user locations are dependent on their serving base station locations and violate the PPP condition from the typical-user viewpoint. Faced with this obstacle, we borrow a modeling assumption that is shown to be tight in [166] and whose validity for our purposes is examined later in the paper: the user locations $\{u_j\}$ belong to another independent homogeneous PPP Φ_u with matched density, i.e., $\lambda_\mathrm{u} = N\lambda_\mathrm{b}$.

6.3.2 Reverse Link

In the reverse link, the receiver under consideration is a base station and the intended transmitters are the N closest users. Borrowing techniques from [167, 168], the analysis could be extended to incorporate reverse link power control and relax the constraint that the intended transmitters be the closest users. While quantitatively very interesting, this extension is not expected to modify the qualitative conclusions because the performance of full-duplex in the reverse link is mainly limited by the strong interference from the base stations.

The aforementioned model can be viewed as a full-duplex network (cf. Fig. 6.1), where each base station simultaneously communicates with the strongest N users in both forward link and reverse link, yet the user distribution is equally favorable for both half-duplex and full-duplex.

To facilitate the readability of the equations, we place $\rightarrow$ and $\leftarrow$ markers atop the forward link and reverse link variables, respectively.

6.4 Signal and Propagation Models

User antennas are unit-gain while base station antennas have a gain G_b. We denote by P_b and P_u the transmit powers of base stations

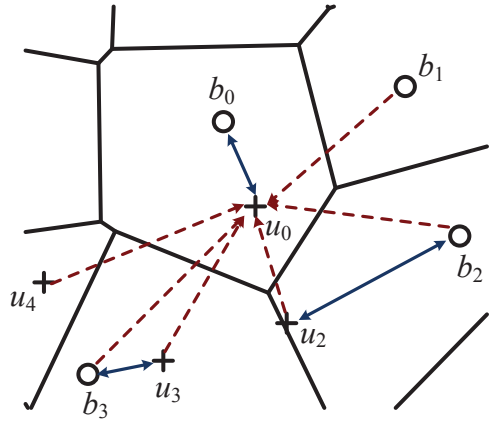

(a) Forward link

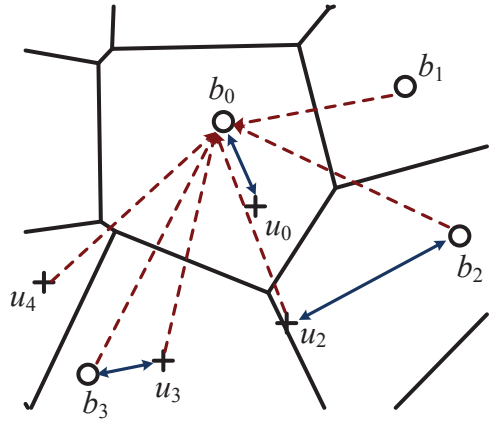

(b) Reverse link

Figure 6.1: Full-duplex cellular network realization. In the forward link, the receiver under consideration is a user (located at u_0) and the transmitter is the closest base station (located at b_0) while, in the reverse link, the receiver under consideration is a base station and the intended transmitter is the closest user. Base station and user locations are indicated by $\circ$ and $+$ markers, respectively. In this example, for illustrative purposes, $\lambda_{\mathrm{b}} = \lambda_{\mathrm{u}}$.

and users, respectively.

6.4.1 Forward Link

By Slivnyak's Theorem [51], we consider a receiving user at the origin and focus the analysis on its link, indexed by 0. This link, whose user and serving base station are respectively located at u_0 (the origin) and b_0, serves as the typical link in the network (cf. Fig. 6.1a). The user at the origin observes

$$\vec{y}_0 = \sqrt{\frac{P_{\mathrm{b}}}{N} G_{\mathrm{b}} \beta \, r_{u_0,b_0}^{-\eta}} \boldsymbol{h}_{b_0,u_0}^{*} \boldsymbol{V}_{b_0} \boldsymbol{s}_{b_0} + \vec{z}_0' \tag{6.1}$$

whose first term is the signal from its serving base station while the second term is the aggregate interference

$$\vec{z}_0' = \sum_{k=1}^{\infty} \sqrt{\frac{P_{\mathrm{b}}}{N} G_{\mathrm{b}} \beta \, r_{u_0,b_k}^{-\eta}} \boldsymbol{h}_{b_k,u_0}^{*} \boldsymbol{V}_{b_k} \boldsymbol{s}_{b_k} + \sum_{j=1}^{\infty} \sqrt{P_{\mathrm{u}} \beta_{\mathrm{u}} \, r_{u_0,u_j}^{-\eta_{\mathrm{u}}}} h_{u_0,u_j} s_{u_j} \tag{6.2}$$

where the first summation spans the interference from other base stations, $\Phi_{\mathrm{b}} \setminus \{b_0\}$, and the second summation spans the interference from other users, $\Phi_{\mathrm{u}} \setminus \{u_0\}$. In turn, β and β_{u} are respectively the pathloss intercepts of base-to-user and user-to-user links, η and η_{u} are the corresponding pathloss exponents, r_{u_0,b_0} is the distance from b_0 to u_0, $\boldsymbol{h}_{b_0,u_0} \in \mathbb{C}^{N \times 1}$ is the fading vector from b_0 to u_0 and $h_{u_0,u_j} \in \mathbb{C}$ is the fading coefficient from u_j to u_0. The entries of $\boldsymbol{h}_{b_k,u_0}$ and h_{u_0,u_j} are IID samples drawn from $\mathcal{N}_{\mathbb{C}}(0,1)$. Meanwhile, $\boldsymbol{V}_{b_0} \in \mathbb{C}^{N \times N}$ is the precoder used by the base station at b_0 to transmit its data symbol vector $\boldsymbol{s}_{b_0} \in \mathbb{C}^{N \times 1}$ while $s_{u_j} \in \mathbb{C}$ is the data symbol transmitted by the user at u_j. The entries of s_{u_0} and $\boldsymbol{s}_{b_0}$ are IID complex Gaussian such that $\mathbb{E}[|s_{u_0}|^2] = 1$ and $\mathbb{E}[\boldsymbol{s}_{b_0} \boldsymbol{s}_{b_0}^{*}] = \boldsymbol{I}_N$. Power allocation is uniform across the N signal streams, which gives $\mathbb{E}[||\boldsymbol{V}_{b_0} \boldsymbol{s}_{b_0}||_2^2] = N$.

Without loss of generality, base station and user locations are indexed in order of increasing distance, i.e., $r_{u_0,b_k} < r_{u_0,b_{k+1}}$ and $r_{u_0,u_j} < r_{u_0,u_{j+1}}$, while the base station at b_0 serves the users at $\{u_n\}_{n=0}^{N-1}$ Under these premises, the data symbol and precoder at b_0 can be respectively written as $\boldsymbol{V}_{b_0} = [\boldsymbol{v}_{u_0,b_0}, \ldots, \boldsymbol{v}_{u_{N-1},b_0}]$ and $\boldsymbol{s}_{b_0} = [s_{u_0,b_0}, \ldots, s_{u_{N-1},b_0}]^T$ with s_{u_0,b_0} the data symbol intended for the user at u_0 and $\boldsymbol{v}_{u_0,b_0}$ the corresponding precoder. With

perfect CSI at the base station, the precoder $\boldsymbol{v}_{u_0,b_0}$ is designed according to the zero-forcing strategy in order to prevent interference [169]. Mathematically, zero-forcing means $\boldsymbol{h}^*_{b_0,u_n}\boldsymbol{v}_{u_0,b_0} = 0$ for $n = 1, \ldots, N-1$, which plugged into (6.1) gives

$$\vec{y}_0 = \sqrt{\frac{P_\mathrm{b}}{N} G_\mathrm{b} \beta \, r^{-\eta}_{u_0,b_0}} \boldsymbol{h}^*_{b_0,u_0} \boldsymbol{v}_{u_0,b_0} s_{u_0,b_0} + \vec{z}'_0. \tag{6.3}$$

6.4.2 Reverse Link

As mentioned earlier, we adopt a two-slope model for the base-to-base pathloss [170]. Denoting by $R_\mathrm{c} = 4\mathsf{h}_\mathrm{b}^2/\lambda$ the critical distance with h_b the base station antenna height and λ the wavelength, the base-to-base pathloss for a given distance r_{b_0,b_k} is then

$$\begin{cases} \beta_\mathrm{b} r^{-\eta_\mathrm{b}}_{b_0,b_k} & r_{b_0,b_k} \leq R_\mathrm{c} \\ \beta_\mathrm{B} r^{-\eta_\mathrm{B}}_{b_0,b_k} & r_{b_0,b_k} > R_\mathrm{c} \end{cases} \tag{6.4}$$

where η_b and β_b are, respectively, the pathloss exponent and intercept of base-to-base links satisfying $r_{b_0,b_k} \leq R_\mathrm{c}$ while η_B and β_B are the pathloss exponent and intercept of base-to-base links satisfying $r_{b_0,b_k} > R_\mathrm{c}$. To analyze the reverse link, we shift the origin to the base station of interest, which observes (cf. Fig. 6.1b)

$$\check{\boldsymbol{y}}_0 = \sum_{n=0}^{N-1} \sqrt{P_\mathrm{u} G_\mathrm{b} \beta \, r^{-\eta}_{b_0,u_n}} \boldsymbol{h}_{b_0,u_n} s_{u_n} + \check{\boldsymbol{z}}'_0 \tag{6.5}$$

whose first term is the signals from its intended users at $\{u_n\}_{n=0}^{N-1}$ while the second term is the aggregate interference

$$\begin{aligned} \check{\boldsymbol{z}}'_0 = &\sum_{j=N}^{\infty} \sqrt{P_\mathrm{u} G_\mathrm{b} \beta \, r^{-\eta}_{b_0,u_j}} \boldsymbol{h}_{b_0,u_j} s_{u_j} + \sum_{k \in \mathcal{K}} \sqrt{\frac{P_\mathrm{b}}{N} G_\mathrm{b}^2 \beta_\mathrm{b} \, r^{-\eta_\mathrm{b}}_{b_0,b_k}} \boldsymbol{H}_{b_0,b_k} \boldsymbol{V}_{b_k} \boldsymbol{s}_{b_k} \\ &+ \sum_{k \notin \mathcal{K}} \sqrt{\frac{P_\mathrm{b}}{N} G_\mathrm{b}^2 \beta_\mathrm{B} \, r^{-\eta_\mathrm{B}}_{b_0,b_k}} \boldsymbol{H}_{b_0,b_k} \boldsymbol{V}_{b_k} \boldsymbol{s}_{b_k} \end{aligned} \tag{6.6}$$

where the first summation spans the interference from other users, $\Phi_\mathrm{u} \setminus \{u_n\}_{n=0}^{N-1}$, and the second and third summations span the interference from other base stations, $\Phi_\mathrm{b} \setminus \{b_0\}$. In (6.6), $\mathcal{K} = \{k : r_{b_0,b_k} \leq R_\mathrm{c}\}$ while $\boldsymbol{H}_{b_0,b_k} \in \mathbb{C}^{N \times N}$ is the fading matrix linking the base station at b_k with the base station at b_0. The base-to-base fading can be modeled as Rayleigh, Rician or disregarded altogether [71]. As

fading is seldom significant in base-to-base links, in this chapter we set $\boldsymbol{H}_{b_0,b_k} = \boldsymbol{I}_N$ [171].

The base station at b_0 applies $\boldsymbol{W}_{b_0} = [\boldsymbol{w}_{b_0,u_0}, \ldots, \boldsymbol{w}_{b_0,u_{N-1}}] \in \mathbb{C}^{N\times N}$ to process its received signal $\overleftarrow{\boldsymbol{y}}_0$, where $\boldsymbol{w}_{b_0,u_n}$ is the zero-forcing filter corresponding to the signal from the user at u_n. At its output, $\boldsymbol{w}_{b_0,u_n}$ gives

$$\boldsymbol{w}_{b_0,u_n}^* \overleftarrow{\boldsymbol{y}}_0 = \sqrt{P_{\mathrm{u}} G_{\mathrm{b}} \beta \, r_{b_0,u_n}^{-\eta}} \, \boldsymbol{w}_{b_0,u_n}^* \boldsymbol{h}_{b_0,u_n} s_{u_n} + \boldsymbol{w}_{b_0,u_n}^* \overleftarrow{\boldsymbol{z}}_0'. \tag{6.7}$$

6.5 Interference Modeling

Leveraging the approach in Section 2.5, the local-average distributions of co-channel interference terms $\vec{z}_0'$ and $\overleftarrow{\boldsymbol{z}}_0'$ (cf. (6.2) and (6.6)) are modeled as zero-mean complex Gaussian with matched conditional covariances $\mathbb{E}[|\vec{z}_0'|^2|\{r_{u_0,b_k}, r_{u_0,u_j}\}]$ and $\mathbb{E}[\overleftarrow{\boldsymbol{z}}_0' \overleftarrow{\boldsymbol{z}}_0'^* | \{r_{b_0,u_j}, r_{b_0,b_k}\}]$, respectively, where the expectations are over the data and fading distributions.

In the forward link, recalling (6.2), the conditional covariance of $\vec{z}_0'$ for given interferer locations is

$$\begin{aligned}
&\mathbb{E}\left[\vec{z}_0' \vec{z}_0'^* | \{r_{u_0,b_k}, r_{u_0,u_j}\}\right] \\
&\quad = \frac{P_{\mathrm{b}} G_{\mathrm{b}} \beta}{N} \sum_{k=1}^{\infty} r_{u_0,b_k}^{-\eta} \mathbb{E}\left[\boldsymbol{h}_{b_k,u_0}^* \boldsymbol{V}_{b_k} \boldsymbol{s}_{b_k} \boldsymbol{s}_{b_k}^* \boldsymbol{V}_{b_k}^* \boldsymbol{h}_{b_k,u_0}\right] \\
&\qquad + P_{\mathrm{u}} \beta_{\mathrm{u}} \sum_{j=1}^{\infty} r_{u_0,u_j}^{-\eta_{\mathrm{u}}} \mathbb{E}\left[h_{u_0,u_j} s_{u_j} s_{u_j}^* h_{u_0,u_j}^*\right] \qquad (6.8) \\
&\quad = \frac{P_{\mathrm{b}} G_{\mathrm{b}} \beta}{N} \sum_{k=1}^{\infty} r_{u_0,b_k}^{-\eta} \mathbb{E}\left[\left(\boldsymbol{h}_{b_k,u_0}^* \boldsymbol{V}_{b_k}\right)\left(\boldsymbol{h}_{b_k,u_0}^* \boldsymbol{V}_{b_k}\right)^*\right] \\
&\qquad + P_{\mathrm{u}} \beta_{\mathrm{u}} \sum_{j=1}^{\infty} r_{u_0,u_j}^{-\eta_{\mathrm{u}}} \mathbb{E}\left[h_{u_0,u_j} h_{u_0,u_j}^*\right] \qquad (6.9) \\
&\quad = P_{\mathrm{b}} G_{\mathrm{b}} \beta \sum_{k=1}^{\infty} r_{u_0,b_k}^{-\eta} + P_{\mathrm{u}} \beta_{\mathrm{u}} \sum_{j=1}^{\infty} r_{u_0,u_j}^{-\eta_{\mathrm{u}}} \qquad (6.10)
\end{aligned}$$

where (6.8) follows from the mutual independence of $\{\boldsymbol{s}_{b_k}\}_{k=1}^{\infty}$ and $\{s_{u_j}\}_{j=1}^{\infty}$ while the first term in (6.10) follows from the fact that $\boldsymbol{h}_{b_k,u_0}^* \boldsymbol{V}_{b_k}$ is a $1 \times N$ matrix with IID zero-mean unit-variance entries such that $\mathbb{E}[|\boldsymbol{h}_{b_k,u_0}^* \boldsymbol{V}_{b_k}|^2] = N$ [165].

Shifting to the reverse link and recalling (6.6), the conditional covariance of $\check{\boldsymbol{z}}_0'$ for given interferer locations equals

$$\begin{aligned}\mathbb{E}\left[\check{\boldsymbol{z}}_0'\check{\boldsymbol{z}}_0'^*|\{r_{b_0,u_j}, r_{b_0,b_k}\}\right] &= P_{\mathrm{u}}G_{\mathrm{b}}\beta\sum_{j=N}^{\infty} r_{b_0,u_j}^{-\eta}\mathbb{E}\left[\boldsymbol{h}_{b_0,u_j}s_{u_j}s_{u_j}^*\boldsymbol{h}_{b_0,u_j}^*\right] \\ &\quad + \frac{P_{\mathrm{b}}G_{\mathrm{b}}^2\beta_{\mathrm{b}}}{N}\sum_{k\in\mathcal{K}} r_{b_0,b_k}^{-\eta_{\mathrm{b}}}\mathbb{E}\left[\boldsymbol{V}_{b_k}\boldsymbol{s}_{b_k}\boldsymbol{s}_{b_k}^*\boldsymbol{V}_{b_k}^*\right] \\ &\quad + \frac{P_{\mathrm{b}}G_{\mathrm{b}}^2\beta_{\mathrm{B}}}{N}\sum_{k\notin\mathcal{K}} r_{b_0,b_k}^{-\eta_{\mathrm{B}}}\mathbb{E}\left[\boldsymbol{V}_{b_k}\boldsymbol{s}_{b_k}\boldsymbol{s}_{b_k}^*\boldsymbol{V}_{b_k}^*\right] \qquad (6.11)\end{aligned}$$

$$\begin{aligned}&= P_{\mathrm{u}}G_{\mathrm{b}}\beta\sum_{j=N}^{\infty} r_{b_0,u_j}^{-\eta}\mathbb{E}\left[\boldsymbol{h}_{b_0,u_j}\boldsymbol{h}_{b_0,u_j}^*\right] \\ &\quad + P_{\mathrm{b}}G_{\mathrm{b}}^2\beta_{\mathrm{b}}\sum_{k\in\mathcal{K}} r_{b_0,b_k}^{-\eta_{\mathrm{b}}}\boldsymbol{I}_N \\ &\quad + P_{\mathrm{b}}G_{\mathrm{b}}^2\beta_{\mathrm{B}}\sum_{k\in\mathcal{K}} r_{b_0,b_k}^{-\eta_{\mathrm{B}}}\boldsymbol{I}_N \qquad (6.12)\end{aligned}$$

$$\begin{aligned}&= \left[P_{\mathrm{u}}G_{\mathrm{b}}\beta\sum_{j=N}^{\infty} r_{b_0,u_j}^{-\eta} + P_{\mathrm{b}}G_{\mathrm{b}}^2\left(\beta_{\mathrm{b}}\sum_{k\in\mathcal{K}} r_{b_0,b_k}^{-\eta_{\mathrm{b}}}\right.\right. \\ &\qquad\qquad \left.\left. +\beta_{\mathrm{B}}\sum_{k\notin\mathcal{K}} r_{b_0,b_k}^{-\eta_{\mathrm{B}}}\right)\right]\boldsymbol{I}_N. \qquad (6.13)\end{aligned}$$

6.6 SIR Distributions

6.6.1 Forward Link

From (6.3) and (6.10), the instantaneous SIR experienced by the typical user in the forward link is

$$\overrightarrow{\mathsf{SIR}}_0 = \frac{\frac{P_{\mathrm{b}}G_{\mathrm{b}}\beta}{N}r_{u_0,b_0}^{-\eta}\mathbb{E}\left[|\boldsymbol{h}_{b_0,u_0}^*\boldsymbol{v}_{u_0,b_0}s_{u_0,b_0}|^2|\{\boldsymbol{h}_{b_0,u_j}\}_{j=0}^{N-1}\right]}{\mathbb{E}\left[|\vec{z}_0'|^2|\{r_{u_0,b_k}, r_{u_0,u_j}\}\right]} \qquad (6.14)$$

$$= \frac{\frac{P_{\mathrm{b}}G_{\mathrm{b}}\beta}{N}r_{u_0,b_0}^{-\eta}|\boldsymbol{h}_{b_0,u_0}^*\boldsymbol{v}_{u_0,b_0}|^2}{P_{\mathrm{b}}G_{\mathrm{b}}\beta\sum_{k=1}^{\infty} r_{u_0,b_k}^{-\eta} + P_{\mathrm{u}}\beta_{\mathrm{u}}\sum_{j=1}^{\infty} r_{u_0,u_j}^{-\eta_{\mathrm{u}}}} \qquad (6.15)$$

$$= \vec{\rho}_0|\boldsymbol{h}_{b_0,u_0}^*\boldsymbol{v}_{u_0,b_0}|^2 \qquad (6.16)$$

where the expectation in the numerator of (6.14) is over s_{u_0,b_0}, conditioned on the known fading (and therefore on the precoders), while

$$\vec{\rho}_0 = \frac{r_{u_0,b_0}^{-\eta}}{N\sum_{j=1}^{\infty} r_{u_0,u_j}^{-\eta_{\mathrm{u}}} + \varpi_{\mathrm{u}} N \sum_{k=1}^{\infty} r_{u_0,b_k}^{-\eta}} \tag{6.17}$$

is the local-average SIR at the typical user in the forward link with

$$\varpi_{\mathrm{u}} = \frac{P_{\mathrm{u}}\beta_{\mathrm{u}}}{P_{\mathrm{b}}G_{\mathrm{b}}\beta}. \tag{6.18}$$

Since the $\boldsymbol{v}_{u_0,b_0}$ is independent of $\boldsymbol{h}_{b_0,u_0}$ in zero-forcing precoding, the precoded channel $\boldsymbol{h}_{b_0,u_0}^{*}\boldsymbol{v}_{u_0,b_0} \sim \mathcal{N}_{\mathbb{C}}(0,1)$ and the power $|\boldsymbol{h}_{b_0,u_0}^{*}\boldsymbol{v}_{u_0,b_0}|^2$ is exponentially distributed with unit mean [165].

Local-Average SIR Distribution

The long-term distribution of the local-average SIR $\vec{\rho}_0$ is derived next by utilizing Lemma 2.5.

Proposition 6.1. For some given $r_{u_0,b_0} = r_0$, the CDF of $\vec{\rho}_0$ is

$$\begin{aligned} F_{\vec{\rho}_0|r_0}(\gamma) \approx 1 - \gamma \frac{e^{\frac{\mathsf{A}}{2}}}{2^{\mathsf{L}}} \sum_{\ell=0}^{\mathsf{L}} \binom{\mathsf{L}}{\ell} \sum_{\mathsf{m}=0}^{\mathsf{M}+\ell} \frac{(-1)^{\mathsf{m}}}{D_{\mathsf{m}}} \\ \cdot \Re\left\{ \frac{1}{\iota} \exp\left(\pi\lambda_{\mathrm{b}} r_0^2 + \frac{2\pi\lambda_{\mathrm{b}} r_0^2 \,(N\iota)^{\frac{2}{\eta}}}{\eta} \bar{\Gamma}\left(\frac{-2}{\eta}, N\iota\right) \right.\right. \\ \left.\left. -\pi N \lambda_{\mathrm{b}} \,(r_0^{\eta} N \varpi_{\mathrm{u}}\, \iota)^{\frac{2}{\eta_{\mathrm{u}}}}\, \Gamma\left(1 - \frac{2}{\eta_{\mathrm{u}}}\right) \right) \right\} \end{aligned} \tag{6.19}$$

where

$$\iota = \frac{(\mathsf{A} + \mathrm{i}\, 2\pi\mathsf{m})\,\gamma}{2} \tag{6.20}$$

while $D_0 = 2$ and $D_{\mathsf{m}} = 1$ for $\mathsf{m} \geq 1$. The parameters A, L and M control the accuracy, and the typical values are $\mathsf{A} = 9.21$, $\mathsf{L} = 5$ and $\mathsf{M} = 8$.

Proof: See Appendix E.1.

Eq. (6.19) can be unconditioned via the density function in (2.14) (with $n = 0$ and $\lambda = \lambda_{\mathrm{b}}$) to obtain the unconditional CDF of local-average SIR,

$$F_{\vec{\rho}_0}(\gamma) = \int_0^{\infty} F_{\vec{\rho}_0|r_0}(\gamma) f_{r_0}(r_0)\, \mathrm{d}r_0. \tag{6.21}$$

Table 6.1: Microcell network settings [171, Scenario 2]

Parameter	Value	Parameter	Value
P_{b}	24 dBm	η	3.75
P_{u}	23 dBm	$\eta_{\mathrm{b}}, \eta_{\mathrm{B}}$	$2, 4$
G_{b}	5 dBi	η_{u}	4
β	-32.9 dB	h_{b}	4 m
β_{b}	-38.45 dB	λ	0.15 m
β_{B}	-49.36 dB	R_{c}	427 m
β_{u}	-55.78 dB	λ_{b}	7.95 base stations/km^2

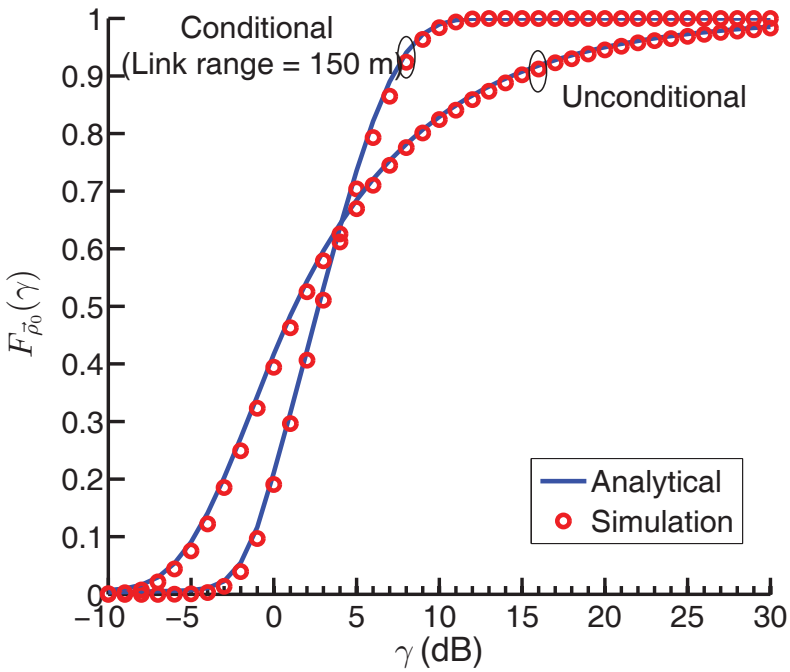

Figure 6.2: CDF of forward link local-average SIR in a full-duplex microcellular network with single-antenna base stations.

Example 6.2. Consider a network with single-antenna base stations of density $\lambda_{\mathrm{b}} = 7.95\,\text{base stations/km}^2$, which amounts to an average of one base station per circular cell of radius 200 m, and with typical values for the powers and the pathloss exponents (cf. Table 6.1). Shown in Fig. 6.2 is a comparison of the CDFs $F_{\vec{\rho}_0|r_0=150}(\gamma)$ and $F_{\vec{\rho}_0}(\gamma)$ in (6.19) and (6.21), with $A = 9.21$, $L = 5$ and $M = 8$, against their Monte-Carlo counterparts. An excellent

match is observed, supporting the validity of the Euler series expansion of the inverse Laplace transform and the PPP assumption for the interfering user locations.

Instantaneous SIR Distribution

Given $\{r_{u_0,b_k}\}$ and $\{r_{u_0,u_j}\}$, the value of $\vec{\rho}_0$ in (6.17) becomes determined. It follows from (6.16) that the forward link SIR exhibits an exponential distribution with local-average $\vec{\rho}_0$ and hence its conditional CDF is

$$F_{\overrightarrow{\mathsf{SIR}}_0|\vec{\rho}_0}(\gamma) = 1 - e^{-\gamma/\vec{\rho}_0}. \tag{6.22}$$

6.6.2 Reverse Link

Recalling (6.7), we can express the instantaneous SIR at the receiving base station corresponding to the reverse link signal stream from u_n as

$$\overleftarrow{\mathsf{SIR}}_{0,n} = \frac{P_{\mathrm{u}} G_{\mathrm{b}} \beta \, r_{b_0,u_n}^{-\eta} \mathbb{E}\left[|\boldsymbol{w}_{b_0,u_n}^* \boldsymbol{h}_{b_0,u_n} s_{u_n}|^2 | \{\boldsymbol{h}_{b_0,u_n}\}_{n=0}^{N-1} \right]}{\boldsymbol{w}_{b_0,u_n}^* \mathbb{E}\left[\overleftarrow{\boldsymbol{z}}_0 \overleftarrow{\boldsymbol{z}}_0^* | \{r_{b_0,u_j}, r_{b_0,b_k}\} \right] \boldsymbol{w}_{b_0,u_n}} \tag{6.23}$$

$$= \overleftarrow{\rho}_{0,n} |\boldsymbol{w}_{b_0,u_n}^* \boldsymbol{h}_{b_0,u_n}|^2 \tag{6.24}$$

where the expectation in (6.23) is over s_{u_n}, conditioned on the known fading (and therefore on the receive filters), while

$$\overleftarrow{\rho}_{0,n} = \frac{r_{b_0,u_n}^{-\eta}}{\sum_{j=N}^{\infty} r_{b_0,u_j}^{-\eta} + \varpi_{\mathrm{b}} \sum_{k \in \mathcal{K}} r_{b_0,b_k}^{-\eta_{\mathrm{b}}} + \varpi_{\mathrm{B}} \sum_{k \notin \mathcal{K}} r_{b_0,b_k}^{-\eta_{\mathrm{B}}}} \tag{6.25}$$

is the reverse link local-average SIR at the typical base station corresponding to the signal stream from u_n with

$$\varpi_{\mathrm{b}} = \frac{P_{\mathrm{b}} G_{\mathrm{b}} \, \beta_{\mathrm{b}}}{P_{\mathrm{u}} \, \beta} \tag{6.26}$$

and

$$\varpi_{\mathrm{B}} = \frac{P_{\mathrm{b}} G_{\mathrm{b}} \, \beta_{\mathrm{B}}}{P_{\mathrm{u}} \, \beta}. \tag{6.27}$$

Local-Average SIR Distribution

Noting that base stations cannot be arbitrarily close in actual deployments, we introduce a parameter $0 < \kappa \leq 1$ such that $r_{b_0,b_1} >$

κR_{c}. We derive the CDF of $\bar{\rho}_0$ in terms of κ, thereby parameterizing the distribution by the guaranteed distance to the strongest interfering base station.

Proposition 6.3. For given $r_{b_0,u_n} = r_n$, $r_{b_0,u_{N-1}} = r_{N-1}$ and $a_n = \frac{r_{b_0,u_n}}{r_{b_0,u_{N-1}}}$, the CDF of $\bar{\rho}_{0,n}$ is[1]

$$
\begin{aligned}
&F_{\bar{\rho}_{0,n}|r_n,a_n}(\gamma) \\
&\quad \approx 1 - \gamma\, \frac{e^{\frac{\mathsf{A}}{2}}}{2^{\mathsf{L}}} \sum_{\ell=0}^{\mathsf{L}} \binom{\mathsf{L}}{\ell} \sum_{\mathsf{m}=0}^{\mathsf{M}+\ell} \frac{(-1)^{\mathsf{m}}}{D_{\mathsf{m}}} \Re\Bigg\{ \frac{1}{\iota}\, \exp\Bigg(\pi N \lambda_{\mathrm{b}} \frac{r_n^2}{a_n^2} + \pi \lambda_{\mathrm{b}} \kappa^2 R_{\mathrm{c}}^2 \\
&\quad + \frac{2\pi N \lambda_{\mathrm{b}}\, r_n^2\, \iota^{\frac{2}{\eta}}}{\eta}\, \bar{\Gamma}\left(\frac{-2}{\eta}, a_n^{\eta}\, \iota \right) + \frac{2\pi \lambda_{\mathrm{b}}\, (r_n^{\eta} \varpi_{\mathrm{B}}\, \iota)^{\frac{2}{\eta_{\mathrm{B}}}}}{\eta_{\mathrm{B}}} \bar{\Gamma}\left(\frac{-2}{\eta_{\mathrm{B}}}, \frac{r_n^{\eta} \varpi_{\mathrm{B}}\, \iota}{R_{\mathrm{c}}^{\eta_{\mathrm{B}}}} \right) \\
&\quad + \frac{2\pi \lambda_{\mathrm{b}} R_{\mathrm{c}}^2}{\eta_{\mathrm{b}}} \left(E_{\frac{\eta_{\mathrm{b}}+2}{\eta_{\mathrm{b}}}} \left(\frac{r_n^{\eta}}{R_{\mathrm{c}}^{\eta_{\mathrm{b}}}} \varpi_{\mathrm{b}}\, \iota \right) - \kappa^2 E_{\frac{\eta_{\mathrm{b}}+2}{\eta_{\mathrm{b}}}} \left(\frac{r_n^{\eta}}{(\kappa R_{\mathrm{c}})^{\eta_{\mathrm{b}}}} \varpi_{\mathrm{b}}\, \iota \right) \right) \Bigg) \Bigg\}
\end{aligned}
\tag{6.28}
$$

where ι, D_m, A, L and M are as in Proposition 6.1.

Proof: See Appendix E.2.

The unconditional CDF of local-average SIR $F_{\bar{\rho}_{0,n}}(\gamma)$ can be computed as

$$
F_{\bar{\rho}_{0,n}}(\gamma) = \int_0^1 \int_0^{\infty} F_{\bar{\rho}_{0,n}|r_n,a_n}(\gamma) f_{r_n,a_n}(r_n, a_n)\, \mathrm{d}r_n\, \mathrm{d}a_n. \tag{6.29}
$$

where $f_{r_n,a_n}(\cdot,\cdot)$ is the joint PDF of r_n and a_n corresponding to $\lambda = N\lambda_{\mathrm{b}}$ in (2.15) and, recall, the first integration variable $a_n (0 \leq n < N-1)$ is the ratio of the distances from a point to its $(n+1)$th and Nth neighbors, with $0 < a_n < 1$.

Instantaneous SIR Distribution

Given $\{r_{b_0,u_j}\}$ and $\{r_{b_0,b_k}\}$, the value of $\bar{\rho}_{0,n}$ in (6.25) becomes determined and it follows from (6.24) that

$$
F_{\overline{\mathsf{SIR}}_{0,n}|\bar{\rho}_{0,n}}(\gamma) = 1 - e^{-\gamma/\bar{\rho}_{0,n}}. \tag{6.30}
$$

[1] One can derive the CDF directly in terms of r_n and r_{N-1} instead of r_n and a_n, but the latter option yields a somewhat more compact expression.

6.7 Spectral Efficiency

6.7.1 Forward Link

Specific Network Geometry

For given $\vec{\rho}_0$, the forward link ergodic spectral efficiency (conditioned on $r_{b_0,u_0} = r_0$) is [172, 173]

$$\vec{C}(\vec{\rho}_0|r_0) = \int_0^\infty \log_2(1+\gamma)\,\mathrm{d}F_{\overrightarrow{\mathsf{SIR}}_0|\vec{\rho}_0,r_0}(\gamma) \tag{6.31}$$

$$= e^{1/\vec{\rho}_0|r_0} E_1\left(\frac{1}{\vec{\rho}_0|r_0}\right)\log_2 e. \tag{6.32}$$

and its CDF equals

$$F_{\vec{C}}(\varsigma) = \mathbb{P}\left[e^{1/\vec{\rho}_0|r_0} E_1\left(\frac{1}{\vec{\rho}_0|r_0}\right)\log_2 e < \varsigma\right]. \tag{6.33}$$

Invoking [174]

$$e^\nu E_1(\nu)\log_2 e \approx 1.4\log_e\left(1+\frac{0.82}{\nu}\right) \tag{6.34}$$

we can approximate (6.33) as

$$F_{\vec{C}|r_0}(\varsigma) \approx F_{\vec{\rho}_0|r_0}\left(\frac{e^{\frac{\varsigma}{1.4}}-1}{0.82}\right), \tag{6.35}$$

which is validated in Example 6.4. Similarly, by leveraging the unconditional local-average SIR $\vec{\rho}_0$, we can compute the corresponding ergodic link spectral efficiency as

$$\vec{C}(\vec{\rho}_0) = e^{1/\vec{\rho}_0} E_1\left(\frac{1}{\vec{\rho}_0}\right)\log_2 e \tag{6.36}$$

and its CDF as

$$F_{\vec{C}}(\varsigma) \approx F_{\vec{\rho}_0}\left(\frac{e^{\frac{\varsigma}{1.4}}-1}{0.82}\right). \tag{6.37}$$

Example 6.4. For the same setting of Example 6.2, the approximate CDFs $F_{\vec{C}|r_0=150}(\varsigma)$ and $F_{\vec{C}}(\varsigma)$ are contrasted in Fig. 6.3, against their Monte-Carlo counterparts. Very good agreements are observed.

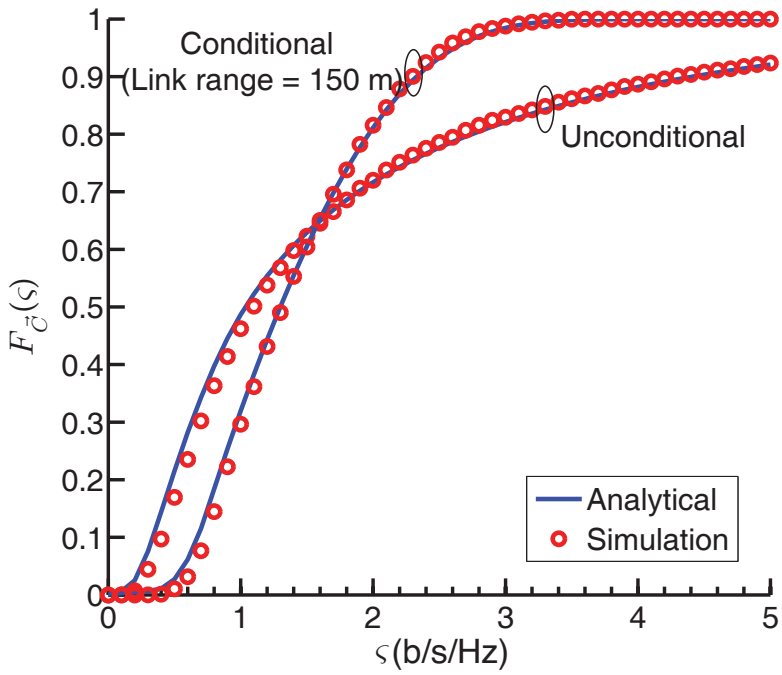

Figure 6.3: CDF of forward link ergodic spectral efficiency in a full-duplex microcellular network with single-antenna base stations.

Average Network Geometry

Next, we average the link spectral efficiency over all possible geometries.

Proposition 6.5. The average link spectral efficiency in the full-duplex cellular network model of Section 5.3 is

$$\bar{\vec{C}} = \int_0^\infty \frac{\log_2 e}{\gamma+1} \int_{r_0>0}^\infty 2\pi\lambda_{\mathrm{b}} \exp\left(\frac{2\pi\lambda_{\mathrm{b}}}{\eta}\, r_0^2 (N\gamma)^{\frac{2}{\eta}}\, \bar{\Gamma}\left(-\frac{2}{\eta}, N\gamma\right) \right.$$
$$\left. -\pi N\lambda_{\mathrm{b}} \left(r_0^\eta N\, \varpi_{\mathrm{u}}\, \gamma\right)^{\frac{2}{\eta_{\mathrm{u}}}}\, \Gamma\left(1-\frac{2}{\eta_{\mathrm{u}}}\right)\right) r_0\, \mathrm{d}r_0\, \mathrm{d}\gamma \tag{6.38}$$

Proof: See Appendix E.3.

Corollary 6.6. For $\eta_{\mathrm{u}} = \eta$, Proposition 6.5 reduces to

$$\vec{\bar{C}} = \int_0^\infty \frac{\log_2 e}{\gamma + 1} \frac{1}{N(N\,\varpi_{\mathrm{u}}\,\gamma)^{\frac{2}{\eta}}\Gamma\left(1 - \frac{2}{\eta}\right) - \frac{2}{\eta}(N\gamma)^{\frac{2}{\eta}}\,\bar{\Gamma}\left(-\frac{2}{\eta}, N\gamma\right)} \,\mathrm{d}\gamma. \tag{6.39}$$

The users served by the base station at b_0 are located at $\{u_n\}_{n=0}^{N-1}$ and their individual ergodic link spectral efficiencies are identically distributed. Thus, the aggregate average spectral efficiency of the users served by the base station at b_0 equals $N\vec{\bar{C}}$.

Example 6.7. For the system parameters in Table 6.1 and $N = 1$, the average spectral efficiency $\vec{\bar{C}}$, computed via (6.39), is 1.78 b/s/Hz while its simulated counterpart is 1.82 b/s/Hz. The simulated result corresponds to the exact mutual information under the non-Gaussian interference in (6.2), evaluated through Monte-Carlo histograms and averaged over many fading realizations and interference locations. The match is excellent, supporting our interference modeling approach.

6.7.2 Reverse Link

Specific Network Geometry

Proceeding as in the forward link, the reverse link ergodic spectral efficiencies of the typical base station (corresponding to the signal stream from u_n) for given $\overleftarrow{\bar{\rho}}_{0,n}$ and $\overleftarrow{\bar{\rho}}_{0,n}|r_n, a_n$ are

$$\overleftarrow{\bar{C}}(\overleftarrow{\bar{\rho}}_{0,n}) = e^{1/\overleftarrow{\bar{\rho}}_{0,n}} E_1\left(\frac{1}{\overleftarrow{\bar{\rho}}_{0,n}}\right) \log_2 e \tag{6.40}$$

$$\overleftarrow{\bar{C}}(\overleftarrow{\bar{\rho}}_{0,n}|r_n, a_n) = e^{1/\overleftarrow{\bar{\rho}}_{0,n}|r_n,a_n} E_1\left(\frac{1}{\overleftarrow{\bar{\rho}}_{0,n}|r_n, a_n}\right) \log_2 e \tag{6.41}$$

with CDFs

$$F_{\overleftarrow{\bar{C}}}(\varsigma) \approx F_{\overleftarrow{\bar{\rho}}_{0,n}}\left(\frac{e^{\frac{\varsigma}{1.4}} - 1}{0.82}\right) \tag{6.42}$$

$$F_{\overleftarrow{\bar{C}}|r_n,a_n}(\varsigma) \approx F_{\overleftarrow{\bar{\rho}}_{0,n}|r_n,a_n}\left(\frac{e^{\frac{\varsigma}{1.4}} - 1}{0.82}\right). \tag{6.43}$$

Average of all Network Geometries

Proposition 6.8. The average per-base-station spectral efficiency in the reverse link is

$$\begin{aligned}\overleftarrow{\bar{C}} = \sum_{n=0}^{N-1} \int_0^\infty \frac{\log_2 e}{\gamma+1} \int_0^1 \int_0^\infty \exp\Bigg(&\pi N\lambda_{\mathrm{b}} \frac{r_n^2}{a_n^2} + \pi\lambda_{\mathrm{b}}\kappa^2 R_{\mathrm{c}}^2 \\ &+ \frac{2\pi N\lambda_{\mathrm{b}} r_n^2\, \gamma^{\frac{2}{\eta}}}{\eta}\, \bar{\Gamma}\left(\frac{-2}{\eta}, a_n^\eta\, \gamma\right) \\ &+ \frac{2\pi\lambda_{\mathrm{b}} R_{\mathrm{c}}^2}{\eta_{\mathrm{b}}} \left(E_{\frac{\eta_{\mathrm{b}}+2}{\eta_{\mathrm{b}}}}\left(\frac{r_n^\eta}{R_{\mathrm{c}}^{\eta_{\mathrm{b}}}} \varpi_{\mathrm{b}}\, \gamma\right) - \kappa^2 E_{\frac{\eta_{\mathrm{b}}+2}{\eta_{\mathrm{b}}}}\left(\frac{r_n^\eta}{(\kappa R_{\mathrm{c}})^{\eta_{\mathrm{b}}}} \varpi_{\mathrm{b}}\, \gamma\right)\right) \\ &+ \frac{2\pi\lambda_{\mathrm{b}} \left(r_n^\eta \varpi_{\mathrm{B}}\, \gamma\right)^{\frac{2}{\eta_{\mathrm{B}}}}}{\eta_{\mathrm{B}}} \bar{\Gamma}\left(\frac{-2}{\eta_{\mathrm{B}}}, \frac{r_n^\eta}{R_{\mathrm{c}}^{\eta_{\mathrm{B}}}} \varpi_{\mathrm{B}}\, \gamma\right)\Bigg) f_{r_n,a_n}(r_n, a_n)\, \mathrm{d}r_n\, \mathrm{d}a_n\, \mathrm{d}\gamma \end{aligned} \tag{6.44}$$

where $f_{r_n,a_n}(r_n, a_n)$ is the joint PDF of r_n and a_n corresponding to $\lambda = N\lambda_{\mathrm{b}}$ in (2.15).

Proof: See Appendix E.4.

For the last term in the summation (i.e., $n = N-1$), $a_n = 1$ while $f_{r_n,a_n}(\cdot,\cdot)$ reduces to $f_{r_{N-1}}(\cdot)$, the PDF of r_{N-1} corresponding to $n = N-1$ and $\lambda = N\lambda_{\mathrm{b}}$ in (2.12), and the inner double integral reduces to a single integral.

For the single-antenna case, plugging $N = 1$ in (6.44) we obtain the more compact expression

$$\begin{aligned}\overleftarrow{\bar{C}} = \int_0^\infty \frac{\log_2 e}{\gamma+1} \int_0^\infty 2\pi\lambda_{\mathrm{b}} r_0 \exp\Bigg(&\pi\lambda_{\mathrm{b}}\kappa^2 R_{\mathrm{c}}^2 + \frac{2\pi N\lambda_{\mathrm{b}} r_0^2\, \gamma^{\frac{2}{\eta}}}{\eta}\, \bar{\Gamma}\left(-\frac{2}{\eta}, \gamma\right) \\ &+ \frac{2\pi\lambda_{\mathrm{b}} R_{\mathrm{c}}^2}{\eta_{\mathrm{b}}} \left(E_{\frac{\eta_{\mathrm{b}}+2}{\eta_{\mathrm{b}}}}\left(\frac{r_0^\eta\, \varpi_{\mathrm{b}}\, \gamma}{R_{\mathrm{c}}^{\eta_{\mathrm{b}}}}\right) - \kappa^2 E_{\frac{\eta_{\mathrm{b}}+2}{\eta_{\mathrm{b}}}}\left(\frac{r_0^\eta\, \varpi_{\mathrm{b}}\, \gamma}{(\kappa R_{\mathrm{c}})^{\eta_{\mathrm{b}}}}\right)\right) \\ &+ \frac{2\pi\lambda_{\mathrm{b}} \left(r_0^\eta\, \varpi_{\mathrm{B}}\, \gamma\right)^{\frac{2}{\eta_{\mathrm{B}}}}}{\eta_{\mathrm{B}}} \bar{\Gamma}\left(-\frac{2}{\eta_{\mathrm{B}}}, \frac{r_0^\eta\, \varpi_{\mathrm{B}}\, \gamma}{R_{\mathrm{c}}^{\eta_{\mathrm{B}}}}\right)\Bigg) \mathrm{d}r_0\, \mathrm{d}\gamma. \end{aligned} \tag{6.45}$$

The derived expressions are not simple enough to provide immediate insight, but they are general and easy-to-evaluate using software packages such as Mathematica and MATLAB. For given system settings, $\vec{\bar{C}}$ and $\overleftarrow{\bar{C}}$ can be solved for either instantaneously or within seconds (depending on whether $N = 1$ or $N > 1$); this is orders of magnitude faster than a Monte-Carlo computation of the exact mutual information under non-Gaussian interference.

6.8 Performance of Full-Duplex Communication

6.8.1 Half-Duplex Baseline

Unlike full-duplex, half-duplex transmission utilizes separate time-frequency signaling channels for the forward and reverse links. Therefore, the half-duplex spectral efficiency must be scaled by $1/2$ for a fair comparison with respect to full-duplex. The half-duplex counterparts to (6.36), (6.21) and (6.38) are then

$$\vec{C}^{\mathrm{HD}}(\vec{\rho}_0) = \frac{1}{2} \lim_{\varpi_{\mathrm{u}} \to 0} \vec{C}(\vec{\rho}_0) \tag{6.46}$$

$$F_{\vec{C}^{\mathrm{HD}}}(\varsigma) \approx \lim_{\varpi_{\mathrm{u}} \to 0} F_{\vec{\rho}_0}\left(\frac{e^{\frac{\varsigma}{0.7}} - 1}{0.82}\right) \tag{6.47}$$

$$\vec{\bar{C}}^{\mathrm{HD}} = \frac{1}{2} \lim_{\varpi_{\mathrm{u}} \to 0} \vec{\bar{C}}. \tag{6.48}$$

where $\varpi_{\mathrm{u}} \to 0$ turns off the forward link user transmissions. Plugging $\vec{\bar{C}}(\cdot)$ into (6.48) and evaluating the integral by virtue of [89, Eq. 3.326.2], $\vec{\bar{C}}^{\mathrm{HD}}$ reduces to

$$\vec{\bar{C}}^{\mathrm{HD}} = \frac{1}{2} \int_0^{\infty} \frac{-\eta \log_2 e}{2(N\gamma)^{\frac{2}{\eta}}(\gamma+1)\,\bar{\Gamma}\left(-\frac{2}{\eta}, N\gamma\right)} \mathrm{d}\gamma. \tag{6.49}$$

Similarly, from Eqs. (6.40), (6.29) and (6.44), we can recover for half-duplex

$$\overleftarrow{C}^{\mathrm{HD}}(\overleftarrow{\rho}_{0,n}) = \frac{1}{2} \lim_{\substack{\varpi_{\mathrm{b}} \to 0 \\ \varpi_{\mathrm{B}} \to 0 \\ \kappa \to 0}} \overleftarrow{C}(\overleftarrow{\rho}_{0,n}) \tag{6.50}$$

$$F_{\overleftarrow{C}^{\mathrm{HD}}}(\varsigma) \approx \lim_{\substack{\varpi_{\mathrm{b}} \to 0 \\ \varpi_{\mathrm{B}} \to 0 \\ \kappa \to 0}} F_{\overleftarrow{\rho}_{0,n}}\left(\frac{e^{\frac{\varsigma}{0.7}} - 1}{0.82}\right) \tag{6.51}$$

$$\overleftarrow{\bar{C}}^{\mathrm{HD}} = \frac{1}{2} \lim_{\substack{\varpi_{\mathrm{b}} \to 0 \\ \varpi_{\mathrm{B}} \to 0 \\ \kappa \to 0}} \overleftarrow{\bar{C}}. \tag{6.52}$$

where $\varpi_{\mathrm{b}} \to 0$ and $\varpi_{\mathrm{B}} \to 0$ turn off the reverse link base station transmissions. Inserting $N = 1$ and $\overleftarrow{\bar{C}}$ into (6.52) and then evaluating the integrals by virtue of [89, Eq. 3.326.2], $\overleftarrow{\bar{C}}^{\mathrm{HD}}$ is seen to

Table 6.2: Macrocell network settings [171, Scenario 8]

Parameter	Value	Parameter	Value
P_{b}	46 dBm	η	3.75
P_{u}	23 dBm	η_{b}	2
G_{b}	15 dBi	η_{B}	4
β	−15.3 dB	η_{u}	4
β_{b}	−38.45 dB	h_{b}	20 m
β_{B}	1.0439 dB	λ	0.15 m
β_{u}	−55.78 dB	R_{c}	10667 m

equal

$$\bar{\bar{C}}^{\mathrm{HD}} = \frac{1}{2}\int_0^\infty \frac{-\eta \log_2 e}{2\,\gamma^{\frac{2}{\eta}}(\gamma+1)\bar{\Gamma}\left(-\frac{2}{\eta},\gamma\right)}\,\mathrm{d}\gamma. \tag{6.53}$$

6.8.2 Performance Evaluation

Armed with the full-duplex expressions derived in Sections 6.6–6.7, and with the half-duplex baselines we just obtained, we can proceed to evaluate the performance advantage that full-duplex can brings about.

Example 6.9. Consider a macrocellular network with typical values for the powers and the pathloss exponents (cf. Table 6.2). Single-antenna base stations with densities 1.27 base stations/km^2 and 0.56 base stations/km^2 are considered, respectively amounting to an average of one base station per circular cell of radii 500 m and 750 m. The intended link distance is $r_{b_0,u_0} = 100$ m while $\kappa = 0.1$ (equivalently, $r_{b_0,b_1} > 1066.7$ m). Fig. 6.4 shows, parameterized by λ_{b}, the CDF of $\bar{\rho}_0$ obtained by applying (6.28). The overwhelming interference among macro base stations—due to the low base-to-base pathloss for distances below R_{c}—yields SIRs that are simply too low for viable full-duplex operation. Through simulations, we have observed this observation to hold with sectorized antennas at the base stations [68].

Having exemplified how full-duplex is not feasible in macrocell reverse links, at least not without additional interference management tailored to full-duplex, we next focus on microcells (cf. Table 6.1).

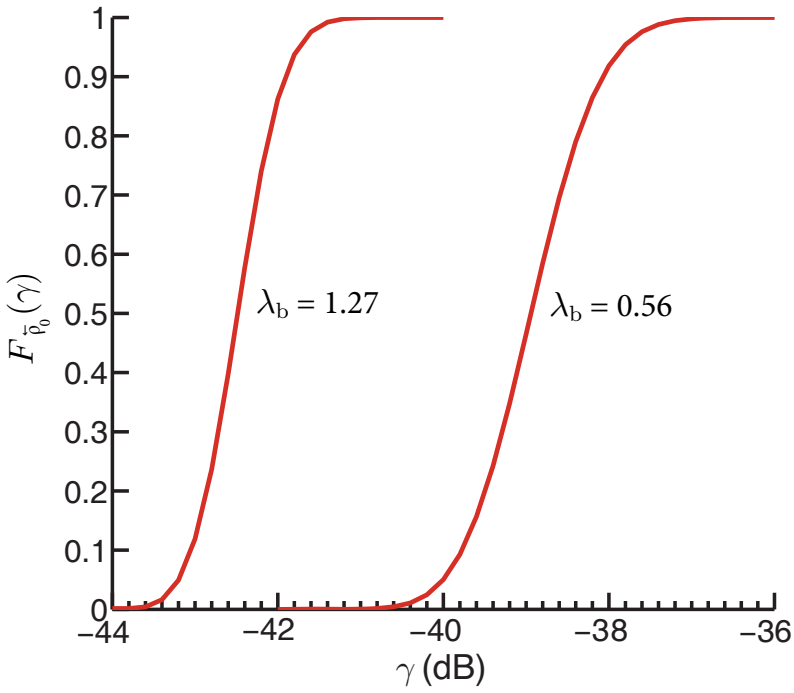

Figure 6.4: CDF of reverse link local-average SIR as function of λ_b (base stations/km^2), for a full-duplex macrocell network with $r_{b_0,u_0} = 100$ m, $N = 1$ and $\kappa = 0.1$ (equivalently, $r_{b_0,b_1} > 1066.7$ m).

Example 6.10. Consider a microcell network with single-antenna base stations, i.e., $N = 1$ and $\lambda_b = \lambda_u$. Fig. 6.5 compares the forward link ergodic spectral efficiency CDFs of full-duplex and half-duplex (cf. (6.37) and (6.47)). Full-duplex is superior to half-duplex in a vast majority of network situations and, as illustrated in the inset of Fig. 6.5, it achieves a spectral efficiency gain factor of 1.9 in 80% of cases. Then, Fig. 6.6 presents the same comparison for the reverse link, with two distinct values for κ. When $\kappa = 3/4$, i.e., when the first interfering base station is within a critical distance of the receiving base station, full-duplex is markedly inferior to half-duplex. However, for $\kappa = 1$, full-duplex is uniformly superior to half-duplex, pointing to the need for a careful planning in full-duplex deployments.

Example 6.11. As a final step, we quantify the average benefits of full-duplex. For the microcell settings in Table 6.1, the forward link average spectral efficiencies (cf. (6.38) and (6.49)) for half-duplex

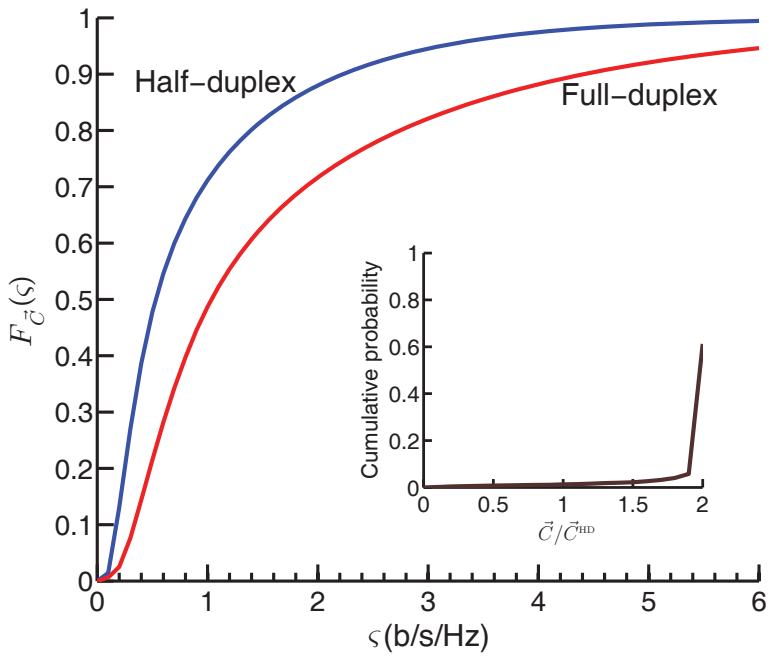

Figure 6.5: Main plot: CDF of forward link ergodic spectral efficiency for a microcell network with half- and full-duplex. Inset: CDF of the ratio of the two spectral efficiencies. In both plots, single-antenna base stations are considered.

and full-duplex are presented in Table 6.3, where the gain factor due to full-duplex is seen to exceed 1.9 for varying N. The corresponding reverse link average spectral efficiencies (cf. (6.44) and (6.52)) are presented in Fig. 6.7, as a function of κ. The full-duplex average spectral efficiency increases with κ and, at $\kappa = 0.925$, it equals the value with half-duplex for $N = 1$; thereafter, the gain increases rapidly. Therefore, full-duplex outperforms half-duplex only if the base stations are apart by at least the critical distance. This is indeed viable in microcell networks because of the relatively short critical distances (hundreds of meters).

Although a blanket utilization of full-duplex is not beneficial, there are situations (cf. Fig. 6.7) in which it is indeed advantageous. This points to a hybrid-duplex system that resorts to full-duplex or half-duplex, whichever is best, depending on the geometry. If the base station density is λ_{b}, then the probability that the neighboring

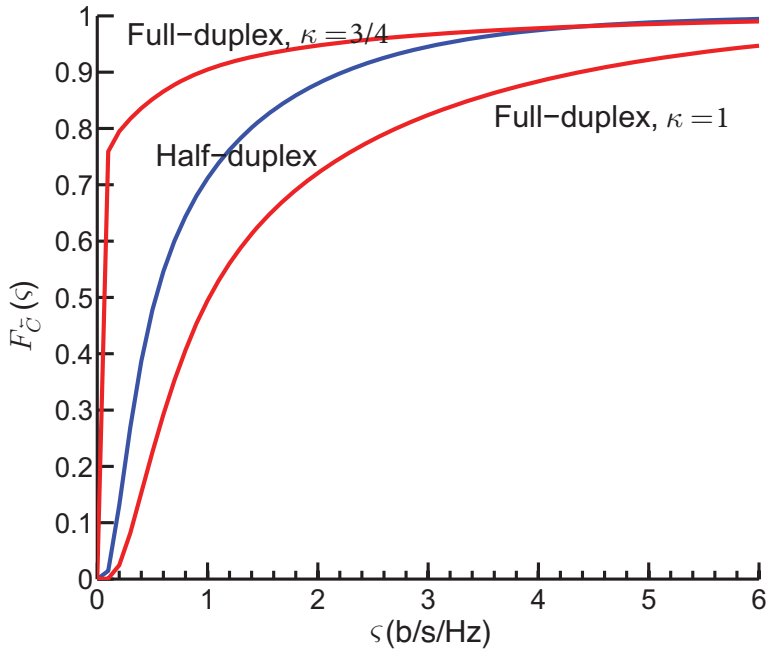

Figure 6.6: CDF of reverse link ergodic spectral efficiency for a single-antenna microcell network with half-duplex and full-duplex.

Table 6.3: Forward link average spectral efficiency (b/s/Hz) for a microcell network with half-duplex and full-duplex

N	$N\vec{C}$	$N\vec{C}^{\mathrm{HD}}$	$\vec{C}/\vec{C}^{\mathrm{HD}}$
1	1.784	0.906	1.969
2	2.657	1.350	1.968
3	3.325	1.690	1.967

base station is apart by at least the critical distance equals $e^{-\pi\lambda_{\mathrm{b}}R_{\mathrm{c}}^2}$, and the fraction of base stations favorable for full-duplex is $e^{-\pi\lambda_{\mathrm{b}}R_{\mathrm{c}}^2}$. Based on this, the average system-level benefits of such a hybrid-duplex system can be quantified. Let us denote by $\bar{\mathcal{C}}^{\mathrm{Hybrid}}$ and $\bar{\mathcal{C}}^{\mathrm{HD}}$ the average area spectral efficiencies (b/s/Hz/km^2) of hybrid-duplex and half-duplex, obtained by scaling the average link spectral effi-

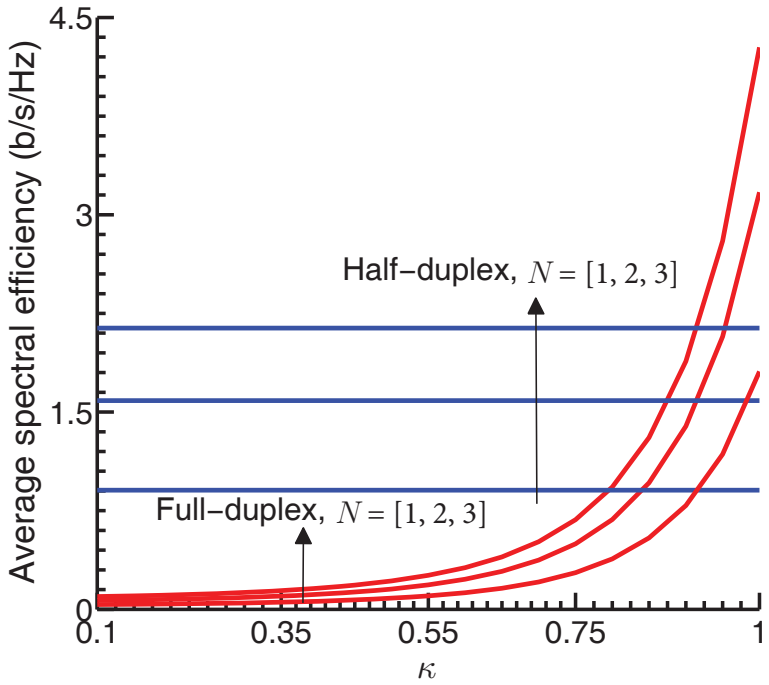

Figure 6.7: Reverse link average spectral efficiency for a microcell network with half-duplex and full-duplex.

ciencies by the corresponding densities of base stations and users:

$$\bar{\mathcal{C}}^{\text{Hybrid}} = e^{-\pi\lambda_{\text{b}}R_{\text{c}}^2}\left(\lambda_{\text{u}}\vec{C} + \lambda_{\text{b}}\overleftarrow{C}\right) + \left(1 - e^{-\pi\lambda_{\text{b}}R_{\text{c}}^2}\right)\left(\lambda_{\text{u}}\vec{C}^{\text{HD}} + \lambda_{\text{b}}\overleftarrow{C}^{\text{HD}}\right) \tag{6.54}$$

$$\bar{\mathcal{C}}^{\text{HD}} = \lambda_{\text{u}}\vec{C}^{\text{HD}} + \lambda_{\text{b}}\overleftarrow{C}^{\text{HD}}. \tag{6.55}$$

Example 6.12. Shown in Fig. 6.8 are the average area spectral efficiencies for half- and hybrid-duplex networks as a function of the base station density, for the microcell settings in Table 6.1. The fraction of full-duplex base stations, $e^{-\pi\lambda_{\text{b}}R_{\text{c}}^2}$, decreases with the base station density λ_{b} and consequently the average area spectral efficiency of hybrid-duplex approaches the value of standalone half-duplex. This manifests again that full-duplex does not blend well with high densification.

As an alternative to gains in spectral efficiency, one can consider the sparsification in infrastructure density that full-duplex can bring

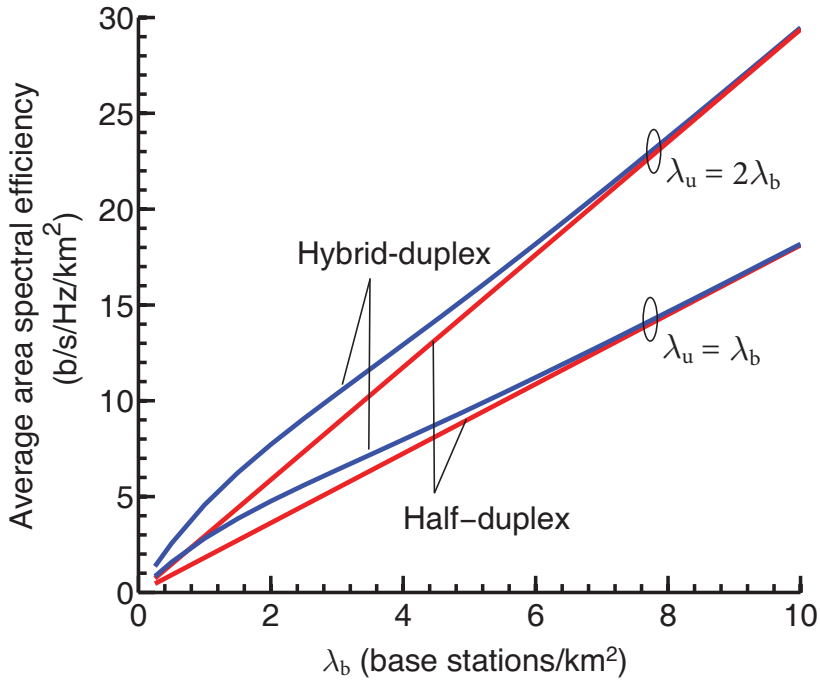

Figure 6.8: Average area spectral efficiency for a microcell network with half-duplex and hybrid-duplex.

about for a given area spectral efficiency (b/s/Hz per unit area). To achieve the same value thereof than a half-duplex network, only $\vec{C}^{\mathrm{HD}}/\vec{C}$ as many base stations per unit area are needed under full-duplex.

6.8.3 System-Level Benefits in a Vodafone Field Test Network

To confirm the robustness of our PPP-based analytical findings, we further consider a Vodafone LTE field test network consisting of 64 base stations over $1\,\mathrm{km}^2$ in the London area [175, Section III], obtain Monte-Carlo results using the geometry of that network, and contrast them with our analysis. As the test network density is very high, the two-slope pathloss model is applied to base-to-user and user-to-user links as well. Users are distributed such that the distance between each base station and its intended user is uniform within $[10, 40]$ m. Heights of 4 m and 1.75 m are considered for the

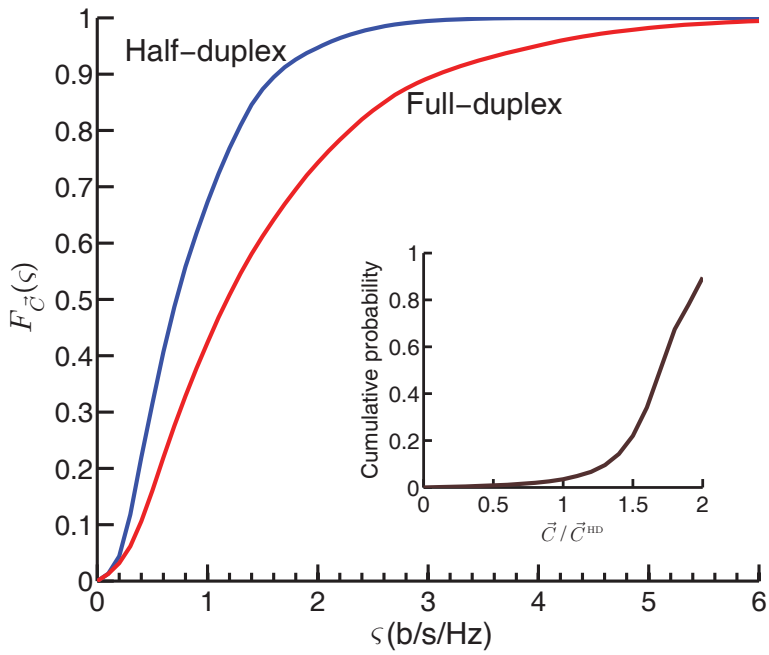

Figure 6.9: Main plot: CDF of forward link spectral efficiency for a Vodafone LTE field test network with half- and full-duplex. Inset: CDF of the ratio of the two spectral efficiencies. In both plots, single-antenna base stations are considered.

base station and user antenna, respectively, with typical 3GPP (3rd generation partnership project) settings [171, Scenario 2].

Shown in Fig. 6.9 is a comparison of the forward link ergodic spectral efficiency CDFs of full-duplex and half-duplex. Consistent with our analysis, full-duplex is virtually always superior to half-duplex and, as illustrated in the inset of Fig. 6.9, it achieves a spectral efficiency gain factor of 1.7 in 50% of cases. Then, the same comparison for the reverse link is presented in Fig. 6.10. Again consistent with our analysis, full-duplex is markedly inferior to half-duplex due to the very dense deployment of base stations.

6.9 Chapter Summary

The introduction of full-duplex transceivers in wireless networks would transform the interference landscape, foregoing long-standing

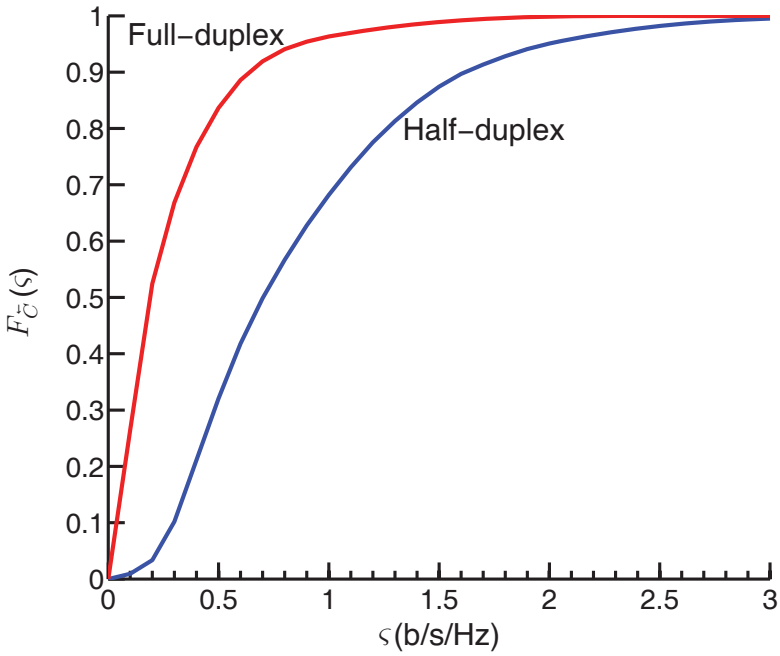

Figure 6.10: CDF of reverse link spectral efficiency for a Vodafone LTE field test network with half-duplex and full-duplex.

interference barriers that have been in place since the inception of wireless communications, chiefly that base stations do not interfere with other base stations. To assess the system-level impact of introducing full-duplex transceivers, we have conducted a stochastic geometry analysis of a full-duplex cellular network and derived expressions for the system-wide distributions of local-average SIR and ergodic spectral efficiency. Variations of the formulation for both single-user and multiuser scenarios have been given. From these expressions, complemented by supporting examples and by simulations on a Vodafone LTE field network, we can conclude the following.

- Full-duplex reverse link is not viable in macrocells due to the excessive interference among base stations. In microcells, where the base-to-base pathloss is higher because of the lower elevations, full-duplex operation may be viable.
- Full-duplex consistently delivers a spectral efficiency gain factor of 1.9 in the forward link of microcell networks. In the

corresponding reverse link, however, full-duplex outperforms half-duplex only if the base stations are apart by at least the critical distance. Thus, full-duplex is at odds with network densification.

For $N > 1$, an interesting variation of the full-duplex architecture considered in our analysis is one where only base stations are full-duplex, while users are half-duplex. Each base station then receives signals from a subset of users while transmitting to another (disjoint) subset. This variation is attractive from a hardware and power consumption vantage, as it eliminates the need for self-interference cancellation at the user devices (where form factors and power are key aspects), and it relaxes the issue of user-user interference. The base-to-base interference, however, is unaffected and thus the bulk of our conclusions continue to apply.

Chapter 7

Conclusion

> Excellence is a continuous process and not an accident.
>
> A. P. J. Abdul Kalam

7.1 Dissertation Summary

This dissertation has advanced the interference models for wireless network analysis and established the fundamental limits of wireless communication systems underpinned by spatial frequency reuse and interference suppression. Based on the analysis, complemented by supporting examples and simulations, we have made progress on the following questions:

1. What is the fundamental role of IA in cellular interference management?
2. How much is the improvement in area spectral efficiency when D2D networks incorporate channel allocation schemes?
3. Is full-duplex communication viable in dense cellular networks?

Interference Alignment

Distributed cooperative schemes such as antenna-domain IA can reduce interference in exchange for a sacrifice in spatial signaling dimensions. Through system-level analysis, IA is found to be beneficial over the standard MIMO spatial multiplexing only in certain

network geometries, corresponding to strong in-cluster and weak out-of-cluster interference. However, these geometries are relatively infrequent and the ensuing improvements in terms of average spectral efficiency for the system are rather small. The above observations have been made under assumptions highly favorable to IA and with a conservative baseline that does not even fully exploit the available CSI. Next, through link-level analysis, the achievable spectral efficiency of pilot-assisted IA has been quantified in the K-user interference channel setting under typical operating conditions such as fading selectivity. The insights obtained from the K-user interference channel apply only to certain geometries of large cellular networks such as cell-edges with high-levels of signal and in-cluster interferences and low-level of out-of-cluster interference. If the channel estimation error and pilot signaling overheads are accounted for, then pilot-assisted IA loses all its advantages over TDMA at vehicular speeds, however remaining somewhat superior at pedestrian speeds. The improvement is minor in the case of FDD, and more significant in the case of TDD. Therefore, the range of operational conditions where IA may be enticing would then be squeezed down very substantially and it might be the case that IA would no longer retain any potential to play a role in cellular interference management.

Channelization Schemes

ITLinQ and FlashLinQ schemes operate by enforcing exclusion regions around transmitters and receivers and avoid the situations of excessive interference in D2D communication networks. Both schemes outperform the unchannelized baseline, with about 20–30% improvement in average area spectral efficiency. The gains are much more sizeable (on the order of seven-fold) for the worst 10% of network geometries. ITLinQ exhibits marginal improvement over FlashLinQ, i.e., the gains in area spectral efficiency are not more than 10% on average. This is in contrast with the claims of the original paper [11] that ITLinQ provides over 100% gain in system spectral efficiency with respect to FlashLinQ. It should be emphasized that, in [11], the tuning of the FlashLinQ parameters was neglected, thus resulting in a conclusion favorable to ITLinQ. Given that there is a growing interest in D2D communication, this information is useful and relevant in a practical sense when implementing any of these advanced channel allocation schemes.

Full-Duplex Communication

The introduction of full-duplex transceivers will disrupt the interference landscape in wireless networks, resulting in a doubling of the co-channel interference sources at each receiver. In the forward link, such additional interference is found to have minor impact and a doubling in spectral efficiency could indeed be approached, especially in microcellular networks. In the reverse link, however, a major difficulty arises in the form of exceedingly strong interference among base stations. This would render full-duplex transmission all but unfeasible in macrocellular networks (unless major countermeasures could be implemented) and undesirable in dense microcellular networks. Only with microcells and sufficient spacing among base stations, such that the base-to-base pathloss exponents are high, does reverse link full duplex pay off. Thus, full duplex does not seem to blend easily with densification.

7.2 Impact of the Work

Based on this thesis work, the following are the positive take-away points for 5G:

- Given its meager gains in spectral efficiencies over standard spatial multiplexing, IA is not a particularly attractive ingredient of 5G. It may, however, have other fruitful applications such as coding solutions for distributed storage exact repair [176–178].
- Due to its incompatibility with network densification and limited system-level benefits for cellular access communication, full duplexing is not expected to play a vital role in 5G wireless systems.
- The potential of D2D communication for 5G wireless systems is promising due to its scalability. Both overlay and underlay options can enhance the area spectral efficiency as long as there exists a reasonable protection against the co-channel interference by means of channel allocation schemes.
- In a nutshell, it is beneficial to concentrate on densifying networks and adding more antennas at the transmitters and receivers, and on utilizing the larger bandwidths available at higher frequencies.

7.3 Future Research Directions

The methodologies and results presented in this dissertation unfold several research avenues of both theoretical and practical interest.

Interference Alignment

Our work settles the inefficacy of IA only in the context of large macrocell networks with dynamic interference patterns. IA might be more favorable to non-cellular network topologies with relatively static environments.

- Indoor local area network, where access points suffer from mutual interference (e.g., apartment area, office building) [179, 180].
- Wearable wireless network, where different devices communicate in and around human bodies in an enclosed space (e.g., commuter train, subway). A finite number of unintended transmitting devices within close proximity create a highly interfering environment [181, 182].

Performance characterizations of IA in the above settings would be desirable.

Channel Allocation Schemes

In all the schemes investigated in the dissertation, power was fixed at each D2D transmitter. Due to the scarcity of power at the battery-operated devices, it is desirable to have power control policies [183, 184], where transmit power levels are adjusted to achieve a specified target SINR at the receivers or to maximize system performance. Power control, an intensely researched topic in the context of wireless networks, can improve spatial frequency reuse by controlling interference in the system.

An improved version of ITLinQ has recently been formulated in [185], which allows for a tighter packing of co-channel D2D links [185]. This scheme, termed ITLinQ+, implements both channel allocation and power control in a distributed fashion. ITLinQ+ is shown (through Monte-Carlo simulations) to improve the system spectral efficiency by 5–20% over ITLinQ in a typical D2D network setup. The analytical characterization of ITLinQ+ could constitute an interesting follow-up within the context of channel allocation schemes.

Full-Duplex Communication

Full-duplex communication is introduced in Chapter 6 without additional base-to-base or user-to-user interference management, and our findings on the potential of full-duplex communication for 5G wireless systems are mostly negative. Further work would be welcome to solidify or tone down these conclusions, and we outline several directions of interest.

- The performance tail of full duplexing in the forward link is curbed by user-to-user interference. Given the availability of multiple channels, users could be parsed onto various sets in ways that avoided excessive interference, and schemes formulated in the context of D2D communication (cf. Chapter 5) could be readily applied.
- In the reverse link, base-to-base interference limits the performance. This issue is well studied in the context of dynamic TDD [171], but for distance base stations. It remains to be seen whether potential solutions such as null forming in elevation [186], cloud radio access network processing [187], or IA (cf. Chapter 3) could achieve sufficient interference suppression. Advantageously, base-to-base links are very stable, hardly subject to fading, but according to our analysis several tens of dB of suppression might be necessary.
- Full duplex improvements in spectral efficiency come at the expense of increased power consumption due to the sophisticated self-interference cancellation circuits [164]. It is thus worth studying full-duplex operation in the context of energy efficiency, a key desideratum for 5G [3, 4].
- Base station antenna patterns in the elevation domain may alleviate base-to-base interference (probably only slightly because their effect on the adjacent base stations is minor). Quantifying this effect would be another interesting refinement of our work.
- The balance between forward link and reverse link traffic, which is immaterial under half-duplex because the corresponding signals do not interfere, becomes relevant with full-duplex. While in the dissertation we have considered balanced traffic, studying the impact of imbalances would be yet another relevant extension.

Apart from the above, one aspect ignored throughout the dissertation is sectorization. Borrowing techniques from [59], the analyses could be extended in that direction. While quantitatively very interesting, however, this extension is not expected to modify the qualitative conclusions in the dissertation.

Appendices

Appendix A

Appendix to Chapter 2

A.1 Proof of Lemma 2.2

Utilizing the PDF $f_{r_n,r_k}(\cdot,\cdot)$ in (2.13) corresponding to $k = N-1$, the joint PDF of r_n and $a_n = r_n/r_{N-1}$ can be computed as

$$f_{r_n,a_n}(r_n,a_n) = f_{r_n,r_{N-1}}(r_n,r_{N-1}) \left| \frac{\partial(r_n,r_{N-1})}{\partial(r_n,a_n)} \right| \tag{A.1}$$

$$= \frac{4(\pi\lambda)^N}{(N-n-2)!\,n!} \left(\frac{r_n^2}{a_n^2} - r_n^2 \right)^{N-n-2} \frac{r_n^{2n+3}}{a_n^3}\, e^{-\frac{\pi\lambda r_n^2}{a_n^2}} \tag{A.2}$$

which reduces to (2.15) after further simplification.

A.2 Proof of Lemma 2.3

Applying Campbell's theorem [51, Theorem 4.1] to expect over the location of all those interferers whose distances lie within $(R_1, R_2]$, we can express $\mathbb{E}[\mathcal{I}]$ as

$$\mathbb{E}\left[\mathcal{I}\right] = 2\pi\lambda \int_{r>R_1}^{R_2} r^{1-\eta}\, \mathrm{d}r \tag{A.3}$$

from which (2.19) follows after solving the integral.

A.3 Proof of Lemma 2.4

Due to the independence of the locations, we can write

$$\mathcal{L}_{\mathcal{I}}(t) = \mathbb{E}\left[e^{-\sum_{k:R_1<r_k<R_2} t\,\beta\, r_k^{-\eta}} \right] \tag{A.4}$$

$$= \mathbb{E}\left[\prod_{k:R_1<r_k<R_2} e^{-t\,\beta\, r_k^{-\eta}}\right] \tag{A.5}$$

Applying the probability generating functional of the PPP [51, Theorem 4.9] to expect over the locations of all those transmitters that lie outside $\mathcal{B}_0(R)$, we can simplify (A.5) as

$$\mathcal{L}_{\mathcal{I}}(t) = \exp\left(-2\pi\lambda \int_{R_1}^{R_2} \left(1 - e^{-t\,\beta\, r^{-\eta}}\right) r\,\mathrm{d}r\right) \tag{A.6}$$

from which (2.21) follows from the variable change $t\,\beta\, r^{-\eta} = \theta$.

A.4 Proof of Lemma 2.5

The CDF of ρ_0 can be expressed as

$$F_{\rho_0}(\gamma) = \mathbb{P}\left[\rho_0 \le \gamma\right] \tag{A.7}$$

$$= \mathbb{P}\left[\frac{1}{\rho_0} \ge 1/\gamma\right] \tag{A.8}$$

$$= 1 - F_{\frac{1}{\rho_0}}\left(1/\gamma\right) \tag{A.9}$$

The closed-form solution of (A.9) is unwieldy in general. Alternatively, we rely on the numerical inversion of the Laplace transform of $F_{1/\rho_0}(\cdot)$, which yields an accurate approximation in a series form for $F_{\rho_0}(\gamma)$ [59].

$$F_{\rho_0}(\gamma) \approx 1 - \gamma\,\frac{e^{\frac{\mathsf{A}}{2}}}{2^{\mathsf{L}}} \sum_{\ell=0}^{\mathsf{L}} \binom{\mathsf{L}}{\ell} \sum_{\mathsf{m}=0}^{\mathsf{M}+b} \frac{(-1)^{\mathsf{m}}}{D_{\mathsf{m}}} \Re\left\{\mathcal{L}_{F_{1/\rho_0}}(t)\right\} \tag{A.10}$$

where $t = \frac{(\mathsf{A}+\mathrm{i}\,2\pi\mathsf{m})\,\gamma}{2}$ while $D_0 = 1$ and $D_{\mathsf{m}} = 1$ for $\mathsf{m} \ge 1$. By utilizing the relation

$$\mathcal{L}_{F_{1/\rho_0}}(t) = \frac{\mathcal{L}_{1/\rho_0}(t)}{t} \tag{A.11}$$

we can rewrite (A.10) as in (2.27).

A.5 Proof of Eq. (2.45)

The link spectral efficiency averaged over all geometries in a cellular network is

$$\bar{C} = \mathbb{E}\left[C(\rho_0)\right] \tag{A.12}$$
$$= \mathbb{E}\left[\mathbb{E}\left[\log_2(1+\mathsf{SIR}_0|\rho_0)\right]\right] \tag{A.13}$$
$$= \mathbb{E}\left[\int_0^\infty \mathbb{P}\left[\log_2(1+\mathsf{SIR}_0|\rho_0) > \varsigma\right] \, \mathrm{d}\varsigma\right] \tag{A.14}$$
$$= \mathbb{E}\left[\int_0^\infty \frac{\log_2 e}{\gamma+1}\left(1 - F_{\mathsf{SIR}_0|\rho_0}(\gamma)\right) \, \mathrm{d}\gamma\right] \tag{A.15}$$
$$= \int_0^\infty \frac{\log_2 e}{\gamma+1}\left(1 - \mathbb{E}\left[F_{\mathsf{SIR}_0|\rho_0}(\gamma)\right]\right) \, \mathrm{d}\gamma \tag{A.16}$$
$$= \int_0^\infty \frac{\log_2 e}{\gamma+1}\mathbb{E}\left[e^{-\gamma/\rho_0}\right] \, \mathrm{d}\gamma \tag{A.17}$$

where the outer and inner expectations in (A.13) are over ρ_0 and over the fading, respectively, while (A.15) follows from the variable change $\varsigma = \log_2(1+\gamma)$. Invoking (2.32) into (A.17), we arrive at (2.45).

Appendix B

Appendix to Chapter 3

B.1 Proof of Proposition 3.1

To obtain the CDF, we need the density function of r_0 conditioned on $a_0 = r_0/r_{K-1}$, which can be obtained, by applying Lemma 2.2 with $\lambda = \lambda_{\mathrm{b}}$, $n = 0$ and $N = K$, as

$$f_{r_0|a_0}(r_0|a_0) = \frac{2\left(\pi\lambda_{\mathrm{b}}\right)^K r_0^{2K-1}}{\Gamma\left(K\right) a_0^{2K}} e^{-\pi\lambda_{\mathrm{b}}(r_0/a_0)^2}. \tag{B.1}$$

Then, (3.19) is obtained by setting $r_{K-1} = r_0/a_0$ in (3.17) and averaging (3.18) over r_0 via the above conditional PDF.

B.2 Proof of Proposition 3.3

First, by applying Lemma 2.2 with $\lambda = \lambda_{\mathrm{b}}$, $n = 0$ and $N = K$, we can express the joint PDF of r_0 and r_{K-1} as

$$f_{r_0,r_{K-1}}(r_0, r_{K-1}) = \frac{4(\pi\lambda_{\mathrm{b}})^K r_0 r_{K-1}}{(K-2)!} e^{-\pi\lambda_{\mathrm{b}} r_{K-1}^2} \left(r_{K-1}^2 - r_0^2\right)^{K-2}. \tag{B.2}$$

Then, the expectation of (3.18) over r_0 and r_{K-1} via (B.2) yields

$$F_{\mathsf{SIR}}(\gamma) = 1 - \int_0^\infty \int_0^{r_{K-1}} e^{-\gamma \frac{2\pi\lambda_{\mathrm{b}}\mathrm{d}}{\eta-2} \frac{r_0^\eta}{r_{K-1}^{\eta-2}}} \frac{4(\pi\lambda_{\mathrm{b}})^K r_0 r_{K-1}}{(K-2)!} e^{-\pi\lambda_{\mathrm{b}} r_{K-1}^2} \cdot \left(r_{K-1}^2 - r_0^2\right)^{K-2} \mathrm{d}r_0 \, \mathrm{d}r_{K-1} \tag{B.3}$$

which, after applying the binomial expansion and solving the inner integral, becomes

$$F_{\mathsf{SIR}}(\gamma) = 1 - \sum_{n=0}^{K-2} \binom{K-2}{n} (-1)^n \frac{4(\pi\lambda_{\mathrm{b}})^K}{\eta\,(K-2)!}\, \alpha_1^{-\frac{2(n+1)}{\eta}} \cdot \int_0^{\infty} \frac{e^{-\pi\lambda_{\mathrm{b}} r_{K-1}^2}}{r_{K-1}^{-1-\nu}}\, \bar{\Gamma}\left(\frac{2(n+1)}{\eta}, \alpha_1 r_{K-1}^2\right) \mathrm{d}r_{K-1} \tag{B.4}$$

where $\alpha_1 = \frac{2\mathsf{d}\gamma\pi\lambda_{\mathrm{b}}}{\eta-2}$ and

$$\nu = 2\left(K - 2 - n + \frac{(n+1)(\eta-2)}{\eta}\right). \tag{B.5}$$

To solve the integral in (B.4), we effect the change of variable $r_{K-1}^2 \to x$ and leverage [89, (6.455.2)] to obtain, after some algebra,

$$F_{\mathsf{SIR}}(\gamma) = 1 - \sum_{n=0}^{K-2} \frac{(-1)^n\,\Gamma(K)}{n!\,(K-2-n)!\,(n+1)}\, (1+\alpha_2\,\gamma)^{-K} \cdot {}_2F_1\left(1, K; 1 + \frac{2(n+1)}{\eta}; \frac{\alpha_2\,\gamma}{1+\alpha_2\,\gamma}\right) \tag{B.6}$$

where $\alpha_2 = \frac{2\mathsf{d}}{\eta-2}$. Finally, we use the transformation formula [89, (9.131.1)] to rewrite (B.6) in the more compact form claimed in (3.21).

B.3 Proof of Proposition 3.4

The proofs of Propositions 3.4 and 3.6 rest on the solution to

$$\mathcal{I}_1(m,y) = \int_0^{\infty} \frac{y^m\,(2^{\gamma}-1)^m}{(1+y\;(2^{\gamma}-1))^{m+K}}\, \mathrm{d}\gamma \tag{B.7}$$

for any reals $m, y \geq 0$. Next, we provide an explicit solution to this integral.

Lemma B.1. For any reals $m, y \geq 0$,

$$\mathcal{I}_1(m,y) = \log_2(e)\, \frac{\Gamma(K)\;\Gamma(m+1)}{\Gamma(K+m+1)}\, {}_2F_1(1, K; m+K+1; 1-y)\,. \tag{B.8}$$

Proof. With a simple change of variable and rescaling,

$$\mathcal{I}_1(m,y) = \frac{\log_2 e}{y^K} \int_0^\infty \frac{e^{-\gamma(K)} \left(1-e^{-\gamma}\right)^m}{\left(1+\frac{1-y}{y}e^{-\gamma}\right)^{m+K}} \,\mathrm{d}\gamma \tag{B.9}$$

which can be solved by virtue of [89, Eq. 3.312.3] giving

$$\begin{aligned}\mathcal{I}_1(m,y) = \frac{\log_2 e}{y^K} \, & \frac{\Gamma(K)\,\Gamma(m+1)}{\Gamma(K+m+1)} \\ & \cdot \, {}_2F_1\left(m+K, K; m+K+1; 1-\frac{1}{y}\right).\end{aligned} \tag{B.10}$$

Transforming the hypergeometric function as per [89, Eq. 9.131.1], (B.10) reduces to (B.8).

□

From (3.30), rewritten as

$$C^{\mathrm{rel}}(a_0) = \mathsf{d} \int_0^\infty \left(1 - F_{\mathsf{SIR}|a_0}(2^\gamma - 1)\right) \,\mathrm{d}\gamma \tag{B.11}$$

with $F_{\mathsf{SIR}|a_0}(\cdot)$ as given in (3.19),

$$C^{\mathrm{rel}}(a_0) = \mathsf{d} \int_0^\infty \left(1 + \frac{2\,a_0^\eta\,\mathsf{d}}{\eta-2}\,(2^\gamma-1)\right)^{-K} \mathrm{d}\gamma \tag{B.12}$$

$$= \mathsf{d}\,\mathcal{I}_1\left(0, \frac{2\,a_0^\eta\,\mathsf{d}}{\eta-2}\right) \tag{B.13}$$

and applying Lemma B.1 with $m=0$ and $y = \frac{2a_0^\eta \mathsf{d}}{\eta-2}$, we obtain the claimed expression in (3.31).

B.4 Proof of Proposition 3.6

Recall that, under joint decoding, the spectral efficiency of IA is that of a $\mathsf{d} \times \mathsf{d}$ Rayleigh-faded MIMO channel with IID entries, which is computed via the marginal distribution of the eigenvalues of a Wishart matrix [105]. Thus,

$$C^{\mathrm{rel}}(a_0) = \mathsf{d} \int_0^\infty F^{\mathsf{c}}_{\omega|a_0}(2^\gamma - 1)\,\mathrm{d}\gamma \tag{B.14}$$

where $F^{\mathrm{c}}_{\omega|a_0}(\cdot)$ is the complementary CDF, conditioned on a_0, of the (unordered) eigenvalues of the Wishart matrix

$$\boldsymbol{Y} = \frac{\rho_0^{\mathrm{IA}}}{d} \boldsymbol{W}_0^* \boldsymbol{H}_0 \boldsymbol{V}_0 \boldsymbol{V}_0^* \boldsymbol{H}_0^* \boldsymbol{W}_0. \tag{B.15}$$

From [105, Eq. 42], the complementary CDF of an (unordered) eigenvalue conditioned on ρ_0^{IA} equals

$$F^{\mathrm{c}}_{\omega|\rho_0^{\mathrm{IA}}}(x) = \frac{1}{\mathsf{d}} \sum_{i=0}^{\mathsf{d}-1} \sum_{j=0}^{i} \sum_{\ell=0}^{2j} \frac{(-1)^\ell \Gamma\left(\ell+1, \frac{\mathsf{d}}{\rho_0^{\mathrm{IA}}} x\right)}{2^{2i-\ell}\ell!} \binom{2i-2j}{i-j} \binom{2j}{j} \binom{2j}{\ell}. \tag{B.16}$$

To obtain $F^{\mathrm{c}}_{\omega|a_0}(\cdot)$, we set $\rho_0^{\mathrm{IA}} = \frac{r_{K-1}^{\eta-2}}{r_0^{\eta}} \frac{\eta-2}{2\pi\lambda_{\mathrm{b}}}$ and $r_{K-1} = r_0/a_0$ in (B.16) and expect over conditional density (B.1) obtaining

$$F^{\mathrm{c}}_{\omega|a_0}(x) = \frac{1}{\mathsf{d}} \sum_{i=0}^{\mathsf{d}-1} \sum_{j=0}^{i} \sum_{\ell=0}^{2j} \frac{(-1)^\ell}{2^{2i-\ell}\ell!} \binom{2i-2j}{i-j} \binom{2j}{j} \binom{2j}{\ell} \mathcal{J}(x) \tag{B.17}$$

where

$$\begin{aligned} \mathcal{J}(x) &= \int_0^\infty \Gamma\left(\ell+1, \frac{2\pi\lambda_{\mathrm{b}} a_0^{\eta-2} r_0^2 \mathsf{d}}{\eta-2} x\right) \frac{2\left(\pi\lambda_{\mathrm{b}}\right)^K r_0^{2K-1}}{\Gamma(K)\, a_0^{2K}} e^{-\pi\lambda_{\mathrm{b}}(r_0/a_0)^2} \mathrm{d}r_0 \\ &= \ell! \sum_{m=0}^{\ell} \frac{1}{m!} \frac{\Gamma(m+K)}{\Gamma(K)} \frac{\left(\frac{2a_0^\eta \mathsf{d}}{\eta-2} x\right)^m}{\left(1+\frac{2a_0^\eta \mathsf{d}}{\eta-2} x\right)^{m+K}} \end{aligned} \tag{B.18}$$

where (B.18) follows from the expansion of the incomplete Gamma function [89, Eq. 8.352.2], which allows solving the integral with the change of variable $r_0^2 \to \mathsf{r}'$.

Combining (B.17) and (B.18) and plugging the resulting expression for $F^{\mathrm{c}}_{\omega|a_0}(\cdot)$ in (B.14), we arrive at

$$\begin{aligned} C^{\mathrm{rel}}(a_0) = &\sum_{i=0}^{\mathsf{d}-1} \sum_{j=0}^{i} \sum_{\ell=0}^{2j} \frac{(-1)^\ell}{2^{2i-\ell}} \binom{2i-2j}{i-j} \binom{2j}{j} \binom{2j}{\ell} \\ &\cdot \sum_{m=0}^{\ell} \frac{1}{m!} \frac{\Gamma(m+K)}{\Gamma(K)} \mathcal{I}_1\left(m, \frac{2\, a_0^\eta\, \mathsf{d}}{\eta-2}\right) \end{aligned} \tag{B.19}$$

where $\mathcal{I}_1(\cdot,\cdot)$ is the integral in Lemma B.1, from which (3.33) follows after further simplifications.

B.5 Proof of Proposition 3.7

The proofs of Propositions 3.7 and 3.8 rest on the solution to

$$\mathcal{I}_2(m,n,y) = \int_0^\infty y^m \left(2^\gamma - 1\right)^m \cdot {}_2F_1\big(K+m, m+\eta'; m+1+\eta'; -y(2^\gamma-1)\big)\, \mathrm{d}\gamma \tag{B.20}$$

for any reals $m, y \geq 0$ and $\eta' = \frac{2(n+1)}{\eta}$ with real $n \geq 0$. Next, we provide an explicit solution to this integral.

Lemma B.2. For any reals $m, y \geq 0$,

$$\mathcal{I}_2(m,n,y) = \frac{(m+\eta')y^{m+1}}{\Gamma(K+m)} \log_2 e \cdot G_{3,3}^{2,3}\left(y \,\middle|\, \begin{matrix} -(m+1), -(m+K), -m-\eta' \\ -(m+1), -1, -m-1-\eta' \end{matrix} \right). \tag{B.21}$$

Proof. The change of variable $(2^\gamma - 1) \to x$ in (B.20) yields

$$\mathcal{I}_2(m,n,y) = \log_2(e)\, y^m \int_0^\infty \frac{x^m}{1+x} \cdot {}_2F_1\big(K+m, m+\eta'; m+1+\eta'; -y\,x\big)\, \mathrm{d}x. \tag{B.22}$$

By virtue of [89, Eq. 9.34.7], the hypergeometric function in (B.22) can be expressed in terms of the Meijer-G function and the resulting integral has the explicit solution in (B.21) according to [89, Eq. 7.811.5]. □

The spectral efficiency is computed as

$$\bar{C} = \mathsf{d} \int_0^\infty \left(1 - F_{\mathsf{SIR}}(2^\gamma - 1)\right) \mathrm{d}\gamma \tag{B.23}$$

with $F_{\mathsf{SIR}}(\cdot)$ as given in (3.21). Plugging (3.21) into (B.23),

$$\bar{C} = \mathsf{d} \sum_{n=0}^{K-2} \frac{(-1)^n\, \Gamma(K)}{n!\,(K-2-n)!\,(n+1)}\, \mathcal{I}_2\left(0, n, \frac{2\mathsf{d}}{\eta - 2}\right) \tag{B.24}$$

where $\mathcal{I}_2(m,n,y)$ was given in Lemma B.2, from which (3.36) follows after replacing $\eta' \to \frac{2(n+1)}{\eta}$ and simplifying.

B.6 Proof of Proposition 3.8

This proof follows an approach similar to the one in Appendix B.4 and some details are thus omitted for brevity. Here, we need to obtain $F_{\omega}^{\mathrm{c}}(\cdot)$, the complementary CDF of the eigenvalues of $\boldsymbol{Y}$ averaged over all possible cluster geometries. To that end, we average $F^{\mathrm{c}}_{\omega|\rho_0^{\mathrm{IA}}}(\cdot)$ in (B.16) over r_0 and r_{K-1} via its joint density, given in (B.2), arriving at

$$F_{\omega}^{\mathrm{c}}(x) = \frac{1}{\mathsf{d}} \sum_{i=0}^{\mathsf{d}-1} \sum_{j=0}^{i} \sum_{\ell=0}^{2j} \frac{(-1)^{\ell}}{2^{2i-\ell}\ell!} \binom{2i-2j}{i-j} \binom{2j}{j} \binom{2j}{\ell} \mathcal{K}(x) \quad \text{(B.25)}$$

where

$$\mathcal{K}(x) = \int_0^{\infty} \int_0^{r_{K-1}} \Gamma\left(\ell+1, \frac{2\pi\lambda_{\mathrm{b}}\mathsf{d}}{\eta-2} \frac{r_0^{\eta}}{r_{K-1}^{\eta-2}} x\right) \frac{4(\pi\lambda_{\mathrm{b}})^K}{(K-2)!} e^{-\pi\lambda_{\mathrm{b}} r_{K-1}^2} \cdot r_0 r_{K-1} \left(r_{K-1}^2 - r_0^2\right)^{K-2} \mathrm{d}r_0 \, \mathrm{d}r_{K-1}. \quad \text{(B.26)}$$

Expanding the incomplete Gamma function as in [89, Eq. 8.352.2], (B.26) turns into a sum where each term is a double integral of the same type that (B.3), solved in Appendix B.2. The same steps are followed here, yielding

$$\mathcal{K}(x) = \frac{2\,\ell!}{\eta} \sum_{m=0}^{\ell} \frac{1}{m!} \sum_{n=0}^{K-2} \frac{(-1)^n \Gamma(K+m)}{n!\,(K-2-n)!\,(m+\eta')} \left(\frac{2\mathsf{d}}{\eta-2} x\right)^m \cdot {}_2F_1\left(K+m, m+\eta'; m+1+\eta'; \frac{-2d}{\eta-2} x\right) \quad \text{(B.27)}$$

where $\eta' = \frac{2(n+1)}{\eta}$.

Combining (B.25) and (B.27) and integrating the result as

$$\bar{C} = \mathsf{d} \int_0^{\infty} F_{\omega}^{\mathrm{c}}(2^{\gamma}-1)\,\mathrm{d}\gamma \quad \text{(B.28)}$$

yields the spectral efficiency

$$\bar{C} = \frac{2}{\eta} \sum_{i=0}^{\mathsf{d}-1} \sum_{j=0}^{i} \sum_{\ell=0}^{2j} \frac{(-1)^{\ell}}{2^{2i-\ell}} \binom{2i-2j}{i-j} \binom{2j}{j} \binom{2j}{\ell} \sum_{m=0}^{\ell} \frac{1}{m!} \cdot \sum_{n=0}^{K-2} \frac{(-1)^n \Gamma(K+m)}{n!\,(K-2-n)!\,(m+\eta')} \mathcal{I}_2\left(m, n, \frac{2\mathsf{d}}{\eta-2}\right) \quad \text{(B.29)}$$

where $\mathcal{I}_2(m,n,y)$ was given in Lemma B.2, from which (3.38) follows after replacing $\eta' \to 2(n+1)/\eta$ and simplifying.

Appendix C

Appendix to Chapter 4

C.1 Proof of Eq. (4.29)

Post-multiplying $\boldsymbol{Y}$ by $\boldsymbol{\Theta}_k^H$, we obtain

$$\boldsymbol{Y}\boldsymbol{\Theta}_k^H = \sqrt{\frac{N_{\mathrm{fb}}\overleftarrow{P}}{KN_{\mathrm{t}}N_{\mathrm{r}}}\left(\frac{N_{\mathrm{pf}}P/N_{\mathrm{t}}}{\sigma_{\mathrm{N}}^2+N_{\mathrm{pf}}P/N_{\mathrm{t}}}\right)^{-1}} \times \underbrace{\begin{bmatrix}\boldsymbol{H}_{k,1}^{\mathrm{r}}\\ \vdots \\ \boldsymbol{H}_{k,K}^{\mathrm{r}}\end{bmatrix}}_{\boldsymbol{H}_k^{\mathrm{r}}} \begin{bmatrix}\hat{\boldsymbol{H}}_{k,1}^{\mathrm{f}} & \cdots & \hat{\boldsymbol{H}}_{k,K}^{\mathrm{f}}\end{bmatrix} + \boldsymbol{Z}\boldsymbol{\Theta}_k^H. \tag{C.1}$$

Given the condition $KN_{\mathrm{t}} \geq N_{\mathrm{r}}$, the application of the orthogonality principle yields the MMSE estimate of the forward channels corresponding to receiver k as

$$\hat{\boldsymbol{H}}_k = \sqrt{\frac{KN_{\mathrm{t}}N_{\mathrm{r}}}{N_{\mathrm{fb}}\overleftarrow{P}}\left(\frac{N_{\mathrm{pf}}P/N_{\mathrm{t}}}{\sigma_{\mathrm{N}}^2+N_{\mathrm{pf}}P/N_{\mathrm{t}}}\right)^{-1}} \cdot \left(\hat{\boldsymbol{H}}_k^{\mathrm{r}H}\hat{\boldsymbol{H}}_k^{\mathrm{r}} + \zeta_1\hat{\boldsymbol{H}}_k^{\mathrm{r}H}\hat{\boldsymbol{H}}_k^{\mathrm{r}} + \zeta_2 I_{N_{\mathrm{r}}}\right)^{-1}\hat{\boldsymbol{H}}_k^{\mathrm{r}}\boldsymbol{Y}\boldsymbol{\Theta}_k^H \tag{C.2}$$

where $\hat{\boldsymbol{H}}_k = \left[\hat{\boldsymbol{H}}_{k,1}, \cdots, \hat{\boldsymbol{H}}_{k,K}\right]$ represents the concatenated estimate of $\boldsymbol{H}_k = \left[\boldsymbol{H}_{k,1}, \cdots, \boldsymbol{H}_{k,K}\right]$ while

$$\zeta_1 = \frac{N_{\mathrm{t}}\sigma_{\mathrm{N}}^2}{PN_{\mathrm{pf}}} \tag{C.3}$$

and

$$\zeta_2 = \left(1+\frac{N_{\mathrm{t}}\sigma_{\mathrm{N}}^2}{PN_{\mathrm{pf}}}\right)\left(\frac{\sigma_{\mathrm{N}}^2 KN_{\mathrm{t}}N_{\mathrm{r}}}{N_{\mathrm{fb}}\overleftarrow{P}} + \frac{N_{\mathrm{r}}\sigma_{\mathrm{N}}^2}{\sigma_{\mathrm{N}}^2+N_{\mathrm{pr}}P/N_{\mathrm{r}}}\right) \tag{C.4}$$

are the MMSE regularization parameters. Define the concatenated estimation error matrix as $\tilde{\boldsymbol{H}}_k = \left[\tilde{\boldsymbol{H}}_{k,1}, \cdots, \tilde{\boldsymbol{H}}_{k,K}\right]$. Since writing $\sigma^2_{\tilde{\boldsymbol{H}}}$ exactly yields rather cumbersome expressions and the MMSE solution approaches the zero-forcing solution at high SNR, the variance of MMSE error is replaced with that of the zero-forcing solution —as done in [165]—which enables neglecting the constants ζ_1 and ζ_2. Then, after further simplifications,

$$\tilde{\boldsymbol{H}}_k = \sqrt{1 + \frac{N_{\mathrm{t}}\sigma_{\mathrm{N}}^2}{N_{\mathrm{pf}}P}}\left[\tilde{\boldsymbol{H}}_k^{\mathrm{f}} + (\hat{\boldsymbol{H}}_k^{\mathrm{r}H}\hat{\boldsymbol{H}}_k^{\mathrm{r}})^{-1}\hat{\boldsymbol{H}}_k^{\mathrm{r}H}\left(1 + \frac{N_{\mathrm{t}}\sigma_{\mathrm{N}}^2}{N_{\mathrm{pf}}P}\tilde{\boldsymbol{H}}_k^{\mathrm{r}}\hat{\boldsymbol{H}}_k^{\mathrm{f}} + \sqrt{\frac{KN_{\mathrm{t}}N_{\mathrm{r}}}{N_{\mathrm{pr}}\overleftarrow{P}}}\boldsymbol{Z}\boldsymbol{\Theta}_k^H\right)\right] \tag{C.5}$$

where the entries of $\tilde{\boldsymbol{H}}_k^{\mathrm{f}}$ are

$$\mathcal{N}_{\mathbb{C}}\left(0, \frac{\sigma_{\mathrm{N}}^2}{\sigma_{\mathrm{N}}^2 + N_{\mathrm{pf}}P/N_{\mathrm{t}}}\right),$$

the entries of $\tilde{\boldsymbol{H}}_k^{\mathrm{r}}$ are

$$\mathcal{N}_{\mathbb{C}}\left(0, \frac{\sigma_{\mathrm{N}}^2}{\sigma_{\mathrm{N}}^2 + N_{\mathrm{pr}}\overleftarrow{P}/N_{\mathrm{r}}}\right)$$

and the entries of $\boldsymbol{Z}$ are uncorrelated $\mathcal{N}_{\mathbb{C}}(0, N_0)$. Utilizing these distributions, the columns of $\tilde{\boldsymbol{H}}_k$ are found to be independent with scaled identity covariance matrices with diagonal entries given by

$$\sigma^2_{\tilde{\boldsymbol{H}}} = \frac{N_{\mathrm{t}}\sigma_{\mathrm{N}}^2}{N_{\mathrm{pf}}P} + \frac{N_0}{(KN_{\mathrm{t}} - N_{\mathrm{r}})\overleftarrow{P}}\left(\frac{N_{\mathrm{r}}^2}{N_{\mathrm{pr}}} + \frac{KN_{\mathrm{t}}N_{\mathrm{r}}}{N_{\mathrm{fb}}}\left(1 + \frac{N_{\mathrm{r}}\sigma_{\mathrm{N}}^2}{N_{\mathrm{pr}}\overleftarrow{P}}\right)\right). \tag{C.6}$$

Again, by invoking the high SNR approximation as earlier and replacing the MMSE estimation error with the zero-forcing estimation error, we obtain the final form as in (4.29).

Appendix D

Appendix to Chapter 5

D.1 Proof of Lemma 5.1

The density of a stationary point process is defined as the ratio of the expected number of points in an arbitrary region $\mathfrak{B}$ to the Lebesgue measure of that region. Using this definition, the density of ITLinQ type I can be written as

$$\lambda_{\Psi_\mathrm{I}} = \frac{1}{\upsilon(\mathfrak{B})}\,\mathbb{E}\left[\sum_{b_k\in\Psi_\mathrm{I}} \mathbb{1}(b_k\in\mathfrak{B})\right] \tag{D.1}$$

$$= \frac{1}{\upsilon(\mathfrak{B})}\,\mathbb{E}\left[\sum_{b_k\in\Phi} \mathbb{1}(e_k=1)\mathbb{1}(b_k\in\mathfrak{B})\right] \tag{D.2}$$

where $\upsilon(\mathfrak{B})$ is the Lebesgue measure of $\mathfrak{B}$ and (D.2) holds due to the construction of Ψ_I, i.e., the process of co-channel transmitter locations for ITLinQ type I. Expanding the expectation in (D.2) by means of the notion of Palm distribution (cf. Section 2.2.3), we obtain

$$\mathbb{E}\left[\sum_{b_k\in\Phi} \mathbb{1}(e_k=1)\mathbb{1}(b_k\in\mathfrak{B})\right] = \int_{\hat{\mathsf{N}}} \sum_{b_k\in\varphi\cap\mathfrak{B}} \mathbb{1}(\hat{\varphi}\in\mathsf{V}_{b_k})\,\hat{\mathsf{P}}(\mathrm{d}\hat{\varphi}) \tag{D.3}$$

$$= \lambda_\mathrm{u}\,\upsilon(\mathfrak{B})\,\hat{\mathsf{P}}_{b_0}(\mathsf{V}) \tag{D.4}$$

where (D.4) follows from the definition of Palm distribution of a marked PPP [51, Section 8.8] while φ and $\hat{\varphi}$ are realizations of Φ and $\hat{\Phi}$, respectively, $\hat{\mathsf{N}}$ is the sample space of $\hat{\Phi}$ and $\hat{\mathsf{P}}_{b_0}(\mathsf{V})$ is the Palm distribution of a stationary marked point process $\hat{\Phi}$ with a

transmitter location conditioned at b_0 and with V the property of $\hat{\Psi}_{\mathrm{I}}$,

$$\mathsf{V} = \mathsf{V}_{b_0} \tag{D.5}$$
$$= \left\{\{b_k\}_{k=1}^{\infty} \cap \mathcal{B}_{u_0}(\mathsf{R}) = \varnothing\right\} \cap \left\{\{u_i\}_{i=1}^{\infty} \cap \mathcal{B}_{b_0}(\mathsf{R}) = \varnothing\right\} \tag{D.6}$$

which represents the channelization condition imposed by ITLinQ type I (cf. Section 5.4.1), with a location conditioned at b_0.

Combining (D.2) and (D.4),

$$\lambda_{\Psi_{\mathrm{I}}} = \lambda_{\mathrm{u}} \hat{\mathsf{P}}_{x_0}(\mathsf{V}) \tag{D.7}$$
$$= \lambda_{\mathrm{u}} \mathbb{P}\left(\hat{\Phi} \in \mathsf{V} | x_0 \in \Phi\right) \tag{D.8}$$
$$= \lambda_{\mathrm{u}} \sum_{n=1}^{N} p_n \mathbb{P}\left(\hat{\Phi} \in \mathsf{V} | x_0 \in \Phi, r_{u_0,b_0} = d_n\right) \tag{D.9}$$

where (D.8) follows from expressing the Palm distribution $\hat{\mathsf{P}}_{b_0}(\mathsf{V})$ in terms of the Palm probability [51, 70], with $\hat{\Phi} \in \mathsf{V}$ meaning that $\hat{\Phi}$ has property V. Recalling (D.6), it can be seen that $\mathbb{P}(\hat{\Phi} \in \mathsf{V} | b_0 \in \Phi, r_{u_0,b_0} = d_n)$ in (D.9) is a function of *(i)* the probability that there exists no co-channel transmitter in the receiver exclusion circle $\mathcal{B}_{u_0}(\mathsf{R}_n)$, and *(ii)* the probability that there exists no co-channel receiver in the transmitter exclusion circle $\mathcal{B}_{b_0}(\mathsf{R}_n)$. Then, conditioned on $r_{u_0,b_0} = d_n$, we have

$$\mathbb{P}(\hat{\Phi} \in \mathsf{V} | b_0 \in \Phi)$$
$$= \mathbb{P}\left(\{\{b_k\}_{k=1}^{\infty} \cap \mathcal{B}_{u_0}(\mathsf{R}_n) = \varnothing\} \cap \{\{v_i\}_{i=1}^{\infty} \cap \mathcal{B}_{b_0}(\mathsf{R}_n) = \varnothing\}\right) \tag{D.10}$$
$$= \mathbb{P}\left(\{u_i\}_{i=1}^{\infty} \cap \mathcal{B}_{b_0}(\mathsf{R}_n) = \varnothing | \{b_k\}_{k=1}^{\infty} \cap \mathcal{B}_{u_0}(\mathsf{R}_n) = \varnothing\right)$$
$$\times \mathbb{P}\left(\{b_k\}_{k=1}^{\infty} \cap \mathcal{B}_{u_0}(\mathsf{R}_n) = \varnothing\right). \tag{D.11}$$

We can affirm that

$$\mathbb{P}\left(\{b_k\}_{k=1}^{\infty} \cap \mathcal{B}_{u_0}(\mathsf{R}_n) = \varnothing\right) = e^{-\pi \lambda_{\mathrm{u}} \mathsf{R}_n^2} \tag{D.12}$$

is the probability that, within a given area, there exists no point of the PPP [51, 70]. Considering Fig. D.1, which illustrates the geometry of the transmitters and receivers of link 0 and link i, we can express the probability $\mathbb{P}\left(\{u_i\}_{i=1}^{\infty} \cap \mathcal{B}_{b_0}(\mathsf{R}_n) = \varnothing\right)$, conditioned on $r_{u_0,b_0} = d_n$ and $\{\{b_k\}_{k=1}^{\infty} \cap \mathcal{B}_{u_0}(\mathsf{R}_n) = \varnothing\}$, as

$$\mathbb{P}\left(\{v_i\}_{i=1}^{\infty} \cap \mathcal{B}_{b_0}(\mathsf{R}_n) = \varnothing\right)$$

$$= \mathbb{P}\left(\cap_{b_i \in \Phi} \{u_i \notin \mathcal{B}_{b_0}(\mathsf{R}_n)\}\right) \tag{D.13}$$

$$= \mathbb{E}\left[\prod_{b_i \in \Phi} \mathbb{1}(u_i \notin \mathcal{B}_{b_0}(\mathsf{R}_n))\right] \tag{D.14}$$

$$= \mathbb{E}\left[\prod_{b_i \in \Phi} \mathbb{E}\left[\mathbb{1}(u_i \notin \mathcal{B}_{b_0}(\mathsf{R}_n))|b_i\right]\right] \tag{D.15}$$

$$= \mathbb{E}\left[\prod_{b_i \in \Phi} \mathbb{P}\left(u_i \notin \mathcal{B}_{b_0}(\mathsf{R}_n)|b_i\right)\right] \tag{D.16}$$

$$= \prod_{\ell=1}^{N} \mathbb{E}\left[\prod_{b_i \in \Phi_\ell} \mathbb{P}\left(u_i \notin \mathcal{B}_{b_0}(\mathsf{R}_n)|b_i\right)\right] \tag{D.17}$$

$$= \exp\left(-\lambda \sum_{\ell=1}^{N} p_\ell \int \left(1 - \mathbb{P}\left(u_i \notin \mathcal{B}_{b_0}(\mathsf{R}_n)|b_i, r_{u_i,b_i} = d_\ell\right)\right) \mathrm{d}b_i\right) \tag{D.18}$$

where Φ_ℓ in (D.17) represents the process of transmitters whose intended link distance is d_ℓ and (D.18) follows from the probability generating functional of the PPP Φ with density λ_{u}; the circular region $\mathcal{B}_{u_0}(\mathsf{R}_n)$ (the shaded circular region in Fig. D.1) is excluded from the integration limit in (D.18) because the transmitters belonging to that region are already deactivated.

As can be seen in Fig. D.1, $\mathbb{P}\left(u_i \notin \mathcal{B}_{b_0}(\mathsf{R}_n)|b_i, r_{u_i,b_i} = d_\ell\right)$ is completely characterized by the distance from the ith link transmitter to the 0th link transmitter r_{b_i,b_0}. First, for $0 < r_{b_i,b_0} \leq |\mathsf{R}_n - d_\ell|$, $\mathbb{P}(u_i \notin \mathcal{B}_{b_0}(\mathsf{R}_n)|b_i, r_{u_i,b_i} = d_\ell) = \mathbb{1}(\mathsf{R}_n < d_\ell)$. Next, by applying the law of cosines to the triangle $b_0 b_i u_i$ in Fig. D.1, we can write

$$r_{u_i,b_0}^2 = r_{b_i,b_0}^2 + d_\ell^2 - 2\, r_{b_i,b_0} d_\ell \cos(\angle b_0 b_i u_i). \tag{D.19}$$

Then, for $|\mathsf{R}_n - d_\ell| < r_{b_i,b_0} \leq \mathsf{R}_n + d_\ell$, we can compute

$$\mathbb{P}\left(u_i \notin \mathcal{B}_{b_0}(\mathsf{R}_n)|b_i, r_{u_i,b_i} = d_\ell\right) = \mathbb{P}\left(r_{u_i,b_0} > \mathsf{R}_n|b_i, r_{u_i,b_i} = d_\ell\right) \tag{D.20}$$

$$= 1 - \frac{1}{\pi} \arccos\left(\frac{r_{b_i,b_0}^2 + d_\ell^2 - \mathsf{R}_n^2}{2\, r_{b_i,b_0} d_\ell}\right) \tag{D.21}$$

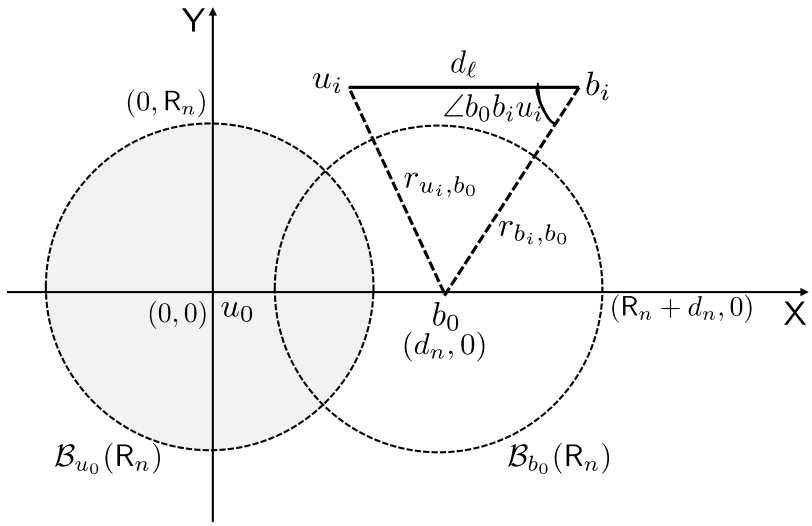

Figure D.1: Illustration of two transmitter-receiver links

where (D.21) follows from invoking r_{u_i,b_0} and then evaluating the probability by making use of the uniform distribution of $\angle b_0 b_i u_i$ in $[0, \pi]$. Finally, for $r_{b_i,b_0} > \mathsf{R}_n + d_\ell$, $\mathbb{P}\left(u_i \notin \mathcal{B}_{b_0}(\mathsf{R}_n) | b_i, r_{u_i,b_i} = d_\ell\right) = 1$.

Putting (D.12) and (D.18) into (D.11), we get

$$\mathbb{P}\left(\hat{\Phi} \in V | b_0 \in \Phi, r_{u_0,b_0} = d_n\right) = \exp\left(-\lambda_{\mathrm{u}} \pi \mathsf{R}_n^2\right) \cdot \exp\left(-\lambda_{\mathrm{u}} \sum_{\ell=1}^{N} p_\ell \int \left(1 - \mathbb{P}\left(u_i \notin \mathcal{B}_{b_0}(\mathsf{R}_n) | b_i, r_{u_i,b_i} = d_\ell\right)\right) \mathrm{d}b_i\right) \tag{D.22}$$

with integration over $\mathcal{B}_{b_0}(\mathsf{R}_n + d_\ell) \backslash \mathcal{B}_{u_0}(\mathsf{R}_n)$ and then, plugging (D.22) into (D.9), we arrive at (5.17), the co-channel link density of ITLinQ type I.

We now derive $\lambda_{\Psi_{\mathrm{II}}}$. Conditioned on mark m, the transmitters (or links) with priority lower than m can be viewed as an independently sampled version of the process Φ and the density of links with a lower mark than m is $m\lambda_{\mathrm{u}}$. By leveraging the derivation of type I density (cf. (5.17)), the probability of retaining a given link with priority m is $e^{-m\lambda_{\mathrm{u}} A(\mathsf{R}_n, d_\ell)}$ with $A(\mathsf{R}_n, d_\ell)$ given in (5.19) . Unconditioning on

m,

$$\lambda_{\Psi_{\mathrm{II}}} = \lambda_{\mathrm{u}} \sum_{n=1}^{N} \int_0^1 e^{-m\lambda_{\mathrm{u}} A(\mathsf{R}_n, d_\ell)} \, \mathrm{d}m \tag{D.23}$$

which yields (5.18), the co-channel link density of ITLinQ type II.

D.2 Proof of Proposition 5.4

The link spectral efficiency averaged over all geometries is computed as

$$\bar{C}(\lambda_{\mathrm{u}}, M, \mu) = \mathbb{E}\left[C(\rho_0)\right] \tag{D.24}$$

where the expectation is over ρ_0. Expanding the above equation

$$\bar{C}(\lambda_{\mathrm{u}}, M, \mu) = \mathbb{E}\left[\mathbb{E}\left[\log_2(1 + \mathsf{SINR}_0 | \rho_0)\right]\right] \tag{D.25}$$

$$= \mathbb{E}\left[\int_0^\infty \mathbb{P}\left[\log_2(1 + \mathsf{SINR}_0 | \rho_0) > \varsigma\right] \, \mathrm{d}\varsigma\right] \tag{D.26}$$

$$= \mathbb{E}\left[\int_0^\infty \frac{\log_2 e}{\gamma + 1} \left(1 - F_{\mathsf{SINR}_0 | \rho_0}(\gamma)\right) \, \mathrm{d}\gamma\right] \tag{D.27}$$

$$= \sum_{n=1}^{N} q_n \int_0^\infty \frac{\log_2 e}{\gamma + 1} \left(1 - F_{\mathsf{SINR}_0 | r_{u_0,b_0} = d_n}(\gamma)\right) \, \mathrm{d}\gamma \tag{D.28}$$

where the outer and inner expectations in (D.25) are over ρ_0 and over the fading, respectively, while (D.27) follows from the variable change $\varsigma = \log_2(1 + \gamma)$ and q_n is the fraction of co-channel links with distance d_n.

To compute the average link spectral efficiency, it is more convenient to replace the average interference $\overline{\sigma^2_{0,\mathrm{out}}}$ with its exact value $\sigma^2_{0,\mathrm{out}}$ in the definition of ρ_0, i.e., we don't apply the averaging over K dominant interferers. This relaxation can only make the model, whose goodness was already validated, even tighter. Then,

$$\rho_0 = \frac{P_{\mathrm{u}} \beta_{\mathrm{u}} \, r_{u_0,b_0}^{-\eta_{\mathrm{u}}}}{\sum_{k=1}^{\infty} P_{\mathrm{u}} \beta_{\mathrm{u}} \, e_k \, r_{u_0,b_k}^{-\eta_{\mathrm{u}}} + \sigma^2_{\mathrm{N}}}. \tag{D.29}$$

The conditional CDF of SINR_0, given $\{r_{u_0,b_k}\}_{k=1}^{\infty}$ and $\{e_k\}_{k=1}^{\infty}$, is

$$F_{\mathsf{SINR}_0 | \rho_0}(\gamma) = 1 - \exp\left[-\gamma \left(\frac{\sigma^2_{\mathrm{N}}}{P_{\mathrm{u}} \beta_{\mathrm{u}} \, r_{u_0,b_0}^{-\eta_{\mathrm{u}}}} + \sum_{k=1}^{\infty} e_k \, r_{u_0,b_k}^{-\eta_{\mathrm{u}}} r_{u_0,b_0}^{\eta_{\mathrm{u}}}\right)\right] \tag{D.30}$$

$$= 1 - \exp\left(-\frac{\gamma}{r_{u_0,b_0}^{-\eta_\mathrm{u}}} \frac{\sigma_\mathrm{N}^2}{P_\mathrm{u}\beta_\mathrm{u}}\right) \prod_{k=1}^{\infty} \exp\left(-\gamma\, e_k\, r_{u_0,b_k}^{-\eta_\mathrm{u}} r_{u_0,b_0}^{\eta_\mathrm{u}}\right). \tag{D.31}$$

First, we average $F_{\mathsf{SINR}_0|\rho_0}(\gamma)$ over the interference, conditioned on $r_{u_0,b_0} = d_n$, to obtain

$$F_{\mathsf{SINR}_0|r_{u_0,b_0}=d_n}(\gamma) = 1 - \exp\left(-\frac{\gamma}{d_n^{-\eta_\mathrm{u}}} \frac{\sigma_\mathrm{N}^2}{P_\mathrm{u}\beta_\mathrm{u}}\right) \cdot \mathbb{E}\left[\prod_{k=1}^{\infty} \exp\left(-\gamma\, e_k\, r_{u_0,b_k}^{-\eta_\mathrm{u}} d_n^{\eta_\mathrm{u}}\right)\right] \tag{D.32}$$

where the expectation is over the process of co-channel transmitter locations Ψ of ITLinQ with density λ_Ψ. To proceed with the analysis, we recall Assumption 1 (cf. Section 5.4.4) that the locations of co-channel transmitters outside the receiver's exclusion region belong to a homogeneous PPP with the density λ_Ψ. At this point, we can apply Lemma 2.4 (cf. (2.22) with $R_1 \to \mathsf{R}_n$, $\eta \to \eta_\mathrm{u}$ and $\lambda \to \lambda_\Psi$) to expect over the locations of all those transmitters that lie outside $\mathcal{B}_{u_0}(\mathsf{R}_n)$ and simplify (D.32) into

$$F_{\mathsf{SINR}_0|r_{u_0,b_0}=d_n}(\gamma) = 1 - \exp\left(-\frac{\gamma}{d_n^{-\eta_\mathrm{u}}} \frac{\sigma_\mathrm{N}^2}{P_\mathrm{u}\beta_\mathrm{u}}\right) \cdot \exp\left(\pi\lambda_\Psi \mathsf{R}_n^2 + \frac{2\pi\lambda_\Psi \gamma^{\frac{2}{\eta_\mathrm{u}}} d_n^2}{\eta_\mathrm{u}} \bar{\Gamma}\left(\frac{-2}{\eta_\mathrm{u}}, \gamma\left(\frac{d_n}{\mathsf{R}_n}\right)^{\eta_\mathrm{u}}\right)\right) \tag{D.33}$$

Next, plugging the resulting conditional CDF $F_{\mathsf{SINR}_0|r_{u_0,b_0}=d_n}(\gamma)$ into (D.28), we obtain the final expression for $\bar{C}(\lambda_\mathrm{u}, M, \mu)$ in (5.30).

Appendix E

Appendix to Chapter 6

E.1 Proof of Proposition 6.1

The distribution of $\vec{\rho}_0$ can be computed over the spatial locations of all interferers in the network. By virtue of Lemma 2.5, the CDF of $\vec{\rho}_0$ can be expressed as

$$F_{\vec{\rho}_0}(\gamma) = 1 - \gamma \, \frac{e^{\frac{\mathsf{A}}{2}}}{2^{\mathsf{L}}} \sum_{\ell=0}^{\mathsf{L}} \binom{\mathsf{L}}{\ell} \sum_{\mathsf{m}=0}^{\mathsf{M}+b} \frac{(-1)^{\mathsf{m}}}{D_{\mathsf{m}}} \Re \left\{ \frac{\mathcal{L}_{1/\vec{\rho}_0}(\iota)}{\iota} \right\}. \tag{E.1}$$

Conditioned on $r_{u_0,b_0} = r_0$, the Laplace transform of $1/\vec{\rho}_0$ is derived as

$$\mathcal{L}_{1/\vec{\rho}_0|r_0}(t) = \mathbb{E}[e^{-t/\vec{\rho}_0}|r_0] \tag{E.2}$$

$$= \mathbb{E}\left[\exp\left(-N \sum_{k=1}^{\infty} \frac{r_{u_0,b_k}^{-\eta}}{r_0^{-\eta}} t - N\varpi_{\mathrm{u}} \sum_{j=1}^{\infty} \frac{r_{u_0,u_j}^{-\eta_{\mathrm{u}}}}{r_0^{-\eta}} t \right) |r_0 \right] \tag{E.3}$$

$$= \mathbb{E}_{\Phi_{\mathrm{b}}}\left[\prod_{k=1}^{\infty} \exp\left(-\frac{r_{u_0,b_k}^{-\eta}}{r_0^{-\eta}} Nt \right) |r_0 \right]$$

$$\cdot \, \mathbb{E}_{\Phi_{\mathrm{u}}}\left[\prod_{j=1}^{\infty} \exp\left(-\frac{r_{u_0,u_j}^{-\eta_{\mathrm{u}}}}{r_0^{-\eta}} N\varpi_{\mathrm{u}} t \right) |r_0 \right] \tag{E.4}$$

$$= \exp\left(\pi\lambda_{\mathrm{b}} r_0^2 + \frac{2\pi\lambda_{\mathrm{b}}}{\eta} r_0^2 (Nt)^{\frac{2}{\eta}} \, \bar{\Gamma}\left(\frac{-2}{\eta}, Nt \right) \right)$$

$$\cdot \exp\left(-\pi N \lambda_{\mathrm{b}} \left(r_0^{\eta} N \varpi_{\mathrm{u}} t \right)^{\frac{2}{\eta_{\mathrm{u}}}} \, \Gamma\left(1 - \frac{2}{\eta_{\mathrm{u}}} \right) \right) \tag{E.5}$$

where (E.2) follows by invoking the definition $\mathcal{L}_{F_{1/\vec{\rho}_0}}$ and then evaluating integration by parts, (E.3) follows from substituting (6.17) in (E.2), (E.4) follows from the fact that the locations of base stations and users are two independent PPPs, and (E.5) follows by separately invoking Lemma 2.4 for base station and user processes Φ_{b} and Φ_{u}, i.e., (2.22) with $R_1 \to r_0$, $\lambda \to \lambda_{\mathrm{b}}$, and (2.23) with $\eta \to \eta_{\mathrm{u}}$ and $\lambda \to N\lambda_{\mathrm{b}}$. Invoking (E.5) into (E.1), we obtain the conditional CDF $F_{\vec{\rho}_0|r_0}(\cdot)$ as in (6.19).

E.2 Proof of Proposition 6.3

By leveraging the derivation of its forward link counterpart, conditioned on $r_{b_0,u_n} = r_n$, $r_{b_0,u_{N-1}} = r_{N-1}$ and $a_n = r_n/r_{N-1}$, the CDF of the reverse link local-average SIR can be expressed as

$$F_{\bar{\rho}_{0,n}|r_n,a_n}(\gamma) = 1 - \gamma \frac{e^{\frac{\mathsf{A}}{2}}}{2^{\mathsf{L}}} \sum_{\ell=0}^{\mathsf{L}} \binom{\mathsf{L}}{\ell} \sum_{\mathsf{m}=0}^{\mathsf{M}+b} \frac{(-1)^{\mathsf{m}}}{D_{\mathsf{m}}} \Re\left\{ \frac{\mathcal{L}_{1/\bar{\rho}_{0,n}|r_n,a_n}(\iota)}{\iota} \right\} \tag{E.6}$$

and the Laplace transform $\mathcal{L}_{1/\bar{\rho}_{0,n}|r_n,a_n}(t)$ is derived as

$$\mathcal{L}_{1/\bar{\rho}_{0,n}|r_n,a_n}(t) = \mathbb{E}[e^{-t/\bar{\rho}_{0,n}}|r_n, a_n] \tag{E.7}$$

$$= \mathbb{E}\left[\exp\left(-\sum_{j=N}^{\infty} \frac{r_{b_0,u_j}^{-\eta}}{r_n^{-\eta}} t - \sum_{k\in\mathcal{K}} \frac{r_{b_0,b_k}^{-\eta_{\mathrm{b}}}}{r_n^{-\eta}} \varpi_{\mathrm{b}}\, t - \sum_{k\notin\mathcal{K}} \frac{r_{b_0,b_k}^{-\eta_{\mathrm{B}}}}{r_n^{-\eta}} \varpi_{\mathrm{B}}\, t\right)\right] \tag{E.8}$$

$$= \mathbb{E}_{\Phi_{\mathrm{u}}}\left[\prod_{j=N}^{\infty} \exp\left(-\frac{r_{b_0,u_j}^{-\eta}}{r_n^{-\eta}}\, t\right)\right] \cdot \mathbb{E}_{\Phi_{\mathrm{b}}}\left[\prod_{k\in\mathcal{K}} \exp\left(-\frac{r_{b_0,b_k}^{-\eta_{\mathrm{b}}}}{r_n^{-\eta}} \varpi_{\mathrm{b}}\, t\right) \prod_{k\notin\mathcal{K}} \exp\left(-\frac{r_{b_0,b_k}^{-\eta_{\mathrm{B}}}}{r_n^{-\eta}} \varpi_{\mathrm{B}}\, t\right)\right] \tag{E.9}$$

$$= \exp\left(\pi N\lambda_{\mathrm{b}} r_{N-1}^2 + \frac{2\pi N\lambda_{\mathrm{b}} r_n^2\, t^{\frac{2}{\eta}}}{\eta} \bar{\Gamma}\left(\frac{-2}{\eta}, \frac{r_n^{\eta}\, t}{r_{N-1}^{\eta}}\right)\right) \cdot \exp\left(\frac{2\pi\lambda_{\mathrm{b}} R_{\mathrm{c}}^2}{\eta_{\mathrm{b}}} \left(E_{\frac{\eta_{\mathrm{b}}+2}{\eta_{\mathrm{b}}}}\left(\frac{r_n^{\eta} \varpi_{\mathrm{b}}\, t}{R_{\mathrm{c}}^{\eta_{\mathrm{b}}}}\right)\right.\right.$$

$$-\kappa^2 E_{\frac{\eta_\mathrm{b}+2}{\eta_\mathrm{b}}}\left(\frac{r_n^\eta \varpi_\mathrm{b}\, t}{(\kappa R_\mathrm{c})^{\eta_\mathrm{b}}}\right)\Bigg)\Bigg)$$
$$\cdot \exp\Bigg(\pi\lambda_\mathrm{b}\kappa^2 R_\mathrm{c}^2$$
$$+\frac{2\pi\lambda_\mathrm{b}}{\eta_\mathrm{B}}\left(r_n^\eta\, \varpi_\mathrm{B}\, t\right)^{\frac{2}{\eta_\mathrm{B}}} \bar{\Gamma}\left(-\frac{2}{\eta_\mathrm{B}}, \frac{r_n^\eta}{R_\mathrm{c}^{\eta_\mathrm{B}}}\, \varpi_\mathrm{B}\, t\right)\Bigg). \tag{E.10}$$

Putting (E.10) into (E.6) with $a_n = r_n/r_{N-1}$, we obtain $F_{\vec{\rho}_{0,n}|r_n,a_n}(\gamma)$ as in (6.28).

E.3 Proof of Proposition 6.5

The user spectral efficiency averaged over all geometries in a full-duplex network is

$$\vec{\bar{C}} = \mathbb{E}\left[\vec{C}(\vec{\rho}_0)\right] \tag{E.11}$$
$$= \mathbb{E}\left[\mathbb{E}\left[\log_2(1+\overrightarrow{\mathsf{SIR}}_0|\vec{\rho}_0)\right]\right] \tag{E.12}$$
$$= \mathbb{E}\left[\int_0^\infty \mathbb{P}\left[\log_2(1+\overrightarrow{\mathsf{SIR}}_0|\vec{\rho}_0) > \varsigma\right]\, \mathrm{d}\varsigma\right] \tag{E.13}$$
$$= \mathbb{E}\left[\int_0^\infty \frac{\log_2 e}{\gamma+1}\left(1 - F_{\overrightarrow{\mathsf{SIR}}_0|\vec{\rho}_0}(\gamma)\right)\, \mathrm{d}\gamma\right] \tag{E.14}$$
$$= \int_0^\infty \frac{\log_2 e}{\gamma+1}\left(1 - \mathbb{E}\left[F_{\overrightarrow{\mathsf{SIR}}_0|\vec{\rho}_0}(\gamma)\right]\right)\, \mathrm{d}\gamma \tag{E.15}$$
$$= \int_0^\infty \frac{\log_2 e}{\gamma+1}\mathbb{E}\left[e^{-\gamma/\vec{\rho}_0}\right]\, \mathrm{d}\gamma \tag{E.16}$$

where the outer and inner expectations in (E.12) are over $\vec{\rho}_0$ and over the fading, respectively, while (E.14) follows from the variable change $\varsigma = \log_2(1+\gamma)$. Invoking (E.5) into (E.16) and then averaging the resulting expression using the density function in (2.14) (with $\lambda = \lambda_\mathrm{b}$), we arrive at (6.38).

E.4 Proof of Proposition 6.8

The per-base station spectral efficiency averaged over all geometries in a full-duplex network is

$$\overleftarrow{\bar{C}} = \sum_{n=0}^{N-1} \mathbb{E}\left[\overleftarrow{\bar{C}}(\overleftarrow{\bar{\rho}}_{0,n})\right] \tag{E.17}$$

$$= \sum_{n=0}^{N-1} \int_0^\infty \frac{\log_2 e}{\gamma+1} \left(1 - \mathbb{E}\left[F_{\overleftarrow{\mathsf{SIR}}_{0,n}|\overleftarrow{\bar{\rho}}_{0,n}}(\gamma)\right]\right) \mathrm{d}\gamma \tag{E.18}$$

$$= \sum_{n=0}^{N-1} \int_0^\infty \frac{\log_2 e}{\gamma+1} \mathbb{E}\left[e^{-\gamma/\overleftarrow{\bar{\rho}}_{0,n}}\right] \mathrm{d}\gamma \tag{E.19}$$

$$= \sum_{n=0}^{N-1} \int_0^\infty \frac{\log_2 e}{\gamma+1} \mathbb{E}\left[\mathbb{E}\left[e^{-\gamma/\bar{\rho}_{0,n}}|r_n, a_n\right]\right] \mathrm{d}\gamma. \tag{E.20}$$

Plugging (E.10) into (E.20) and then averaging the resulting expression by means of the PDF in (2.15) with $\lambda = N\lambda_\mathrm{b}$, we obtain the result in (6.44).

Bibliography

Each reference indicates the pages where it appears.

[1] Cisco System Inc., "Cisco Visual Networking Index: Global mobile data traffic forecast update, 2015-2020," Feb. 2016. 1

[2] Qualcomm Inc., "5G - vision for the next generation of connectivity," May 2015, available online: https://www.qualcomm.com/documents/whitepaper-5g-vision-next-generation-connectivity. 1, 2

[3] F. Boccardi, R. W. Heath Jr., A. Lozano, T. Marzetta, and P. Popovski, "Five disruptive technology directions for 5G," *IEEE Commun. Mag.*, vol. 52, no. 2, pp. 74–80, Feb. 2014. 85, 143

[4] J. G. Andrews, S. Buzzi, W. Choi, S. Hanly, A. Lozano, A. C. K. Soong, and J. C. Zhang, "What will 5G be?" *IEEE J. Select. Areas Commun.*, vol. 32, no. 6, pp. 1065–1082, Jun. 2014. 1, 2, 8, 85, 143

[5] C. E. Shannon, "A mathematical theory of communication," *Bell Syst. Tech. J.*, vol. 27, no. 3, pp. 379–423, Jul. 1948. 2

[6] Qualcomm Inc., "LTE Advanced–evolving and expanding into new frontiers," Aug. 2014, available online: https://www.qualcomm.com/invention/technologies/lte/lte-carrier-aggregation. 3, 8

[7] Z. Pi and F. Khan, "An introduction to millimeter-wave mobile broadband systems," *IEEE Commun. Mag.*, vol. 49, no. 6, pp. 101–107, Jun. 2011. 3

[8] T. S. Rappaport, S. Sun, R. Mayzus, H. Zhao, Y. Azar,

K. Wang, G. N. Wong, J. K. Schulz, M. Samimi, and F. Gutierrez, "Millimeter wave mobile communications for 5G cellular: It will work!" *IEEE Access*, vol. 1, no. 1, pp. 335–349, Aug. 2013.

[9] S. Rangan, T. Rappaport, and E. Erkip, "Millimeter-wave cellular wireless networks: Potentials and challenges," *IEE Proc.*, vol. 102, no. 3, pp. 366–385, Mar. 2014. 3

[10] A. S. A. C. Geng, N. Naderializadeh and S. A. Jafar, "On the optimality of treating interference as noise," *IEEE Trans. Inform. Theory*, vol. 61, no. 4, pp. 1753–1767, Apr. 2015. 4

[11] N. Naderializadeh and A. S. Avestimehr, "ITLinQ: A new approach for spectrum sharing in Device-to-Device communication systems," *IEEE J. Select. Areas Commun.*, vol. 32, no. 6, pp. 1139–1151, Jun. 2014. 5, 10, 86, 88, 90, 91, 140

[12] D. Lee, H. Seo, B. Clerckx, E. Hardouin, D. Mazzarese, S. Nagata, and K. Sayana, "Coordinated Multipoint Transmission and Reception in LTE-advanced: deployment scenarios and operational challenges," *IEEE Commun. Mag.*, vol. 50, no. 2, pp. 148–155, Feb. 2012. 5

[13] M. K. Karakayali, G. J. Foschini, and R. A. Valenzuela, "Network coordination for spectrally efficient communications in cellular systems," *IEEE Wireless Commun. Mag.*, vol. 3, no. 14, pp. 56–61, Aug. 2006. 5

[14] V. Cadambe and S. A. Jafar, "Interference alignment and the degrees of freedom of the K-user interference channel," *IEEE Trans. Inform. Theory*, vol. 54, no. 8, pp. 3425–3441, Aug. 2008. 5, 37

[15] M. Maddah-Ali, A. Motahari, and A. Khandani, "Communication over MIMO X channels: Interference alignment, decomposition, and performance analysis," *IEEE Trans. Inform. Theory*, vol. 54, no. 8, pp. 3457–3470, Aug. 2008. 5, 37

[16] S. A. Jafar, "Interference alignment: A new look at signal dimensions in a communication network," *Foundations and Trends in Communications and Information Theory*, vol. 7, no. 9, pp. 1–136, 2011. 6, 57

[17] S. Catreux, P. F. Driessen, and L. J. Greenstein, "Simulation results for an interference-limited multiple-input multiple-output cellular system," *IEEE Commun. Lett.*, vol. 4, no. 11, pp. 334–336, Nov. 2000. 7

[18] K. Gomadam, V. Cadambe, and S. Jafar, "A distributed nu-

merical approach to interference alignment and applications to wireless interference networks," *IEEE Trans. Inform. Theory*, vol. 57, no. 6, pp. 3309–3322, Jun. 2011. 7, 40, 43

[19] C. Suh and D. Tse, "Interference alignment for cellular networks," in *Proc. Annual Allerton Conf. Commun., Cont., Computing*, Sep. 2008, pp. 1037–1044. 7, 38

[20] C. Suh, M. Ho, and D. Tse, "Downlink interference alignment," *IEEE Trans. Commun.*, vol. 59, no. 9, pp. 2616–2626, Sep. 2011.

[21] D. Aziz, F. Boccardi, and A. Weber, "System-level performance study of interference alignment in cellular systems with base-station coordination," in *Proc. IEEE Int. Symp. Pers., Indoor, Mobile Radio Commun.*, Sydney, Australia, Sep. 2012, pp. 1177–1182. 7

[22] R. Mungara, G. George, and A. Lozano, "System-level performance of distributed cooperation," in *Proc. Annual Asilomar Conf. Signals, Syst., Comp.*, Nov. 2012, pp. 1561–1565. 8, 38

[23] O. E. Ayach, A. Lozano, and R. W. Heath Jr., "On the overhead of interference alignment: Training, feedback, and cooperation," *IEEE Trans. Wireless Commun.*, vol. 11, no. 11, pp. 4192–4203, Nov. 2012. 8, 55, 59, 60, 69, 70

[24] Viavi Solutions Inc., "Extreme non-uniformity of cellular networks – the answer: Small cells," Feb. 2016, available online: http://www.slideshare.net/SmallCellForum1/extreme-nonuniformity-of-cellular-networks-the-answer-small-cells. 8

[25] A. Asadi, Q. Wang, and V. Mancuso, "A survey on device-to-device communication in cellular networks," *IEEE Commun. Surveys Tuts.*, vol. 16, no. 4, pp. 1801–1819, Fourth Quarter 2014. 9

[26] B. Kaufman and B. Aazhang, "Cellular networks with an overlaid device to device network," in *Proc. Annual Asilomar Conf. Signals, Syst., Comp.*, Oct. 2008, pp. 1537–1541. 10, 86

[27] G. Fodor, E. Dahlman, G. Mildh, S. Parkvall, N. Reider, G. Miklós, and Z. Turányi, "Design aspects of network assisted Device-to-Device communications," *IEEE Commun. Mag.*, vol. 50, no. 3, pp. 170–177, Mar. 2012. 85

[28] S. Andreev, A. Pyattaev, K. Johnsson, O. Galinina, and Y. Koucheryavy, "Cellular traffic offloading onto network-assisted Device-to-Device connections," *IEEE Commun. Mag.*, vol. 52, no. 4, pp. 20–31, Apr. 2014. 10, 86

[29] G. George, R. K. Mungara, and A. Lozano, "An analytical framework for Device-to-Device communication in cellular networks," *IEEE Trans. Wireless Commun.*, vol. 14, no. 11, pp. 6297–6310, Nov. 2015. 10, 86, 88, 96

[30] A. Lozano and D. C. Cox, "Integrated dynamic channel assignment and power control in TDMA mobile wireless communication systems," *IEEE J. Select. Areas Commun.*, vol. 17, pp. 2031–2040, Nov. 1999. 10

[31] X. Wu, S. Tavildar, S. Shakkottai, T. Richardson, J. Li, R. Laroia, and A. Jovicic, "FlashLinQ: A synchronous distributed scheduler for peer-to-peer ad hoc networks," *IEEE/ACM Trans. Networking*, vol. 21, no. 4, pp. 1215–1228, Aug. 2013. 10, 86, 87, 105

[32] M. Duarte and A. Sabharwal, "Full-duplex wireless communications using off-the-shelf radios: Feasibility and first results," in *Proc. Annual Asilomar Conf. Signals, Syst., Comp.*, Pacific Grove, CA, Nov. 2010, pp. 1558–1562. 11, 111

[33] J. I. Choi, M. Jain, K. Srinivasan, P. Levis, and S. Katti, "Achieving single channel, full duplex wireless communication," in *Proc. ACM int. conf. on Mobile comp. and net.*, Sep. 2010, pp. 1–12.

[34] M. Jain, J. I. Choi, T. Kim, D. Bharadia, S. Seth, K. Srinivasan, P. Levis, S. Katti, and P. Sinha, "Practical, real-time, full duplex wireless," in *Proc. ACM int. conf. on Mobile comp. and net.*, Sep. 2011, pp. 301–312.

[35] D. Bharadia, E. McMilin, and S. Katti, "Full duplex radios," in *Proc. ACM SIGCOMM*, vol. 43, no. 4, Aug. 2013, pp. 375–386. 11, 111

[36] S. Hong, J. Brand, J. Choi, M. Jain, J. Mehlman, S. Katti, and P. Levis, "Applications of self-interference cancellation in 5G and beyond," *IEEE Commun. Mag.*, vol. 52, no. 2, pp. 114–121, Feb. 2014. 11, 111

[37] Z. Zhang, X. Chai, K. Long, A. V. Vasilakos, and L. Hanzo, "Full duplex techniques for 5G networks: self-interference cancellation, protocol design, and relay selection," *IEEE Commun. Mag.*, vol. 53, no. 5, pp. 128–137, May 2015.

[38] X. Zhang, W. Cheng, and H. Zhang, "Full-Duplex transmission in PHY and MAC layers for 5G mobile wireless networks," *IEEE Wireless Commun. Mag.*, vol. 22, no. 5, pp. 112–121, Oct. 2015. 11, 111

[39] D. Kim, H. Lee, and D. Hong, "A survey of in-band full-duplex transmission: From the perspective of PHY and MAC layers," *IEEE Commun. Surveys Tuts.*, vol. 17, no. 4, pp. 2017–2046, FourthQuarter 2015. 11, 111

[40] Z. Tong and M. Haenggi, "Throughput analysis for wireless networks with full-duplex radios," in *Proc. IEEE Wireless Commun. and Networking Conf.*, Mar. 2015, pp. 717–722. 11, 112

[41] M. Mohammadi, H. A. Suraweera, Y. Cao, I. Krikidis, and C. Tellambura, "Full-duplex radio for uplink/downlink wireless access with spatially random nodes," *IEEE Trans. Commun.*, vol. 63, no. 12, pp. 5250–5266, Dec. 2015. 112

[42] C. Psomas and I. Krikidis, "Outage analysis of full-duplex architectures in cellular networks," in *Proc. IEEE Veh. Technol. Conf.*, May 2015, pp. 1–5. 112

[43] S. Goyal, P. Liu, S. Hua, and S. Panwar, "Analyzing a full-duplex cellular system," in *Proc. Conf. Inform. Sciences Syst. (CISS)*, Mar. 2013, pp. 1–6. 112

[44] J. Lee and T. Q. S. Quek, "Hybrid full-/half-duplex system analysis in heterogeneous wireless networks," *IEEE Trans. Wireless Commun.*, vol. 15, no. 5, pp. 2883–2895, May 2015. 11, 112

[45] S. Musa and W. Wasylkiwskyj, "Co-channel interference of spread spectrum systems in a multiple user environment," *IEEE Trans. Commun.*, vol. 26, no. 10, pp. 1405–1413, Oct. 1978. 12, 22

[46] E. S. Sousa and J. A. Silvester, "Optimum transmission ranges in a direct-sequence spread-spectrum multihop packet radio network," *IEEE J. Select. Areas Commun.*, vol. 8, no. 5, pp. 762–771, Jun. 1990.

[47] S. Weber and J. G. Andrews, "Transmission capacity of wireless networks," *Foundations and Trends in Networking*, vol. 7, no. 2-3, pp. 109–281, 2012. 12, 22

[48] J. G. Andrews, F. Baccelli, and R. K. Ganti, "A tractable approach to coverage and rate in cellular networks," *IEEE Trans. Commun.*, vol. 59, no. 11, pp. 3122–3134, Nov. 2011. 12, 22, 30

[49] J. G. Andrews, R. K. Ganti, M. Haenggi, N. Jindal, and S. Weber, "A primer on spatial modeling and analysis in wireless networks," *IEEE Commun. Mag.*, vol. 48, pp. 156–163, Nov.

2010. 12

[50] M. Haenggi, J. G. Andrews, F. Baccelli, O. Dousse, and M. Franceschetti, "Stochastic geometry and random graphs for the analysis and design of wireless networks," *IEEE J. Select. Areas Commun.*, vol. 27, no. 7, pp. 1029–1046, May 2009.

[51] M. Haenggi, *Stochastic Geometry for Wireless Networks.* Cambridge, U. K.: Cambridge Univ. Press, 2012. 19, 22, 24, 25, 26, 116, 147, 148, 159, 160

[52] H. S. Dhillon, R. K. Ganti, F. Baccelli, and J. G. Andrews, "Modeling and analysis of K-tier downlink heterogeneous cellular networks," *IEEE J. Select. Areas Commun.*, vol. 30, no. 3, pp. 550–560, Apr. 2012. 22

[53] S. Mukherjee, "Distribution of downlink SINR in heterogeneous cellular networks," *IEEE J. Select. Areas Commun.*, vol. 30, no. 3, pp. 575–585, Apr. 2012. 22

[54] S. Singh, H. S. Dhillon, and J. G. Andrews, "Offloading in heterogeneous networks: Modeling, analysis, and design insights," *IEEE Trans. Wireless Commun.*, vol. 12, no. 5, pp. 2484–2497, May 2013.

[55] H. ElSawy, E. Hossain, and M. Haenggi, "Stochastic geometry for modeling, analysis, and design of multi-tier and cognitive cellular wireless networks: A survey," *IEEE Commun. Surveys Tuts.*, vol. 15, no. 3, pp. 996–1019, Third Quarter 2013.

[56] F. Baccelli, B. Blaszczyszyn, and F. Tournois, "Downlink admission/congestion control and maximal load in CDMA networks," in *Proc. IEEE INFOCOM*, vol. 1, Mar. 2003, pp. 723–733. 22

[57] C. H. Lee and M. Haenggi, "Interference and outage in Poisson cognitive networks," *IEEE Trans. Wireless Commun.*, vol. 11, no. 4, pp. 1392–1401, Apr. 2012. 22, 86, 87

[58] A. Guo and M. Haenggi, "Asymptotic deployment gain: A simple approach to characterize the SINR distribution in general cellular networks," *IEEE Trans. Commun.*, vol. 63, no. 3, pp. 962–976, Mar. 2015.

[59] B. Blaszczyszyn and M. Karray, "Spatial distribution of the SINR in Poisson cellular networks with sector antennas," *IEEE Trans. Wireless Commun.*, vol. 15, no. 1, pp. 581–593, Jan. 2016. 12, 28, 144, 148

[60] A. Lozano and N. Jindal, "Are yesterday's information-

theoretic fading models and performance metrics adequate for the analysis of today's wireless systems?" *IEEE Commun. Mag.*, vol. 50, no. 11, pp. 210–217, Nov. 2012. 12

[61] R. K. Mungara, D. Morales-Jiménez, and A. Lozano, "System-level performance of interference alignment," in *Proc. IEEE Global Commun. Conf.*, Dec. 2014, pp. 3977–3982. 14

[62] ——, "System-level performance of interference alignment," *IEEE Trans. Wireless Commun.*, vol. 14, no. 2, pp. 1060–1070, Feb. 2015. 14

[63] R. K. Mungara, G. George, and A. Lozano, "Pilot-assisted interference alignment in time-selective fading channels," in *Proc. IEEE Global Commun. Conf.*, Dec. 2013, pp. 3977–3982. 15

[64] ——, "Overhead and spectral efficiency of pilot-assisted interference alignment in time-selective fading channels," *IEEE Trans. Wireless Commun.*, vol. 13, no. 9, pp. 4884–4895, Sep. 2014. 15

[65] R. K. Mungara, X. Zhang, A. Lozano, and R. W. Heath Jr., "On the spatial spectral efficiency of ITLinQ," in *Proc. Annual Asilomar Conf. Signals, Syst., Comp.*, Nov. 2014, pp. 1806–1810. 15

[66] ——, "Performance evaluation of ITLinQ and FlashLinQ for overlaid device-to-device communication," in *Proc. IEEE ICC Workshop Device-to-Device Commun. Cell. Wireless Netw. (ICC'15)*, Jun. 2015, pp. 596–601.

[67] ——, "Analytical characterization of ITLinQ: Channel allocation for Device-to-Device communication networks," *IEEE Trans. Wireless Commun.*, vol. 15, no. 5, pp. 3603–3615, May 2016. 15

[68] R. K. Mungara and A. Lozano, "Interference surge in full-duplex wireless systems," in *Proc. Annual Asilomar Conf. Signals, Syst., Comp.*, Nov., pp. 21–25. 15, 129

[69] R. K. Mungara, I. Thibault, and A. Lozano, "Full-duplex MIMO in cellular networks: System-level performance," *IEEE Trans. Wireless Commun.*, 2016, submitted. 15

[70] D. Stoyan, W. S. Kendall, and J. Mecke, *Stochastic Geometry and its Applications*. New York, USA: John Wiley & Sons Ltd, 1995. 19, 24, 26, 160

[71] A. F. Molisch, "A generic model for MIMO wireless propagation channels in macro- and microcells," *IEEE Trans. Signal*

Processing, vol. 52, no. 1, pp. 61–71, Jan. 2004. 20, 117

[72] C. C. Chan and S. V. Hanly, "Calculating the outage probability in a CDMA network with spatial poisson traffic," *IEEE Trans. Veh. Technol.*, vol. 50, no. 1, pp. 183–204, Jan. 2001. 22, 28

[73] M. Z. Win, P. C. Pinto, and L. A. Shepp, "A mathematical theory of network interference and its applications," *Proc. IEEE*, vol. 97, no. 2, pp. 205–230, Feb. 2009. 22

[74] A. Ghasemi and E. S. Sousa, "Interference aggregation in spectrum-sensing cognitive wireless networks," *IEEE J. Select. Topics Signal Processing*, vol. 2, no. 1, pp. 41–56, Feb. 2008. 22, 28

[75] V. Chandrasekhar and J. G. Andrews, "Uplink capacity and interference avoidance for two-tier femtocell networks," *IEEE Trans. Wireless Commun.*, vol. 8, no. 7, pp. 3498–3509, Jul. 2009. 22

[76] A. Guo and M. Haenggi, "Spatial stochastic models and metrics for the structure of base stations in cellular networks," *IEEE Trans. Wireless Commun.*, vol. 12, no. 11, pp. 5800–5812, 2013. 22

[77] N. Deng, W. Zhou, and M. Haenggi, "The Ginibre point process as a model for wireless networks with repulsion," *IEEE Trans. Wireless Commun.*, vol. 14, no. 1, pp. 107–121, Jan. 2015.

[78] M. Afshang and H. S. Dhillon, "Spatial modeling of device-to-device networks: Poisson cluster process meets Poisson hole process," in *Proc. Annual Asilomar Conf. Signals, Syst., Comp.*, Pacific Grove, CA, Nov. 2015, pp. 317–321.

[79] C. Saha, M. Afshang, and H. S. Dhillon, "Enriched K-tier HetNet model to enable the analysis of user-centric small cell deployments," available online: http://arxiv.org/abs/1606.06223/. 22

[80] B. Blaszczyszyn, M. K. Karray, and H. P. Keeler, "Wireless networks appear poissonian due to strong shadowing," *IEEE Trans. Wireless Commun.*, vol. 14, no. 8, pp. 4379–4390, Aug. 2015. 22, 27, 90

[81] H. P. Keeler, N. Ross, and A. Xia, "When do wireless network signals appear Poisson?" 2014, available online: http://arxiv.org/abs/1411.3757/.

[82] G. George, R. K. Mungara, A. Lozano, and M. Haenggi., "Er-

godic spectral efficiency in MIMO cellular networks," *IEEE Trans. Wireless Commun.*, 2016, submitted. 22, 27, 90

[83] A. Baddeley, I. Bárány, R. Schneider, and W. Weil, *Stochastic Geometry*. Heidelberg: Springer, 2007. 23

[84] M. Haenggi, "On distances in uniformly random networks," *IEEE Trans. Inform. Theory*, vol. 51, no. 10, pp. 3584–3586, Oct. 2005. 25

[85] F. J. Martín-Vega, F. J. López-Martínez, G. Gomez, and M. C. Aguayo-Torres, "Multi-user coverage probability of uplink cellular systems: A stochastic geometry approach," in *Proc. IEEE Global Commun. Conf.*, Dec. 2014, pp. 3989–3994. 25

[86] J. Guo, S. Durrani, and X. Zhou, "Outage probability in arbitrarily-shaped finite wireless networks," *IEEE Trans. Commun.*, vol. 62, no. 2, pp. 699–712, Feb. 2014. 28

[87] J. Abate and W. Whitt, "Numerical inversion of Laplace transforms of probability distributions," *ORSA J. Compt.*, vol. 7, no. 1, pp. 36–43, 1995. 29

[88] C. A. O'cinneide, "Euler summation for Fourier series and Laplace transform inversion," *Commun. Statist. -Stochastic Models*, vol. 13, no. 2, pp. 315–337, 1997. 29

[89] I. S. Gradshteyn and I. M. Ryzhik, *Table of Integrals, Series, and Products*, 7th ed. San Diego: Academic Press, 2007. 29, 49, 128, 152, 153, 154, 155, 156

[90] R. W. Heath Jr., M. Kountouris, and T. Bai, "Modeling heterogeneous network interference using Poisson point processes," *IEEE Trans. Signal Processing*, vol. 61, no. 16, pp. 4114–4126, Aug. 2013. 30

[91] A. Lapidoth and S. Shamai, "Fading channels: how perfect need "perfect side information" be?" *IEEE Trans. Inform. Theory*, vol. 48, no. 5, pp. 1118–1134, May 2002. 31

[92] I. Shomorony and A. S. Avestimehr, "Worst-case additive noise in wireless networks," *IEEE Trans. Inform. Theory*, vol. 59, no. 6, pp. 3833–3847, Jun. 2013. 31

[93] M. Haenggi, "On distances in uniformly random networks," *IEEE Trans. Inform. Theory*, vol. 51, no. 10, pp. 3584–3586, Oct. 2005. 33, 99

[94] W. C. Y. Lee, "Estimate of channel capacity in Rayleigh fading environments," *IEEE Trans. Veh. Technol.*, vol. 39, no. 3, pp. 187–189, Aug. 1990. 34, 46, 62

[95] L. Ozarow, S. Shamai, and A. D. Wyner, "Information theoretic considerations for cellular mobile radio," *IEEE Trans. Veh. Technol.*, vol. 43, no. 2, pp. 359–378, May 1994. 34, 46, 62

[96] A. Lozano, R. W. Heath Jr., and J. G. Andrews, "Fundamental limits of cooperation," *IEEE Trans. Inform. Theory*, vol. 59, no. 9, pp. 5213–5226, Sep. 2013. 38

[97] A. Papadogiannis, D. Gesbert, and E. Hardouin, "A dynamic clustering approach in wireless networks with multi-cell cooperative processing," in *Proc. IEEE Int. Conf. Commun.*, May 2008, pp. 4033–4037. 38

[98] N. Lee, D. Morales-Jimenez, A. Lozano, and R. W. Heath Jr., "Spectral efficiency of dynamic coordinated beamforming: A stochastic geometry approach," *IEEE Trans. Wireless Commun.*, vol. 14, no. 1, pp. 230–241, Jan. 2015. 38, 40

[99] L. Ruan, V. K. N. Lau, and M. Z. Win, "The feasibility conditions for interference alignment in MIMO networks," *IEEE Trans. Signal Processing*, vol. 61, no. 8, pp. 2066–2077, Nov. 2013. 40

[100] K. Gulati, B. L. Evans, J. G. Andrews, and K. R. Tinsley, "Statistics of co-channel interference in a field of Poisson and Poisson-Poisson clustered interferers," *IEEE Trans. Signal Processing*, vol. 58, no. 12, pp. 6207–6222, Dec. 2010. 40

[101] B. Nosrat-Makouei, J. G. Andrews, R. W. Heath Jr., and R. K. Ganti, "MIMO interference alignment in random access networks," in *Proc. Annual Asilomar Conf. Signals, Syst., Comp.*, Nov. 2011, pp. 641–645.

[102] N. Pappas and M. Kountouris, "Performance analysis of distributed cooperation under uncoordinated network interference," in *Proc. IEEE Int. Conf. Acoust., Speech, Signal Processing*, May 2014, pp. 6181–6185.

[103] M. D. Renzo and P. Guan, "A mathematical framework to the computation of the error probability of downlink MIMO cellular networks by using stochastic geometry," *IEEE Trans. Commun.*, vol. 62, no. 8, pp. 2860–2879, Aug. 2014. 40

[104] F. Beukers, "Gauss' hypergeometric function," in *Arithmetic and geometry around hypergeometric functions*, ser. Progress in Mathematics. Switzerland: Birkhäuser Verlag Basel, 2007, vol. 260, pp. 23–42. 45

[105] H. Shin and J. H. Lee, "Capacity of multiple-antenna fading channels: spatial fading correlation, double scattering, and keyhole," *IEEE Trans. Inform. Theory*, vol. 49, no. 10, pp. 2636–2647, Oct. 2003. 47, 153, 154

[106] M. Maddah-Ali and D. Tse, "Completely stale transmitter channel state information is still very useful," *IEEE Trans. Inform. Theory*, vol. 58, no. 7, pp. 4418–4431, Jul. 2012. 57

[107] R. Tresch and M. Guillaud, "Cellular interference alignment with imperfect channel knowledge," in *Proc. IEEE Int. Conf. Commun.*, Jun. 2009, pp. 1–5. 58, 64

[108] B. Nosrat-Makouei, J. G. Andrews, and R. W. Heath Jr., "MIMO interference alignment over correlated channels with imperfect CSI," *IEEE Trans. Signal Processing*, vol. 59, no. 6, pp. 2783–2794, Jun. 2011. 58

[109] J. Reitterer and M. Rupp, "Interference alignment in UMTS Long Term Evolution," in *Proc. European Sign. Proc. Conf.*, Barcelona, Spain, Sep. 2011, pp. 1094–1098. 58

[110] B. Hassibi and B. M. Hochwald, "How much training is needed in multiple-antenna wireless links?" *IEEE Trans. Inform. Theory*, vol. 49, no. 4, pp. 951–963, Apr. 2003. 58

[111] B. Xie, Y. Li, H. Minn, and A. Nosratinia, "Interference alignment under training and feedback constraints," in *Proc. IEEE Global Commun. Conf.*, Dec. 2011, pp. 1–6. 58

[112] A. Lozano, J. G. Andrews, and R. W. Heath Jr., "Spectral efficiency limits in pilot-assisted cooperative communications," in *Proc. IEEE Int. Symp. Inform. Theory*, Jul. 2012. 58

[113] J. Thukral and H. Bölcskei, "Interference alignment with limited feedback," in *Proc. IEEE Int. Symp. Inform. Theory*, Jun. 2009, pp. 1759–1763. 58, 59

[114] R. T. Krishnamachari and M. K. Varanasi, "Interference alignment under limited feedback for MIMO interference channels," in *Proc. IEEE Int. Symp. Inform. Theory*, Jun. 2010, pp. 619–623. 59

[115] M. Rezaee and M. Guillaud, "Limited feedback for interference alignment in the K-user MIMO interference channel," in *Proc. IEEE Inform. Theory Workshop*, Sep. 2012, pp. 667–671. 59

[116] O. E. Ayach and R. W. Heath Jr., "Interference alignment with analog channel state feedback," *IEEE Trans. Wireless Commun.*, vol. 11, no. 2, pp. 626–636, Feb. 2012. 58, 59, 69,

70

[117] N. Jindal, "MIMO broadcast channels with finite-rate feedback," *IEEE Trans. Inform. Theory*, vol. 52, no. 11, pp. 5045–5060, Nov. 2006. 59

[118] W. Santipach and M. L. Honig, "Capacity of beamforming with limited training and feedback," in *Proc. IEEE Int. Symp. Inform. Theory*, Jul. 2006, pp. 376–380. 59

[119] ——, "Optimization of training and feedback overhead for beamforming over block fading channels," *IEEE Trans. Inform. Theory*, vol. 56, no. 12, pp. 6103–6115, Dec. 2010.

[120] M. Kobayashi, N. Jindal, and G. Caire, "Traning and feedback optimization for multiuser MIMO downlink," *IEEE Trans. Commun. Syst.*, vol. 59, no. 8, pp. 2228–2240, Aug. 2011. 59

[121] Q. Sun, D. C. Cox, H. C. Huang, and A. Lozano, "Estimation of continuous flat-fading MIMO channels," *IEEE Trans. Wireless Commun.*, vol. 1, no. 4, pp. 549–553, oct 2002. 59

[122] V. Pohl, P. H. Nguyen, V. Jungnickel, and C. V. Helmolt, "Continuous flat-fading MIMO channels: Achievable rate and optimal length of the training and data phases," *IEEE Trans. Wireless Commun.*, vol. 4, no. 4, pp. 1889–1900, Jul. 2005. 74

[123] N. Jindal and A. Lozano, "A unified treatment of optimum pilot overhead in multipath fading channels," *IEEE Trans. Commun.*, vol. 58, no. 10, pp. 2939–2948, oct 2010. 59, 77

[124] A. Lapidoth and S. Shamai, "Fading channels: How perfect need perfect side information be?" *IEEE Trans. Inform. Theory*, vol. 48, no. 5, pp. 1118–1134, May 2002. 64

[125] M. Medard, "The effect upon channel capacity in wireless communications of perfect and imperfect knowledge of the channel," *IEEE Trans. Inform. Theory*, vol. 46, no. 3, pp. 933–946, May 2000. 64

[126] A. Lozano, "Interplay of spectral efficiency, power and Doppler spectrum for reference-signal-assisted wireless communication," *IEEE Trans. on Wireless Communications*, vol. 7, no. 12, pp. 5020–5029, Dec. 2008. 64, 82

[127] T. Marzetta, "BLAST training: estimating channel characteristics for high capacity space-time wireless," in *Proc. Annual Allerton Conf. Commun., Cont., Computing*, vol. 37, Sep. 1999, pp. 958–966. 68

[128] T. L. Marzetta and B. M. Hochwald, "Fast transfer of channel state information in wireless systems," *IEEE Trans. Signal*

Processing, vol. 54, no. 4, pp. 1268–1278, Apr. 2006. 69

[129] A. Lozano, A. M. Tulino, and S. Verdú, "High-SNR power offset in multiantenna communication," *IEEE Trans. Inform. Theory*, vol. 51, no. 12, pp. 4134–4151, Dec. 2005. 74

[130] A. Ghosh, J. Zhang, J. G. Andrews, and R. Muhamed, *Fundamentals of LTE*. Prentice-Hall, 2010. 76

[131] Y. Lin and Y. Hsu, "Multihop cellular: A new architecture for wireless communications," in *Proc. IEEE INFOCOM*, vol. 3, Mar. 2000, pp. 1273–1282. 85

[132] K. Doppler, M. Rinne, C. Wijting, C. B. Ribeiro, and K. Hugl, "Device-to-Device communication as an underlay to LTE-advanced networks," *IEEE Commun. Mag.*, vol. 47, no. 12, pp. 42–49, Dec. 2009.

[133] L. Lei, Z. Zhong, C. Lin, and X. Shen, "Operator controlled Device-to-Device communications in LTE-advanced networks," *IEEE Trans. Wireless Commun.*, vol. 19, no. 3, pp. 96–104, Jun. 2012.

[134] 3GPP TR 22.803 V1.0.0, "Feasibility Study for Proximity Services (ProSe) (Release 12)," 3rd Generation Partnership Project 3GPP, www.3gpp.org, Tech. Rep., Aug. 2012. 85

[135] J. Seppälä, T. Koskela, T. Chen, and S. Hakola, "Network controlled Device-to-Device (D2D) and cluster multicast concept for LTE and LTE-A networks," in *Proc. IEEE Wireless Commun. and Networking Conf.*, Mar. 2011, pp. 986–991. 85

[136] X. Lin, R. Ratasuk, A. Ghosh, and J. G. Andrews, "Modeling, analysis, and optimization of multicast Device-to-Device transmissions," *IEEE Trans. Wireless Commun.*, vol. 13, no. 8, pp. 4346–4359, Aug. 2014. 85

[137] N. Golrezaei, A. Molisch, A. G. Dimakis, and G. Caire, "Femtocaching and Device-to-Device collaboration: A new architecture for wireless video distribution," *IEEE Commun. Mag.*, vol. 51, no. 4, pp. 142–149, Apr. 2013. 85

[138] N. Golrezaei, P. Mansourifard, A. Molisch, and A. G. Dimakis, "Base-station assisted Device-to-Device communications for high-throughput wireless video networks," *IEEE Trans. Wireless Commun.*, vol. 13, no. 7, pp. 3665–3676, Jul. 2014. 85

[139] X. Bao, U. Lee, I. Rimac, and R. R. Choudhury, "Data Spotting: Offloading cellular traffic via managed Device-to-Device data transfer at data spots," *ACM SIGMOBILE Mobile Comput. Commun. Rev.*, vol. 14, no. 3, pp. 37–39, Jul. 2010. 85,

86

[140] N. K. Pratas and P. Popovski, "Underlay of low-rate machine-type D2D links on downlink cellular links," in *Proc. IEEE ICC Workshop on M2M Communications for Next Generation IoT*, Jun. 2014, pp. 423–428. 85

[141] C. Hsu and H. Hsieh, "Design and analysis for effective proximal discovery in Machine-to-Machine wireless networks," in *Proc. IEEE ICC Workshop on M2M Communications for Next Generation IoT*, Jun. 2014, pp. 477–482. 85

[142] M. S. Corson, R. Laroia, J. Li, T. Richardson, and G. Tsirtsis, "Toward proximity-aware internetworking," *IEEE Wireless Commun. Mag.*, vol. 17, no. 6, pp. 26–33, Dec. 2010. 85

[143] M. S. Corson, R. Laroia, J. Li, V. D. Park, T. Richardson, G. Tsirtsis, and S. Uppala, "Flashlinq: Enabling a mobile proximal internet," *IEEE Wireless Commun. Mag.*, vol. 20, no. 5, pp. 110–117, Oct. 2013. 85

[144] X. Lin, J. G. Andrews, and A. Ghosh, "Spectrum sharing for Device-to-Device communication in cellular networks," *IEEE Trans. Wireless Commun.*, vol. 13, no. 12, pp. 6727–6740, Dec. 2014. 86, 88

[145] Q. Ye, M. Al-Shalash, C. Caramanis, and J. G. Andrews, "Resource optimization in device-to-device cellular systems using time-frequency hopping," *IEEE Trans. Wireless Commun.*, vol. 13, no. 10, pp. 5467–5480, Oct. 2014. 86

[146] N. Lee, X. Lin, J. G. Andrews, and R. W. Heath Jr., "Power control for D2D underlaid cellular networks: Modeling, algorithms and analysis," *IEEE J. Select. Areas Commun.*, vol. 33, no. 1, pp. 1–13, Jan. 2015. 86

[147] D. Wu, J. Wang, R. Q. Hu, Y. Cai, and L. Zhou, "Energy-efficient resource sharing for mobile Device-to-Device multimedia communications," *IEEE Trans. Veh. Technol.*, vol. 63, no. 5, pp. 2093–2103, Jun. 2014. 86

[148] A. Hasan and J. G. Andrews, "The guard zone in wireless ad hoc networks," *IEEE Trans. Wireless Commun.*, vol. 6, no. 3, pp. 897–906, Mar. 2007. 86

[149] F. Baccelli, J. Li, T. Richardson, S. Shakkottai, S. Subramanian, and X. Wu, "On optimizing CSMA for wide area ad-hoc networks," in *Proc. Int. Symp. Modell. Opt. Mobile, Ad-hoc Wireless Netw.*, May 2011, pp. 354–359. 98

[150] D. Torrieri and M. C. Valenti, "Exclusion and guard zones

in DS-CDMA Ad Hoc networks," *IEEE Trans. Commun.*, vol. 61, no. 6, pp. 2468–2476, Jun. 2013. 87

[151] G. Alfano, M. Garetto, and E. Leonardi, "New directions into the stochastic geometry analysis of dense CSMA networks," *IEEE Trans. Mobile Comput.*, vol. 13, no. 2, pp. 324–336, Feb. 2014. 86

[152] M. Haenggi, "Mean interference in hard-core wireless networks," *IEEE Commun. Lett.*, vol. 15, no. 8, pp. 792–794, Aug. 2011. 86, 91, 97

[153] Y. Zhong, W. Zhang, and M. Haenggi, "Stochastic analysis of the mean interference for the RTS/CTS mechanism," in *Proc. IEEE Int. Conf. Commun.*, Jun. 2014, pp. 1996–2001. 86, 87, 91

[154] S. Cho and W. Choi, "Relay cooperation with guard zone to combat interference from an underlaid network," in *Proc. IEEE Global Commun. Conf.*, Dec. 2011, pp. 1–5. 86

[155] X. Wu, S. Tavildar, S. Shakkottai, T. Richardson, J. Li, R. Laroia, and A. Jovicic, "FlashLinQ: A synchronous distributed scheduler for peer-to-peer ad hoc networks," in *Proc. Annual Allerton Conf. Commun., Cont., Computing*, Sep. 2010, pp. 514–521. 86

[156] F. Baccelli, B. Blaszczyszyn, and P. Muhlethaler, "Stochastic analysis of spatial and opportunistic Aloha," *IEEE J. Select. Areas Commun.*, vol. 27, no. 7, pp. 1105–1119, Sep. 2009. 88

[157] M. Haenggi, "Local delay in Poisson networks with and without interference," in *Proc. Annual Allerton Conf. Commun., Cont., Computing*, Sep. 2010, pp. 1482–1487. 88

[158] F. Baccelli, J. Li, T. Richardson, S. Shakkottai, S. Subramanian, and X. Wu, "On optimizing CSMA for wide area ad-hoc networks," in *Proc. Int. Symp. Modell. Opt. Mobile, Ad-hoc Wireless Netw.*, May 2011, pp. 354–359. 88

[159] N. Lee, F. Baccelli, and R. W. Heath Jr., "Spectral efficiency scaling laws in dense random wireless networks with multiple receive antennas," *IEEE Trans. Inform. Theory*, vol. 62, no. 3, pp. 1344–1359, Mar. 2016. 88

[160] P. Madhusudhanan, J. G. Restrepo, Y. E. Liu, and T. X. Brown, "Carrier to Interference ratio analysis for the shotgun cellular system," in *Proc. IEEE Global Commun. Conf.*, Honolulu, USA, Nov. 2009, pp. 1–6. 89

[161] B. Cho, K. Koufos, and R. Jäntti, "Bounding the mean inter-

ference in Matérn type II hard-core wireless networks," *IEEE Wireless Commun. Lett.*, vol. 2, no. 5, pp. 563–566, Oct. 2013. 97

[162] H. Yoon, J. S. Kim, S. J. Bae, B. Choi, and M. Y. Chung, "Performance analysis of FlashLinQ with various yielding threshold values," in *Proc. Int. Conf. ICT Convergence*, Oct. 2012, pp. 477–478. 106

[163] X. Zhang and J. G. Andrews, "Downlink cellular network analysis with multi-slope path loss models," *IEEE Trans. Commun.*, vol. 63, no. 5, pp. 1881–1894, May 2015. 108

[164] D. Bharadia and S. Katti, "Full duplex MIMO radios," in *Proc. 11th USENIX Symposium on Networked Systems Design and Implementation*, Apr. 2014, pp. 359–372. 112, 143

[165] G. Caire, N. Jindal, M. Kobayashi, and N. Ravindran, "Multiuser MIMO achievable rates with downlink training and channel state feedback," *IEEE Trans. Inform. Theory*, vol. 56, no. 6, pp. 2845–2866, Jun. 2010. 113, 118, 120, 158

[166] A. AlAmmouri, H. ElSawy, O. Amin, and M. S. Alouini, "In-band full-duplex communications for cellular networks with partial uplink/downlink overlap," in *Proc. IEEE Global Commun. Conf.*, Dec. 2015, pp. 1–7. 114

[167] T. D. Novlan, H. S. Dhillon, and J. G. Andrews, "Analytical modeling of uplink cellular networks," *IEEE Trans. Commun.*, vol. 12, no. 6, pp. 2669–2679, Jun. 2013. 114

[168] J. G. Andrews, A. K. Gupta, and H. S. Dhillon, "A primer on cellular network analysis using stochastic geometry," 2016, available online: https://arxiv.org/abs/1604.03183/. 114

[169] L. Choi and R. D. Murch, "A transmit preprocessing technique for multiuser MIMO systems using a decomposition approach," *IEEE Trans. Wireless Commun.*, vol. 3, no. 1, pp. 20–24, Jan. 2004. 117

[170] T. Sarkar, Z. Ji, K. Kim, A. Medouri, and M. Salazar-Palma, "A survey of various propagation models for mobile communication," *IEEE Antennas Propagat. Mag.*, vol. 45, no. 3, pp. 51–82, Jun. 2003. 117

[171] 3GPP TR 36.828 V11.0.0, "Further Enhancements to LTE Time Division Duplex (TDD) for Downlink-Uplink (DL-UL) Interference Management and Traffic Adaptation," 3rd Generation Partnership Project 3GPP, www.3gpp.org, Tech. Rep., Jun. 2012. 118, 121, 129, 135, 143

[172] W. C. Y. Lee, "Estimate of channel capacity in rayleigh fading environments," *IEEE Trans. Veh. Technol.*, vol. 39, no. 3, pp. 187–189, Aug. 1990. 124

[173] L. Ozarow, S. Shamai, and A. D. Wyner, "Information theoretic considerations for cellular mobile radio," *IEEE Trans. Veh. Technol.*, vol. 43, no. 2, pp. 359–378, May 1994. 124

[174] S. Catreux, P. F. Driessen, and L. J. Greenstein, "Data throughputs using multiple-input multiple-output (MIMO) techniques in a noise-limited cellular environment," *IEEE Trans. Wireless Commun.*, vol. 1, no. 2, pp. 226–235, Apr. 2002. 124

[175] H. Elshaer, F. Boccardi, M. Dohler, and R. Irmer, "Downlink and uplink decoupling: A disruptive architectural design for 5G networks," in *Proc. IEEE Global Commun. Conf.*, Dec. 2014, pp. 1798–1803. 134

[176] C. Suh and K. Ramchandran, "Exact-repair MDS code construction using interference alignment," *IEEE Trans. Inform. Theory*, vol. 57, no. 3, pp. 1425–1442, Mar. 2011. 141

[177] N. B. Shah, K. V. Rashmi, P. V. Kumar, and K. Ramchandran, "Interference alignment in regenerating codes for distributed storage: Necessity and code constructions," *IEEE Trans. Inform. Theory*, vol. 58, no. 4, pp. 2134–2158, Apr. 2012.

[178] V. R. Cadambe, S. A. Jafar, H. Maleki, K. Ramchandran, and C. Suh, "Asymptotic interference alignment for optimal repair of MDS codes in distributed storage," *IEEE Trans. Inform. Theory*, vol. 59, no. 5, pp. 2974–2987, May 2013. 141

[179] F. Adib, S. Kumar, O. Aryan, S. Gollakota, and D. Katabi, "Interference alignment by motion," in *Proc. ACM int. conf. on Mobile comp. and net.*, Sep. 2013, pp. 279–290. 142

[180] B. Chen, V. Yenamandra, and K. Srinivasan, "Interference alignment using shadow channel," in *Proc. IEEE INFOCOM*, Apr. 2015, pp. 2128–2136. 142

[181] K. Venugopal, M. C. Valenti, and R. W. Heath Jr., "Interference in finite-sized highly dense millimeter wave networks," in *Proc. IEEE Int. Symp. Inform. Theory and its Applications*, Feb. 2015, pp. 175–180. 142

[182] G. George and A. Lozano, "Impact of reflections in enclosed mmwave wearable networks," in *Proc. IEEE Int. Works. on Comput. Adv. in Multi-Sensor Adaptive Process.*, Dec. 2015,

pp. 201–204. 142

[183] G. J. Foschini and Z. Miljanic, "A simple distributed autonomous power control algorithm and its convergence," *IEEE Trans. Veh. Technol.*, vol. 42, no. 4, pp. 641–646, Apr. 1993. 142

[184] P. Hande, S. Rangan, M. Chiang, and X. Wu, "Distributed uplink power control for optimal SIR assignment in cellular data networks," *IEEE/ACM Trans. Networking*, vol. 16, no. 6, pp. 1420–1433, Dec. 2008. 142

[185] X. Yi and G. Caire, "ITLinQ+: An improved spectrum sharing mechanism for device-to-device communications," in *Proc. Annual Asilomar Conf. Signals, Syst., Comp.*, Nov. 2015, pp. 1310–1314. 142

[186] Y. Choi and H. Shirani-Mehr, "Simultaneous transmission and reception: Algorithm, design and system level performance," *IEEE Trans. Wireless Commun.*, vol. 12, no. 12, pp. 5992–6010, Dec. 2013. 143

[187] O. Simeone, E. Erkip, and S. Shamai, "Full-duplex cloud radio access networks: An Information-Theoretic viewpoint," *IEEE Wireless Commun. Lett.*, vol. 3, no. 4, pp. 413–416, Aug. 2014. 143

– Notes –

– Notes –

– Notes –

– Notes –